Journal of Heat Transfer

Published Monthly by ASME

VOLUME 127 • NUMBER 6 • JUNE 2005

ASME
SETTING THE STANDARD
1880 2005

HEAT TRANSFER DIVISION
Chair, **R. D. SKOCYPEC**
Vice Chair, **M. K. JENSEN**
Past Chair, **Y. BAYAZITOGLU**
Secretary, **T. W. TONG**
Treasurer, **CHANG H. OH**
Member, **RODNEY W. DOUGLASS**

Editor, **V. DHIR** (2005)

Associate Editors,
S. ACHARYA (2006)
N. K. ANAND (2006)
G. CHEN (2005)
J. N. CHUNG (2005)
A. F. EMERY (2005)
B. FAROUK (2006)
S. V. GARIMELLA (2007)
C. P. GRIGOROPOULOS (2006)
S. G. KANDLIKAR (2007)
J. M. KHODADADI (2007)
K. KIHM (2005)
J. H. LIENHARD V (2006)
P. M. LIGRANI (2006)
R. M. MANGLIK (2006)
C. H. OH (2007)
R. PITCHUMANI (2007)
V. PRASAD (2005)
R. P. ROY (2007)
K. A. THOLE (2007)
S. THYNELL (2005)
S. PRATAP VANKA (2005)

PUBLICATIONS DIRECTORATE
Chair, **ARTHUR G. ERDMAN**

OFFICERS OF THE ASME
President, **HARRY ARMEN**
Executive Director,
VIRGIL R. CARTER
Treasurer,
T. PESTORIUS

PUBLISHING STAFF
Managing Director, Engineering
THOMAS G. LOUGHLIN

Director, Technical Publishing
PHILIP DI VIETRO

Production Coordinator
COLIN McATEER

Production Assistant
MARISOL ANDINO

RESEARCH PAPERS

Conduction

Evaporation, Boiling, and Condensation

Experimental Techniques

Forced Convection

Natural and Mixed Convection

Porous Media

(Contents continued on inside back cover)

This journal is printed on acid-free paper, which exceeds the ANSI Z39.48-1992 specification for permanence of paper and library materials. ♾™
♲ 85% recycled content, including 10% post-consumer fibers.

Transactions of the ASME, Journal of Heat Transfer (ISSN 0022-1481) is published monthly by The American Society of Mechanical Engineers, Three Park Avenue, New York, NY 10016. Periodicals postage paid at New York, NY and additional mailing offices. POSTMASTER: Send address changes to Transactions of the ASME, Journal of Heat Transfer, c/o THE AMERICAN SOCIETY OF MECHANICAL ENGINEERS, 22 Law Drive, Box 2300, Fairfield, NJ 07007-2300. **CHANGES OF ADDRESS** must be received at Society headquarters seven weeks before they are to be effective. Please send old label and new address. **STATEMENT from By-Laws.** The Society shall not be responsible for statements or opinions advanced in papers or ... printed in its publications (B7.1, Para. 3).
COPYRIGHT © 2005 by The American Society of Mechanical Engineers. For authorization to photocopy material for internal or personal use under those circumstances not falling within the fair use provisions of the Copyright Act, contact the Copyright Clearance Center (CCC), 222 Rosewood Drive, Danvers, MA 01923, tel: 978-750-8400, www.copyright.com. Request for special permission or bulk copying should be addressed to Reprints/Permission Department.
Canadian Goods & Services Tax Registration #126148048

Downloaded 05 Feb 2011 to 141.219.44.39. Redistribution subject to ASME license or copyright; see http://www.asme.org/terms/Terms_Use.cfm

(**Contents continued**)

Journal of Heat Transfer **Volume 127, Number 6** **JUNE 2005**

TECHNICAL BRIEFS

The ASME Journal of Heat Transfer is abstracted and indexed in the following:

Applied Science and Technology Index, Chemical Abstracts, Chemical Engineering and Biotechnology Abstracts (Electronic equivalent of Process and Chemical Engineering), Civil Engineering Abstracts, Compendex (The electronic equivalent of Engineering Index), Corrosion Abstracts, Current Contents, E & P Health, Safety, and Environment, Ei EncompassLit, Engineered Materials Abstracts, Engineering Index, Enviroline (The electronic equivalent of Environment Abstracts), Environment Abstracts, Environmental Engineering Abstracts, Environmental Science and Pollution Management, Fluidex, Fuel and Energy Abstracts, Index to Scientific Reviews, INSPEC, International Building Services Abstracts, Mechanical & Transportation Engineering Abstracts, Mechanical Engineering Abstracts, METADEX (The electronic equivalent of Metals Abstracts and Alloys Index), Petroleum Abstracts, Process and Chemical Engineering, Referativnyi Zhurnal, Science Citation Index, SciSearch (The electronic equivalent of Science Citation Index), Theoretical Chemical Engineering

Downloaded 05 Feb 2011 to 141.219.44.39. Redistribution subject to ASME license or copyright; see http://www.asme.org/terms/Terms_Use.cfm

An Effective Unit Cell Approach to Compute the Thermal Conductivity of Composites With Cylindrical Particles

Deepak Ganapathy

Kulwinder Singh

Patrick E. Phelan[1]

Phone: (480) 965-1625
e-mail: phelan@asu.edu

Department of Mechanical and Aerospace Engineering, Arizona State University, Tempe, AZ 85287-6106

Ravi Prasher[2]

Assembly Technology Development, Intel Corporation, Chandler, AZ 85226-3699

This paper introduces a novel method, combining effective medium theory and the finite differences method, to model the effective thermal conductivity of cylindrical-particle-laden composite materials. Typically the curvature effects of cylindrical or spherical particles are ignored while calculating the thermal conductivity of composites containing such particles through numerical techniques, such that the particles are modeled as cuboids or cubes. An alternative approach to mesh the particles into small volumes is just about impossible, as it leads to highly intensive computations to get accurate results. On the other hand, effective medium theory takes the effect of curvature into account, but cannot be used at high volume fractions because it does not take into account the effects of percolation. In this paper, a novel model is proposed where the cylindrical particles are still treated as squares (cuboids), but to capture the effect of curvature, an effective conductivity is assigned to the particles by using the effective medium approach. The authors call this the effective unit cell approach. Results from this model for different volume fractions, on average, have been found to lie within ±5% of experimental thermal conductivity data. [DOI: 10.1115/1.1915387]

Introduction

Particle-laden composite materials are widely used in applications ranging from electronics cooling [1] to space craft [2]. Composite materials made of particles and base matrixes such as ceramics or polymers are widely used for electrical, thermal and structural reasons [1]. It is relatively easy to compute the thermal conductivity of particle-laden systems either in the small particle volume fraction regime, or the very high particle volume fraction regime, as several approximations can be invoked [3]. For the intermediate particle volume fraction regime, one has to normally resort to numerical techniques such as the finite differences method [4] or percolation models [5] to compute the thermal conductivity of composites. A review of literature suggests that in numerical simulations typically the particles are assumed to be squares/rectangles in two-dimensional problems, or cubes/cuboids in three-dimensional problems [4–7]. To simulate a circular geometry such as cylinders or spheres, various researchers have used a cubical geometry and applied a shape factor to account for the curvature effects [7,8]. This is primarily done to simplify the calculations. For example, in the finite differences method, it becomes very easy to define the grid if the geometry of the particles is assumed to follow a square or rectangular shape. Ideally, to simulate spherical or circular particles, one should also discretize the particles into a large number of grids to accurately capture the flow of heat from the matrix to the particle and also within the particle as shown in Fig. 1. Due to the curvature effect, the heat flow lines in the circular geometry are very different from those for the square geometry. The effect of curvature becomes even more important as the volume fraction crosses the percolation threshold [5] because after the percolation threshold, the particles are in close contact with each other resulting in more constriction of the heat flow lines around the particles. Discretizing the particles into a large number of elements can capture the curvature effect and is conceptually very simple, but will lead to a time-consuming code due to the size of the bulk composite. For this reason, the particles are normally assumed to be square or rectangular so that the particle itself can be taken as a node. However, this method suffers from two flaws and will always give a higher value of thermal conductivity for circular/spherical particle-laden systems when compared to a case where computation is done with discretization of the particles as well. The first reason is that it does not take care of the constriction of the heat flow lines due to the curvature effect, and the second reason is that it assigns a higher effective conductivity to the square unit cell, because the circular unit cell would have approximately only 78% of the high conductivity material and less surface area. A shape factor will *not* account for the change in volume and surface area.

Effective medium theory, on the other hand, takes the curvature effect into account [9] by assigning an appropriate temperature distribution to the particles, but is valid only for small volume fractions due to the inherent assumptions regarding the temperature distribution in the matrix [9]. In this paper, a novel technique is introduced for modeling the thermal conductivity of composites with inclusions. The method is validated for the specific case of a composite with cylindrical inclusions in a direction perpendicular to the length of the cylinder, as shown in Fig. 2, which essentially models the particle as square but also considers the curvature effect on the effective conductivity of the unit cell. The effect of the thermal boundary resistance at the interface between the two phases is also taken into account. This modeling methodology is a combination of the effective medium theory and the square unit cell approach. Since the grid is still square for numerical simulation, the computational method is similar to the usual square unit cell approach, but with a more accurate prediction of thermal conductivity compared to the square geometry approach. The authors call this model the effective unit cell model (EUCM). EUCM is compared with detailed finite element simulations of a few configurations, using the commercial software ANSYS™, to check the validity of this modeling approach to capture the cur-

---

[1] Corresponding author

[2] Adjunct Professor, Department of Mechanical and Aero Space Engineering, Arizona State University.

Contributed by the Heat Transfer Division for publication in the JOURNAL OF HEAT TRANSFER. Manuscript received October 6, 2003. Final manuscript received January 15, 2005. Review conducted by: C. P. Grigoropoulos

Copyright © 2005 by ASME

Downloaded 06 Dec 2010 to 193.140.21.150. Redistribution subject to ASME license or copyright; see http://www.asme.org/terms/Terms_Use.cfm

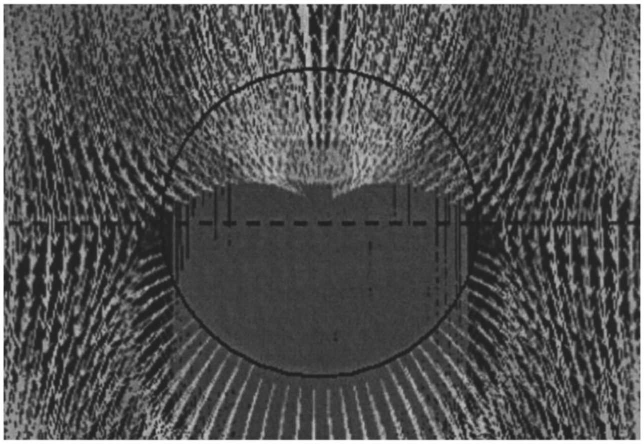

Fig. 1 ANSYS™ simulation showing constriction of heat flux lines around a circular particle

vature effect. EUCM is also compared with results from the usual square grid method, and experimental data from the literature.

Finite element simulations in ANSYS™ show the merits and limitations of this method. Comparisons with previously proposed models show this model's improved accuracy in predicting the thermal conductivity of particle-laden composites. Results from this model are within ±5% of experimental data [10] available for one such composite containing alumina fibers in a polyimide base, used in electronic packaging applications.

Modeling Methodology

The method proposed is hereby referred to as the Effective Unit Cell Model (EUCM). Uniaxial cylindrical fibers are considered to be distributed randomly in a continuous matrix of dimensions large enough to neglect size effects [7]. The geometry of the problem allows one to treat this as a two-dimensional problem of unit depth [4].

The EUCM involves the construction of a resistance network to model the thermal conductivity of the composite. For this purpose, the composite is discretized into square-shaped unit cells. The cylindrical filler particles are assumed to be randomly distributed among a rectangular lattice as shown in Fig. 2. As can be seen, the particle distribution function depends on the square unit cell size. So, only ordered systems of particles can be treated by this method. The composite is meshed in such a way that the grid size equals the diameter of the cylindrical filler particles present in the composite. For the sake of simplicity, all the filler particles are assumed to have the same diameter.

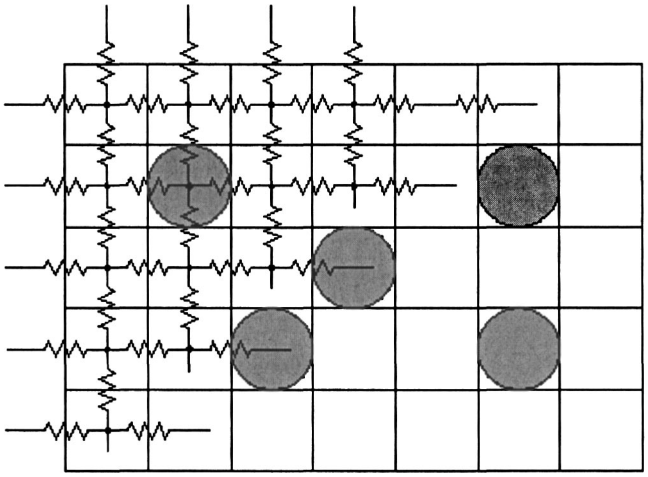

Fig. 2 Cross section of composite showing how the resistance network is constructed. Shaded regions represent higher conductivity filler particles.

The overall resistance to heat flow of the composite is accounted for by building a resistance network through the composite [4]. Each node in the resistance network represents one unit cell. The trick is to determine the resistance to heat flow between any two nodes. For this, the resistance offered by a unit cell is required. In our case, only two types of cells are present because of our assumption that all the fillers have the same diameter. The resistance of a unit cell, R, is defined as

$$R = \frac{L}{k} \tag{1}$$

where L is the overall length of the composite (m), and k is the thermal conductivity ($\mathrm{W\,m^{-1}\,K^{-1}}$). For those unit cells containing only the matrix, the matrix conductivity is taken as the value of k in Eq. (1). For unit cells containing a circular particle, the average thermal conductivity of the cell is used for calculating the resistance. The average thermal conductivity is modeled considering a single fiber placed in an infinite medium and its derivation will be discussed in the next section.

The composite is configured to lie between a heat source at temperature T_1 (upper surface) and a heat sink at temperature T_2 (lower surface). Each discrete unit cell is taken as a node in the resistance network [4]. Nodes are assumed to be at temperatures that represent the average temperature of the unit cell. Now, using a heat balance relation at every node, a system of equations is generated that can be solved to find the temperature at each node. Knowing the temperatures, the heat flow through the composite can be calculated, and thereafter the thermal conductivity. For analysis purposes, the heat transfer coefficients at the upper and lower surfaces of the composite are taken to be infinity. Finite values can also be taken but since only the bulk composite conductivity is to be considered, the surface heat transfer coefficients are assumed to be infinite. Also, this allows one to assume a constant temperature boundary condition on the top and bottom of the composite. The sides of the composite are treated as being insulated to ensure that no heat flows out through those sides [4], thus guaranteeing a unidirectional conductivity.

Since in a typical composite the actual distribution of the fillers within the composite would be unknown, the filler particles are randomly assigned to various node positions within the grid, based on the volume fraction, and the overall conductivity is calculated. The average from a number of such runs is taken as the effective conductivity of the composite [4]. The particle distribution function is thus not completely random because of its dependence upon the square grid, but by iteration, its behavior is statistically averaged.

Effective Unit Cell Model (EUCM)

The method employed to model the resistance offered by a unit cell containing a filler element in an infinite medium is described below. The temperature fields inside and outside the cylindrical dispersion are assumed to be of the general form [9,11,12]

$$T_d = rA\cos\theta \tag{2}$$

$$T_m = \nabla Tr\cos\theta + (B/r)\cos\theta \tag{3}$$

where T_d is the temperature inside the filler particle (K), T_m is the temperature of the surrounding matrix (K), r, θ are cylindrical coordinates, ∇T is temperature gradient ($\mathrm{K\,m^{-1}}$), and A,B are constants to be determined. The temperature distributions are assumed to be of this form to take into account the circular shape of the particles. This allows us to consider the effect of curvature on the heat flow lines.

Downloaded 06 Dec 2010 to 193.140.21.150. Redistribution subject to ASME license or copyright; see http://www.asme.org/terms/Terms_Use.cfm

The effect of the dispersion on the temperature distribution of the surrounding matrix is given by Eq. (3). The dispersion plays almost no part in influencing the matrix far from the particle, as is evident from the second term of Eq. (3). However, the overall temperature gradient would affect the matrix everywhere and this is represented by the first term in Eq. (3). To solve for the unknown constants A and B, the following boundary conditions are applied at the interface between the matrix and filler [9]:

$$k_d \frac{\partial T_d}{\partial r} = k_m \frac{\partial T_m}{\partial r} \tag{4}$$

$$T_d - T_m = -\frac{k_d}{h_c}\frac{\partial T_d}{\partial r} \tag{5}$$

where k_d is the thermal conductivity of a filler particle ($\mathrm{W\,m^{-1}\,K^{-1}}$), k_m is the thermal conductivity of the matrix ($\mathrm{Wm^{-1}\,K^{-1}}$), T_d, T_m are the respective temperatures (K), and h_c is the thermal contact conductance between a particle and the matrix ($\mathrm{m^2\,K\,W^{-1}}$). These boundary conditions represent that the heat flux is continuous [Eq. (4)], and that there exists a thermal boundary resistance [Eq. (5)]. The absence of the boundary resistance implies that the temperature field is continuous across the boundary and this is the boundary condition for the original derivation by Maxwell [11]. Upon solving Eqs. (2) and (3), the temperature fields are given as

$$T_d = \nabla Tr\cos\theta \frac{2\left(\frac{k_m}{k_d}\right)}{\left(\frac{k_m}{k_d}\right)+\left(\frac{k_m}{ah_c}\right)+1} \tag{6}$$

$$T_m = \nabla Tr\cos\theta + \frac{\nabla Ta^2\cos\theta}{r}\frac{\left(\frac{k_m}{k_d}\right)+\left(\frac{k_m}{ah_c}\right)-1}{\left(\frac{k_m}{k_d}\right)+\left(\frac{k_m}{ah_c}\right)+1} \tag{7}$$

From these results, one can note that when $h_c \to \infty$, T_d and T_m reduce to Rayleigh's solution [12]:

$$T_d = \nabla Tr\cos\theta\frac{2k_m}{k_m+k_d} \tag{8}$$

$$T_m = \nabla Tr\cos\theta + \frac{\nabla Ta^2\cos\theta}{r}\left(\frac{k_m-k_d}{k_m+k_d}\right) \tag{9}$$

Now that the temperature distribution is known, the effective thermal conductivity can be calculated as follows. For convenience, Eqs. (6) and (7) are transformed into Cartesian form,

$$T_d = \nabla Tx\frac{2\left(\frac{k_m}{k_d}\right)}{\left(\frac{k_m}{k_d}\right)+\left(\frac{k_m}{ah_c}\right)+1} \tag{10}$$

$$T_m = \nabla Tx + \frac{\nabla Ta^2x}{x^2+y^2}\frac{\left(\frac{k_m}{k_d}\right)+\left(\frac{k_m}{ah_c}\right)-1}{\left(\frac{k_m}{k_d}\right)+\left(\frac{k_m}{ah_c}\right)+1} \tag{11}$$

Consider the small differential strip $ABCD$ shown in Fig. 3. At the center of the unit cell, the heat flux in the x direction, Q, flowing through the differential strip is

$$dQ = -k_d\left.\frac{\partial T_d}{\partial x}\right|_{x=0} \tag{12}$$

The average thermal conductivity of the differential strip, k_{ABCD}, is determined from:

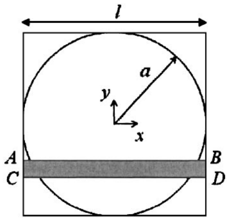

Fig. 3 Unit cell with dispersion (temperature gradient along the *x*-direction)

$$dQ = -k_{ABCD}\left(\frac{T_{BD}-T_{AC}}{l}\right) \tag{13}$$

where l is the grid size.

The temperatures at the ends of the strip are taken to be uniform because the strip is very small. Combining Eqs. (10)–(13), k_{ABCD} can be determined using simple algebra. The expression obtained is independent of the external artificially applied temperature gradient, as expected. This expression is then integrated over the entire cell length in the y direction to calculate the overall thermal conductivity of the unit cell, k_{unit},

$$k_{\mathrm{unit}} = \frac{k_m(1-C_1)}{l}\int_{-l/2}^{l/2}\frac{(y^2+(l/2)^2)}{(y^2+(l/2)^2+a^2C_1)}dy \tag{14}$$

where C_1 is a constant defined as,

$$C_1 = \frac{(k_m/k_d)+(k_m/ah_c)-1}{(k_m/k_d)+(k_m/ah_c)+1} \tag{15}$$

Taking the grid size to be the same as the particle diameter, the final expression for k_{unit} is obtained:

$$k_{\mathrm{unit}} = k_m(1-C_1)\left[1-\frac{C_1}{\sqrt{C_1+1}}\tan^{-1}\left(\frac{1}{\sqrt{C_1+1}}\right)\right] \tag{16}$$

Equation (16) is the average, or overall, thermal conductivity of a unit cell containing a filler particle, when the grid size is equal to the particle diameter. The thermal conductivity obtained by this equation is independent of the size of the unit cell, which is logical because if the scale of the unit cell changes, the volume fraction and orientation of each material would still remain the same. This value is then used to calculate the resistance offered by this type of unit cell in the network. Even though it has been modeled based on an infinite medium, it can readily be used for the resistance network because the overall system is sufficiently large, compared to the unit cell, to assume it to be infinite. If an average gap between the particles exists, it can be incorporated either via this equation or later through the application of a corresponding interfacial resistance. It becomes increasingly difficult to capture the heat flow accurately in FEA methods as the particles come closer because of the difficulty in meshing the small gap between the particles. All simulations in this work assume the worst possible case, that there exists zero gap between the particles when the particles are touching each other.

Before proceeding to the simulation of the resistive network, the results of a few simple checks performed on the general equation [Eq. (14)] are described below.

Case (1): When the dispersion and the matrix are the same material, the conductivity of the unit cell is equal to that of the matrix.

If $k_d = k_m$ and $h_c \to \infty$, then $k_{\mathrm{unit}} = k_m$.

Case (2): When the dispersion is a perfect insulator, the conductivity of the unit cell is zero.

If $k_d = 0$ and $h_c \to 0$, then $k_{\mathrm{unit}} = 0$.

These results are expected under these conditions and show the model's validity for the above limiting cases.

Downloaded 06 Dec 2010 to 193.140.21.150. Redistribution subject to ASME license or copyright; see http://www.asme.org/terms/Terms_Use.cfm

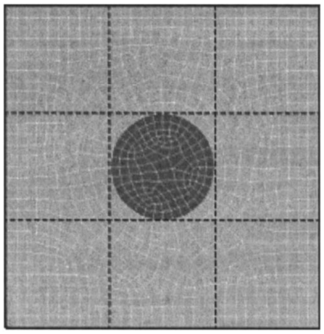

Fig. 4 Completely meshed ANSYS™ model for a 3×3 matrix with center filler particle

From this knowledge of the resistances, let us now proceed to the resistance network model. A known temperature gradient is applied to the composite. The system of linear equations is generated in a straightforward manner by summing up all the heat flows for each node and equating to zero. The general equation employed at node (i,j) is [4]:

$$\frac{T_{i-1,j}-T_{i,j}}{R_{ij,1}}+\frac{T_{i,j+1}-T_{i,j}}{R_{ij,3}}+\frac{T_{i+1,j}-T_{i,j}}{R_{ij,2}}+\frac{T_{i,j-1}-T_{i,j}}{R_{ij,4}}=0 \quad (17)$$

where T is the temperature (K), R_{ij} the resistance between nearest neighbor unit cells, and i, j the indices used for meshing the composite. The number of equations obtained will be equal to the number of nodes. This matrix system is solved to obtain the temperature of each node.

Knowing the temperatures at each node, the total heat flowing through the composite can be determined. Considering the heat transfer coefficients of the upper and lower surfaces, the following expression for the overall thermal resistance of the bulk composite and its surface per unit area is obtained, R_{eff}:

$$R_{\mathrm{eff}}=\frac{1}{h_1A}+\frac{H}{k_{\mathrm{eff}}A}+\frac{1}{h_2A}=\frac{T_1-T_2}{QA} \quad (18)$$

$$k_{\mathrm{eff}}=\frac{HQh_1h_2}{(T_1-T_2)h_1h_2-Q(h_1+h_2)} \quad (19)$$

where k_{eff} is the effective composite thermal conductivity ($\mathrm{W\,m^{-1}\,K^{-1}}$), L,H the dimensions of the composite (m), h_1 and h_2 the heat transfer coefficients of the upper and lower surfaces ($\mathrm{m^2\,K\,W^{-1}}$), T_1 and T_2 the temperatures of the upper and lower surfaces of the composite (K), and Q the heat flux through the composite ($\mathrm{W\,m^{-2}}$). The effective conductivity of the composite, k_{eff}, is calculated from the above expression.

In order to obtain a statistically significant average value for k_{eff}, the simulations are run a number of times. The number of iterations was varied between 1 and 1000, and an optimal value of 200 iterations (corresponding to an average error of 0.3%) is used in this paper. This error is calculated by assuming that the thermal conductivity obtained by using 1000 iterations is correct. Round-off and truncation errors are considered negligible, and thus our numerical uncertainty is estimated as ±0.3%.

Results

One of the first comparisons made was with the accurate solution given by a finite element package [13], ANSYS™—Release 5.7. A number of configurations of the composite, Figs. 4–6, were modeled in ANSYS™ and the results obtained are compared with the EUCM (Table 1). All the configurations studied are such that no filler particle is in contact with the upper or lower boundary of the composite. This is to ensure that the artificially enforced constant temperature boundary conditions on these surfaces do not invalidate the boundary conditions assumed in deriving the conductivity of the unit cell, k_{unit}. This error diminishes as the particle size becomes smaller relative to the domain size.

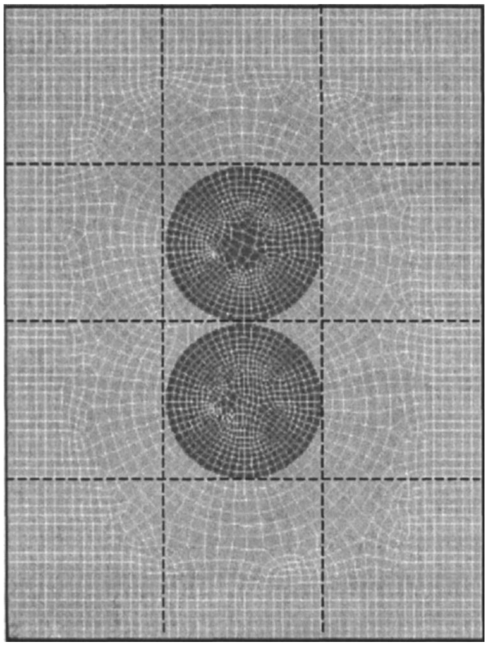

Fig. 5 Completely meshed 4×3 ANSYS™ model with 2 filler particles

To ensure that the results are independent of the thickness of the computational domain, the effect of the thickness of the composite in the heat flow direction was considered. This nondimensional domain size, D, is defined as the smaller length of the composite cross section divided by the particle diameter. Its effect is such that at larger D, the bulk composite property is recovered. At smaller values of D, it is well known that effective conductivity of the composite increases compared to the bulk value [6] due to a decrease in the percolation threshold. It is also well known that this effect is more pronounced for larger conductivity contrast as shown in Fig. 7 because percolation effects are more pronounced for large conductivity contrast. Therefore care should be taken when comparing the computational model with experimental data. The data in the current study are those of a bulk material and so all simulations have been run at a D value of 15 to ensure that bulk properties are obtained. Figure 7 shows that this is an acceptable value. Also, the boundary condition invalidation error discussed earlier is the reason why the smallest volume that has been simulated for FEA comparison is a D value of 3. Generally, D values of 2 are also acceptable but anything smaller will invalidate the boundary conditions assumed and so are not considered.

Mesh sensitivity calculations performed show that the results from ANSYS™ become independent of the mesh size at about 0.3 units of length for the studied configurations. In other words, the ratio of the grid size in the ANSYS™ method to that in the EUCM method is 0.3. This mesh size is used for all ANSYS™ computations.

Table 1 presents the comparison of thermal conductivity values between the "exact" solution from ANSYS™ and the EUCM model for the different configurations. Even for the coarsest mesh of the configuration in Fig. 4, ANSYS™ divides the composite into approximately 900 elements. This makes it computationally challenging when dealing with large-sized composites and consequently the largest composite system treated in this paper for comparison with ANSYS™ is a 5×5 matrix.

The comparison shows us that the EUCM model remains accu-

Downloaded 06 Dec 2010 to 193.140.21.150. Redistribution subject to ASME license or copyright; see http://www.asme.org/terms/Terms_Use.cfm

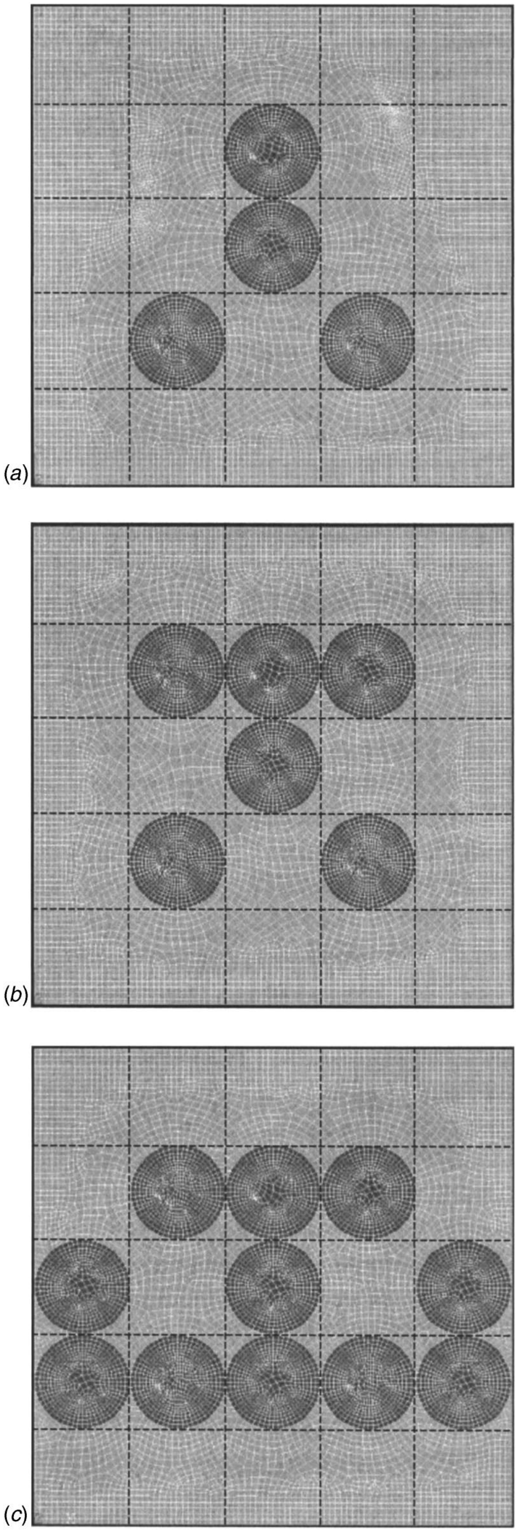

Fig. 6 *(a)* **Completely meshed 5×5 ANSYS™ model with 4 filler particles** *(b)* **Completely meshed 5×5 ANSYS™ model with 6 filler particles** *(c)* **Completely meshed 5×5 ANSYS™ model with 11 filler particles**

Table 1 Comparison of ANSYS™ and EUCM results for the effective thermal conductivity of various configurations. Terms within brackets represent the number of grids created to obtain the result.

Configuration of composite	Effective Thermal Conductivity, k_{eff} (W m^{-1} K^{-1})	
	ANSYS™	EUCM
Figure 4	0.174 (~2500)	0.171 (3×3)
Figure 5	0.214 (~4000)	0.207 (4×4)
Figure 6a	0.206 (~7500)	0.195 (5×5)
Figure 6b	0.223 (~9000)	0.214 (5×5)
Figure 6c	0.295 (~12000)	0.297 (5×5)

rate even though it meshes the composite into only a few unit cells. This makes it computationally viable while still maintaining accuracy. On the other hand, FE methods (like ANSYS™) do not have any limitations on particle arrangement. And meshing algorithms for 2D volumes take only a modest amount of time even on a personal computer. The real advantage of the EUCM model is that it can be used to simulate the *effective* properties of real bulk composites, which for random composites can only be given in terms of a statistical average. Here, for example, in the results to follow, a total of 200 runs are performed for each data point. To perform the equivalent calculation in ANSYS™ would thus require positioning the particles, remeshing, and running the code 200 times, which if done manually would be exceedingly time-consuming. In view of this, several simple geometries, Figs. 4–6, are used for comparing EUCM with ANSYS™ with the sole purpose of establishing the accuracy of the EUCM model.

The EUCM has been found to be accurate while at the same time being computationally viable. It is able to portray random distributions of the filler particles while also allowing preferential distribution. These two reasons make it a powerful technique for studying the thermal conductivity of particle-laden systems.

In Fig. 8, the EUCM prediction of the average thermal conductivity for the studied composite, alumina fibers (27 W m^{-1} K^{-1}) in a polyimide base (0.146 W m^{-1} K^{-1}), is compared with experimental data [10] and the EMT approach [9]. The figure also shows the calculated thermal conductivity of square cross-section fibers [4] for the range of volume fractions.

It is found that the EUCM model matches to within ±5% of the experimental data while the EMT predicts a much lower thermal conductivity for volume fractions greater than the percolation threshold (~0.4) [5].

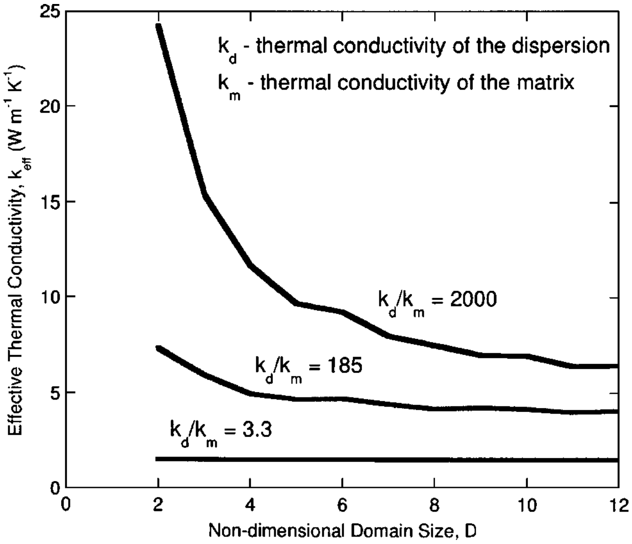

Fig. 7 Effect of ***D*** **on the effective conductivity of the composite at a volume fraction of 0.4. Larger** ***D*** **signifies bulk property of composite. Ratio of 185 corresponds to the composite for which experimental data [10] is available.**

Downloaded 06 Dec 2010 to 193.140.21.150. Redistribution subject to ASME license or copyright; see http://www.asme.org/terms/Terms_Use.cfm

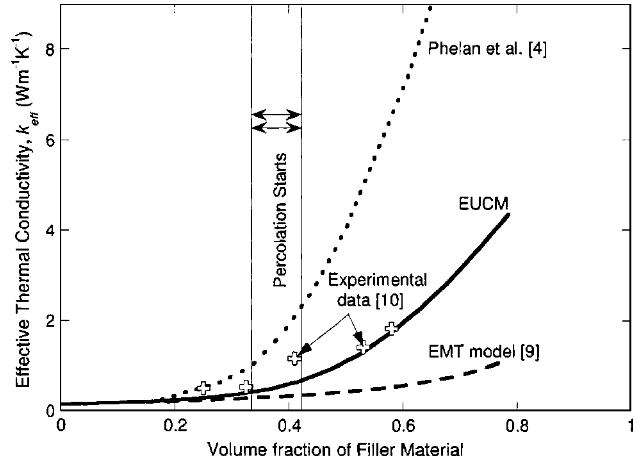

Fig. 8 Comparison of various models with experimental data [10], for $h_c = \infty$ W m^{-2} K^{-1}

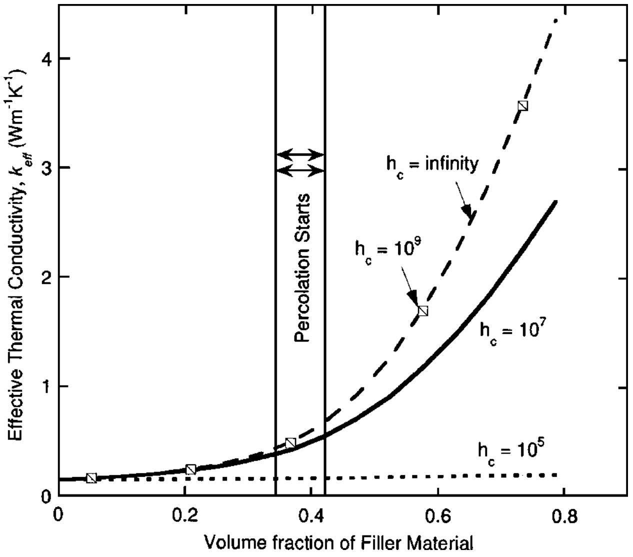

Fig. 9 Effect of varying h_c (W m^{-2} K^{-1}) predicted by EUCM

In terms of the physics of phase transitions, the percolation threshold gives the position of a phase transition. At a phase transition, the system changes its behavior qualitatively for one particular value of a continuously varying parameter. After the percolation threshold, the probability of the particles being in contact with one another becomes large and the effect of particles interacting with each other cannot be neglected. When high conductivity particles are in contact with one another, they produce a path of low resistance for heat to flow and this would contribute to an increase in the effective conductivity [14,15]. For this reason, the impact of the geometric distribution, termed as percolation, become critical.

At high volume fractions, the EMT fails to account for the percolation phenomenon because simple summation of the influence of different filler particles on the matrix will not take this into account. The interactions between the neighboring filler particles become more and more important as the volume fraction and consequently the probability that particles are going to be close to each other increases. Since the EMT assumes noninteracting filler particles, it consistently predicts a lower-than-actual conductivity at high volume fractions.

In the EUCM model, the temperature of any node depends on the properties of all the unit cells. Since the coefficients of the linear temperature equations, Eq. (17), are the resistances, all the nodal temperatures depend on the resistance and the position of each unit cell. Thus the temperature distribution of the bulk composite takes into consideration the interactions between every filler particle in the composite by solving the implicit system of equations. This is why EUCM works much better than EMT at high volume fractions.

Figure 8 also shows that for the same volume fraction, a composite having square-shaped filler particles will have a much higher effective conductivity than a composite with circular fillers. It can be understood that the transport property of a composite material depends a great deal upon the shape of the inclusions. The conductivity of a material is just the ratio of the heat flux to the temperature difference and so depends on its cross-sectional area. A square element having a much larger cross-sectional contact area as compared to a circular inclusion will have an effective conductivity much higher than the conductivity of a composite with cylindrical inclusions that can have only a point contact. This is because constriction and spreading resistances exist whenever heat flows from one region to another of different cross section. The term constriction is used to describe the situation where heat flows into a narrower region and spreading is used to describe the case where heat flows out of a narrow region into a larger cross-sectional area [16]. This constriction of the heat lines inside the cylindrical dispersion is accounted for by the derived temperature distribution and hence the EUCM takes into account the effect of shape.

Finally, Fig. 9 presents the effect of varying the value of thermal contact conductance h_c for the same set of materials as in Fig. 8, where the value of the contact resistance between the particles and the matrix was assumed to be zero when comparing the EUCM with the experimental data [10]. The composite studied is used as an interface material for electronic packaging applications, and so it is reasonable to expect h_c to be high. The figure exists just to prove that the assumed h_c is of the correct magnitude and no further validation for it is presented.

Figure 9 shows that the thermal contact resistance adversely affects the total thermal conductivity of the composite. It is often useful to consider a dimensionless variable called the Biot number when discussing thermal contact resistance between particles and a matrix. The particle Biot number, Bi, is defined as [7]:

$$\mathrm{Bi} = \frac{R_c k_m}{2a} \tag{20}$$

where $R_c = h_c^{-1}$ is the thermal contact resistance (m^2 K W^{-1}) between a particle and the matrix, k_m the thermal conductivity of the base matrix (W m^{-1} K^{-1}), and a the particle radius (m). For $h_c = 10^5$ W m^{-2} K^{-1}, it is found that the conductivity of the composite does not change at all even when the particle volume fraction is much higher than the percolation threshold. This is the critical value of the particle size for which the conductivity of a unit cell with filler particle is approximately equal to that of the matrix. The physical meaning of the critical particle diameter is that if the particle diameter is less than the critical diameter, the conductivity of the composite is less than that of the matrix [7].

It is seen that R_c has a large effect even at maximum volume fraction. This is to be expected since there will be more particles impeding the heat flow at high volume fraction, and very high values of R_c can even cause the effective conductivity of the composite to be lower than that of the matrix [7].

Discussion

The EUCM method is being introduced to facilitate computation of the thermal conductivity of particulate composites. The particles in this paper have been taken to be cylindrical in shape; however, particles of different shapes can also be modeled similarly. For treating different particle shapes, it becomes necessary to obtain the appropriate expression for the effective conductivity

Downloaded 06 Dec 2010 to 193.140.21.150. Redistribution subject to ASME license or copyright; see http://www.asme.org/terms/Terms_Use.cfm

of the unit cell, similar to the work by Hasselman et al. and Nan et al. [9,17]. Once this is done, the network can be built as before and the effective property can be determined. It is important to remember that this model can simulate only quasi-ordered systems of particles that are constrained to fit within the unit cells. Also, since composites can have particles of different sizes, adaptive meshing can be used for modeling. This versatility of the EUCM makes it appealing. Adaptive meshing has a broad sense and one can continuously find more efficient modeling techniques. For instance, if the particles were considered to be ellipsoidal in shape, a unit cell would be defined as a rectangular grid that encompasses the entire ellipse, or it can be defined as a square grid containing one half of the ellipse. Both these styles of modeling would essentially be just as accurate and one of these can be chosen depending on the application.

Close packing of the particles can also be accommodated by defining hexagonal meshes which would permit a particle to be in contact with six particles rather than the four in the square mesh used in this paper. Also, by using a nonuniform grid, the distribution function can be made completely random. The nonuniform grids can be converted to a uniform mesh in the second step of the resistance calculation. These kinds of advanced meshes would permit a higher packing fraction and better particle distribution function than currently possible and will be the focus of our future work.

The authors have found no additional experimental data for the case of cylindrical inclusions discussed in the paper. It is the objective of future work to simulate a three-dimensional system of spherical particles for which there exists numerous experimental data. Face-centered and body-centered structures can be modeled quite easily in the three-dimensional system, thus increasing the efficiency of the distribution function.

At low volume fractions, it may seem advantageous to keep the grid size larger than the particle. This way, the composite can be divided into fewer unit cells making the modeling even more computationally efficient. But such an action would result in increasing the dependence of the particle position on the grid employed. This decrease in the efficiency of the particle distribution function might be satisfactory for systems where the particle arrangement is highly ordered, and it has been determined that this change in the grid size introduces an error of a very small magnitude ($\sim 0.01\%$). However, this would be a compromise on the distribution function efficiency and it is recommended that the grid size be kept equal to the particle diameter. Also, at high volume fractions, increasing the grid size would lead to percolation being neglected because the particles would be forced to *not* be in contact with each other. So above the percolation threshold, which is approximately 0.35–0.4 in volume fraction [5], the grid size *has* to be kept equal to the particle diameter.

Conclusions

The EUCM has been shown to be an efficient method to model the effective thermal conductivity of uniaxial fiber composites with cylindrical inclusions. It is able to model the effect of percolation that the EMT fails to account for, and it takes into account the effect of curvature of the particles that the usual square particle methods do not consider. Compared to detailed finite element analysis simulations, the EUCM yields predicted conductivity values within ±5%, but with substantially less computational cost. The power of the method lies in its ability to portray any kind of composite correctly, taking into account both the shape of the individual components and the effect of percolation. Particles of different sizes and shapes can also be modeled by using adaptive meshing. Different properties, like the electrical conductivity and dielectric permittivity of a material, can also be predicted.

Nomenclature

a = radius of cylindrical inclusions (m)
A = cross-sectional area to heat flow (m^2)
Bi = Biot number defined by Eq. (20)
C_1 = constant defined by Eq. (15)
∇T = temperature gradient ($\mathrm{K\,m^{-1}}$)
D = nondimensional domain size (height, H, divided by particle diameter, $2\times a$)
h_c = thermal contact conductance ($\mathrm{W\,m^{-2}\,K^{-1}}$)
H = overall height of composite (m)
k = thermal conductivity ($\mathrm{W\,m^{-1}\,K^{-1}}$)
l = grid size (m)
L = overall length of composite (m)
Q = heat flux ($\mathrm{W\,m^{-2}}$)
r,θ = cylindrical coordinates
R = thermal resistance ($\mathrm{m^2\,K\,W^{-1}}$)
R_c = thermal contact resistance ($\mathrm{m^2\,K\,W^{-1}}$)
T = temperature (K)
x,y = Cartesian coordinates

Subscripts

1 = upper surface
2 = lower surface
3 = right surface of unit cell
4 = left surface of unit cell
A–D = differential strip in Fig. 3
d = dispersion property
eff = overall composite property
i,j = indices for mesh
m = matrix property
unit = unit cell property

References

[1] Prasher, R. S., 2001, “Surface Chemistry and Characteristics Based Model for the Thermal Contact Resistance of Fluidic Interstitial Thermal Interface Materials,” J. Heat Transfer, **123**, pp. 969–975.
[2] Smith, B., O’Callaghan, P. W., and Probert, S. D., 1984, “Use of Interstitial Materials for Thermal Contact Conductance Control,” in Proc. AIAA 22nd Aerospace Sciences Meeting, January 1984, Reno, Nevada, 1–8.
[3] Thorvert, J. F., Wary, F., and Adler, P. M., 1990, “Thermal Conductivity of Random Media and Regular Fractals,” J. Appl. Phys., **68**, pp. 3672–3883.
[4] Phelan, P. E., and Niemann, R. C., 1998, “Effective Thermal Conductivity of a Thin, Randomly Oriented Composite Material,” J. Heat Transfer, **120**, pp. 971–976.
[5] Devpura, A., Phelan, P. E., and Prasher, R. S., 2000, “Percolation Theory Applied to the Analysis of Thermal Interface Materials in Flip-Chip Technology,” Thermomechanical Phenomena in Electronic Systems-Proceedings of the Intersociety Conference, Las Vegas, Nevada, May 2000, 1, 21–28.
[6] Devpura, A., Phelan, P. E., and Prasher, R. S., 2000, “Percolation Theory Applied to Study the Effect of Shape and Size of the Filler Particles in Thermal Interface Materials,” in Proc. of International Mechanical Engineering Congress and Exposition, Orlando, November 2000.
[7] Devpura, A., Phelan, P. E., and Prasher, R. S., 2001, “Size Effects on the Thermal Conductivity of Polymers Laden with Highly Conductive Filler Particles,” Microscale Thermophys. Eng., **5**, pp. 177–189.
[8] Nielsen, L. E., 1974, “The Thermal and Electrical Conductivity of Two-Phase Systems,” Ind. Eng. Chem. Fundam., **13**, pp. 17–20.
[9] Hasselman, D. P. H., and Johnson, L. F., 1987, “Effective Thermal Conductivity of Composites with Interfacial Thermal Barrier Resistance,” J. Compos. Mater., **21**, pp. 508–515.
[10] Zhang, H., Onn, D. G., and Bolt, J. D., 1989, “Ceramic Fiber Composites for Electronic Packaging: Thermal Transport Properties,” Mater. Res. Soc. Symp. Proc., **167**, pp. 187–192.
[11] Maxwell, J. C., 1954, *A Treatise on Electricity and Magnetism*, Dover, New York, Vol. 1, pp. 435–441.
[12] Lord, Rayleigh, 1892, “On the Influence of Obstacles Arranged in Rectangular Order upon the Properties of a Medium,” Philos. Mag., **34**, pp. 481–502.
[13] Moaveni, S., 1999, *Finite Element Analysis: Theory and Application with ANSYS*, Prentice–Hall, Upper Saddle River, NJ.
[14] Stauffer, D., and Aharony, A., 1992, *Introduction to Percolation Theory*, Taylor & Francis, London.
[15] Cusack, N. K., 1987, *The Physics of Structurally Disordered Matter: An Introduction*, Adam Hilger, Bristol, Philadelphia, pp. 226–228.
[16] Lee, S., Seaho, Song V. A., and Moran, K. P., 1995, “Constriction/Spreading Resistance Model for Electronics Packaging,” ASME/JSME Thermal Engineering Conference, Vol. 4, pp. 199–206.
[17] Nan, Ce-Wen, Birringer, R., Clarke, David, R., and Gleiter, H., 1997, “Effective Thermal Conductivity of Particulate Composites with Interfacial Thermal Resistance,” J. Appl. Phys., **81**(10), pp. 6692–6699.

Downloaded 06 Dec 2010 to 193.140.21.150. Redistribution subject to ASME license or copyright; see http://www.asme.org/terms/Terms_Use.cfm

Heat Flux Determination From Measured Heating Rates Using Thermographic Phosphors

D. G. Walker
Department of Mechanical Engineering,
Vanderbilt University,
Nashville, TN 37235-1592
e-mail: greg.walker@vanderbilt.edu

A new method for measuring the heating rate (defined as the time rate of change of temperature) and estimating heat flux from the heating rate is proposed. The example problem involves analytic heat conduction in a one-dimensional slab, where the measurement location of temperature or heating rate coincides with the location of the estimated heat flux. The new method involves the solution to a Volterra equation of the second kind, which is inherently more stable than Volterra equations of the first kind. The solution for heat flux from a measured temperature is generally a first kind Volterra equation. Estimates from the new approach are compared to estimates from measured temperatures. The heating rate measurements are accomplished by leveraging the temperature dependent decay rate of thermographic phosphors (TGP). Results indicate that the new data-reduction method is far more stable than the usual minimization of temperature residuals, which results in errors that are 1.5–12 times larger than those of the new approach. Furthermore, noise in TGP measurements was found to give an uncertainty of 4% in the heating rate measurement, which is comparable to the noise introduced in the test case data. Results of the simulations and the level of noise in TGP measurements suggest that this novel approach to heat flux determination is viable. [DOI: 10.1115/1.1915389]

Introduction

Aerospace vehicles often encounter deleterious heating environments during high-speed flight. Accurate characterization of heating loads, then, is crucial to survivability of aerospace structures. In controlled tunnel tests, prediction of a heat flux incident on a test article can provide meaningful information concerning the environment that a full-scale structure will experience, whereas temperature measurements typically do not scale well from tunnel to flight conditions. Herein lies the necessity to predict heat fluxes. However, characterization of heating loads (or heat flux) in tests is not trivial because direct measurement is difficult.

Although the prediction of heat fluxes contains inherent challenges, several methods have evolved to accomplish the task with varying degrees of success. The most obvious approach to predicting heat fluxes is direct measurement with a heat flux gauge [1,2]. These gauges usually consist of a thermopile and actually measure temperature differences across a thin substrate. Assuming that the thermal conductivity and thickness of the substrate can be characterized, the heat flux can be calculated in terms of the temperature difference using Fourier's law. However, this approximation assumes that the temperature distribution in the sensor is linear, which, for transient conditions, is not strictly valid. The approximation theoretically improves as the thickness of the substrate is reduced. However, the signal to noise ratio is also reduced for thin substrates. Consequently, heating loads with high frequency transients cannot be measured accurately [1]. In general the problems associated with measurements from heat flux gauges include slow response time, flow disturbance, calibration and limited spatial resolution.

Alternatives include direct measurement via a calorimeter [3]. The heat flux can be obtained by measuring the temperature change in time of a known thermal mass. Like the heat flux gauge, these devices often suffer from slow response time and flow disturbance. Furthermore, the estimation of the heat flux from the actual measurement is complicated by the fact that the heat load may not be uniform across a surface because of lateral heat conduction [4]. Recently, new techniques for heat flux determination such as thermochromatic liquid crystals (TLC) [5] have become more popular. Conceptually, this process involves layers of crystals in thin films aligning themselves based on temperature gradients. The orientation can be inferred from spectral measurements of reflected light. The technique can provide high-density surface measurements but currently suffers from lagging response times [6] and a limited temperature range.

An attractive alternative for predicting heat fluxes is the direct measurement of temperature followed by a data reduction technique to estimate the incident flux [7] (often called the inverse heat conduction problem). In general, temperature measurement can be accomplished with acceptable precision and accuracy [8] with high frequency components [9] compared to heat flux measurements. In fact, thin film temperature measurements have become so robust and used so extensively to predict heat fluxes that the literature will often incorrectly refer to these types of measurements as heat flux measurements. However, this approach introduces its own set of difficulties. It is well known that the inverse heat conduction problem is ill-posed in the sense of Hadamard [10]. To be considered well-posed, solutions must have the following properties: existence, uniqueness, and stability. The inverse heat conduction problem is often formulated as an integral equation, which fails the uniqueness and stability tests [11]. This means that error in the heat flux estimate is unbounded [11, Theorem 1.17]. Consequently, random noise in the measurement, which is unavoidable, may become arbitrarily large.

When the conduction problem is linear and one-dimensional, analytic solutions can often be obtained for the heat flux using Duhamel's theorem [12,13]. These solutions often contain unacceptable errors [14] and lateral conduction effects are difficult to resolve [15]. Numerical analogs to these analytic methods have been developed to handle nonlinear conduction problems [16]. Unfortunately, these methods require numerical derivatives, which only exacerbate the instabilities of inverting the conduction equation [11,17].

To deal with the inherent instability of inverse problems, many researchers have developed techniques to damp large oscillations

---

Contributed by the Heat Transfer Division for publication in the JOURNAL OF HEAT TRANSFER. Manuscript received: August 19, 2003; final manuscript received: October 5, 2004; Review conducted by: George S. Dulikravich.

Copyright © 2005 by ASME

Downloaded 06 Dec 2010 to 193.140.21.150. Redistribution subject to ASME license or copyright; see http://www.asme.org/terms/Terms_Use.cfm

in the solution, such as regularization [18] and future time methods [7]. These approaches require a certain amount of bias to be added to the solution and they usually relax the exact matching of data to obtain a "fit" of the measured data by the model. The residual, which is the difference between the model temperature and the measurement, is minimized with respect to the unknown flux. Although these solution methods have proven to be extremely practical and successful, the solution requires a bit of art. Too much bias and the solution will not match the data; too little bias and the solution will contain large oscillations. Note that these solution approaches have been studied extensively, and the appropriate level of bias is usually obtained by requiring the residual to be of the order of the measurement noise [11].

Despite the apparent difficulties of reducing temperature data, the advantages of temperature measurement devices coupled with inverse techniques make this approach to heat flux determination attractive. For example, because temperature measurement devices are usually thinner than heat flux gauges [19], the time response is much better and the effect on the incident flows can be minimized. In addition, temperature measurements are easier to calibrate and the data reduction is not limited to one-dimensional estimation [20]. Therefore, it can be argued that temperature measurements and inverse data reduction techniques are preferable.

Despite advances in techniques devised to solve ill-posed problems and account for noisy data, the fact remains that appropriate data reduction remains a balancing act between introducing smoothing bias and amplification of noise. In many cases, solutions still contain unacceptable errors [12]. The present work suggests that many of the stability problems associated with the inverse heat conduction problem can be mitigated by measuring a different quantity, namely the heating rate [21,22]. The heating rate in the present context is defined as the time rate of change of temperature for a given location and time. It will be shown that the data reduction is inherently more stable if this quantity could be measured. However, no method existed (until now) to measure the heating rate directly. The heating rate approach represents a departure from typical heat flux determination methods such as those discussed briefly above, because the temperature is not explicitly required for the estimation of heat flux.

If the heating rate could be measured, the solution of the conduction equation for an unknown boundary flux becomes a Volterra equation of the second kind. It is well known that first kind Volterra equations are ill-posed in the sense of Hadamard [10], and that second-kind equations are not. In fact, many inverse solutions involve approximating the ill-posed equation by converting it to a Volterra equation of the second kind [23].

The objectives of the present work are to demonstrate a stable method for estimating heat flux from measured heating rates and to describe a technique to measure heating rate. The estimation component involves test problems with specific boundary/initial conditions and simulated noise, which is a common approach to evaluating inverse methods. The measurement technique involves the temperature sensitive decay rate of thermographic phosphors (TGP) [24]. Although TGPs have been used to measure temperature (particularly for remote measurement), the current approach will leverage particular properties of TGPs to obtain measurements, which are proportional to the heating rate, not temperature.

Thermographic phosphors are rare-earth-doped ceramics that fluoresce when exposed to ultraviolet radiation or similar excitation. In general, the intensity, frequency line shift, and decay rate are all temperature dependent. As a result, they have been used for remote temperature sensing in many applications [25]. Many materials have been used and tuned for specific applications with a great deal of success [26–28]. However, they have never been used to predict a heating rate. It is the strong dependence of the decay rate on temperature that will be leveraged to acquire a heating rate. This simple proof-of-concept described herein demonstrates the ability to extract heat fluxes with far greater accuracy than previously possible.

Theory

The following linear heat diffusion example will be used for illustration purposes. Assume one-dimensional conduction in a slab of length L. The governing equation for temperature change is given as

$$\frac{\partial^2\theta}{\partial\eta^2}=\frac{\partial\theta}{\partial\xi}, \quad 0<\eta<1, \quad \xi>0, \tag{1}$$

subject to the boundary conditions

$$-\left.\frac{\partial\theta}{\partial\eta}\right|_{\eta=0}=Q(\xi), \tag{2}$$

$$\theta(1,\xi)=0, \tag{3}$$

and the initial condition

$$\theta(\eta,0)=0. \tag{4}$$

The spatial and temporal coordinate have been nondimensionalized (i.e., $\eta=x/L$, $\xi=\alpha t/L^2$, where α is the thermal diffusivity). The heat flux $Q(\xi)$ at $\eta=0$ is a continuous function of ξ and is presumed known. Using integral transforms, the infinite series solution is found to be [29]

$$\theta(\eta,\xi)=2\sum_{m=1}^{\infty}\cos(\beta_m\eta)\int_0^{\xi}Q(\xi')e^{\beta_m^2(\xi'-\xi)}d\xi', \tag{5}$$

where the eigenvalues are the positive roots of $\cos(\beta_m)=0$, i.e., $\beta_m=(2m-1)\pi/2$ where $m=1,2,3,\ldots$.

If the heat flux $Q(\xi)$ is unknown, Eq. (5) is a Volterra equation of the first kind for a known temperature, and the solution is unstable for discrete temperature measurements. Because TGP measurement is an optical technique, measurements can only be made on the surface ($\eta=0$). If we assume that the temperature on the surface is measured at N discrete times, then an estimate for the unknown heat flux can be found using standard inverse solution techniques. It can be argued that because measurements are restricted to the boundary, inverse methods are not required. In this case, the measured surface temperature can be treated as a boundary condition for the forward conduction solution. The heat flux can then be obtained by differentiating this solution. Because measurements are discrete and contain noise, however, inverse techniques can serve to stabilize the solution [14].

In the present work, the solution for the heat flux from measured temperatures involves inverting Eq. (5). For simplicity, we assume that the time increment between each discrete measurement is constant ($\Delta\xi$) and that the integral over all times in Eq. (5) is written as a summation of integrals over each time step. The discrete temperature solution at the surface then becomes

$$Y_r=2\sum_{m=1}^{\infty}\sum_{i=1}^{r}\int_{\xi_{i-1}}^{\xi_i}Q(\xi')e^{\beta_m^2(\xi'-\xi_r)}d\xi', \tag{6}$$

where Y indicates that the temperature is a discrete measurement at the surface, not a continuous function, and r indexes time such that $\xi_r=r\Delta\xi$, $r=0,1,2,\ldots$ and $Y(\xi_r)=Y_r$. Now, the heat flux is approximated analytically by assuming a piecewise integrable function $Q(\xi')$ over each time step and solving for the unknown function parameters at each time step. Note that a piecewise constant assumption would theoretically work here. However, the summation in the heating rate formulation (developed later) does not converge in a finite number of terms without additional assumptions. Therefore the following linear approximation is considered:

Downloaded 06 Dec 2010 to 193.140.21.150. Redistribution subject to ASME license or copyright; see http://www.asme.org/terms/Terms_Use.cfm

$$Q(\xi') = Q_i - \frac{Q_i - Q_{i-1}}{\Delta\xi}(\xi_i - \xi'), \tag{7}$$

where $\Delta\xi$ is the time step size, $\xi_{i-1} < \xi' \leq \xi_i$, and $Q_i = Q(\xi_i)$. The integration can be performed analytically leading to a set of N algebraic equations

$$Y_r = 2\sum_{m=1}^{\infty}\left\{\sum_{i=1}^{r}\frac{Q_i}{\beta_m^2}\left[e^{\beta_m^2(\xi_i-\xi_r)} - e^{\beta_m^2(\xi_{i-1}-\xi_r)}\right] - \sum_{i=1}^{r}\frac{Q_i - Q_{i-1}}{\beta_m^4\Delta\xi}\left[e^{\beta_m^2(\xi_i-\xi_r)} - e^{\beta_m^2(\xi_{i-1}-\xi_r)}(1+\beta_m^2\Delta\xi)\right]\right\}. \tag{8}$$

Note that Y_0 and Q_0 are assumed to be zero. The solution of the foregoing expression leads to an estimate of the heat flux at each time step.

The proposed approach to predicting heat flux requires measurement and calculation of the heating rate. A heating rate can be found analytically by differentiating Eq. (5) with respect to time. The formulation for heating rate, given as

$$\Lambda(\eta,\xi) = \frac{\partial\theta}{\partial\xi}(\eta,\xi) = 2\sum_{m=1}^{\infty}\cos(\beta_m\eta)\left[Q(\xi) - \beta_m^2\int_0^{\xi}Q(\xi')e^{\beta_m^2(\xi'-\xi)}d\xi'\right], \tag{9}$$

suggests that the nature of the solution for heat flux is not as ill-conditioned because Eq. (9) is a Volterra equation of the second kind [30,31]. The solution approach for heat flux follows the solution from a measured temperature by evaluating Eq. (9) at the surface ($\eta=0$) and inverting. As before, the heat flux can be calculated analytically by assuming an integrable form of the heat flux over the time step and integrating. It is not immediately clear that the infinite series in Eq. (9) converges in a finite number of terms because $\Sigma_{m=1}^{\infty}Q(\xi)\to\infty$. In fact, convergence cannot be guaranteed for all functions (see Appendix). However, the Appendix shows that the infinity cancels for reasonable choices of $Q(\xi')$. For this reason, the piecewise linear function for heat flux [Eq. (7)] was chosen. This approach represents one of the simplest functions that is integrable and whose series also converges.

As before, the heat flux is determined at each time when a heating rate is measured at the surface ($\eta=0$). The integral of Eq. (9) is converted to a sum of integrals over each time step giving

$$H_r = 2\sum_{m=1}^{\infty}\left[Q_r - \beta_m^2\sum_{i=1}^{r}\int_{\xi_{i-1}}^{\xi_i}Q(\xi')e^{\beta_m^2(\xi'-\xi_r)}d\xi'\right], \tag{10}$$

where r indexes the measurements and H indicates a discrete measurement, not a continuous function. Similarly, $H_r = H(\xi_r)$ and $Q_r = Q(\xi_r)$ is implied. After applying the piecewise linear heat flux [Eq. (7)], a set of N algebraic equations is recovered as

$$H_r = 2\sum_{m=1}^{\infty}\left\{Q_r - \sum_{i=1}^{r}Q_i\left[e^{\beta_m^2(\xi_i-\xi_r)} - e^{\beta_m^2(\xi_{i-1}-\xi_r)}\right] + \sum_{i=1}^{r}\frac{Q_i - Q_{i-1}}{\beta_m^2\Delta\xi}\left[e^{\beta_m^2(\xi_i-\xi_r)} - e^{\beta_m^2(\xi_{i-1}-\xi_r)}(1+\beta_m^2\Delta\xi)\right]\right\}. \tag{11}$$

See the Appendix for full development and convergence of Eq. (11). Now the unknown heat fluxes can be solved algebraically given the heating rate measurements.

The approach for estimating heat fluxes from both measured temperatures and measured heating rate is an exact matching technique often called Stolz's method [32]. While this is not strictly an inverse method because no bias is introduced to smooth the solution, the point of the present work is to demonstrate how the use of heating rate measurements does not require the introduction of bias to obtain stable solutions. Therefore, the exact matching approach will be used to highlight the difference between the methods.

The measurement of heating rate from TGPs is not a direct measurement. Instead, the intensity of phosphor emission is measured at a sample rate that is higher than the decay rate. After a phosphor is excited (usually by an ultraviolet light pulse), the concentration of excitation centers (excited electrons) is governed by the differential equation [33]

$$\tau\frac{dn}{dt} + n = 0, \tag{12}$$

where τ is the lifetime of an excitation center. Assuming that τ is a constant in time, the solution can be written as

$$\frac{I}{I_o} = \frac{n}{n_o} = \exp\left[-\frac{t}{\tau}\right], \tag{13}$$

where the intensity I is proportional to n, and I_o and n_o are values at the beginning of the decay. The decay time τ can be estimated from a series of intensity measurements collected during the decay. If we assume that the phosphor has been completely and carefully characterized, the decay time is a material property that is a well-known function of temperature. Calibration curves are generated that relate τ to temperature for a given phosphor. By estimating τ from a single pulse, we can deduce the temperature from these calibration curves. This approach is commonly used to predict temperature from phosphor decay measurements [33]. For many interesting engineering problems, though, the temperature is not constant in time. Because the lifetime τ is generally a function of temperature, we expect τ to change in time as well. Therefore, we have augmented the model in Eq. (13) to use a first-order Taylor series expansion of the decay time to introduce the derivative of τ. Now the normalized intensity,

$$\frac{I}{I_o} = \exp\left[-\frac{t}{\tau + \dfrac{d\tau}{dt}t}\right], \tag{14}$$

contains three parameters (I_o, τ, and $d\tau/dt$) that are estimated from a series of intensity measurements using standard parameter estimation techniques [34]. This simplistic approach is strictly valid for small variations in temperature only because the derivative of the decay time is considered to be a perturbation of τ. In general, $\tau(T(t))$, so if the temperature changes significantly, the governing equation for electron concentration, must be solved for specific time dependencies of τ on time. For steady-state data (as in the present analysis), $d\tau/dt$ should be identically zero. Therefore, this approximation is justified for the present work.

The heating rate can now be computed using the chain rule as

$$\frac{d\theta}{dt} = \frac{d\theta}{d\tau}\frac{d\tau}{dt}, \tag{15}$$

where $d\theta/d\tau$ is a temperature dependent material property and is derived from the same calibration curves used to obtain temperature from decay time. The parameter of interest ($d\tau/dt$) is obtained through a fit of intensity measurements. Through test cases, we will demonstrate that prediction of $d\tau/dt$ and subsequent data reduction of $d\theta/dt$ to heat flux is inherently more stable than estimating heat flux from temperature measurements.

Results

Data reduction. To compare different methods for predicting heat flux, a known analytic function was chosen as the exact heat flux, Q, to which all estimates will be compared. Table 1 lists each type of heat flux that was examined. The exact analytic solutions to both the temperature, Y, and the heating rate, H, [Eqs. (5) and

Downloaded 06 Dec 2010 to 193.140.21.150. Redistribution subject to ASME license or copyright; see http://www.asme.org/terms/Terms_Use.cfm

Table 1 Reported values are norms of the error between the exact heat flux, Q, and the estimated heat flux Q_e, i.e., $|Q-Q_e|$ where e corresponds to the type of estimate given by the column labels

Test Case	Y	Y_n	H	H_n	H_d
zero	0	1.5171	0	0.1178	0.9488
triangle	0.0006	1.5171	0.0006	0.1181	0.9656
sine	0.3998	1.5509	0.9215	0.9149	1.9987
square	0.4914	1.4693	0.9735	0.9363	1.1972

(9), respectively] were calculated to provide the measurement data from which the estimates were derived. The time step is $\Delta\xi = 0.02$ giving 51 samples within the $\xi = 1$ duration of the experiment. Normally distributed random noise was added to the measurements to evaluate how the estimators behave when measurement error exists in the temperature, Y_n, and heating rate, H_n. The magnitude of the noise added to the temperature data has a standard deviation of $\sigma = 0.02$, which provides visual evidence of errors in the temperature for unity heat fluxes.

To provide a meaningful and fair comparison between the heating rate and temperature estimation approaches, it is not clear how much noise should be added to the heating rate data. After all, the noise is primarily a function of the measurement equipment, which is entirely different than temperature measurement devices. As a first approximation, the same noise level could be added to both data sets. However, for a given heat flux, the magnitude of the variation in heating rate is larger than the variation in temperature. For example, given a triangular heat flux with a value of unity at the peak, the maximum temperature rise is approximately 0.5. The maximum heating rate is approximately 2. Therefore, the signal is 4 times that of the temperature data. Consequently, to make the signal to noise ratio between the two data sets comparable, a noise level of 0.08 was added to the heating rate data to obtain H_n. Of course the relative magnitude of each signal varies depending on the heat flux. Nevertheless, the triangular heat flux was considered to be representative of all fluxes tested and in all cases the amount of noise added to the heating rate was four times that added to the temperature data. Note that this approach hardly seems fair in the zero flux case, when there should be zero signal.

To provide an additional comparison, a second heating rate is generated by differencing the noisy temperature data Y_n. Because noisy data is being differentiated, we expect errors associated with these data H_d to be large. Table 1 reports the error norms $|Q - Q_e|$, where Q is the exact heat flux and Q_e is the estimated heat flux indicated in the table for each set of fabricated data. In general, the errors associated with estimation based on the heating rate are less than the errors for the temperature data.

The estimates were obtained assuming a piecewise linear heat flux as described in Eqs. (11) and (8). In the case of zero flux and triangular flux, the linear approximation matches exactly with the analytic heat flux. Therefore, the error in the estimates using exact data (Y and H in Table 1) are nonzero but small. These values are nonzero because the infinite series is approximated with a finite number of terms. The number of terms used in each case was 2000. The norm of the error associated with 2000 terms is of the order of 10^{-4} for the triangular case. Using exact data for the sine case, for example, still yields a nonzero error because the integral of the piecewise linear approximation does not match the analytic solution exactly.

To establish the statistical significance of the difference between the estimates derived from different data, the sample mean $\overline{x}$ and sample variance s^2 of the errors for each simulation were calculated. Further, the distributions were checked for normality by plotting the standardized normal scores against the observed errors. A linear shape verified that all errors are normally distributed. To ensure that none of the methods contain significant bias in the solution—meaning that the estimates were consistently either over- or underpredicted—the calculated mean of the error was compared to a mean of zero. In all cases, the significance test, given by

$$\frac{\overline{x} - \mu_0}{s/\sqrt{n}} \geqslant t(\alpha; n-1), \quad \mu_0 = 0, \tag{16}$$

was satisfied for the two-sided 95% confidence level. Therefore, the use of Eqs. (8) and (11) do not introduce significant bias. Evaluation of the "quality" of the estimates proceeds from a comparison of the variances. Because the focus of this work is to evaluate the heating rate approach to that of a temperature measurement approach, the null hypothesis assumes that variances of the errors between any two estimates are equal. If the null hypothesis is accepted, the two approaches generate estimates whose errors are statistically similar. The alternative hypothesis is that the variance of the temperature approach (σ_1^2) is larger than that of any other approach (σ_2^2).

$$H_0: \sigma_1^2 = \sigma_2^2 \tag{17}$$

$$H_1: \sigma_1^2 > \sigma_2^2 \tag{18}$$

Because we are claiming that noise becomes amplified, the variance of the noise is a good measure of the amount of amplification. The ratio of variances has an F-distribution $[F(\alpha; N, N) = s_1^2/s_2^2]$ for given degrees of freedom $N = n-1 = 50$ for both samples [35]. At a confidence level of 95%, $F = 1.6125$. Therefore, the null hypothesis must be rejected for any ratio greater than 1.6125, which means that the difference in the variance is statistically significant. Table 2 shows the values for the comparison between errors from the temperature approach and the two heating rate approaches. Based on this significance test, the only simulations where the variance could not be considered significantly different is Q_{H_d} for the sinusoidal and square heat flux cases. In all other tests, the null hypothesis is rejected and the heating rate approach is considered "better" than the temperature approach.

Table 2 Significance test for variance of errors between the temperature case and the indicated heating rate approach. For values greater than $F(0.05;50,50) = 1.6125$, the hypothesis that the variances are equal must be rejected.

Test Case	H_n	H_d
zero	166.2	2.560
triangle	166.2	2.471
sine	2.898	0.602
square	2.472	1.507

The first test case examined is the zero heat flux. The exact surface temperature is zero in this case, but the temperature signal with added noise is nonzero and shown in Fig. 1. From the zero heat flux, a zero heat rate is also found (shown in Fig. 2 along with noisy data). The first noisy signal H_n was obtained by adding normally distributed random values with a standard deviation of $\sigma = 0.08$ (four times the noise assigned to the temperature signal) to the zero signal. The second noisy signal was generated by calculating a backward difference of the noisy temperature data Y_n. This is a simplistic approach to obtaining a heating rate that demonstrates how noise in the temperature is amplified by differencing. The standard deviation of noise inherent to H_d is $s = 0.95$, which is nearly 50 times that of the temperature data and more than 11 times that of H_n.

Heat flux estimates for the zero flux case are shown in Fig. 3 for the noisy temperature and heating rate data sets. It is immediately

Downloaded 06 Dec 2010 to 193.140.21.150. Redistribution subject to ASME license or copyright; see http://www.asme.org/terms/Terms_Use.cfm

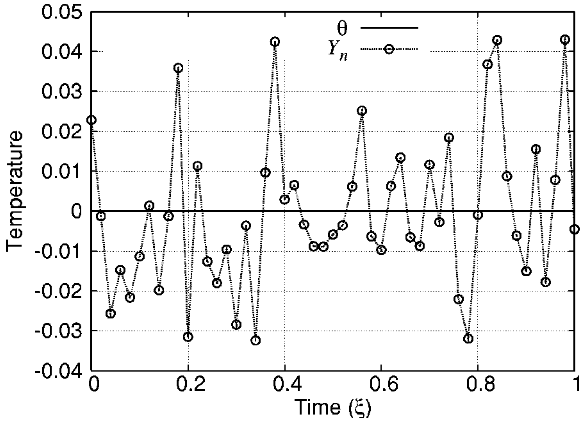

Fig. 1 The temperature response to a zero heat flux is shown with and without added noise. The normally distributed random noise has a standard deviation of σ=0.02. Lines are added to guide the eye.

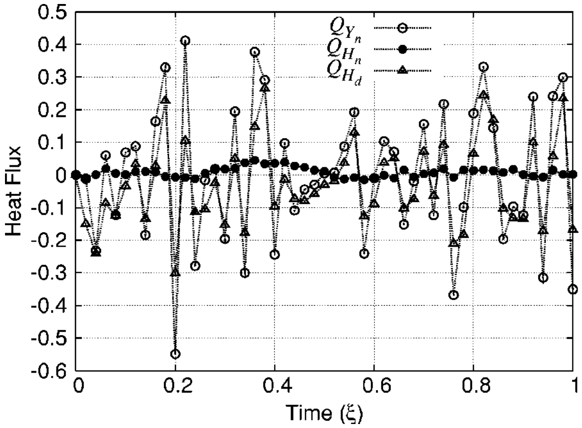

Fig. 3 The heat flux estimates of the zero flux case from temperature measurements Y_n, heat rate measurements H_n and differenced temperatures H_d. The lines connecting the estimates merely guide the eye.

obvious that the estimates produced from the heating rate data are far superior to estimates from temperature data. As listed in Table 1, the norm of the errors is 12.9 times larger for the temperature data and 8.05 times larger for the differenced heating rate data as compared to the noisy heating rate data H_n. Ironically, the differencing of temperature data H_d seems to produce better estimates than the temperature data Y_n. This plot and the reported errors also indicate how much the errors are amplified. Table 3 shows the error in the estimate normalized by the error in the measurement. This ratio of error in the estimate to error in the measurement (noise) is given as

$$E/N = \frac{|Q - Q_{Y_n}|}{|Y - Y_n|}, \tag{19}$$

where the temperature data and estimates can be replaced by the corresponding heating rate data and estimates. For the estimates from temperature measurements Y_n, the error to noise ratio is approximately 11 for the triangular and zero flux cases, but the error to noise ratio of estimates from the heating rate H_n is 0.2 and from differenced heating rate H_d is 0.1. The E/N ratio for H_d is so low because the noise level in the signal is so high. Therefore, this metric does not allow quantitative evaluation of the estimates from measurements but provides a sense of how each method amplifies the noise. In fact, the E/N ratio for both H_d and H_n should be comparable when compared to the E/N ratio for Y_n.

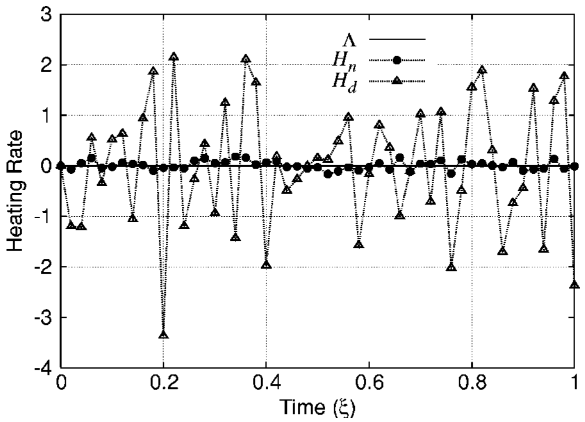

Fig. 2 The heating rate response to a zero heat flux is shown with and without added noise. The normally distributed random noise (H_n) has a standard deviation of 0.08, and a central differencing of the noisy temperature Y_n is used to produce H_d, which has a standard deviation of 0.94. The lines connecting the points merely guide the eye.

The next test case examined is the triangular heat flux, whose surface temperature history is shown in Fig. 4 with and without additional noise. As in the zero flux case, the noisy signal is obtained by adding a normally distributed random component with standard deviation of σ=0.02. Visually, the noise is a small percentage of the actual signal (~4%). The noisy temperature history is used to predict heat fluxes by inverting Eq. (5) with the method described above. This is inherently an unstable process, and the estimate from noisy data, Q_{Y_n} in Fig. 5 shows that small errors become amplified in the solution. No attempt to relax the

Table 3 Amplification of noise can be deduced from the ratio of the norm of the errors in the estimate to the norm of the noise in the measurements. Larger numbers indicate that the amplification of noise is greater.

Test Case	Y_n	H_n	H_d
zero	11.14	0.293	0.106
triangle	11.14	0.194	0.106
sine	11.39	1.506	0.100
square	10.79	1.541	0.111

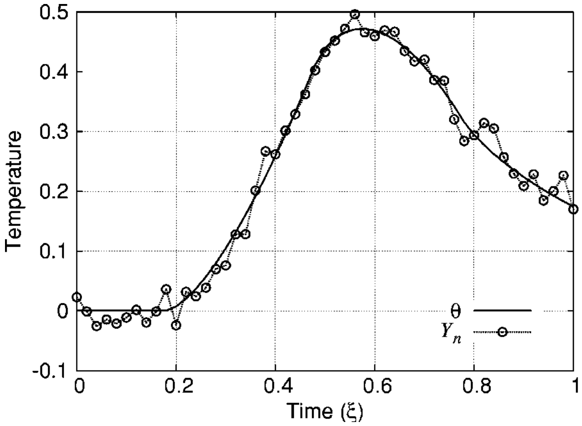

Fig. 4 The exact temperature response to a triangular heat flux profile (see Fig. 5). The noisy signal has a normally distributed random noise with standard deviation σ=0.02.

Downloaded 06 Dec 2010 to 193.140.21.150. Redistribution subject to ASME license or copyright; see http://www.asme.org/terms/Terms_Use.cfm

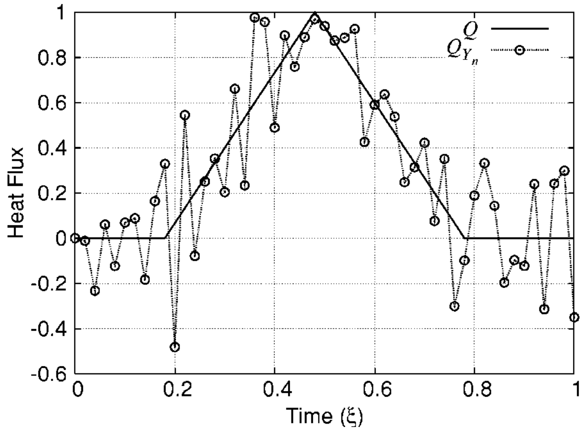

Fig. 5 The heat flux history estimates are derived from the temperatures in Fig. 4. The estimate from noisy data, Q_{Y_n}, demonstrate how small errors become amplified. The lines merely guide the eye.

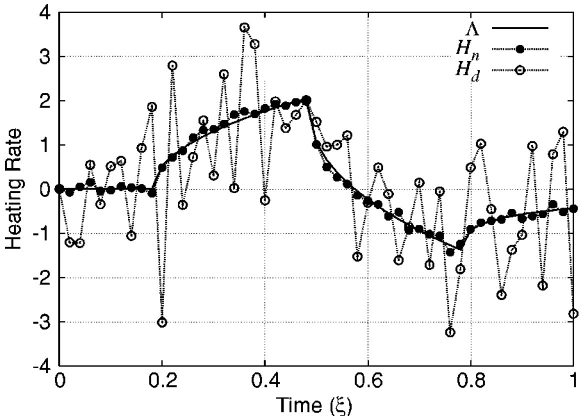

Fig. 7 Heating rate measurement data for the triangular case with an without added noise are shown. The lines merely guide the eye.

solution, introduce bias or otherwise implement any stabilization technique was made. In practice, a true inverse procedure would be implemented to achieve less noisy results than the exact matching procedure used here. In fact, the zero residual method (often called Stolz's method [32]) is a worst-case scenario. However, the method was chosen to illustrate that estimates from a noisy heating rate can provide reasonable and accurate estimates without bias. Figure 6 shows the estimates produced from the heating rate data sets, which are shown in Fig. 7. Both sets of estimates appear to match the exact solution closer than the estimates in Fig. 5. Note how closely the heating rate measurements with noise H_n visually matches the exact solution. The results suggest that direct matching solution of the Volterra equation of the second kind is not nearly as sensitive to measurement errors as the Volterra equation of the first kind. In fact, the error in the noisy estimate, Q_{H_n} appears to be damped, and the solution contains little bias and almost no noise. However, the surprising feature is that Q_{H_d}, which was produced from a signal H_d (open triangles in Fig. 7) whose noise is 20% of the actual signal, faithfully reproduces the original heat flux with errors comparable to Q_{Y_n}. Table 1 demonstrates that the estimates from all varieties of the heating rate (H, H_n, and H_d) contain very little error.

The next case examined (sine-wave heat flux) does not have an analytic solution that can be modeled exactly with a piecewise linear approximation. Therefore, there is an error inherent to the estimates even with exact data. For this demonstration, a sinusoidal heat flux with a frequency of the order of the Nyquist frequency was selected. The high-frequency component in this data will further exercise the methods. The exact temperature response to a sine-wave heat flux is shown in Fig. 8. Similarly the heating rate measurements are shown in Fig. 9. In both cases, even the exact data appear to be noisy because of the piecewise linear approximation and the high-frequency content of the heat

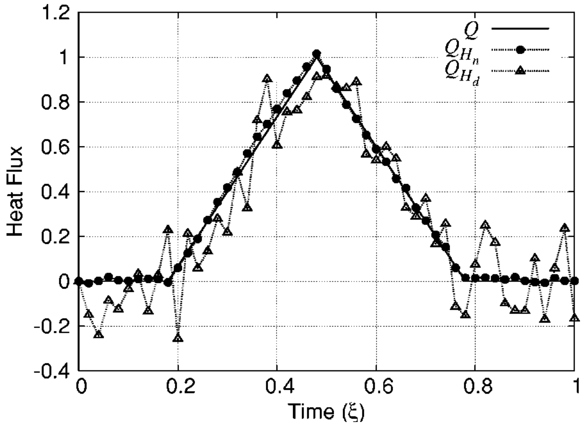

Fig. 6 Heat flux estimates derived from heating rate data using an exact matching scheme. Noise in the measured data is not amplified as in case of temperature data. The lines merely guide the eye.

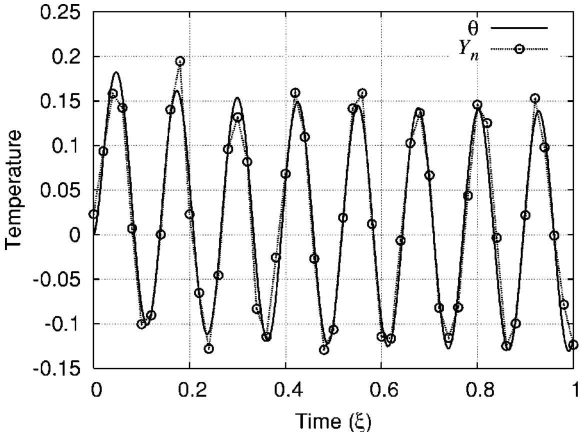

Fig. 8 Temperature solution to a sin wave heat flux with and without added noise

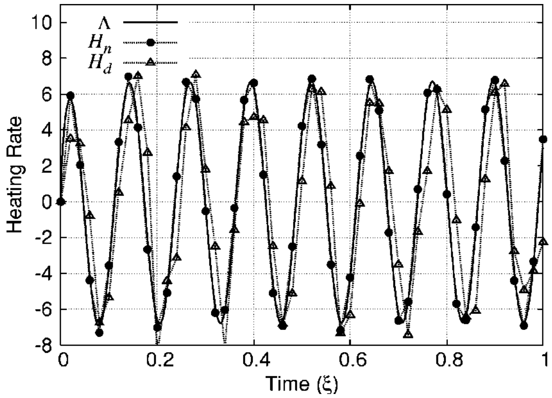

Fig. 9 Heating rate measurements of the sinusoidal heat flux with and without noise

Downloaded 06 Dec 2010 to 193.140.21.150. Redistribution subject to ASME license or copyright; see http://www.asme.org/terms/Terms_Use.cfm

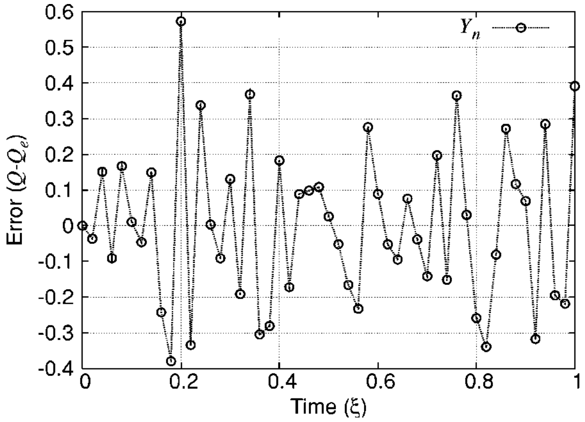

Fig. 10 Error in the heat flux estimates derived from temperature measurements for the sinusoidal case

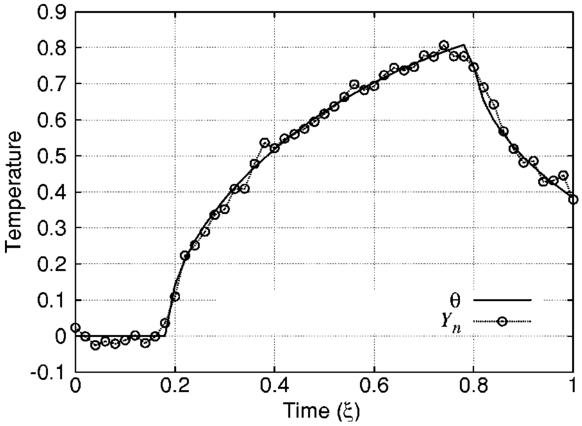

Fig. 12 Temperature solution to a square wave heat flux with and without added noise

flux.

Figures 10 and 11 show the difference in the flux instead of the actual estimate (i.e., $Q-Q_e$). The apparent periodicity of the error in the estimates from the heating rate measurements (Fig. 11) indicate some bias in the solution. In fact, the heating rate under predicts the flux by an average of 12% at the peaks. The bias is a result of the piecewise linear approximation and, incidentally, is still smaller than the error associated with the estimates derived from temperature data (see Fig. 10).

The final test case is particularly interesting because of the discontinuity inherent to a square flux. At the point when the flux is instantaneously turned on, the heating rate would theoretically be infinite. A measurement of this sort is not physically possible, and a piecewise linear approximation of the flux will not capture this discontinuity. However, the temperature remains finite and measurable. Therefore, we expect significant errors at the times when the flux is turned on and off for the hating rate case and errors similar to previous test cases for the temperature measurements. Temperature measurements and heating rate measurements are shown in Figs. 12 and 13, respectively. Note that the magnitude of the heating rate is large at the discontinuity compared to the other test cases. Also, the reader is reminded that the amount of noise added to the measurements is 0.02 and 0.08 to the temperature and heating rate measurements respectively. The estimates derived from temperature measurements (Fig. 14) exhibit the usual amplification of noise as the previous test cases. However, the estimates derived from heating rates (Fig. 15) show somewhat different behavior than the previous test cases. The heating rate measurement does not capture the discontinuity well. In fact, the error shows up as a bias for all times after the jump. Interestingly, the norm of the error is comparable to that from temperature measurements. Nevertheless, noise is often more desirable than bias if an experimenter must choose between the two. This artifact, however, does not necessarily mean that heating rate can not be considered a desirable quantity to measure. For example, Fig. 16 shows how

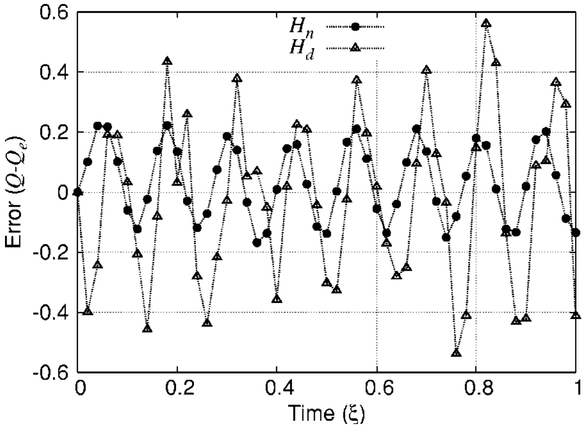

Fig. 11 Error in the heat flux estimates derived from heating rate data for the sinusoidal case

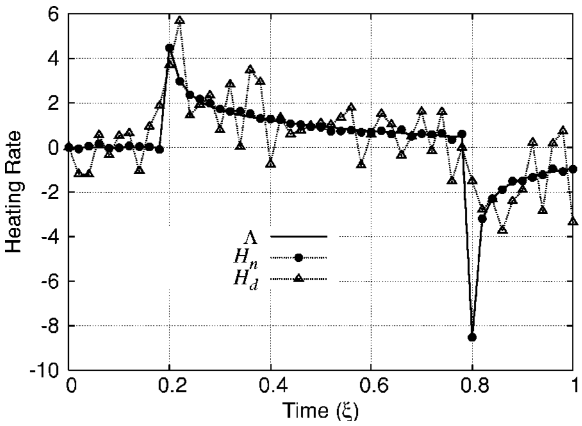

Fig. 13 Heating rate measurements of the square heat flux with and without noise

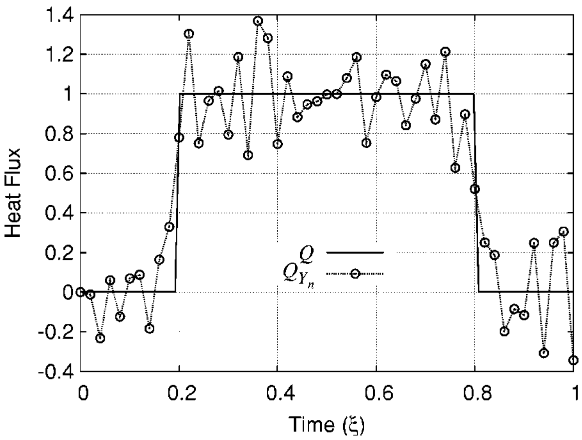

Fig. 14 The heat flux history estimates are derived from the temperatures in Fig. 12. The estimate from noisy data, Q_{Y_n}, demonstrate how small errors become amplified. The lines merely guide the eye.

Downloaded 06 Dec 2010 to 193.140.21.150. Redistribution subject to ASME license or copyright; see http://www.asme.org/terms/Terms_Use.cfm

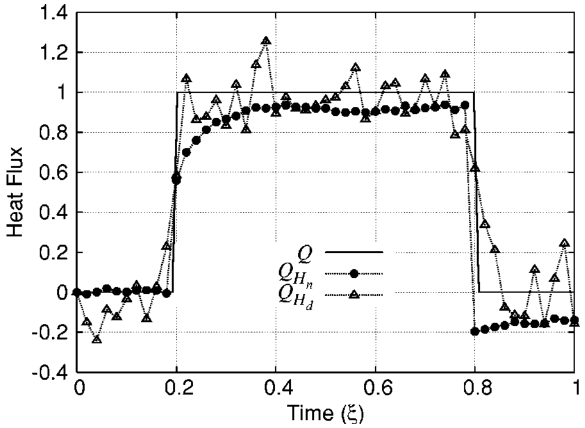

Fig. 15 Heat flux estimates derived from heating rate data (see Fig. 13) using an exact matching scheme. Noise in the measured data is not amplified as in case of temperature data. The lines merely guide the eye.

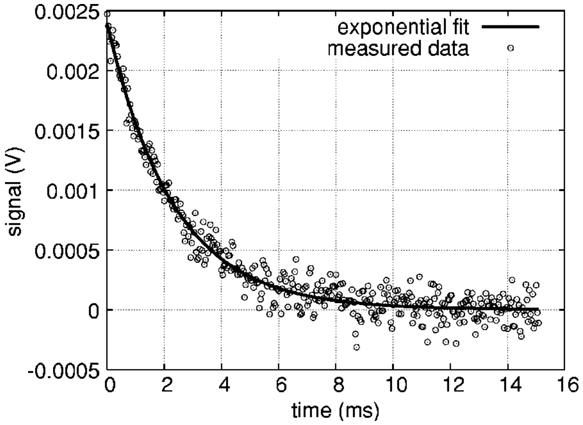

Fig. 17 Phosphor emission from $La_2O_2S:Eu$ after LED excitation was turned off. The data was translated so that the peak emission occurs at $t=0$ ms. Fitting parameters are shown in Table 4.

the error (and therefore, bias) decreases with increased sample rate, which is contrary to temperature measurement behavior. In fact, for high sample rates, errors associated with temperature data are orders of magnitude greater than those associated with heating rate measurements. Consequently, the possibility for eliminating bias in the heating rate estimates exists, but measurement noise is omnipresent in estimates from temperature data.

Estimation of τ by decay measurement. As a demonstration of heating rate determination, the phosphor $La_2O_2S:Eu$ was measured at steady state to characterize the effects of noise. Single shot data are shown in Fig. 17 along with an exponential fit of the data [see Eq. (13)]. The estimated parameters are $\tau=2.31$ ms and $I_0=0.00239$ V. At steady state, the heating rate, and therefore the change in decay time, is expected to be near zero. Therefore estimates of the decay time τ should be consistent between models [Eqs. (13) and (14)] and the change in the decay time $d\tau/dt$ from Eq. (14) should be negligible. From the estimates using the new model [Eq. (14)], the decay time is 2.21 ms, which is 5% different than the constant model, and the change in decay time is 0.022 s/s, which is smaller than the noise in the estimate for τ and considered negligible. Because of the noise in the measured signal, the change in heating rate is nonzero. However, note that photomultiplier tube (PMT) measurements are inherently noisy and no electronic means were used to smooth or average the data. Despite the noise, the change in decay time has little contribution to the overall intensity decay (see Table 4). Further the decay times predicted from each model are consistent. As a side effect of the estimation procedure, we can also obtain the maximum intensity, which is also consistent between models. The errors in the estimates given by 95% confidence intervals is of the order of the noise introduced in the data reduction test cases discussed in the previous section. Therefore, the magnitude of the errors observed in the estimates of the test cases is comparable to what we might expect to obtain from TGP measurements.

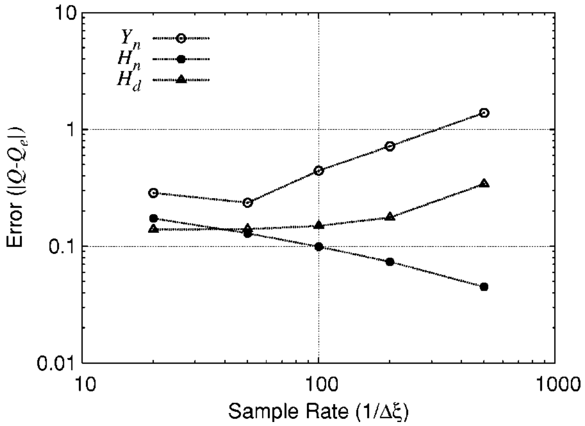

Fig. 16 Norm of the error for estimates derived from the measurements indicated on a log–log scale. Errors are normalized with the total number of samples.

Based on noise in the steady-state single-shot measurement, we can evaluate the errors in the estimation procedure when the temperature changes during the decay. Data were fabricated by assuming $\tau=2.31$ ms from the actual measurement. Then an artificial $d\tau/dt=0.3$ was added in Eq. (14) to obtain a new intensity measurement. The error due to noise in the actual measurement was then superimposed onto the exact signal, resulting in noisy data that includes a nontrivial change in decay time. Figure 18 shows the fit of fabricated data using the typical constant decay model [Eq. (13)] and the new model, which includes the change in the decay time [Eq. (14)]. If the decay time changes, as in the foregoing example, then a significant difference between the fits of Eqs. (13) and (14) are seen (Fig. 18). Table 5 gives the estimated parameters for the foregoing example. Agreement between the linearly varying model and the fabricated data is exceptional demonstrating that the measurement noise may not affect heating rate determination from phosphor measurements. However, transient measurements need to be made to verify the utility of the method.

The uncertainty in the $d\tau/dt$ estimate is 3.3% of the actual estimate. In addition, the uncertainty in the estimate of τ is 4.2% of the actual estimate. Because the estimate of τ and estimate of $d\tau/dt$ are related to temperature and heating rate, respectively, the data suggest that noise in each measurement should also be ~4%. In fact, this is the level of noise that was used in the preceding example test cases. Therefore, these measurements from TGPs indicate that the example test cases are valid estimates of the errors we expect to see in practice.

Conclusions

A new approach to predicting heat flux is proposed, which may improve heat flux estimates by reducing instabilities inherent in temperature to heat flux data reduction methods. By measuring the heating rate, the integral equation for heat flux becomes a Volterra equation of the second kind, which is inherently more stable than the first kind. Analysis confirms that the method is more stable and can accommodate more noise than an approach that uses tem-

Downloaded 06 Dec 2010 to 193.140.21.150. Redistribution subject to ASME license or copyright; see http://www.asme.org/terms/Terms_Use.cfm

Table 4 Estimates of decay time parameters based on measured phosphor data

	I_o (V)	τ (ms)	$d\tau/dt$
constant	$2.33 \times 10^{-3} \pm 2.76 \times 10^{-5}$	2.31 ± 0.038	n/a
linear	$2.42 \times 10^{-3} \pm 3.3 \times 10^{-5}$	2.21 ± 0.080	0.022 ± 0.0153

Table 5 Estimates of decay time parameters based on fabricated phosphor data

	I_o (V)	τ (ms)	$d\tau/dt$
exact	2.33×10^{-3}	2.31	0.3
constant	$1.93 \times 10^{-3} \pm 2.93 \times 10^{-5}$	5.20 ± 0.116	n/a
linear	$2.40 \times 10^{-3} \pm 3.6 \times 10^{-5}$	2.27 ± 0.095	0.303 ± 0.010

perature measurements. The method for measuring heating rate uses thermographic phosphors, which is already being used to measure temperatures.

Evaluations of the measurement technique indicate that the TGP measurement noise is similar in magnitude to temperature measurement noise. Consequently, estimates from heating rate data are expected to be much more stable and accurate than estimates from temperature measurements. Therefore, TGPs may prove to be an excellent heat flux determination technique where surface measurements can be made optically.

However, the example measurements are preliminary and future work will improve the reliability of the estimates. Furthermore, work needs to be done to characterize TGPs for these types of measurements. For example, the decay rate, excitation frequency, emission frequency, temperature range, and proximity sensitivities need to be tuned for each application. Despite the work that needs to be performed to raise the process to a production level, significant and inherent advantages can be seen from the foregoing proof-of-concept.

Acknowledgments

The author would like to thank Steve Allison at Oak Ridge National Laboratory for his experience and knowledge on making thermographic phosphor measurements and to Jay Frankel at the University of Tennessee for useful conversations on reduction of heat rate data. Furthermore, encouragement and guidance was provided by John Ahner in the Mathematics Department at Vanderbilt. The author would like to thank the reviewers whose comments and persistence greatly strengthened the paper.

Nomenclature

t = time
H = heating rate measurements or hypothesis
I = phosphor emission intensity
L = conduction domain length
Q = normalized heat flux
M = number of terms in the series
N = number of measurements
R = residual
Y = measured temperatures

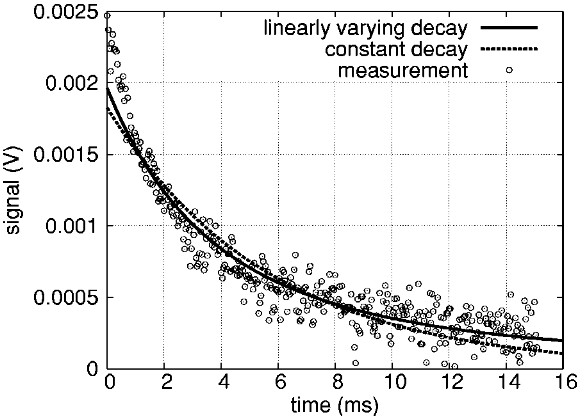

Fig. 18 Fit of fabricated noisy emission data using the constant and linear decay models

Greek

β = eigenvalues
θ = normalized temperature change
η = normalized spatial dimension
Λ = normalized heating rate
τ = phosphor decay time
ξ = normalized time
Φ = basis functions

subscripts/superscripts

d = difference
i = summation index
m = eigenvalue index
n = noisy
o = initial value
r = measurement index

Appendix

It is not immediately clear that the heating rate Eq. (9), evaluated at the surface will converge because of the first term in the summation.

$$\Lambda(\xi) = 2\sum_{m=1}^{\infty}\left[Q(\xi) - \beta_m^2\int_0^{\xi} Q(\xi')e^{\beta_m^2(\xi'-\xi)}d\xi'\right]. \tag{20}$$

Using integration by parts, the integral term can be expressed as

$$\beta_m^2\int_0^{\xi} Q(\xi')e^{\beta_m^2(\xi'-\xi)}d\xi' = [Q(\xi')e^{\beta_m^2(\xi'-\xi)}]_0^{\xi} - \int_0^{\xi}\frac{dQ(\xi')}{d\xi'}e^{\beta_m^2(\xi'-\xi)}d\xi' \tag{21}$$

$$= Q(\xi) - Q(0)e^{-\beta_m^2\xi} - \int_0^{\xi}\frac{dQ(\xi')}{d\xi}e^{\beta_m^2(\xi'-\xi)}d\xi' \tag{22}$$

Now the heat flux $Q(\xi)$ in Eq. (22) cancels with the heat flux in Eq. (20) to give an equivalent infinite series

$$\Lambda(\xi) = 2\sum_{m=1}^{\infty}\left[Q(0)e^{-\beta_m^2\xi} + \int_0^{\xi}\frac{dQ(\xi')}{d\xi'}e^{\beta_m^2(\xi'-\xi)}d\xi'\right] \tag{23}$$

Now the offending infinity has been eliminated. Because $0 < \xi' < \xi$, each term in the series contains an exponential with a negative exponent. As the eigenvalue increases, all terms will approach zero if the heat flux derivative is a bounded function. This assumption is not unreasonable because it represents a physical quantity and will not likely approach infinity. However, the series still may not converge because the value of the exponential will approach unity at the upper limit of the integral. Therefore, the convergence is undetermined because the function is pointwise bounded, not uniformly bounded.

Despite our inability to prove convergence in general, we can show that certain discretized forms of Eq. (20) do converge. Note that Eq. (23) should not be discretized directly as in Eq. (10), unless the first term is also summed and evaluated at the beginning of each discrete time step.

Downloaded 06 Dec 2010 to 193.140.21.150. Redistribution subject to ASME license or copyright; see http://www.asme.org/terms/Terms_Use.cfm

If we assume that the heat flux can be approximated by some piecewise function, the integral in Eq. (20) can be expressed as a sum of integrals

$$H_r = 2\sum_{m=1}^{\infty}\left\{Q_r - \beta_m^2\sum_{i=1}^{r}\int_{\xi_{i-1}}^{\xi_i} Q(\xi')e^{\beta_m^2(\xi'-\xi_r)}d\xi'\right\}, \tag{24}$$

where the functions are evaluated at discrete times, such that $\xi_r = r\Delta\xi$, $r=1,2,3,\ldots$, $\xi_0=0$, $H_r=H(\xi_r)$, $H_0=0$, $Q_r=Q(\xi_r)$, $Q_0=0$.

Now assume that the heat flux is given by some integrable function between time steps. The simplest is perhaps a constant, such that the value during the time step is also the value at the later time step.

$$Q(\xi') = Q_i, \quad \xi_{i-1} < \xi' \leq \xi_i. \tag{25}$$

Because $Q(\xi)$ is a constant, it can be taken outside of the integral, and the integral can be evaluated exactly.

$$H_r = 2\sum_{m=1}^{\infty}\left\{Q_r - \beta_m^2\sum_{i=1}^{r} Q_i\frac{1}{\beta_m^2}[e^{\beta_m^2(\xi_i-\xi_r)} - e^{\beta_m^2(\xi_{i-1}-\xi_r)}]\right\}. \tag{26}$$

The final term in the internal summation can be evaluated separately to obtain

$$H_r = 2\sum_{m=1}^{\infty}\left\{Q_r - Q_r[1 - e^{-\beta_m^2\Delta\xi}] - \sum_{i=1}^{r-1} Q_i[e^{\beta_m^2(\xi_i-\xi_r)} - e^{\beta_m^2(\xi_{i-1}-\xi_r)}]\right\}. \tag{27}$$

The advantage of this is that now the offending infinity in the outer summation has been canceled.

$$H_r = 2\sum_{m=1}^{\infty}\left\{Q_r e^{-\beta_m^2\Delta\xi} - \sum_{i=1}^{r-1} Q_i[e^{\beta_m^2(\xi_i-\xi_r)} - e^{\beta_m^2(\xi_{i-1}-\xi_r)}]\right\}. \tag{28}$$

Each term in the summations can be expressed as some constant (the heat flux at a point in time the sum of exponential). All the exponential terms can be expressed with an integer multiple of $\Delta\xi$ as

$$e^{-\beta_m^2 n\Delta\xi}, \quad n = 1,2,3,\ldots. \tag{29}$$

By examining the ratio of subsequent terms in each infinite sum,

$$\lim_{m\to\infty}\frac{a_{m+1}}{a_m} = \lim_{m\to\infty}\frac{e^{[(2m+1)\pi/2]^2 n\Delta\xi}}{e^{[(2m-1)\pi/2]^2 n\Delta\xi}} = r, \tag{30}$$

we can determine whether the summation will converge. Following Cauchy, if the value of the limit r is less than one, the infinite summations will converge by the ratio test [36]. In the present case, the limit approaches zero,

$$r = \lim_{m\to\infty} e^{-2m\pi^2 n\Delta\xi} = 0, \tag{31}$$

for any positive n and m. Because each summation will converge, the entire the equation converges.

Note that convergence can only be found as an artifact of the discretization. For example, if we define the constant heat flux to be the value at the time preceding the step,

$$Q(\xi') = Q_{i-1}, \quad \xi_{i-1} \leq \xi' < \xi_i, \tag{32}$$

the convergence is not so well behaved. In this case, the discrete heat rate is given as

$$H_r = 2\sum_{m=1}^{\infty}\left\{Q_r - \beta_m^2\sum_{i=1}^{r} Q_{i-1}\frac{1}{\beta_m^2}[e^{\beta_m^2(\xi_i-\xi_r)} - e^{\beta_m^2(\xi_{i-1}-\xi_r)}]\right\}, \tag{33}$$

once the constant heat flux is removed from the integral and the integral is evaluated. Similar to the previous example, we can evaluate the final term of the summation separately.

$$H_r = 2\sum_{m=1}^{\infty}\left\{Q_r - Q_{i-1}[1 - e^{-\beta_m^2\Delta\xi}] - \sum_{i=1}^{r-1} Q_{i-1}[e^{\beta_m^2(\xi_i-\xi_r)} - e^{\beta_m^2(\xi_{i-1}-\xi_r)}]\right\}. \tag{34}$$

In this case, we end up with a term where $n=0$. The limit given by Eq. (31) approaches one and convergence is undetermined.

For a piecewise linear heat flux approximation as presented in Eq. (7), the heating rate is given by Eq. (11). By considering the term where $i=r$ separately as before, Eq. (11) becomes

$$H_r = 2\sum_{m=1}^{\infty}\left\{Q_r - Q_r[1 - e^{-\beta_m^2\Delta\xi}] - \sum_{i=1}^{r-1} Q_i[e^{\beta_m^2(\xi_i-\xi_r)} - e^{\beta_m^2(\xi_{i-1}-\xi_r)}] + \frac{Q_r - Q_{r-1}}{\beta_m^2\Delta\xi}[1 - e^{-\beta_m^2\Delta\xi}(\beta_m^2\Delta\xi - 1)] + \sum_{i=1}^{r-1}\frac{Q_i - Q_{i-1}}{\beta_m^2\Delta\xi}[e^{\beta_m^2(\xi_i-\xi_r)} - e^{\beta_m^2\Delta\xi}(\beta_m^2\Delta\xi - 1)]\right\}. \tag{35}$$

The Q_r terms cancel. All other terms except one contain an exponential with a negative exponent, which has already been shown to converge [see Eq. (31)]. The last term to consider is

$$\frac{Q_r - Q_{r-1}}{\Delta\xi}\sum_{m=1}^{\infty}\frac{1}{\beta_m^2} = \frac{Q_r - Q_{r-1}}{\Delta\xi}\frac{4}{\pi^2}\sum_{m=1}^{\infty}\frac{1}{(2m-1)^2}. \tag{36}$$

It can be shown that $\Sigma_{m=1}^{\infty}1/m^p$ converges if and only if $p>1$ (Corollary 4.3.7 from Belding and Mitchell [36]). Because $1/m^2 > 1/(2m-1)^2$ for large m, the series in Eq. (36) converges by the comparison test. Now because each series in the equation converges, the equation for heating rate converges.

References

[1] Holmberg, D. G., and Diller, T. E., 1995, "High-frequency heat flux sensor calibration and modeling," J. Fluids Eng., **117**, pp. 659–664.

[2] Piccini, E., Guo, S. M., and Jones, T. V., 2000, "The development of a new direct-heat-flux gauge for heat-transfer facilities," Meas. Sci. Technol., **11**, pp. 342–349.

[3] Diller, T. E., and Kidd, C. T., 1997, "Evaluation of numerical methods for determining heat flux with a null point calorimeter," in *Proceedings of the 42nd International Instrumentation Symposium*, Research Triangle Park, NC, pp. 251–262.

[4] Buttsworth, D. R., and Jones, T. V., 1997, "Radial conduction effects in transient heat transfer experiments," Aeronaut. J., **101**, pp. 209–212.

[5] Ireland, P. T., and Jones, T. V., 2000, "Liquid crystal measurements of heat transfer and surface shear stress," Meas. Sci. Technol., **11**, pp. 969–986.

[6] Newton, P. J., Yan, Y., Stevens, N. E., Evatt, S. T., Lock, G. D., and Owen, J. M., 2003, "Transient heat transfer measurements using thermochromic liquid crystal. Part 1: An improved technique," Int. J. Heat Fluid Flow, **24**, pp. 14–22.

[7] Beck, J. V., Blackwell, B., and St. Claire, Jr., C. R., 1985, *Inverse Heat Conduction: Ill-Posed Problems*, Wiley–Interscience, NY.

[8] Guo, S. M., Lai, C. C., Jones, T. V., Oldfield, M. L. G., Lock, G. D., and Rawlinson, A. J., 1998, "The application of thin-film technology to measure turbine-vane heat transfer and effectiveness in a film-cooled, engine-simulated environment," Int. J. Heat Fluid Flow, **19**, pp. 594–600.

[9] Dinu, C., Beasley, D. E., and Figliola, R. S., 1998, "Frequency response characteristics of an active heat flux gage," J. Heat Transfer, **120**, pp. 577–582.

[10] Hadamard, J., 1923, *Lectures on Cauchys Problems in Linear Partial Differential Equations*, Yale University Press, New Haven, CT.

[11] Kirsch, A., 1996, *An Introduction to the Mathematical Theory of Inverse Problems*, Springer, Berlin, Vol. 120.

[12] Cook, W. J., 1970, "Determination of heat transfer rates from transient surface temperature measurements," AIAA J., **8**, pp. 1366–1368.

[13] Kendall, D. N., and Dixon, W. P., 1966, "Heat transfer measurements in a hot shot wind tunnel," IEEE Trans. Aerosp. Electron. Syst., **AES-3**, pp. 596–603.

[14] Walker, D. G., and Scott, E. P., 1997, "Evaluation of estimation methods for high unsteady heat fluxes from surface measurements," AIAA J., **12**, pp. 543–551.

[15] Buttsworth, D. R., and Jones, T. V., 1998, "A fast-response high spatial resolution total temperature probe using a pulsed heating technique," J. Turbomach., **120**, pp. 612–617.

[16] Dunn, M. G., George, W. K., Rae, W. J., Woodward, S. H., Moller, J. C., and

Downloaded 06 Dec 2010 to 193.140.21.150. Redistribution subject to ASME license or copyright; see http://www.asme.org/terms/Terms_Use.cfm

Seymour, P. J., 1986, "Heat flux measurements for the rotor of a full-stage turbine: Part II: Description of analysis technique and typical time-resolved measurements," ASME J. Turbomach., **108**, pp. 98–107.

[17] Ehrich, F. F., 1954, "Differentiation of experimental data using least squares fitting," J. Aeronaut. Sci., **22**, pp. 133–134.

[18] Tikhonov, A. N., and Arsenin, V. Y., 1977, *Solutions of Ill-Posed Problems*, V. H. Winston & Sons, Washington, D.C.

[19] George, W. K., Rae, W. J., Seymour, P. J., and Sonnenmeier, J. R., 1987, "An evaluation of analog and numerical techniques for unsteady and heat transfer measurements with thin film gauges in transient facilities," in *Proceedings of the ASME/JSME Thermal Engineering Joint Conference*, Honolulu, HI, Vol. 2, pp. 611–617.

[20] Walker, D. G., Scott, E. P., and Nowak, R. J., 2000, "Estimation methods for 2D conduction effects of shock-shock heat fluxes from temperature measurements," AIAA J., **14**, pp. 533–539.

[21] Frankel, J. I., and Keyhani, M., 1999, "Inverse heat conduction: The need for heat rate data for design and diagnostic purposes," in *Proceedings of the 18th LASTED International Conference on Modeling, Identification and Control*, Innsbruck, Austria, February.

[22] Frankel, J., and Osborne, G., 2004, "Motivation for the development of heating/cooling rate and heat flux rate sensors for engineering applications," in *Proceedings of the 42nd AIAA Aerospace Sciences Meeting and Exhibit*.

[23] Lamm, P. K., 1995, "Future-sequential regularization methods for ill-posed volterra equations," J. Math. Anal. Appl., **195**, pp. 469–494.

[24] Walker, D. G., and Schetz, J. A., 2003, "A new technique for heat flux determination," in *Proceedings of the ASME Summer Heat Transfer Conference*, Las Vegas, NV.

[25] Allison, S. W., and Gillies, G. T., 1997, "Remote thermometry with thermographic phosphors: Instrumentation and applications," Rev. Sci. Instrum., **68**, pp. 2615–2650.

[26] Sholes, R. R., 1980, "Fluorescent decay thermometry with biological applications," Rev. Sci. Instrum., **51**, pp. 882–884.

[27] Feist, J. P., and Heyes, A. L., 2000, "The characterization of $Y_2O_2S:Sm$ powder as a thermographic phosphor for high temperature applications," Meas. Sci. Technol., **11**, pp. 942–947.

[28] Allison, S. W., Cates, M. R., Noel, B. W., and Gillies, G. T., 1988, "Monitoring permanent-magnet motor heating with phosphor thermometry," IEEE Trans. Instrum. Meas., **37**, pp. 637–641.

[29] Necati Özişik, M., 1968, *Boundary Problems of Heat Conduction*, Dover, New York.

[30] Kress, R., 1989, *Linear Integral Equations*, Vol. 82 in Applied Mathematical Sciences, Springer-Verlag, Berlin.

[31] Corduneanu, C., 1991, *Integral Equations and Applications*, Cambridge University Press, Cambridge.

[32] Stolz, Jr. G., 1960, "Numerical solutions to an inverse problem of heat conduction for simple shapes," J. Heat Transfer, **82**, pp. 20–26.

[33] Shionoya, S., and Yen, W. M., editors, 1999, *Phosphor Handbook*, CRC Press, Boca Raton.

[34] Beck, J. V., and Arnold, K. J., 1977, *Parameter Estimation in Engineering and Science*, Wiley, New York.

[35] Hogg, Robert V., and Ledolter, Johannes, 1992, *Applied Statistics for Engineers and Physical Scientists*, 2nd ed., Macmillan, NY.

[36] Belding, D. F., and Mitchell, K. J., 1991, *Foundation of Analysis*, Prentice–Hall, NJ.

Downloaded 06 Dec 2010 to 193.140.21.150. Redistribution subject to ASME license or copyright; see http://www.asme.org/terms/Terms_Use.cfm

Condensation From Pure Steam and Steam–Air Mixtures on Integral-Fin Tubes in a Bank

Adrian Briggs
e-mail: A.Briggs@qmul.ac.uk

Sritharan Sabaratnam

Department of Engineering, Queen Mary,
University of London, Mile End Road, Mile End,
London, E1 4NS, United Kingdom

Data are reported for condensation of steam with and without the presence of air on three rows of integral-fin tubes situated in a bank of plain tubes. The data cover a wide range of vapor velocities and air concentrations. Unlike previously reported data for plain tubes using the same test bank and apparatus, the heat-transfer coefficients for the finned tubes were largely unaffected by vapor velocity. When compared to a plain tube of fin-tip diameter and at the same vapor side temperature difference, heat-transfer enhancement ratios between 3.7 and 4.9 were found for the finned tubes compared to a plain tube in quiescent vapor conditions, while values between 1.9 and 3.9 were found when compared to a plain tube at the same vapor velocity. When compared to the plain tubes, the heat transfer to the finned tubes was much more susceptible to the presence of noncondensing gas (air) in the vapor, with enhancement ratios falling as low as 1.5 compared to the plain tubes when even small concentrations of air were present.

[DOI: 10.1115/1.1915371]

Introduction

The mechanism of condensation heat-transfer from pure, quiescent vapor onto single integral-fin tubes is relatively well understood (see for instance, Marto [1], Briggs and Rose [2]). Surface tension induced pressure gradients drain condensate from the tips and flanks of the fins, thinning the film and enhancing the local heat-transfer coefficient, while at the bottom of the tube condensate is retained in the inter-fin spaces leading to a decrease in heat transfer to this part of the tube. Models which include all of these factors, e.g., Honda et al. [3] and Briggs and Rose [4] have shown good agreement with the large amount of experimental data available. When banks of tubes are considered, however, the situation is more complex, involving interactions between vapor and condensate and changing conditions down the bank as vapor is removed by condensation. Experimental data for condensation of refrigerants on banks of integral-fin tubes (see for instance Honda et al. [5–7], Briggs et al. [8]) suggest that the enhancing effect of vapor velocity seen during condensation on plain tubes is much less significant on finned tubes, while the detrimental effect of condensate inundation on tubes low in the bank is also less important. The situation, however, is still far from fully understood. Previous work on single tubes has highlighted the importance of obtaining experimental data for fluids with a wide range of thermophysical properties and tubes with a wide range of geometries in order to fully understand the mechanisms involved. To this end, this paper presents experimental data for condensation of steam on integral-fin tubes in a staggered bank. The fin geometry was chosen, based on earlier work on single tubes, to be near optimum for condensation of steam.

Apparatus and Data Reduction

Figure 1 shows a diagram of the test rig. Steam was generated in a stainless steel boiler containing 25 electric immersion heaters of nominal power 10 kW each. From the boiler the steam traveled through a 180° bend and then through a 1.5 m long calming section before entering the test section vertically downwards. The test section and the sections just before and after it were made from anodized cast aluminium alloy modules and all other parts of the test rig loop were made of stainless steel. An auxiliary condenser, containing ten rows of integral-fin tubes with four and five tubes per row, was positioned below the test section to condense the remaining vapor. The condensate was returned to the boiler by gravity.

Two banks of tubes (shown schematically in Fig. 2) were tested. Both were housed in a rectangular test section having internal length 272 mm, width 52.4 mm, and height 250 mm. PTFE bushes insulated the test tubes from the body of the test section. Both banks consisted of ten rows of two and one tubes per row in a staggered, equilateral triangular arrangement with a diagonal pitch of 26.2 mm. The single-tube rows were fitted with noncondensing dummy half tubes. One side of the test section was fitted with a glass window to allow observation of the tubes.

The results for the first tube bank have been reported previously in Briggs and Sabaratnam [9]. In this case all 15 test tubes were plain copper tubes with outer diameter of 19.1 mm, inner diameter 12.7 mm, and condensing length 272 mm. In the second test bank, the results from which are reported in detail here, the plain tubes in rows 5, 6, and 7 where replaced by copper tubes with rectangular cross-section integral fins. The finned tubes had the following dimensions: fin-tip diameter 19.1 mm, internal diameter 12.7 mm and fin thickness, height and spacing 1 mm, 1.5 mm, and 1.5 mm, respectively. These dimensions were based on the results of previous work on single integral-fin tubes and are close to optimum for condensation of steam.

Each row of tubes was cooled separately by water with the coolant inlet temperatures and flow rates the same for all rows. The heat-transfer rate to each row was calculated from the coolant flow rate and temperature rise. The coolant flow rate to each row was measured using variable-aperture, float-type flowmeters with an uncertainty of 2%. The coolant temperature rise in each row was measured by a 10-junction thermopile, with junctions placed in well-insulated mixing chambers at inlet and exit of each tube row to ensure adequate isothermal immersion. Upstream vapor temperature and pressure were measured using a stainless-steel sheathed K-type thermocouple and a U-tube mercury manometer respectively. All the thermocouples were calibrated against a precision platinum resistance thermometer, itself calibrated to an accuracy of 0.001 K. The uncertainty in temperature measurement using the thermocouples was estimated at less than 0.1 K, and that for the coolant temperature rise, measured with the ten-junction

---

Contributed by the Heat Transfer Division for publication in the JOURNAL OF HEAT TRANSFER. Manuscript received August 31, 2004. Final manuscript received December 22, 2004. Review conducted by: Raj M. Manglik.

Copyright © 2005 by ASME

Downloaded 06 Dec 2010 to 193.140.21.150. Redistribution subject to ASME license or copyright; see http://www.asme.org/terms/Terms_Use.cfm

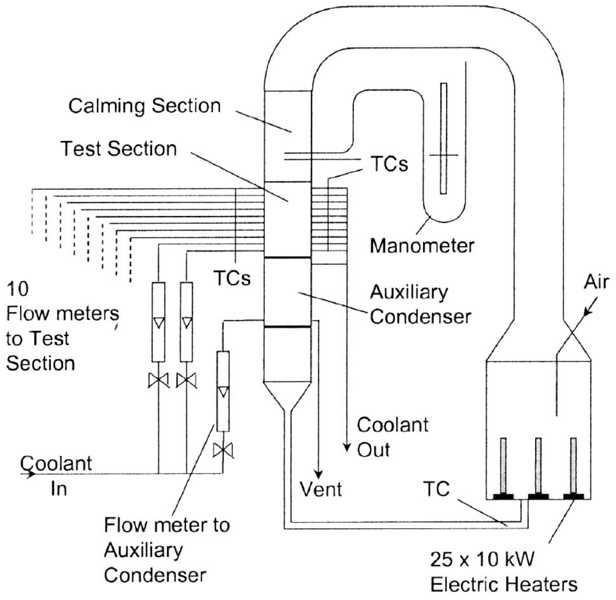

Fig. 1 Apparatus (TC indicates position of thermocouple)

thermopiles, was estimated at 0.01 K. The range of coolant temperature rise in the tests was 0.9 K to 17.2 K. The vapor-side, heat-transfer coefficient, α is defined as follows:

$$\alpha = \frac{q}{(T_v - T_{wo})} \tag{1}$$

where q is the heat flux calculated from the coolant flow rate and temperature rise, and based on the outside surface area of the plain tube or the fin-tip envelope area of the finned tube, T_v is the local steam or steam–air temperature and T_{wo} is the mean outside wall surface temperature of the plain tubes in the row or the mean fin-root temperature of the finned tubes.

The plain tubes in both banks were instrumented with four thermocouples each, embedded in the walls at the mid-point of the tube and at angles of 22.5 deg, 112.5 deg, 202.5 deg, and 292.5 deg to the vertical. The thermocouples were fitted in 2.7 mm deep slots in the tube walls and covered by copper strips, soldered in place. The local inner and outer surface temperatures of the tubes were calculated from the thermocouple readings by assuming uniform radial conduction through the tube wall. T_{wo} was taken as the arithmetic mean of the four outside wall temperatures.

The finned tubes in the second bank were uninstrumented and in this case the vapor-side, heat-transfer coefficient was found by subtracting the coolant and wall resistances from the measured overall thermal resistance. To obtain a correlation for the coolant-side, heat-transfer coefficient the data for the instrumented plain tubes in rows 5, 6, and 7 of the plain tube bank were used. Care was taken in the design and construction of the two tube banks to ensure that the plain and finned tubes had identical internal geometry, including the entrance, exit and transfer passages for the coolant, to ensure that the measured coolant-side correlations obtained from the instrumented plain tubes could be used with the uninstrumented finned tubes. The coolant-side data for the instrumented plain tube rows are shown in Fig. 3, plotted on the basis of the Seider and Tate [10] correlation for turbulent flow in a pipe. It can be seen from Fig. 3 that the data are well represented by equations of the form

$$\mathrm{Nu}_c = A_c \,\mathrm{Re}_c^{0.8}\, \mathrm{Pr}_c^{1/3} \left(\frac{\mu_c}{\mu_{wi}}\right)^{0.14} \tag{2}$$

where $A_c = 0.0284$ for rows 5 and 7 and $A_c = 0.0307$ for row 6. The slightly different value for row 6 is due to the fact that this row had only one active tube while rows 5 and 7 had 2. It should also be noted that the coefficients A_c in Eq. (2) are slightly higher than the often quoted value of 0.027 from the original work of Seider and Tate due to the short tubes used in the present work. Equation (2) was used to calculate the coolant-side resistance of the three uninstrumented finned tube rows. This was subtracted, along with the tube wall resistance, calculated assuming uniform radial conduction (inside surface to fin root diameter) from the measured overall resistance, to obtain the vapor-side, heat-transfer coefficient.

The mass flow rate of steam at approach to the test section was calculated from the power input to the boiler. A small correction was made for the heat-loss from the well-insulated apparatus. Account was also taken of the energy required to heat the injected air from its inlet temperature to the temperature of the resulting mixture. An energy balance was performed between energy supplied to the boilers and energy removed via the coolant and thermal losses. The discrepancy was never greater than 4%. Air was injected into the boiler, below the level of the liquid to ensure good mixing with the steam, and its flow rate was measured using a variable-aperture, float-type flowmeter. The mass fraction of air, W_u, in the steam–air mixture at approach to the test section was

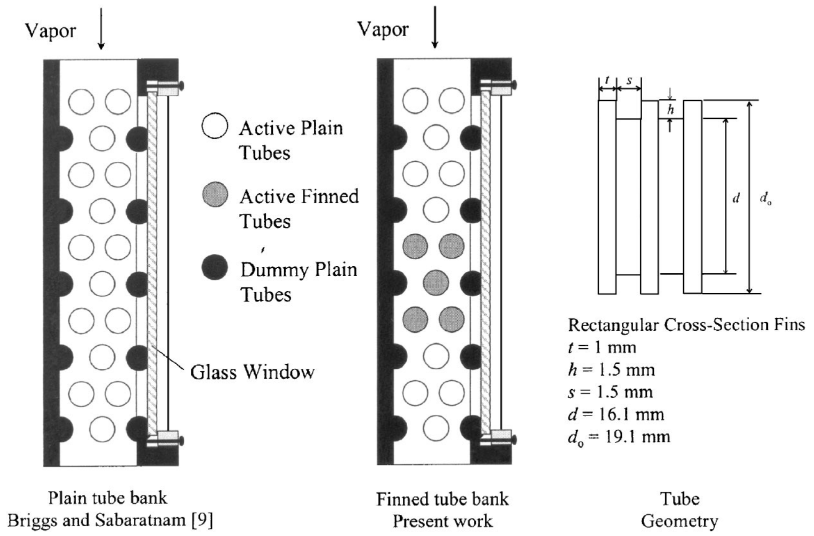

Fig. 2 Test sections and tube geometry

Downloaded 06 Dec 2010 to 193.140.21.150. Redistribution subject to ASME license or copyright; see http://www.asme.org/terms/Terms_Use.cfm

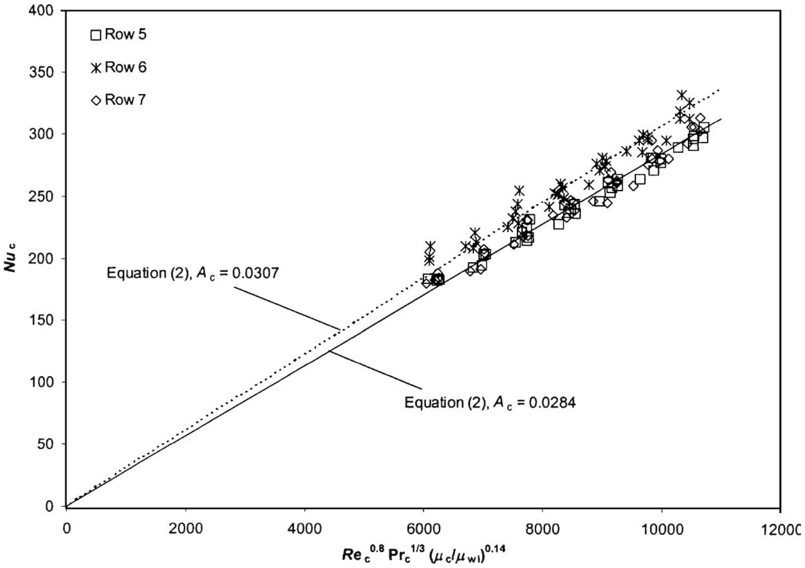

Fig. 3 Coolant-side data for instrumented plain tubes

calculated from the mass flow rates of the steam and air, and also from the measured pressure and temperature upstream of the test section, assuming saturation conditions and using the Gibbs–Dalton, ideal-gas mixture equations, which give

$$W = \frac{P - P_s(T)}{P - (1 - M_v/M_g)P_s(T)} \tag{3}$$

The estimated uncertainty in the measurement of W_u was ±0.002 for both methods, while the difference between values obtained by the two methods was always less than 0.002. The values obtained from the steam and air mass flow rates were used in all subsequent calculations.

The vapor flow rate and air concentration at approach to each row were calculated by subtracting the mass of steam condensed on upstream rows from the flow rate upstream of the bank. The temperature of the steam–air mixture at approach to each row was then calculated from Eq. (3) assuming negligible pressure drop down the bank. Estimates of the pressure drop through the bank indicated that the resulting overestimate of the calculated vapor temperature would never exceed 0.1 K. The "bulk" vapor temperature, T_v, "bulk" air concentration, W_b, and local vapor velocity, U_v appropriate to a given row was taken as the arithmetic mean of the upstream and downstream values.

Great care was taken to ensure the results where not effected by either dropwise condensation or, in the case of the pure steam tests, noncondensing gas. To prevent the former the test tubes were cleaned thoroughly before insertion into the test section using a dilute chromic acid bath and the test tubes were visually checked during all test runs by means of the glass window fitted to one side of the test section. To minimize noncondensing gas (air) in the test section during tests with nominally pure steam, the whole apparatus was tested for leaks between runs. This was done by evacuating the apparatus with a vacuum pump and then sealing it and monitoring the internal pressure over a period of approximately 10 h. With an initial pressure of around 1 kPa the increase in pressure over this period was never greater than 1 kPa. In any case all tests were conducted slightly above atmospheric pressure which would itself prevent air in-leakage. The noncondensing gas content in the vapor upstream of the test section was also monitored during the runs with pure steam, using the measured temperature and pressure and Eq. (3). Using this method the measured noncondensing gas content for the nominally pure steam tests was never greater than 0.002, which is within the uncertainty of the measurement.

An uncertainty analysis was carried out on the results using the method of Kline and McClintock [11]. This method uses the estimated uncertainties in the experimental measurements (e.g., in coolant flow rate, coolant temperature rise, etc.) and calculates the propagation of these uncertainties in the reported results (e.g., heat flux, vapor-side temperature difference, etc.). Using this method and the uncertainties in the measured parameters given above the calculated uncertainty in the vapor mass flow rate (and hence the vapor velocity) at the entrance to the test section was never greater than 2%. The uncertainty in the heat flux to the test tubes was never greater than 3%, the main contribution to this value being the uncertainty in the coolant flow rate. The combined uncertainties in the heat flux and the vapor mass flow rate are in line with the small discrepancies in the energy balance for the whole apparatus discussed above. The main uncertainty in the vapor-side heat-transfer coefficient arose from the use of Eq. (2) to calculate the coolant-side thermal resistance. The uncertainty in Eq. (2) was estimated as 5%, based on the scatter in the experimental data seen in Fig. 3. The propagation of this uncertainty in the calculated vapor-side heat-transfer coefficient depends on the balance of thermal resistances between the coolant side, the tube wall and the vapor-side. The two extremes were: (1) condensation from steam–air mixtures on the plain tubes, where the coolant-side resistance was between 45% and 65% of the total (depending on coolant flow rate) and the resulting uncertainty in the vapor-side coefficient was between 4% and 11%; and (2) condensation of pure steam on the finned tubes, where the coolant-side resistance was between 55 and 80% of the total, and the resulting uncertainty in the vapor-side coefficient was between 7% and 25%. (Note that in all cases the wall resistance was never greater than 8% of the total and its calculation only dependent on the measured heat flux and the tube geometry. Its contribution to the uncertainty in the vapor-side coefficient was therefore always small.)

Results for Pure Steam

All tests were performed at a little above atmospheric pressure and were repeated on different days to ensure accuracy and consistency. For pure steam, results were obtained for steam velocities at approach to the test section between 4.5 and 10.5 m/s and coolant velocities between 1.6 and 3.2 m/s.

Plain Tubes. Figure 4 shows the present results for the plain tube rows (i.e., rows 1–4 and 8–10). The results are compared to those of Briggs and Sabaratnam [9] who, as described earlier, used

Downloaded 06 Dec 2010 to 193.140.21.150. Redistribution subject to ASME license or copyright; see http://www.asme.org/terms/Terms_Use.cfm

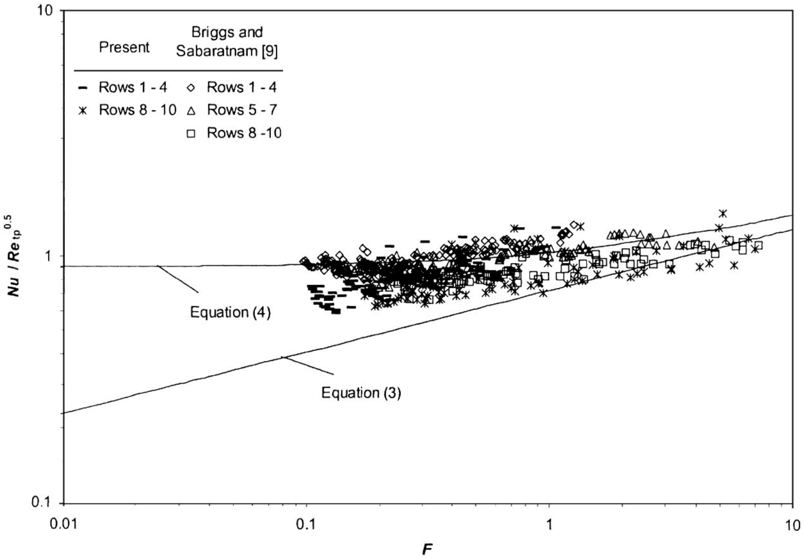

Fig. 4 Results for pure steam condensing on plain tube rows for present and previous investigations

the same apparatus but with ten rows of plain tubes. Also shown in Fig. 4 are the theoretical lines of Nusselt [12] for free convection and Shekriladze and Gomelauri [13], who used the asymptotic, infinite condensation rate approximation to model the vapor-shear at the liquid–vapor interface. The Nusselt result can be written

$$\frac{\mathrm{Nu}}{\mathrm{Re}_{\mathrm{tp}}^{1/2}} = 0.728F^{1/4} \tag{4}$$

while the result of Shekriladze and Gomelauri can be written (see Rose [14]) as

$$\frac{\mathrm{Nu}}{\mathrm{Re}_{\mathrm{tp}}^{1/2}} = \frac{0.9 + 0.728F^{1/2}}{(1 + 3.44F^{1/2} + F)^{1/4}} \tag{5}$$

Note that Eq. (5) tends to Eq. (4) for large F (low vapor velocity) and to $\mathrm{Nu}/\mathrm{Re}_{\mathrm{tp}}^{1/2}=0.9$ for small F (high vapor velocity). In Fig. 4 and elsewhere in this report the local vapor velocity U_v is based on the total cross-sectional area of the test section normal to the flow and the arithmetic mean of the vapor volume flow rates upstream and downstream of the row. The present results are in good agreement with those of Briggs and Sabaratnam [9]. It can be seen that Eq. (5) is in reasonable agreement with both the present and earlier data indicating that the decrease in vapor velocity is the main reason for the decrease in heat-transfer coefficient down the bank. There is some evidence, however, that the data for the lower rows of the bank are somewhat lower [relative to Eq. (5)] than those for the upper rows, suggesting that condensate inundation may play a minor role. This is more noticeable for rows 8–10 of the present data where the condensate inundation rate on these last three rows is larger than in the earlier investigation due to the presence of the three finned tube rows in the bank and the consequent higher condensation rate on these rows. In Fig. 4, a small amount of the data was omitted for rows 8–10, where the local vapor velocity fell below 0.5 m/s. At these low velocities air was able to enter the bottom of the test section and neither Eq. (4) and (5) would be expected to predict the data under these conditions. In the above comparisons, the local bulk vapor velocity used was based on the overall cross-sectional area of the test section. While it is not obvious which area is the correct one for calculation of the local vapor velocity for the case of a tube bank, the use of the minimum area between the tubes and the mean-void area (i.e., the total volume of the test bank not occupied by tubes divided by its height) resulted in less good agreement with Eq. (5).

Finned Tubes. Figure 5 shows the variation of heat flux with vapor-side temperature difference for the finned tube rows (rows 5, 6, and 7) as well as the plain tube data of Briggs and Sabaratnam [9] for the same three rows. Data are shown for four vapor velocities at approach to the test bank, namely 4.6 m/s, 6.1 m/s, 7.5 m/s, and 9.2 m/s. (Note that the vapor velocities given in Fig. 5 are values for the relevant row and so cover a range of velocities, due to varying condensation rates above this row.) The finned tube rows exhibit heat fluxes between 2.5 and 3.5 times higher than the plain tubes at the same vapor-side temperature difference. For the plain tubes there is a clear effect of vapor velocity on the heat flux with higher vapor velocities leading to higher heat flux at a given vapor-side temperature difference due to thinning of the condensate film by vapor shear, and consequently the data fall above the free-convection model of Nusselt [12]. For the finned tubes, however, there is no measurable effect of vapor velocity on heat-transfer rate. This result may be due to the fact that the surface tension induced radial pressure gradients in the condensate film continue to drain liquid from the fin tips to the fin root and this mechanism out ways the circumferential drainage caused by vapor shear. Also, a significant portion of the tube area is on the fin flanks and root where it will be partially shielded from the effects of vapor shear.

Also shown in Fig. 5 are the data of Wanniarachchi et al. [15] for a single tube with fin dimensions the same as those of the present investigation but with a slightly larger fin–tip diameter (22.1 mm compared to 19.1 mm in the present investigation). Despite the small difference in geometry and the fact that the earlier data are for a lower vapor velocity of 1 m/s, good agreement can be seen with the present data, confirming that vapor velocity has a very limited effect on the condensation heat transfer in this case. Also shown in Fig. 5 is the theoretical result for the present finned tube geometry using the relatively simple, semiempirical model of Briggs and Rose [4] for free-convection condensation of pure vapor on finned tubes. The theory is in reasonable agreement with the experimental data.

Figure 6 shows the variation in vapor-side, heat-transfer coefficient with row for the present data and the earlier data of Briggs and Sabaratnam [9]. Separate plots are shown for 3 different coolant flow rates with 4 vapor approach velocities shown on each plot. Note that the ranges of vapor velocity given in this case represent the decrease in vapor velocity down the bank. Thus the higher vapor velocity quoted is that at the first row while the

Downloaded 06 Dec 2010 to 193.140.21.150. Redistribution subject to ASME license or copyright; see http://www.asme.org/terms/Terms_Use.cfm

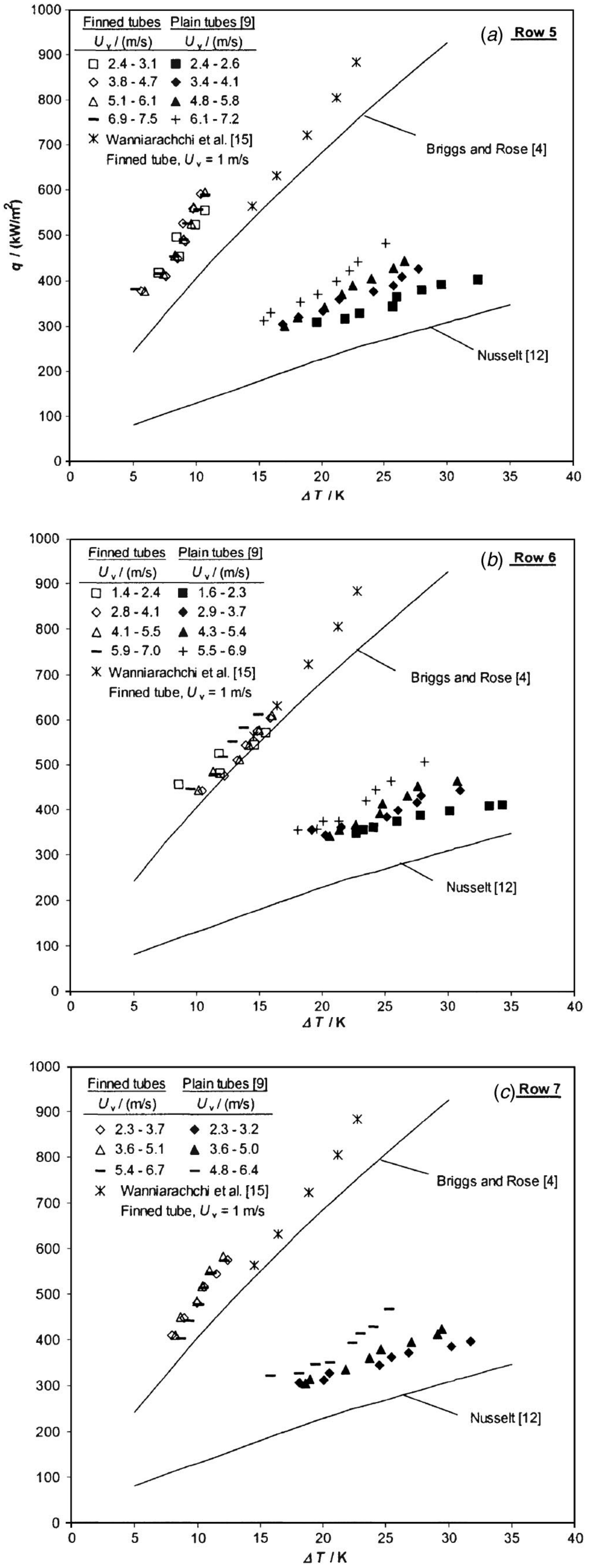

Fig. 5 Results for pure steam condensing on plain and finned tube rows

lower value is that at the tenth row. Figure 6 underlines the good agreement between the present and earlier data for the first four rows previously seen in Fig. 4. In most cases a decrease in heat-transfer coefficient down the bank is evident for both tube banks. This is particularly evident when the approach velocity is very low (approximately 4.5 m/s) and the coolant velocity is quite high (2.6 m/s and above) and is due mainly to the rapid decrease in vapor velocity down the bank rather than to condensate inundation. As pointed out earlier, it is also possible that at very low local vapor velocities, air may have entered the bottom of the test section and effected the heat-transfer to the lower rows, leading to the very low heat-transfer coefficients seen for rows 8–10 in Figs. 6(*a*) and 6(*b*). In a few cases, where the vapor velocity is high all through the bank and the air effect mentioned above would not be present, there is a slight increase in the vapor-side coefficient on the last two rows of the bank. The reason for this is unclear but possible explanations may include turbulence in the condensate film or exit effects from the bank. Its occurrence in many of the data sets [e.g., in Figs. 6(*b*) and 6(*c*)] would tend to suggest this is a real phenomena and not simply scatter in the experimental data. Also evident in Fig. 6 is the enhancing effect of vapor velocity on the heat transfer to each individual row of plain tubes and the absence of any similar effect on the three rows of finned tubes.

Heat Transfer Enhancement Ratios. When assessing the effectiveness of enhanced surfaces during heat transfer it is useful to define an enhancement ratio which indicates the ratio of heat-transfer coefficients for finned and plain tubes under specified conditions. For condensation on single finned tubes at low vapor velocity a convenient enhancement ratio is given by

$$\varepsilon_{\Delta T} = \left(\frac{\mathrm{Nu}_{\text{finned tube}}}{\mathrm{Nu}_{\text{plain tube}}}\right)_{\text{same }\Delta T} \qquad (6)$$

where $Nu_{\text{plain tube}}$ is for a plain tube of outside diameter equal to the fin-tip diameter of the finned tube. Furthermore, it has been shown in numerous experimental investigations (see for instance Briggs et al. [16]) that for low vapor velocity, both plain and finned tubes exhibit approximately the same dependence of heat flux on vapor-side temperature difference (i.e., q approximately proportional to $\Delta T^{3/4}$) and hence $\varepsilon_{\Delta T}$ as defined by Eq. (6) is independent of ΔT.

In the case of a bank of finned tubes, the situation is more complex, since the enhancement ratio should be evaluated for the same vapor velocity as well as the same vapor-side temperature difference. To do this curves of the form

$$\frac{\mathrm{Nu}}{\mathrm{Re}_{\mathrm{tp}}^{1/2}} = AF^n \qquad (7)$$

were fitted to the experimental data for the three finned tube rows and to the equivalent three rows of plain tubes from the earlier data of Briggs and Sabaratnam [9]. In the case of the plain tubes, fits to the three rows separately gave very similar results and so a global fit to all three rows together was used. The results are shown in Table 1. It can be seen that the fits to the finned tube rows gave n very close to 0.25 illustrating the weak dependence of heat-transfer coefficient on vapor velocity. (Note that for pure free-convection, as in the Nusselt [12] expression, $n=0.25$ and $A=0.728$.) The values of A when n is fixed equal to 0.25 are also listed in Table 1. Figure 7 shows the data for these rows with curve fit lines also shown.

From the results of the above curve fitting we can define and evaluate two enhancement ratios for the finned tube rows. The first is defined as the ratio of the Nusselt number for the finned tube to that of a plain tube with fin-tip diameter at the same vapor-side temperature difference, found from the Nusselt [12] model [Eq. (4)] i.e., for zero vapor velocity.

Downloaded 06 Dec 2010 to 193.140.21.150. Redistribution subject to ASME license or copyright; see http://www.asme.org/terms/Terms_Use.cfm

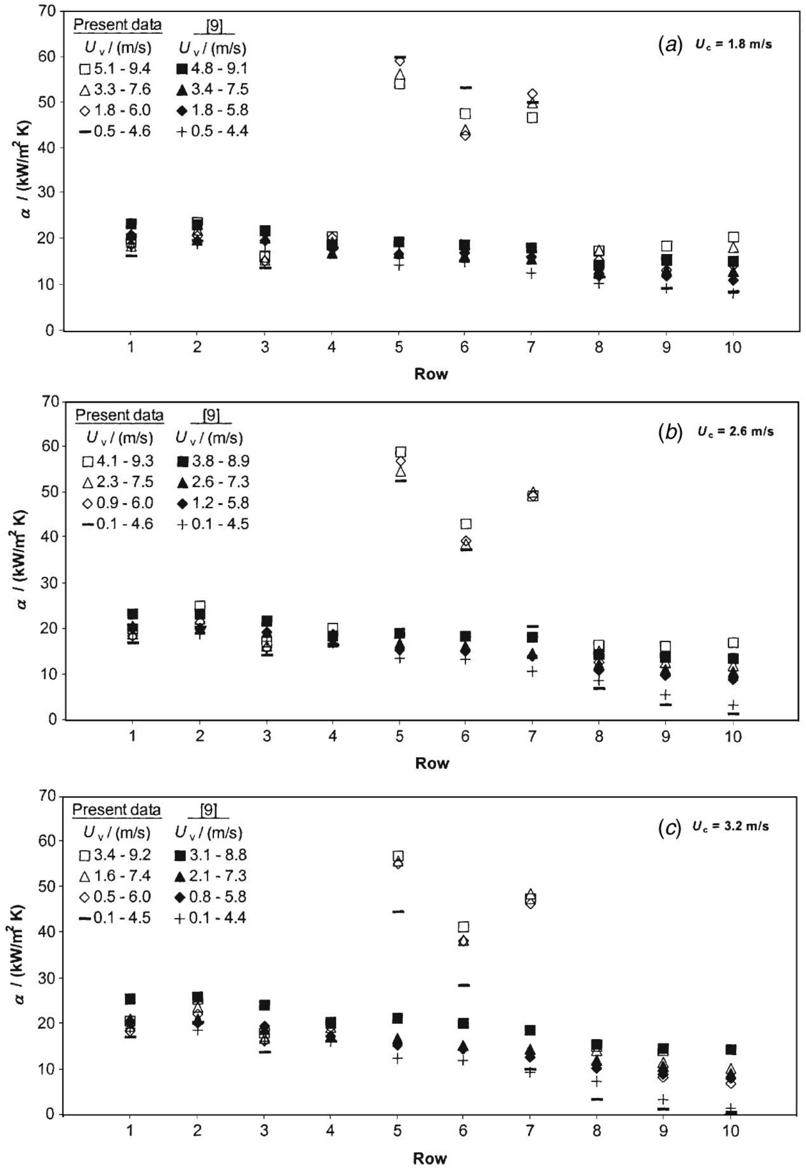

Fig. 6 Variation of vapor-side heat-transfer coefficients with row for pure steam condensing on plain and finned tube banks

$$\varepsilon_{\Delta T,0} = \left(\frac{\mathrm{Nu}_{\mathrm{finned}}}{\mathrm{Nu}_{\mathrm{Nusselt}}}\right)_{\mathrm{same}\ \Delta T} = \left(\frac{A_{\mathrm{finned}}(n=0.25)}{0.728}\right) \tag{8}$$

and the second is the ratio of Nusselt numbers for the finned and plain tubes at the same value of the parameter F, i.e., at the same vapor-side temperature difference and vapor velocity, calculated as follows:

$$\varepsilon_{\Delta T,U_v} = \left(\frac{\mathrm{Nu}_{\mathrm{finned}}}{\mathrm{Nu}_{\mathrm{plain}}}\right)_{\mathrm{same}\ \Delta T,U_v} = \left(\frac{A_{\mathrm{finned}}(n=0.25)}{A_{\mathrm{plain}}(n=0.11)}\right)F^{0.14} \tag{9}$$

It can be seen that the first of these enhancement ratios is a constant. The second however is a function of F, and hence of vapor-side temperature difference and vapor velocity. The calculated en-

Table 1 Curve fits and enhancement ratios

Tube (row)	Plain (5, 6, 7)	Finned (5)	Finned (6)	Finned (7)
A	1.04	3.54	2.68	3.16
n	0.11	0.22	0.23	0.24
A (n = 0.25)	1.17	3.53	2.67	3.16
$\varepsilon_{\Delta T,\mathrm{o}}$	-	4.85	3.67	4.34
$\varepsilon_{\Delta T,U_v}$ / F	-	3.39	2.57	3.04
$\varepsilon_{\Delta T,U_v}(F = 0.4)$	-	3.85	2.92	3.46
$\varepsilon_{\Delta T,U_v}(F = 10)$	-	2.46	1.86	2.20

Downloaded 06 Dec 2010 to 193.140.21.150. Redistribution subject to ASME license or copyright; see http://www.asme.org/terms/Terms_Use.cfm

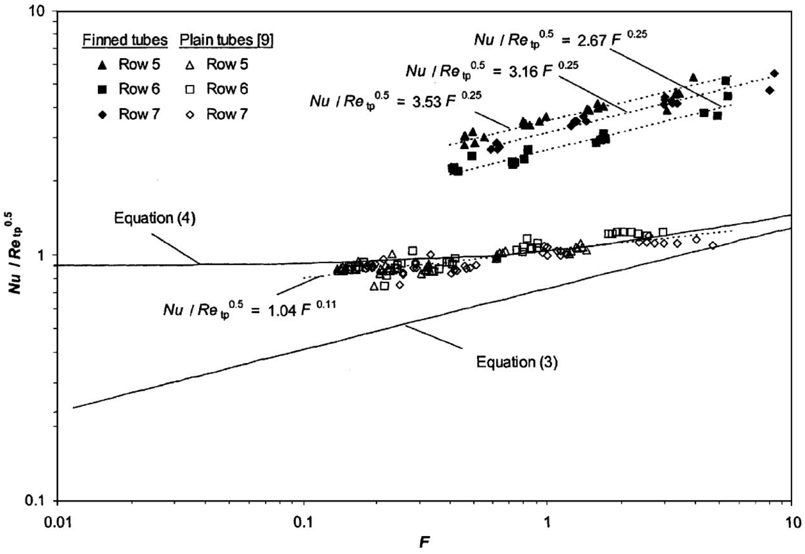

Fig. 7 Curve fit lines for pure steam plain and finned tube data

hancement ratios for each of the three finned rows are listed in Table 1. In the case of the second enhancement ratio, two values are given for each finned tube row, evaluated at the extreme values of the parameter F for the present finned tube data.

Results for Steam–Air Mixtures

As with the pure steam case, all the steam–air tests were performed at a little above atmospheric pressure and were repeated on different days to ensure accuracy and consistency. For steam–air mixtures, results were obtained for approach velocities between 4.5 and 7.2 m/s, coolant velocities between 1.6 and 3.2 m/s, and air concentrations at approach to the test section up to 7.8% by mass.

Figure 8 shows the variation in vapor-side, heat-transfer coefficient down the bank for a representative sample of the data. Note that the ranges of air concentrations given represent the increase in air concentration down the bank. Thus the lower air concentration quoted is that at the first row while the higher value is that at the tenth row. Data of Briggs and Sabaratnam [9] for the bank of ten plain tubes are also shown. The variation in heat-transfer coefficient down the bank for steam–air mixtures is similar to that for pure vapor. For all upstream vapor velocities the data for larger upstream air concentrations show lower vapor-side, heat-transfer coefficients on the plain tubes at the top of the bank as expected. On the finned tubes in rows 5, 6, and 7, the effect of air on the heat-transfer coefficient is much more marked than on the plain tubes, with very small air concentrations leading to reductions in heat-transfer coefficients of up to 50%. This effect is much stronger than on the equivalent plain tubes, as can be seen by comparing the present data for the finned tube rows, 5, 6, and 7, with finned tubes to those of Briggs and Sabaratnam [9] for the same three rows of plain tubes. This observation is particularly noteworthy since the plain tube data are for a much higher range of air concentrations than the finned tube data. The result of this is that the effectiveness of the fins in enhancing the vapor-side, heat-transfer coefficient is significantly reduced when air is present in the steam. The effective enhancement ratio with air present is as low as 1.5, compared to values up to 3.8 for pure steam (see above). As we saw for the pure-steam data, the effect of vapor shear in thinning the film and enhancing the heat-transfer coefficient is greatly reduced when fins are added to the tubes, due partly to areas of the tube between the fins being "sheltered" from the full effect of vapor shear. When air is present, vapor velocity normally acts to prevent high air concentrations building up at the liquid–vapor interface as vapor is removed by condensation, and hence the effects of air are mitigated somewhat when substantial vapor velocity is present. If areas of the finned tube surface are sheltered from vapor velocity effects then air-concentrations will build up at the surface more easily and the effects of air will be more noticeable for finned tubes than for plain tubes.

The steam–air data are compared below with the theory of Rose [17] for forced-convection condensation on a single horizontal tube, in the presence of a noncondensing gas. The theoretical result is here expressed as a relationship between the heat flux and the difference in air mass fraction between the bulk vapor and that at the condensate surface.

$$\frac{qd}{h_{\mathrm{fg}}\rho_v D} = 0.5\,\mathrm{Re}_v^{1/2}\left\{\left[1 + 2.28\,\mathrm{Sc}^{1/3}\left(\frac{W_i}{W_b} - 1\right)\right]^{1/2} - 1\right\} \qquad (10)$$

In Lee and Rose [18], it was shown that Eq. (10) gave good agreement with experimental data for single tubes and for various vapor–gas combinations and conditions.

To compare the experimental data directly to Eq. (10), it is necessary to know the steam–air composition at the vapor-condensate interface, W_i, which can be found from Eq. (3), with P_s taken at T_i, the temperature at the interface. T_i was calculated from the measured heat flux and wall temperature using the curve fits to the pure steam data represented by Eq. (7) and using the values of A listed in Table 1 (with $n=0.25$ for the finned tubes and $n=0.11$ for the plain tubes). The results are shown in Fig. 9. The steam–air velocity, air concentration, and steam–air temperature were calculated from the upstream values and the measured heat fluxes to each row as described above. Arithmetic means of the values above and below the row were used in Fig. 9. As earlier, the steam–air velocity used in place of the "free-stream" velocity of the single-tube theory was that based on the overall test-section area. The diffusion coefficient was evaluated at $(T_v+T_i)/2$ using the equation given by Reid and Sherwood [19]. The density of the steam–air mixture was evaluated by assuming an ideal-gas mixture and viscosity was obtained by the method of Wilke [20]. Arithmetic means of the values of density and viscosity at the interface temperature, T_i and the local bulk temperature, T_v, were used in Fig. 9.

It can be seen in Fig. 9 that the data for the plain tubes are much higher than the single tube theory of Rose [17]. In Briggs and Sabaratnam [9], where these data are discussed in more detail, it was suggested that this was due to mixing and recirculation of the steam–air mixture as it flowed through the tube bank, which would prevent large air concentrations building up at the liquid–

Downloaded 06 Dec 2010 to 193.140.21.150. Redistribution subject to ASME license or copyright; see http://www.asme.org/terms/Terms_Use.cfm

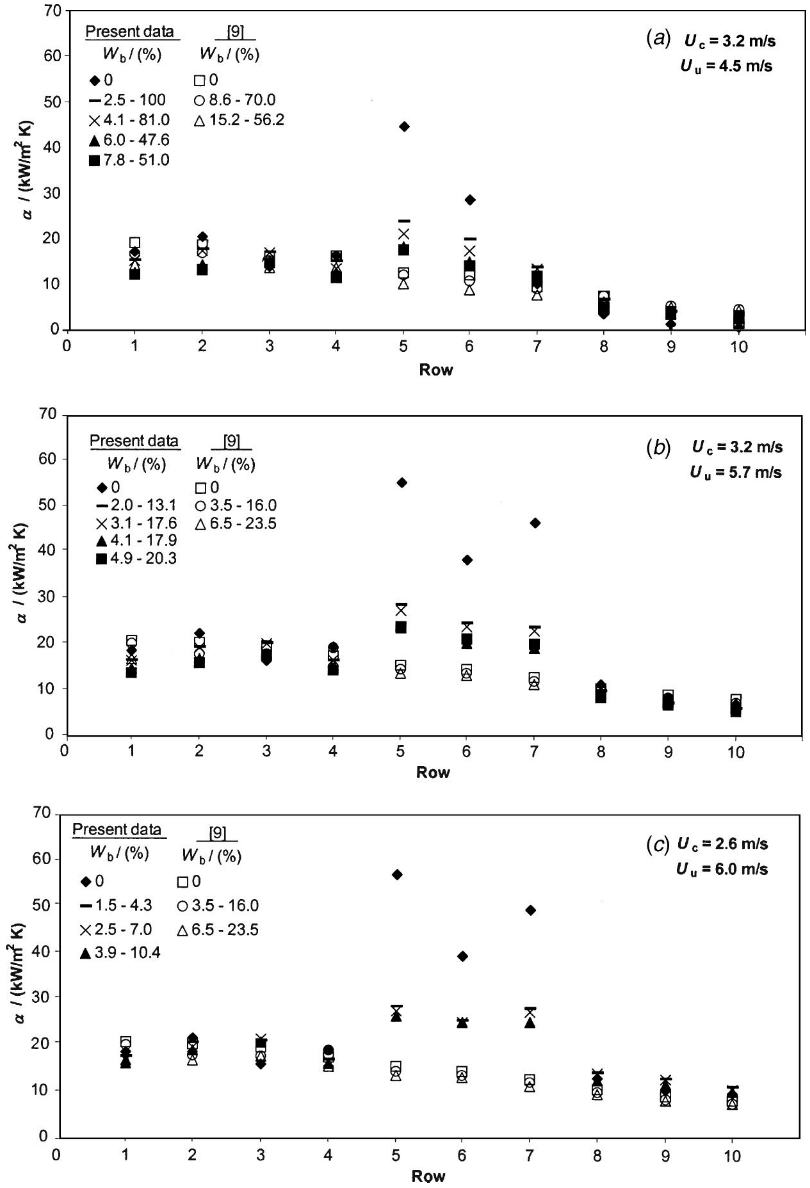

Fig. 8 Variation of vapor-side, heat-transfer coefficients with row for steam–air mixtures condensing on finned tube bank

vapor interface. For the finned tubes, the data are closer to the plain tube theory. This could be explained by air concentrations building up in the interfin spaces where the tube surface is somewhat sheltered from the vapor velocity.

Conclusions

Experimental data are reported for condensation of atmospheric steam, with and without the presence of air, on a tube bank containing three rows of integral-fin tubes. For the pure steam case the vapor-side, heat-transfer coefficients for the finned tubes where essentially independent of local vapor velocity and were between 2.5 and 3.5 times higher than those measured for plain tubes at the same vapor-side temperature difference and vapor velocity and placed in the same position in the tube bank. Two representative heat-transfer enhancement ratios where suggested for condensation from pure vapors on enhanced tubes in a bank. The first was defined as the Nusselt number of the finned tube divided by that for a plain tube calculated from the Nusselt [12] model for condensation of quiescent vapor and the second as the Nusselt number of a finned tube divided by that of a plain tube at the same vapor-side temperature difference and vapor velocity. The first of these ratios was found to be constant for the present data while the second was a function of vapor velocity and vapor-side temperature difference. Values of these two enhancement ratios are listed for the present data in Table 1.

For the steam–air data, the finned tubes showed a much larger decrease in vapor-side heat-transfer coefficients with air concentration than the plain tubes. This resulted in enhancements in vapor-side, heat-transfer coefficients due to the fins of only about 1.5 when even small concentrations of air were present, compared to values up to 3.5 for pure steam.

Nomenclature

A = constant in Eq. (7)
A_c = constant in Eq. (2)
c_{pc} = specific isobaric heat capacity of coolant
D = diffusion coefficient
d = outside diameter of plain tube or fin-tip diameter of finned tube

Downloaded 06 Dec 2010 to 193.140.21.150. Redistribution subject to ASME license or copyright; see http://www.asme.org/terms/Terms_Use.cfm

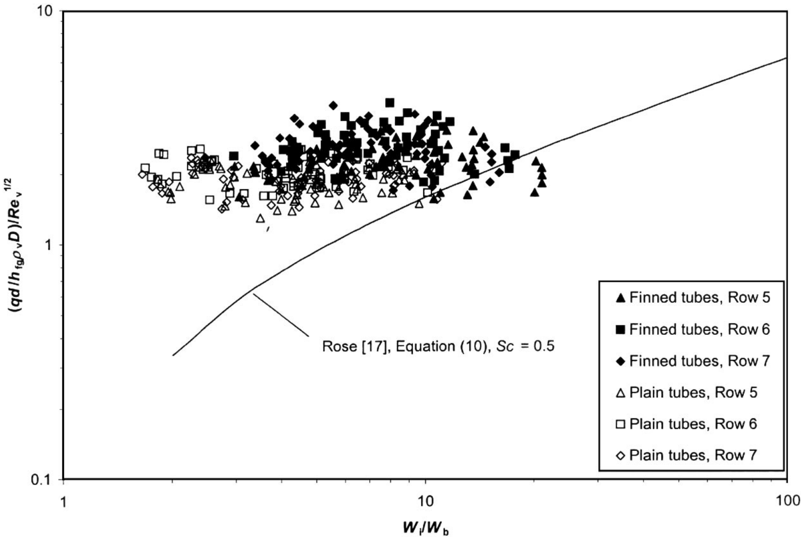

Fig. 9 Comparison of steam–air data for plain and finned tube banks with single tube theory

d_i = inside diameter of tube

F = dimensionless parameter, $(\mu g d h_{\mathrm{fg}}/kU_v^2\Delta T)$

g = specific force of gravity

h_{fg} = specific enthalpy of evaporation

k = thermal conductivity of condensate

k_c = thermal conductivity of coolant

M_g = molar mass of air

M_v = molar mass of steam

Nu = condensate Nusselt number, $(\alpha d/k)$

Nu_c = coolant Nusselt number, $(\alpha_c d_i/k_c)$

n = constant in Eq. (7)

P = pressure

$P_s(T)$ = saturation pressure at temperature T

Pr_c = coolant Prandtl number, $(\mu_c c_{pc}/k_c)$

q = heat flux based on outside surface area of plain tube or fin-tip envelope area of finned tube

q_i = heat flux based on inside surface area of tube

Re_c = coolant Reynolds number, $(\rho_c U_c d_i/\mu_c)$

$\mathrm{Re}_{\mathrm{tp}}$ = two-phase Reynolds number, $(\rho U_v d/\mu)$

Re_v = steam or steam–air Reynolds number, $(\rho_v U_v d/\mu_v)$

Sc = schmidt number, $(\mu_v/D\rho_v)$

T = temperature

T_i = temperature at condensate–vapor interface

T_c = coolant temperature (mean of inlet and outlet temperatures for row)

T_v = local steam or steam–air temperature (arithmetic mean of upstream and downstream temperatures for tube row)

T_{wo} = mean outside wall temperature of plain tube or mean fin-root temperature of finned tube

T_{wi} = mean inside wall temperature of tube

U_c = coolant velocity

U_u = steam or steam–air velocity upstream of test section

U_v = local steam or steam–air velocity based on overall cross-sectional area of test section and the arithmetic mean of the upstream and downstream volume flow rate

W = mass fraction of air in steam–air mixture

W_b = local "bulk" mass fraction of air in steam–air mixture (arithmetic mean of upstream and downstream values for tube row)

W_i = mass fraction of air in steam–air mixture at condensate–vapor interface

W_u = mass fraction of air in steam–air mixture upstream of test section

α = vapor-side, heat-transfer coefficient, $(q/(T_v - T_{wo}))$

α_c = coolant-side, heat-transfer coefficient, $(q_i/(T_{wi} - T_c))$

ΔT = vapor-side temperature difference, $(T_v - T_{wo})$

$\varepsilon_{\Delta T}$ = enhancement ratio for a single finned tube in stationary vapor, i.e., Nusselt number for finned tube based on fin-tip diameter, divided by Nusselt number for plain tube with fin-tip diameter at the same ΔT

$\varepsilon_{\Delta T,0}$ = enhancement ratio for finned tube in a bank, i.e., Nusselt number for finned tube based on fin–tip diameter, divided by Nusselt number for plain tube with fin-tip diameter, calculated from Nusselt [12] theory at the same ΔT

$\varepsilon_{\Delta T,U_v}$ = enhancement ratio for finned tube in a bank, i.e., Nusselt number for finned tube based on fin–tip diameter, divided by Nusselt number for plain tube with fin–tip diameter at the same ΔT and U_v

μ = viscosity of condensate

μ_c = viscosity of coolant

μ_v = viscosity of steam or steam–air mixture

μ_{wi} = viscosity of coolant evaluated at T_{wi}

ρ = density of condensate

ρ_c = density of coolant

ρ_v = density of steam or steam–air mixture

References

[1] Marto, P. J., 1988, "An Evaluation of Film Condensation on Horizontal Integral Fin Tubes," ASME J. Heat Transfer, **110**, pp. 1287–1305.

[2] Briggs, A., and Rose, J. W., 1999, "An Evaluation of Models for Condensation Heat Transfer on Low-Finned Tubes," J. Enhanced Heat Transfer, **6**, pp. 51–60.

[3] Honda, H., Nozu, S., and Uchima, B., 1987, "A Generalised Prediction Method for Heat Transfer During Film Condensation on a Horizontal Low-Finned Tube," in Proc. 2nd ASME-JSME_Thermal Eng. Joint. Conf., Vol. 4, pp. 385–392.

[4] Briggs, A., and Rose, J. W., 1994, "Effect of fin efficiency on a model for condensation heat transfer on a horizontal, integral-fin tube," Int. J. Heat Mass Transfer, **37** (Suppl. 1), pp. 457–463.

Downloaded 06 Dec 2010 to 193.140.21.150. Redistribution subject to ASME license or copyright; see http://www.asme.org/terms/Terms_Use.cfm

[5] Honda, H., Uchima, B., Nozu, S., Nakata, H., and Torigoe, E., 1991, "Film Condensation of R-113 on In-Line Bundles of Horizontal Finned Tubes," ASME J. Heat Transfer, **113**, pp. 479–486.
[6] Honda, H., Uchima, B., Nozu, S., Torigoe, E., and Imai, S., 1992, "Film Condensation of R-113 on Staggered Bundles of Horizontal Finned Tubes," ASME J. Heat Transfer, **114**, pp. 442–449.
[7] Honda, H., Takamatsu, H., and Kim, K., 1994, "Condensation of CFC-11 and HCFC-123 in In-Line Bundles of Horizontal Finned Tubes: Effect of Fin Geometry," J. Enhanced Heat Transfer, **1**, pp. 197–209.
[8] Briggs, A., Bui, H. H., and Rose, J. W., 2000, "Condensation of Refrigerant on Banks of Smooth and Finned Tubes," in Proc. 20th IIR Int. Cong. of Refrigeration, Sydney, Vol. 2, Paper No. 518, pp. 2620–2626.
[9] Briggs, A., and Sabaratnam, S., 2003, "Condensation of Steam in the Presence of Air on a Single Tube and a Tube Bank," Int. J. Energy Res., **27**, pp. 301–314.
[10] Sieder, E. N., and Tate, G. E., 1936, "Heat Transfer and Pressure Drop of Liquids in Tubes," Ind. Eng. Chem., **28**, pp. 1429–1435.
[11] Kline, S. J., and McClintock, F. A., 1953, "Describing Uncertainties in Single-Sample Experiments," Mech. Eng. (Am. Soc. Mech. Eng.), pp. 3–8.
[12] Nusselt, W., 1916, "Die Oblerflachenkondensation des Wasserdamfes," Z. Ver. Dt. Ing., **60**, pp. 569–575.
[13] Shekriladze, I. G., and Gomelauri, V. I., 1966, "Theoretical Study of Laminar Film Condensation of Flowing Vapor," Int. J. Heat Mass Transfer, **9**, pp. 581–591.
[14] Rose, J. W., 1984, "Effect of Pressure Gradient in Forced-Convection Film Condensation on a Horizontal Tube," Int. J. Heat Mass Transfer, **27**, pp. 39–47.
[15] Wanniarachchi, A. S., Marto, P. J., and Rose, J. W., 1985, "Film Condensation of Steam on Horizontal Finned Tubes: Effect of Fin Spacing, Thickness and Height," Multiphase Flow and Heat Transfer, **ASME HTD-47**, pp. 93–99.
[16] Briggs, A., Wen, X. L., and Rose, J. W., 1992, "Accurate Heat Transfer Measurements for Condensation on Horizontal, Integral-Fin Tubes," ASME J. Heat Transfer, **114**, pp. 719–726.
[17] Rose, J. W., 1980, "Approximate Equations for Forced-Convection Condensation in the Presence of a Non-Condensing Gas on a Flat Plate and Horizontal Tube," Int. J. Heat Mass Transfer, **23**, pp. 539–546.
[18] Lee, W. C., and Rose, J. W., 1984, "Forced-Convection Film Condensation on a Horizontal Tube With and Without Non-Condensing Gases," Int. J. Heat Mass Transfer, **27**, pp. 519–528.
[19] Reid, R. C., and Sherwood, T. K., 1966, *The Properties of Gases and Liquids*, 2nd ed., McGraw–Hill, NY.
[20] Wilke, C. R., 1950, "A Viscosity Equation for Gas Mixtures," J. Chem. Phys., **18**, pp. 517–519.

Downloaded 06 Dec 2010 to 193.140.21.150. Redistribution subject to ASME license or copyright; see http://www.asme.org/terms/Terms_Use.cfm

M. R. Anderson
Senior Performance Engineer
Calpine Corporation,
104 Woodmere Road,
Folsom, CA 95630
e-mail: michael.anderson@calpine.com

J. W. Baughn
Professor
Fellow ASME
Department of Mechanical and Aeronautical
Engineering, University of California, Davis, One
Shields Avenue,
Davis, CA 95616
e-mail: jwbaughn@ucdavis.edu

Liquid-Crystal Thermography: Illumination Spectral Effects. Part 1—Experiments

Experiments have been performed to examine the spectral effects of the illumination source on the hue-temperature characteristics of thermochromic liquid crystals (TLCs) used in a liquid-crystal thermography system. Five illumination sources were compared in this study. It was found that "full spectrum" sources, which have a relatively uniform radiant intensity across the visible spectrum, tend to have the lowest temperature uncertainties and the broadest useful ranges, which are desirable calibration attributes. Radiation in the infrared, which leads to (usually undesirable) heating of a test surface, and in the ultraviolet, which can damage TLCs, are discussed for the various light sources. Experimental observations of the effect that UV damage has on liquid crystal calibrations are also provided. The use of a new method called background subtraction and the use of white balancing are investigated as methods of improving the calibration characteristics of TLCs. The uncertainty in temperature associated with different illumination sources and both background subtraction and white balancing is determined and discussed. It is shown that these methods can reduce the uncertainty in some cases.
[DOI: 10.1115/1.1909207]

Background

Early uses of thermochromic liquid crystals (TLCs) to measure temperature used a single color (usually yellow) to produce a single isotherm. Moffat [1] and Jones [2] provide an overview of liquid-crystal characteristics and their use in heat transfer testing. Early applications include those of Cooper et al. [3] and Hippensteele et al. [4]. Baughn [5] provides a review of five different methods of determining heat transfer coefficients using a narrowband TLC.

More recently a range of temperatures has been measured with TLCs by relating the color or hue to temperature. Hollingsworth et al. [6] were among the first to obtain R, G, and B information from a single image, which was converted into hue. After calibration, the hue field produces the surface temperature distribution (thermography) and the heat transfer distribution. Camci et al. [7] also used a hue-capturing technique. The peak intensity has been related to a particular temperature (e.g., [8,9]).

Several different representations for hue have been proposed Farina [10]. Hay and Hollingsworth [11] suggested the following representation, which is used throughout the present work:

$$\text{Hue} = \arctan\left[\frac{\sqrt{3}(G-B)}{2R-G-B}\right] \tag{1}$$

Hay and Hollingsworth [11] report uncertainties of about 7% of the useful range. Baughn et al. [12] showed that median filtering can reduce the uncertainties significantly (for example, to about 3.7% with a 5×5 median filter). Hay and Hollingsworth [11] suggest that the response of a chiral nematic liquid crystal (CNLC) may be affected by temperature gradient. Ireland and Jones [13] explain this affect of the temperature gradient. Anderson and Baughn [14] showed that hysteresis in microencapsulated TLC can be as much as 20–60% of the useful temperature range when cooled rather than heated.

There are a number of overviews of the liquid crystalline state (e.g., [1,2,11,15–17]). To reduce irreversible damage from solvents and UV radiation TLCs are commonly microencapsulated (i.e., the TLC material is encased in a polymer coating, forming spheres). Microencapsulated TLCs are used in all of the results presented here.

It is generally understood that the perceived color (or hue) from a liquid-crystal-coated surface is a function of the spectral characteristics of the illumination source, the reflecting surface and the sensing device [7,9,10]. Wang et al. [9] state that knowledge of these spectral characteristics could be used to predict the intensity-temperature relation. Predicting this relation with an accuracy comparable to an actual calibration is unlikely because of the need for precise knowledge of the characteristics of each imaging component (e.g., each new TLC coating may yield different reflectivity characteristics). Greater understanding of the effect each component has on the resulting calibration, however, would be useful.

Hay and Hollingsworth [11] provided extensive hue-temperature calibration data for three polymer-dispersed (nonencapsulated) CNLCs. They found a similarity between the shape of the three calibration curves. They also state that several other researchers found similar shaped hue-temperature relations for other TLC mixtures when using the same definition of hue. They developed a general polynomial equation to collapse three different calibration curves to a single universal equation. With this general calibration equation they suggest that only six images (hue-temperature pairs) are necessary to apply the general equation to any CNLC, although they do say that other CNLCs should be tested to confirm this.

Farina et al. [10] describes a method of reducing the effect of background light source spectral distribution on hue-temperature calibration by normalizing the signal to a set of reference colors. They state that when background lighting is present, the perceived color of the microencapsulated TLC surface tends to shift toward the color of the background light. This is true, however, it is more rigorous to say that the measured color, or hue, tends to shift (or be attenuated) toward the background hue of the TLC-coated surface whether background lighting is present or not.

A wide variety of light sources have been used to illuminate TLC coated surfaces in the past, e.g., room lighting [8], tungsten [7,19], halogen [20–22], flood lamps [6], a 3200 K white light source [10], fluorescent [9,11,23], Halolux [18], Xenon short arc

---

Contributed by the Heat Transfer Division for publication in the JOURNAL OF HEAT TRANSFER. Manuscript receieved: June 27, 2004. Final manuscript received: January 8, 2005. Review conducted by: Kenneth Kihm.

Copyright © 2005 by ASME

Downloaded 06 Dec 2010 to 193.140.21.150. Redistribution subject to ASME license or copyright; see http://www.asme.org/terms/Terms_Use.cfm

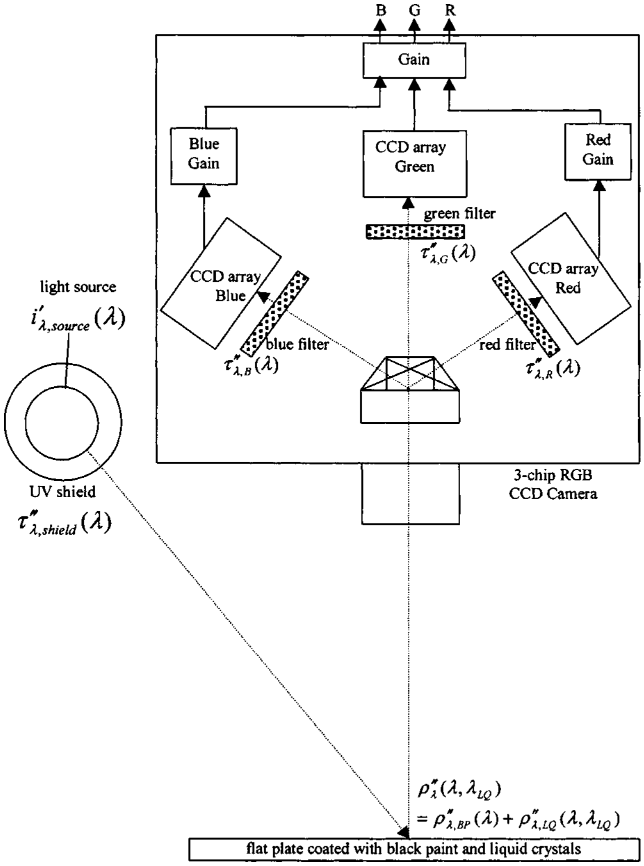

Fig. 1 Diagram of liquid-crystal thermography system

lamp [24], and studio lighting [25]. Some sources were used to produce minimal UV output, some to produce minimal IR heating, some to provide "white light," some for high intensity and some for mere convenience. Some of the sources listed also included IR filters to reduce radiant heating of the TLC surface, which may have altered the spectral distribution illuminating the surface.

Hay and Hollingsworth [11] compared four different methods of numerically representing color (three of which were hue based) to produce color-temperature calibrations in an effort to determine the "best" method. The main criteria for comparison were the maximum effective width of the calibration range and the minimum uncertainty in temperature.

The experimental study reported here has been carried out to examine the effect of the illumination spectrum on the hue-temperature calibration of a typical liquid-crystal thermography system. Five different illumination sources were used, and as expected, the illumination source was found to have a significant effect on the shape of the hue-temperature calibration curve. As a rule, therefore, a general calibration equation, as suggested by Hay and Hollingsworth [11], should not be transported from one experimental configuration to another. The use of background subtraction and white balancing are investigated as methods of improving the calibration characteristics.

Liquid-Crystal Thermography System

A diagram of the liquid-crystal thermography system used in these experiments is shown in Fig. 1. For a discussion of the nomenclature for the radiation terms in this diagram see Part 2 of this paper on theory [26]. The system consists of a diffuse illumination source with its own spectral distribution that depends on the source of the illumination. The illumination source is surrounded by an optional UV shield. The incident light is reflected from a surface coated with black paint and microencapsulated thermochromic liquid crystals. The surface reflectivity can be a function of both wavelength and surface temperature. The reflected light enters a three-chip CCD camera and is split into three beams. These beams pass through red, green, and blue filters, respectively, and are finally received by their respective red, green, and blue CCD arrays. The red and blue signals pass through optional red and blue gains allowing complete control of the relative magnitudes of red, green, and blue (i.e., allowing the system to be white balanced). Finally, all three signals pass through an overall gain and the resulting signal is sent to the frame capture card for digitization. Please note that this system is similar to that for a single-chip CCD camera where the red, green, and blue components are obtained from an array of pixels on a single chip with $R,G,$ and B filters on the individual pixels. In this case, the $R,G,$ and B components are not colocated, but if it is assumed that the neighboring $R,G,$ and B components can be used for each pixel (the normal assumption made in liquid-crystal thermography), then this system will give similar results.

In the current treatment, angular effects are not considered. The illumination source position and viewing angles remain constant.

Experimental Setup and Procedure

For these measurements, a 2 cm thick copper calibration block was used to provide a uniform temperature during both heating and cooling. It was airbrushed with a thin coat of Hallcrest BG-1 black paint and then with a microencapsulated R35C5W liquid crystal from Hallcrest Inc. The copper block was placed on a coil heater and the CCD camera was mounted directly above the block. A black drape was placed over the system to minimize room light and reflected light. The calibration block temperature was measured using an embedded calibrated thermistor. A Sony XC-003 three-chip RGB CCD camera and a Matrox Meteor RGB image acquisition board were used to capture the RGB images, which were saved in TIFF format as 8-bit integer data (scale 0-255) with a resolution of $640\times480\times3$. A rectangular piece of gray cardboard was mounted next to the liquid-crystal strip to provide reference during and between runs. Prior to each run, three reference gray squares from a Macbeth color checker chart were placed above the calibration block and an image was taken of them to provide a standard reference for white balance. The three Macbeth squares were neutral 3.5, 5, and 6.5.

Six runs were performed using the following five illumination sources:

1. Tungsten filament [(3200 K), GE 100 W soft white],
2. SoLux [(4700 K) 38° beamspread, tungsten-halogen based],
3. Fluorescent with UV filter [GE 20 W T-12 cool white with Spectrum 574 filter],
4. Fluorescent [(4100 K), GE 20 W T-12 cool white],
5. Vita-Light [(5500 K) 20 W T-12 24″ full spectrum fluorescent].

The sources are listed in the order in which they were tested. This order was chosen such that testing would progress from minimum UV output to a maximum UV output. The first source was rechecked at the end of testing to determine the magnitude of UV damage to the surface coating.

Each run was done in heating with the starting temperature between 22 °C and 25 °C to avoid hysteresis effects [14]. Data was taken at approximately 0.15 °C increments between 36 °C and 44 °C, which covers the useful range for this liquid crystal. Images were acquired and temperatures were recorded simultaneously during a slow transient heating that was kept below 0.3 °C/min. This heating rate results in an approximate temperature variation throughout the plate on the order of 0.01 °C which is satisfactory for these experiments.

The tests were performed one at a time over the course of a week. Each light source was removed from the test rig and replaced by a subsequent light in the same location ensuring that the

Downloaded 06 Dec 2010 to 193.140.21.150. Redistribution subject to ASME license or copyright; see http://www.asme.org/terms/Terms_Use.cfm

angle of incidence to the plate and the distance from the plate was the same for each run. This angle was approximately 45 deg and the light was ~0.2 m from the plate. Because of the variation in light intensity for the different illumination sources, the iris setting on the camera was adjusted for each run to avoid signal saturation (R,G, and B values are limited to the range 0–255). Iris setting variations result in the same percentage change in each of the R,G, and B components and therefore do not affect hue [27]. All of the gain settings on the camera were set to 0 and the color temperature was set to 5600 K.

Processing of the image data was performed in MATLAB. Hue, saturation, and value data were calculated using MATLAB's RGB2HSV function with results in the range 0 to 1. This algorithm used to calculate hue, is equivalent to Eq. (1) (which was suggested in Hay and Hollingsworth [11]) with a maximum difference in hue of 0.003, which is negligible compared to hue standard deviations in TLC images of ~0.01–0.1.

Saturation is a measure of the spread between the R,G, and B values and is calculated by

$$S = \frac{\max(RGB) - \min(RGB)}{\max(RGB)} \tag{2}$$

and value is a measure of the brightness and is equal to the maximum of R,G, and B.

For each image of each run, two regions were analyzed, one for the reference gray and one for the TLC. The areas analyzed were 10 pixels × 100 pixels representing approximately 2 × 20 mm. Each area was chosen parallel to the light source to minimize illumination intensity variations and to minimize the TLC illumination angle effect [28]. HSV data was calculated from the RGB data for each pixel in the two areas and then the statistical information (mean, standard deviation, minimum, and maximum) was determined for each of the six components.

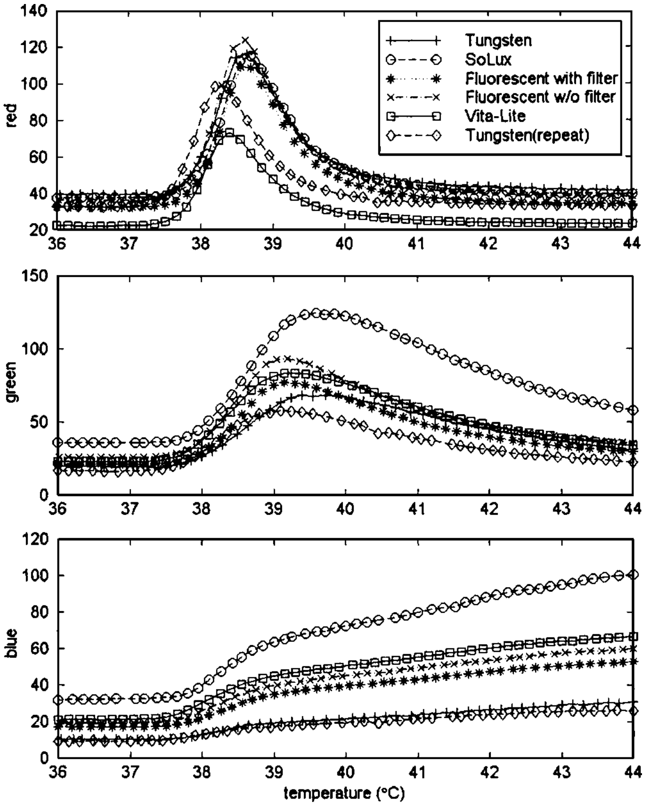

Fig. 2 Experimental RGB output versus temperature

Experimental Results

Experimental red, green, and blue data versus temperature results are shown in Fig. 2. This data consists of six curves for the five different illumination sources. As noted earlier, the testing was performed in order of increasing UV output. The tungsten illumination source was re-tested at the end of the series to determine the magnitude of UV damage incurred, and both sets of tungsten data are presented. There was obvious damage from the Vita-Lite, resulting in curve shifts to lower temperature for both the Vita-Lite and the repeated Tungsten sources. Anderson [27] shows that the Vita-Lite source can cause measurable damage to TLC's in a matter of minutes, however, the cool white fluorescent with protective UV shield led to no measurable damage over 20 hr of exposure. The relative shapes of the curves are still reasonable however and the data is still useful for this analysis. The original Tungsten data did not incur UV damage and will be used in this analysis (the repeated Tungsten data is not used).

It is evident from the red component data that color play begins at approximately 37.5 °C. Data at temperatures below this value represent the background component due to the reflection of incident light from the black paint, liquid crystal microcapsule material, binder material, and the liquid crystals (outside the range of color play). This background accounts for approximately 30% of the peak signal for each of the three components. If a source has a large spectral variation in emissive output, such as the tungsten source which has a high red component and low blue component, this background reflection can cause significant attenuation of the hue curve. The R,G, and B background values for the SoLux source, which has a relatively flat spectrum, are comparable to one another. However, the R,G, and B background values for the tungsten source have a significant variation in R,G, and B values; the maximum blue component is about 80% less than the maximum red component.

Experimental hue saturation and value curves are shown in Fig. 3. Hues below about 37 °C represent the background hues, since the values are constant below this temperature. The useful hue-temperature calibration range for this data depends on the illumination source but in general is about 38.5 °C to 43 °C. The tungsten and fluorescent sources have background hues near 0.0 (which represent red). However, the saturation curves show that the tungsten bulb has a much higher saturation, which means that there is a larger variation in magnitude between the largest and smallest component (see Eq. (2)), whereas, for the cool white fluorescent sources the three components are closer to one another. The saturation curve also shows that the flatter spectrum sources (SoLux and the Vita-Lite) have very low background saturation. These relative magnitudes of saturation are a function not only of the light source spectral characteristics but also of the camera gains (which were zero for these tests) and camera color temperature setting (which was 5600 K for these tests). A 3200 K color temperature setting would lower the red component and increase the blue component causing the tungsten source to have a smaller saturation and the flatter sources to have a larger saturation and a hue closer to pure blue (0.67). The strong saturation of the tungsten bulb shows itself in the hue curve as the liquid crystal proceeds to higher and higher temperatures. At temperatures above about 40 °C the strong red background component overpowers the other two components and attenuates the hue keeping it within about 0.1 of its background value.

The flatter spectrum sources tend to have a higher and more uniform saturation over a majority of the useful range. The value curves relate to the intensity of the reflected light entering the CCD. The magnitude is not of interest since it can be affected by distance between the illumination source and TLC-coated surface for example. The two full spectrum sources offer the highest average values over the useful range when normalized. As will be discussed shortly, higher saturation and value lead to lower uncertainty.

Downloaded 06 Dec 2010 to 193.140.21.150. Redistribution subject to ASME license or copyright; see http://www.asme.org/terms/Terms_Use.cfm

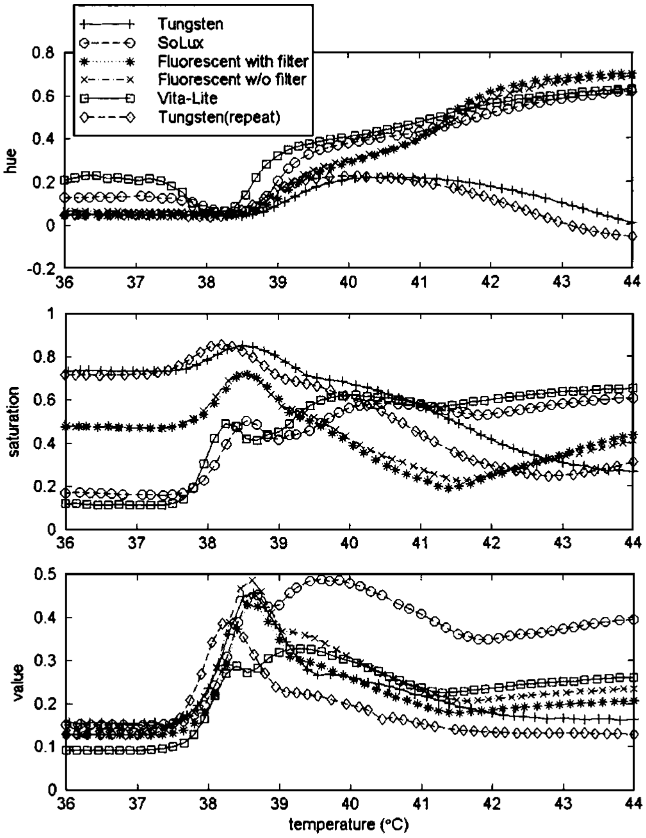

Fig. 3 Experimental HSV output versus temperature

Effect of Illumination Source on Uncertainty. The choice of illumination source can result in variations in hue-temperature sensitivities as well as variations in saturation and value characteristics over the useful range, which may lead to higher or lower temperature uncertainties over various regions of the useful range. Depending on the nature of the experiment and the specific data reduction equation, the contribution of the surface temperature uncertainty may be a major or minor contributor to the overall uncertainty. The uncertainty in the temperature using a TLC hue calibration can be determined by following the approach of Hay and Hollingsworth [11]. They suggest determining the uncertainty in temperature using a root-sum-square of the SEE (standard error of estimate) for the calibration curve and the precision error associated with the standard deviation of the hue from pixel to pixel. Using a coverage factor of 2 (to provide a standard 95% confidence level) the uncertainty in temperature is given by

$$U_T = 2 \times (\mathrm{SEE}^2 + S_T{}^2)^{1/2} \tag{3}$$

where the precision limit is determined by

$$S_T = S_h \times \frac{\partial T}{\partial h} \tag{4}$$

The SEE is a measure of how well the curve fit describes the calibration data and can be determined by performing multiple calibrations. It is assumed that the SEE is primarily a function of reproducibility of a particular test condition and will be approximately the same for the five illumination sources tested. A comparison of the uncertainty in temperature associated with the five illumination sources tested, therefore, will concentrate on the effect of illumination source on temperature precision limit.

The temperature precision limit is determined from the sensitivity of temperature to hue, $\partial T/\partial h$, and the hue precision limit S_h, which is simply the standard deviation of hue. The hue standard deviation can be described as decreasing with increasing saturation or increasing value and can vary from one light source to another. Except for the tungsten source, all of the sources produce a hue that goes through about the same overall hue change (0.6) over the same temperature change (about 5 °C), resulting in an average sensitivity of about 8 °C/unit hue (hue is dimensionless). If the hue-temperature curve were a straight line this would be the sensitivity at every hue, however, the hue-temperature curves have regions of higher and lower sensitivity. The nature of each curve depends on, among other things, the light source. Not even the theoretically flat spectrum source has a linear hue-temperature relation due to the nature of the CCD filter transmissivities. So the obvious questions are What is the dependence of overall experimental uncertainty on illumination source? And, is there a light source that will produce the lowest uncertainty in temperature measurement?

There are many different experimental techniques that utilize TLCs. Each technique may have a different ideal illumination source in regards to lowering uncertainty. For example in a basic resistive coating analysis (ignoring radiation and 2D effects) the heat transfer coefficient is determined from the ohmic heating of the resistive coating q'', the ambient temperature and the surface temperature (i.e., through TLCs).

$$h = \frac{q''}{T_s - T_{\mathrm{amb}}} \tag{5}$$

As T_s approaches T_{amb} (which is lower) the uncertainty in h would increase if the hue-temperature calibration were linear (assuming the uncertainty in heat flux were unchanged). It might be advantageous to sacrifice uncertainty at higher temperatures to have lower temperature uncertainty at the lower temperatures and therefore balance out the overall uncertainty.

Another common experimental technique is the step transient technique which is performed either in heating (e.g., [25]) or in cooling (e.g., [29]). In cooling, it can be shown that the uncertainty in h increases with increased surface temperature and therefore it may be advantageous to have lower surface temperature uncertainty at higher temperatures. When a heating transient is performed, however, the opposite is true. In this case, an increased uncertainty in h is associated with the decrease in surface temperature and it may be advantageous to have lower temperature uncertainties at lower temperature, as was the case for the resistive coating method.

Figure 4 shows the standard deviation in hue, the sensitivity of temperature to hue and the resulting temperature precision limit for each of the five light sources tested experimentally. This data covers a temperature range of 38 to 44 °C, which spans the useful calibration range for this liquid crystal. As discussed previously, the temperature precision limit is the product of the standard deviation in hue and the sensitivity of temperature to hue and it is directly related to the uncertainty in temperature. The useful range depends on the light source and on some personal criteria for what is useful and what is not. The Tungsten source has a useful range of about 1 °C due to the discontinuity in the temperature/hue sensitivity which is a direct consequence of the large attenuation of the hue-temperature curve (see Fig. 3). The two flatter spectrum sources (the Vita-Lite and SoLux sources), exhibit the lowest uncertainties and the broadest useful ranges. The two fluorescent sources, filtered and unfiltered, exhibit comparable uncertainties but a narrower useful range. The calibration sensitivities of the two cool white fluorescent and the two full spectrum sources are comparable. The lower uncertainties of the two flatter spectrum sources relative to the cool white fluorescent sources are largely because of their higher saturation's, especially at higher temperatures, which are due to their larger percentage of illumination at lower wavelengths (see part 2 [26]). The various sources do not offer much of a trade-off in temperature uncertainty between the higher and lower temperatures. In general the better illumination sources for any TLC technique, based on temperature uncertainty, are the flatter spectrum sources.

Downloaded 06 Dec 2010 to 193.140.21.150. Redistribution subject to ASME license or copyright; see http://www.asme.org/terms/Terms_Use.cfm

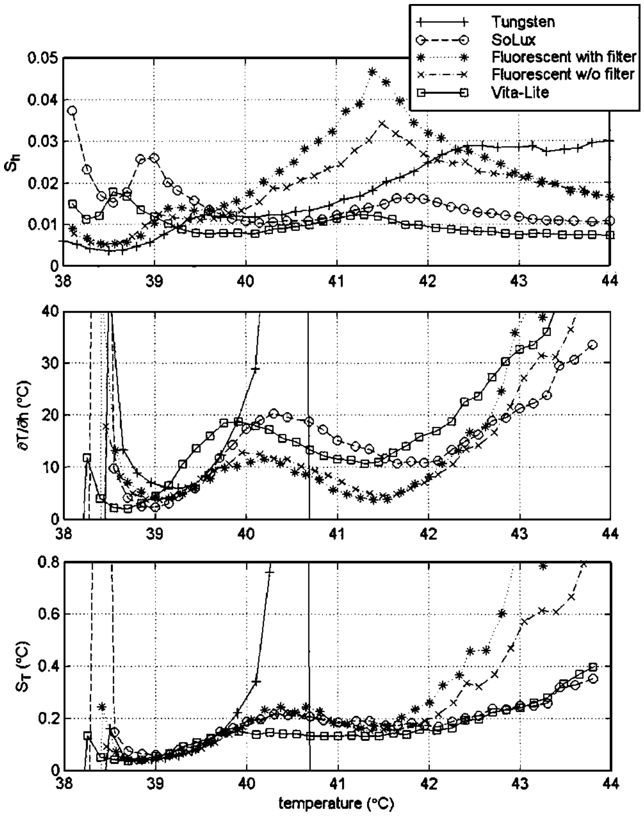

Fig. 4 Experimental hue-temperature sensitivity and uncertainty for various illumination sources

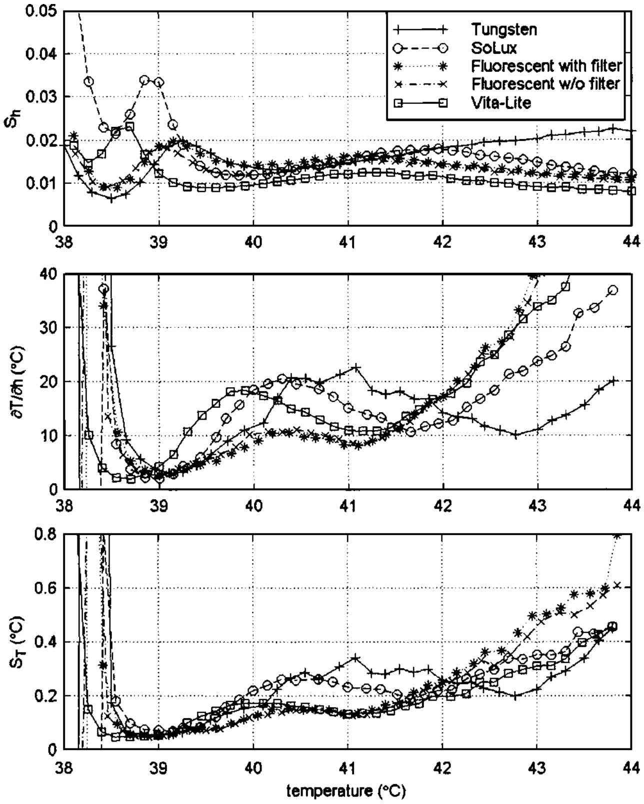

Fig. 6 Experimental hue-temperature sensitivity and uncertainty for various illumination sources after background subtraction

Background Subtraction. Red, green, and blue background values for each source were determined by averaging the five lowest temperature data points for each set of data. These background values were then subtracted from their respective set of data. There is no change in the shape of the red, green, and blue curves; the only difference is that each of the curves is shifted down such that the value of each of the components is zero below the start of color play. There are, however, significant changes in the hue and saturation curves as shown in Fig. 5. In the case of the tungsten source this change is quite significant. The hue curve for the tungsten source yields a usable, monotonically increasing hue-temperature calibration after background subtraction. In addition, for each source, there is an increase in saturation over much of the useful range. Value is not shown here because it is no longer meaningful after background subtraction is performed.

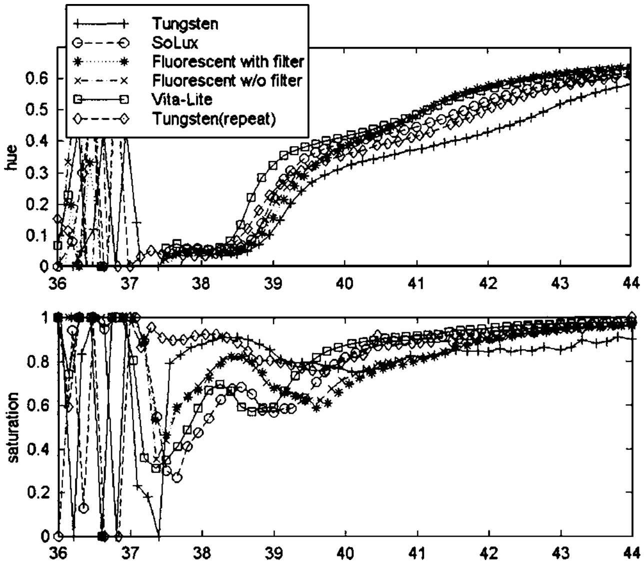

Fig. 5 Experimental hue and saturation data after background subtraction

As mentioned previously, background reflection tends to attenuate the liquid crystal reflection. For example, compare the original experimental hue data (Fig. 3) to the experimental hue data after background subtraction (Fig. 5). The original background hue for both of the cool white fluorescent sources is about 0.05. Recall that our hue definition is a periodic function. When the hue for the cool white fluorescent sources is below 0.55, the hue is attenuated toward lower hues and when the hue is above 0.55, the hue is attenuated toward higher hues. This results in a flattening of the hue-temperature curve near a hue of 0.55 and an increased slope on each side of this. This behavior is reduced when background subtraction is applied. The effect that the background has on the hue curve is directly related to the saturation; the greater the saturation, the greater the hue attenuation. The Tungsten source, without background subtraction, has the largest background saturation of about 0.8, and this background results in such a large attenuation that the hue never exceeds 0.2.

Hues greater than 0.67 (pure blue) and less than 0.0 (pure red) are sometimes encountered in hue-temperature calibrations. These hues arise from the background reflection overpowering the liquid crystal reflection and would not be possible during color play if the background reflection were zero. Similarly, the upturns in hue below 30 °C are due to the background overpowering the liquid crystal reflection. Rather than the liquid-crystal reflection being measured at these hues, it is better described as the lack of liquid-crystal reflection that is being measured.

Background subtraction can lead to a reduction in temperature uncertainty as illustrated in Fig. 6. The tungsten source, which

Downloaded 06 Dec 2010 to 193.140.21.150. Redistribution subject to ASME license or copyright; see http://www.asme.org/terms/Terms_Use.cfm

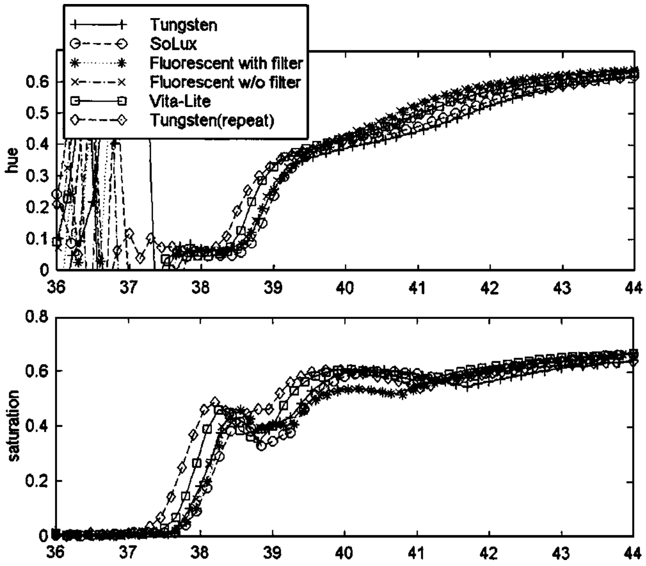

Fig. 7 Experimental HSV output versus temperature after white balancing

previously had a nonmonotonic behavior in the hue data, now has uncertainties and a useful range on the order of the other sources. There is not much change in the uncertainties for the flat spectrum (Vita-Lite or Solux) sources. The increased saturation in the two cool white sources results in a lower standard deviation in hue and as a result a lower temperature uncertainty and broader useful range.

White Balancing. White balancing is another way of normalizing the relative magnitude of R, G, and B background values. This can be done in the camera by focusing on the background and then adjusting the red and blue gains such that the red and blue output is equal to the green output. This differs from the background subtraction method in that it involves multiplication rather than subtraction and it is not based on the physical foundation that the background subtraction method is. White balancing would produce a different hue-temperature calibration curve than either the original calibration or the background subtracted calibration. In addition, the uncertainty in temperature over the useful range would be different. Behle et al. [18], in search of an optimum white balance, obtained hue-temperature relations with various levels of hue attenuation including severe attenuation, similar to that obtained previously for the tungsten source, due to one of the *RGB* components being significantly mismatched from the others.

White balancing of the experimental data was performed post processing, as opposed to changes in the camera settings which are sometimes used. The experimental R, G, and B data was white balanced independently for each light source by multiplying both the R and B data sets by constants so that the resulting average background values were equal to the average Green background value for the respective light source.

The resulting *RGB* data is similar to the original *RGB* data. The white balanced hue and saturation data, which was calculated from the white balanced *RGB* data, is shown in Fig. 7. The hue data for the white balancing case indicates a greater collapse between illumination sources than resulted from background subtraction. It is not known if there is a physical reason why this should be the case, but if independence of light source was a goal, then perhaps white balancing would produce the most universal curve. The most notable difference between the hue curves after white balancing compared to the hue curves after background subtraction is the effect on the curve resulting from the tungsten source, which are pulled more closely inline with the other sources. White balancing had a very similar effect on the hue-temperature sensitivity to that of background subtraction.

Summary and Conclusions

Five illumination sources were compared experimentally to examine their effects on the hue-temperature calibration and to determine if one source was significantly better. The sources consisted of a tungsten light source, two cool white fluorescent light sources (one with a UV filter and one without), and two “full” spectrum sources (a Vita-Lite fluorescent source and a Solux tungsten based source). It was found that the two full spectrum sources generally had the best calibration attributes (lowest uncertainties and broadest useful ranges). The Vita-Lite, however, was shown to cause significant UV damage (hue-temperature curve shift) to the liquid crystal, even within a matter of minutes. The Solux light is specially designed to minimize UV output (ergo its use in museums). The calibration attributes of the two cool white fluorescent bulbs were close to those of the full spectrum but with about a 20% reduction in useful temperature range (even after background subtraction). The fluorescent sources have a lower thermal emission than the Tungsten or Solux and caused no measurable UV damage to the TLC, even after subjecting the surface to 20 hr of exposure for the case of the cool white fluorescent with the UV shield. For the system configuration used, the tungsten source led to severe attenuation of the hue-temperature calibration, which resulted in a significant decrease in the useful temperature range. For these experiments, the CCD camera color temperature was set on 5600 K. If the 3200 K setting had been used, the tungsten source would have been better behaved which was demonstrated by both background subtraction and by white balancing. The Vita-Lite with a protective UV filter may offer the ideal combination of low-temperature uncertainty, broad bandwidth, minimal radiant heating and negligible UV damage and may be a good choice for future work.

The importance of background reflection was examined and it was found that background reflection tends to attenuate the hue-temperature calibration curve toward the background hue value. If the background R, G, and B values are highly mismatched (high background saturation), this attenuation can make the hue-temperature curves unusable.

It is common for a calibration to be performed on one surface and testing to be performed on another surface. In many instances an isothermal calibration block is used to provide a well-defined temperature for calibration, which the experimental apparatus can not easily provide. Even though the same illumination and imaging configuration is used, the variation in black paint and TLC coverage may lead to biases in hue-temperature calibrations between the two surfaces. In situ calibration has been professed by many researchers (e.g., [12]) and the effect of background reflection discussed here strongly supports this practice. Background subtraction was shown as a possible method of overcoming calibration variations due to variations in the background and TLC coating characteristics, both from one surface to another or within different areas of the same surface. Background subtraction was also found to result in a lower temperature uncertainty and a broader calibration range. White balancing was also investigated and was found to have an effect on the calibration data similar to that of the background subtraction method but was not based on sound physical reasoning as was the background subtraction method.

Nomenclature

H, hue = hue (color) level in HSV color space (Eq. (1))
R or red = red component from RGB color space
B or blue = blue component from RGB color space
G or green = green component from RGB color-space
S or saturation = saturation (redness/pinkness) level in HSV color space (Eq. (2))

Downloaded 06 Dec 2010 to 193.140.21.150. Redistribution subject to ASME license or copyright; see http://www.asme.org/terms/Terms_Use.cfm

V or value = brightness level in HSV color space
S_h = precision limit in hue
S_T = precision limit in temperature
U_T = uncertainty in temperature
q'' = heat flux

Subscripts

amb = ambient condition
T = temperature
s = surface

Acronyms

TLC = thermochromic liquid crystal
CCD = charge-coupled device
UV = ultraviolet
IR = infrared
SEE = standard error of estimate
CNLC = chiral nematic liquid crystal
CIE = International Commission on Illumination

References

[1] Moffat, R. J., 1990, "Experimental Heat Transfer," *Proc. 9th Int. Heat Transfer Conference*, Jerusalem, Israel, Vol. 1, 187–205.
[2] Jones, T. V., 1992, "The Use of Liquid Crystals in Aerodynamic and Heat Transfer Testing," *Transport Phenomena in Heat and Mass Transfer: Proc. of Fourth Int. Symp. on Transport Phenomena in Heat and Mass Transfer (ISTP-IV), Sydney, Australia, 14-19 July, 1991, Organized Under the Auspices of the Pacific Center of Thermal-Fluids Engineering/*, J. A. Reizes, ed., Amsterdam, Elsevier, NY, pp. 1242–1273.
[3] Cooper, T. E., Field, R. J., and Meyer, R. J., 1975, "Liquid-Crystal Thermometry and Its Application to the Study of Convective Heat Transfer," ASME J. Heat Transfer **97**, pp. 442–450.
[4] Hippensteele, S. A., Russell, L. M., and Torres, F. J., 1986, "Use of a Liquid-Crystal and Heater-Element Composite for Quantitative, High-Resolution Heat-Transfer Coefficients on a Turbine Airfoil Including Turbulence and Surface-Roughness Effects," *Winter Annual Meeting of ASME, Anaheim, Dec. 7-12, ASME, NY* pp. 105–120.
[5] Baughn J. W., 1995, "Liquid Crystal Methods for Studying Turbulent Heat Transfer," Int. J. Heat Fluid Flow **16**(5), pp. 365–375.
[6] Hollingsworth, D. K., Boehman, A. L., Smith, E. G., and Moffat, R. J., 1989, "Measurement of Temperature and Heat Transfer Coefficient Distributions in a Complex Flow Using Liquid Crystal Thermography and True-Color Image Processing," *ASME Collected Papers in Heat Transfer, HTD-Vol 123, Winter Annual Meeting of ASME, San Francisco, Dec. 10–15, ASME, NY*, pp. 35–42.
[7] Camci, C., Kim, K., and Hippensteele, S. A., 1992, "A New Hue Capturing Technique for the Quantitative Interpretation of Liquid Crystal Images Used in Convective Heat Transfer Studies," ASME J. Turbomach. **114**(4), pp. 765–775.
[8] Kim, Y. W, Reynolds, S. A., 1995, "Simultaneous Measurement of Surface Temperature and Heat Flux Using a Composite Slab," Exp. Heat Transfer **8**(4), pp. 281–292.
[9] Wang, Z., Ireland, P. T., and Jones, T. V., 1995, "An Advanced Method of Processing Liquid Crystal Video Signals From Transient Heat Transfer Experiments," ASME J. Turbomach. **117**(1), pp. 184–189.
[10] Farina, D. J., Hacker, J. M., Moffat, R. J., and Eaton, J. K., 1994, "Illuminant Invariant Calibration of Thermochromic Liquid Crystals," Exp. Therm. Fluid Sci. **9**(1), pp. 1–12.
[11] Hay, J. L, and Hollingsworth, D. K., 1996, "A Comparison of Trichromic Systems for Use in the Calibration of Polymer-Dispersed Thermochromic Liquid Crystals," Exp. Therm. Fluid Sci. **12**(1), pp. 1–12.
[12] Baughn, J. W., Anderson, M. R., Mayhew, J. E., and Wolf, J. D., 1999, "Hysteresis and Uncertainty of Thermochromic Liquid Crystal Temperature Measurement Based on Hue," ASME J. Heat Transfer **121**, pp. 1067–1072.
[13] Ireland, P. T., and Jones, T. V., 2000, "Liquid Crystal Measurements of Heat Transfer and Surface Shear Stress," Meas. Sci. Technol. **11**(7), pp. 969–986.
[14] Anderson, M. R., and Baughn, J. W., 2004, "Hysteresis in Liquid Crystal Thermography," ASME J. Heat Transfer **126**, pp. 339–346.
[15] Fergason, J. L., 1964, "Liquid Crystals," Sci. Am.
[16] Hallcrest Inc., 1991, *Handbook of Thermochromic Liquid Crystal Technology, Sales Literature*, Hallcrest Inc., Glenview, IL.
[17] Stasiek, J., 1997, "Thermochromic Liquid Crystals and True Colour Image Processing in Heat Transfer and Fluid-Flow Research," Heat and Mass Transfer **33**(1-2), pp. 27–39.
[18] Behle, M., Schulz, K., Leiner, W., and Fiebig, M., 1996, "Color-Based Image Processing to Measure Local Temperature Distributions by Wide-Band Liquid Crystal Thermography," Applied Scientific Research **56**(2-3), pp. 113–143.
[19] Syson, B. J., Pilbrow, R. G., and Owen, J. M., 1996, "Effect of Rotation of Thermochromic Liquid Crystal," Int. J. Heat Fluid Flow **17**, pp. 491–499.
[20] Akino, N., Kunugi, T., Ichimiya, K., Mitsushiro, K., and Ueda, M., 1989, "Improved Liquid-Crystal Thermometry Excluding Human Color Sensation," ASME J. Heat Transfer **111**(4), pp. 558–565.
[21] Nozaki, T., Mochizuki, T., Kaji, N., and Mori, Y. H., 1995, "Application of Liquid-Crystal Thermometry to Drop Temperature Measurements," Exp. Fluids **18**(3), pp. 137–144.
[22] Batchelder, K. A., and Moffat, R. J., 1998, "Surface Flow Visualization Using the Thermal Wakes of Small Heated Spots," Exp. Fluids **25**(2), pp. 104–107.
[23] Watwe, A. A., and Hollingsworth, D. K., 1994, "Liquid Crystal Images of Surface Temperature During Incipient Pool Boiling," Exp. Therm. Fluid Sci. **9**(1), pp. 22–33.
[24] Dabiri, D., and Gharib, M., 1991, "Digital Particle Image Thermometry: Method and Implementation," Exp. Fluids **11**(2-3), pp. 77–86.
[25] Metzger, D. E., Bunker, R. S., and Bosch, G., 1991, "Transient Liquid Crystal Measurement of Local Heat Transfer on a Rotating Disk With Jet Impingement," ASME J. Turbomach. **113**(1), pp. 52–59.
[26] Anderson, M. R. and Baughn, J. W., 2005, "Thermochromic Liquid Crystal Thermography: Illumination Spectral Effects Part 2: Theory," **127**.
[27] Anderson, M. R., 1999, "Thermochromic Liquid Crystal Thermography: Hysteresis, Illumination and Imaging System Effects, Image Processing and Applications," Ph.D. dissertation, University of CA, Davis.
[28] Fergason, J. L., 1968, "Liquid Crystals in Nondestructive Testing," Appl. Opt. **7**(9), pp. 1729–1737.
[29] Baughn, J. W., and Yan, X, 1991, "A Preheated-Wall Transient Method for Measurements of the Heat Transfer From a Surface to an Impinging Jet," *Heat Transfer in Single Phase Flows, Proc. of 1991 Eurotherm Seminar Nr. 25*, pp. 1–7.

Downloaded 06 Dec 2010 to 193.140.21.150. Redistribution subject to ASME license or copyright; see http://www.asme.org/terms/Terms_Use.cfm

Thermochromic Liquid Crystal Thermography: Illumination Spectral Effects. Part 2—Theory

M. R. Anderson
Senior Performance Engineer
Calpine Corporation,
104 Woodmere Road,
Folsom, CA 95630
e-mail: michael.anderson@calpine.com

J. W. Baughn
Professor
Fellow ASME
Department of Mechanical and Aeronautical Engineering, University of California, Davis, One Shields Avenue, Davis, CA 95616
e-mail: jwbaughn@ucdavis.edu

A theoretical model of a Thermochromic Liquid Crystal (TLC) imaging system was developed to aid in understanding the results of experiments on spectral effects and to investigate the various factors affecting the hue-temperature calibration of TLC's. The factors in the model include the spectral distribution of the illumination source and UV filter, surface reflection of both the TLC and background, and the sensing device (camera) spectral characteristics and gain settings. It was found that typical hue-temperature calibration curves could not be entirely explained by a TLC reflectivity model with either a monochromatic spike or a narrow bandwidth reflectivity, which is often assumed. Experimental results could be explained, however, by a model that reflects over a relatively large band of wavelengths. The spectral characteristics of the five illumination sources (those for which experiments were performed) were considered. Background reflection, which commonly accounts for 30%–50% of the reflected light, was found to significantly attenuate the hue-temperature calibration curves toward the background hue value. The effect of the illumination source on the hue-temperature calibration curves is demonstrated and several experimentally observed phenomena are explained by the results of the theoretical calculations, specifically the spectral reflective properties of the liquid crystals and the transmissivity of the R, G, and B filters in the image capture camera. [DOI: 10.1115/1.1915388]

Background

A background of the use of Thermochromic Liquid Crystals (TLC's) in liquid crystal thermography is given in Part 1: Experiments. In the present paper, Part 2: Theory, the objective is to increase the understanding of the spectral characteristics of TLC's and the effect of the spectral characteristics of the illumination source on the hue-temperature calibration of TLC's. This is accomplished by preparing a theoretical model of a liquid crystal thermography system and comparing the theoretical results to experimental results.

As noted in Part 1, several different representations for hue have been proposed [1]. Hay and Hollingsworth [2] suggested the following representation, which is used throughout the present work.

$$\text{Hue} = \arctan\left[\frac{\sqrt{3}(G-B)}{2R-G-B}\right] \tag{1}$$

It is generally understood that the perceived color (or hue) from a liquid crystal coated surface is a function of the spectral characteristics of the illumination source, the reflecting surface and the sensing device [1,3–5]. Wang et al. [4] state that knowledge of these spectral characteristics could be used to predict the intensity-temperature relation. This is also true for the hue-temperature calibration of a TLC. Predicting this relation with accuracy comparable to an actual calibration is unlikely due to the need for precise knowledge of the characteristics of each imaging component including the TLC (e.g., each new TLC coating may yield different reflectivity characteristics) and an accurate theoretical model of the various processes in the system. Nevertheless, a greater understanding of the effect each component has on the resulting calibration would be useful and can be obtained from the theoretical model described here.

Hay and Hollingsworth [2] provided extensive hue-temperature calibration data for three polymer-dispersed (nonencapsulated) CNLCs (Chiral Nematic Liquid Crystals). They found a similarity between the shape of the three calibration curves. They also state that several other researchers found similar shaped hue-temperature relations for other TLC mixtures when using the same definition of hue. They developed a general polynomial equation to collapse three different calibration curves to a single universal equation. With this general calibration equation they suggest that only 6 images (hue-temperature pairs) are necessary to apply the general equation to any CNLC, although they do say that other CNLCs should be tested to confirm this.

The theoretical model of a liquid crystal thermography system provided here is intended to provide a better understanding of the effect that each component in the system has on the hue-temperature calibration. Several factors including the choice of illumination source were found to have a significant effect on the shape of the hue-temperature calibration curve. As a rule, therefore, a general calibration equation, as suggested by Hay and Hollingsworth [2], should not be transported from one experimental configuration to another.

The assumed spectral distributions for the illumination sources used in this study include a theoretically flat spectrum and those five sources used in the experiments of Part 1 [1]. The five are a tungsten source, a modified Halogen source, and three different fluorescent sources.

Theory

Three components are required for the perception of color from a surface, an illumination source, an object to reflect the illumination, and a sensor to perceive the image [6]. Here, the sensor is a 3-chip RGB CCD camera connected to a PC computer. The object reflecting the illumination consists of a surface painted first with black paint and then with microencapsulated thermochromic liquid crystal coating. The choice of illumination source can greatly influence the characteristics of the liquid crystal calibration. In general, the flatter the spectral distribution of the light

---

Contributed by the Heat Transfer Division for publication in the JOURNAL OF HEAT TRANSFER. Manuscript received: June 27, 2004; final manuscript received: January 12, 2005. Review conducted by: Kenneth Kihm.

Copyright © 2005 by ASME

Downloaded 06 Dec 2010 to 193.140.21.150. Redistribution subject to ASME license or copyright; see http://www.asme.org/terms/Terms_Use.cfm

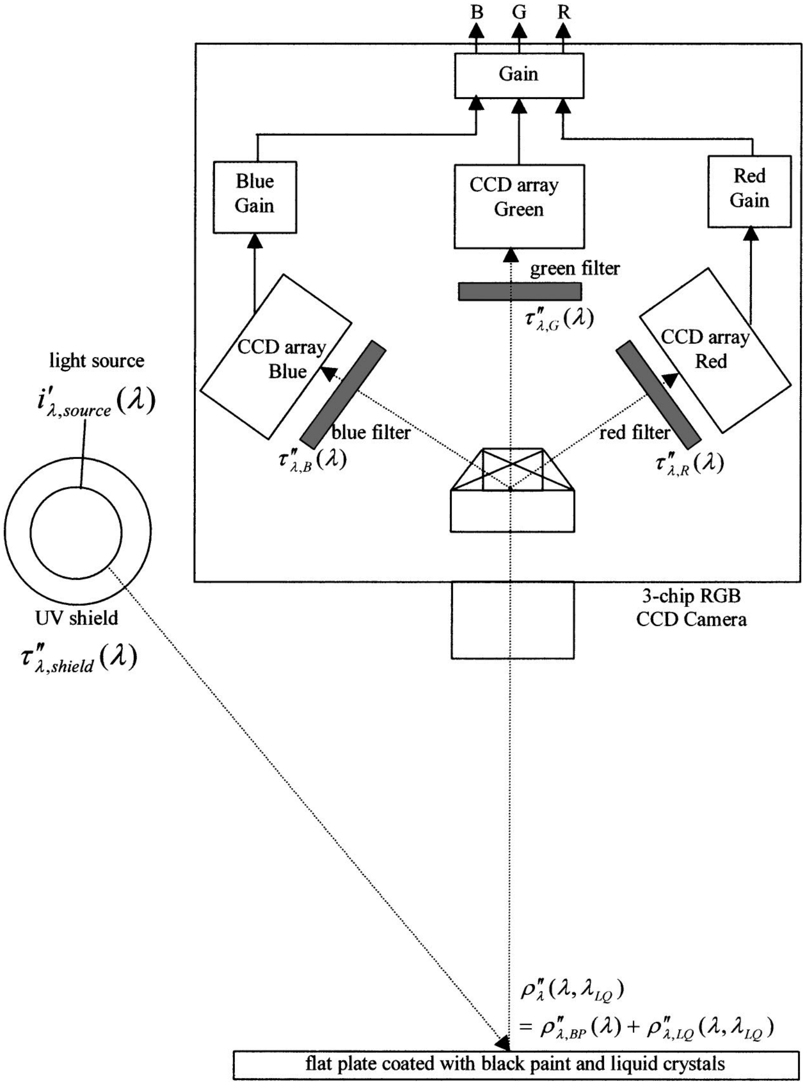

Fig. 1 **Diagram of liquid crystal thermography system with illumination model**

source used, the better the sensitivity of the liquid crystal over the visible range, as shown in the experiments and explained by this model. However, a flatter spectrum is sometimes accompanied by a higher than usual UV component which can lead to degradation of the liquid crystal and therefore a reduction in repeatability.

A theoretical model of the TLC thermography system used in the experimental study has been developed (Fig. 1). The system consists of a diffuse illumination source with its own spectral distribution that depends on the source of the illumination. The illumination source is surrounded by an optional UV shield. The incident light is reflected from a surface coated with black paint and microencapsulated thermochromic liquid crystals. The surface reflectivity can be a function of both wavelength and surface temperature. The reflected light enters a 3-chip CCD camera and is split into three beams. These beams pass through red, green, and blue filters, respectively, and are finally received by accompanying red, green, and blue CCD arrays. The red and blue signals pass through optional red and blue gains allowing complete control of the relative magnitudes of red, green, and blue (i.e., allowing the system to be white balanced). Finally all three signals pass through an overall gain and the resulting signal is sent to the frame capture card for digitization. Please note that this model also works for a single chip CCD camera where the red, green, and blue components are obtained from an array of R, G, and B filters on the single chip. In this case, the R, G, and B components

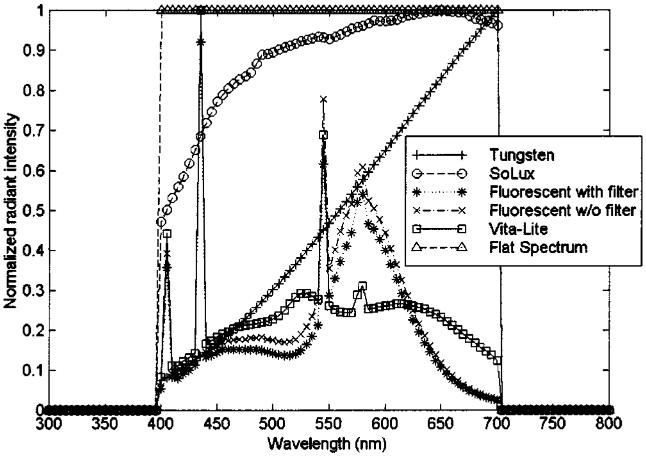

Fig. 2 **Normalized spectral distribution of several light sources**

Downloaded 06 Dec 2010 to 193.140.21.150. Redistribution subject to ASME license or copyright; see http://www.asme.org/terms/Terms_Use.cfm

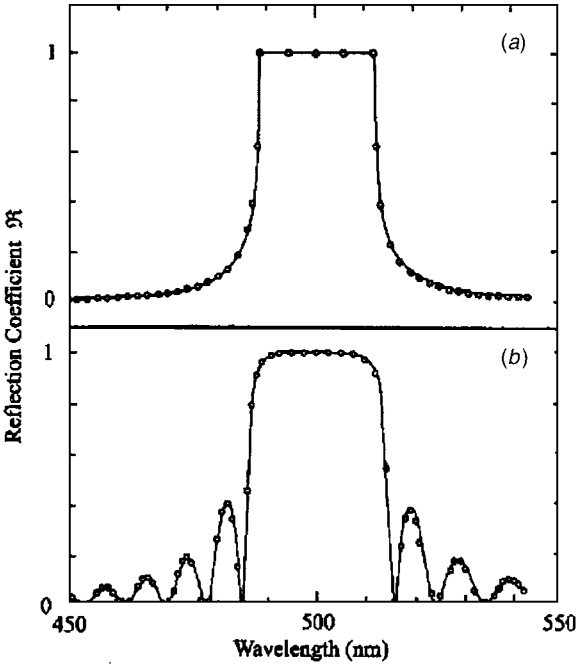

Fig. 3 Spectral reflection coefficient for light normally incident on a chiral nematic planar film (*a*) semi-infinite slab and (*b*) finite slab (from Coles [17])

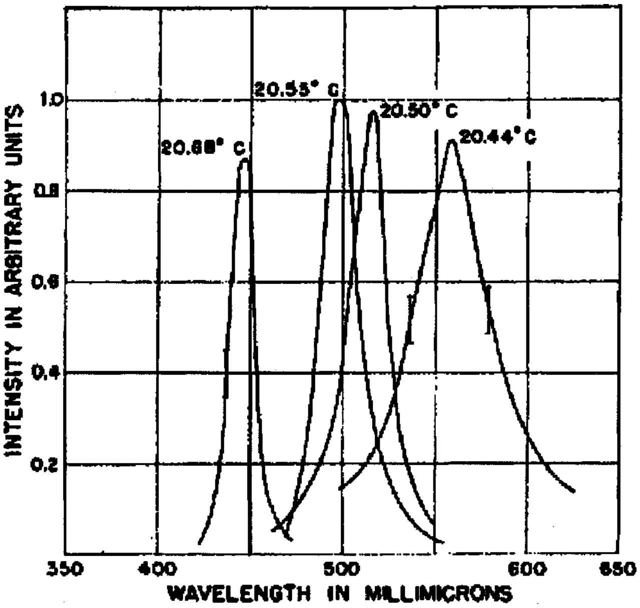

Fig. 4 Intensity of selectively reflected light as a function of wavelength. Material Cholesteryl oleyl carbonate (from Ennulat [18]).

are not co-located but if it is assumed that the neighboring R, G, and B components can be used for each pixel (the normal assumption made in liquid crystal thermography), then this system will give the same results.

In the current treatment, angular effects are not considered. It is assumed that the illumination and viewing angles remain constant.

The theoretical model starts with an assumed illumination source with a prescribed spectral distribution whose radiant intensity is given by $i'_{\lambda,\text{source}}$. After passing through a filter with a prescribed transmittance the radiant intensity incident upon the reflecting surface with thermochromic liquid crystals is given by

$$i'_{\lambda,i}(\lambda) = \tau''_{\lambda,\text{shield}}(\lambda)^{*} i'_{\lambda,\text{source}}(\lambda) \tag{2}$$

We are following the nomenclature of Siegel and Howell [7]. The subscript lambda denotes a specular quantity, the single prime denotes a unidirectional quantity and the double prime denotes a bidirectional quantity. The radiant intensity of the reflected energy is given by

$$i''_{\lambda,\text{ref}}(\lambda,\lambda_{\text{LQ}}) = \rho''_{\lambda}(\lambda,\lambda_{\text{LQ}})^{*} i'_{\lambda,i}(\lambda) \tag{3}$$

where the reflectivity is a function of both the background and the liquid crystal temperature. After passing through the red filter in the CCD camera, the radiant intensity incident on the red CCD chip is given by

$$i''_{\lambda,R}(\lambda,\lambda_{\text{LQ}}) = \tau''_{\lambda,R}(\lambda)^{*} i''_{\lambda,\text{ref}}(\lambda,\lambda_{\text{LQ}}) \tag{4}$$

The CCD chip itself cannot distinguish between wavelengths and instead each pixel integrates all energy hitting it, of which only the filtered red wavelengths have been permitted to pass. The signal output by one pixel in the red array is given by

$$R_1(\lambda_{\text{LQ}}) = \int_{\text{vis}} i''_{\lambda,R}(\lambda,\lambda_{\text{LQ}})\,d\lambda \tag{5}$$

A gain can be used to increase or decrease the red signal:

$$R_2(\lambda_{\text{LQ}}) = \text{RGain}^{*} R_1(\lambda_{\text{LQ}}) \tag{6}$$

and an overall gain can be used to increase the R, G, and B components proportionally:

$$R(\lambda_{\text{LQ}}) = \text{Gain}^{*} R_2(\lambda_{\text{LQ}}) \tag{7}$$

Combining Eqs. (2)–(7) yields:

$$R(\lambda_{\text{LQ}}) = \text{Gain}^{*}\text{RGain}^{*} \int_{\text{vis}} \tau''_{\lambda,R}(\lambda)\rho''_{\lambda}(\lambda,\lambda_{\text{LQ}})\tau''_{\lambda,\text{shield}}(\lambda) i'_{\lambda,\text{source}}(\lambda)\,d\lambda \tag{8}$$

The reflectivity of the surface can be broken into two contributions, one from the background, which is assumed to be independent of temperature, and the other from the microencapsulated liquid crystals, which is a function of temperature.

$$\rho''_{\lambda}(\lambda,\lambda_{\text{LQ}}) = \rho''_{\lambda,\text{BP}}(\lambda) + \rho''_{\lambda,\text{LQ}}(\lambda,\lambda_{\text{LQ}}) \tag{9}$$

This assumes that the total background reflection is the same regardless of reflection by the liquid crystals. As discussed later in the section on background radiation, this may not be the case. Using Eq. (9), Eq. (8) can be broken into contributions from the background and from the liquid crystals.

$$R(\lambda_{\text{LQ}}) = \text{Gain}^{*}\text{RGain}^{*}\left[\int_{\text{vis}} \tau''_{\lambda,R}(\lambda)\rho''_{\lambda,\text{BP}}(\lambda)\tau''_{\lambda,\text{shield}}(\lambda) i'_{\lambda,\text{source}}(\lambda)\,d\lambda + \int_{\text{vis}} \tau''_{\lambda,R}(\lambda)\rho''_{\lambda,\text{LQ}}(\lambda,\lambda_{\text{LQ}})\tau''_{\lambda,\text{shield}}(\lambda) i'_{\lambda,\text{source}}(\lambda)\,d\lambda\right] \tag{10}$$

The green and blue output can be formulated similarly, although the green signal does not have an independent gain setting of its own (only two independent gains are necessary to adjust the relative magnitudes of the three components).

$$G(\lambda_{\text{LQ}}) = \text{Gain}^{*}\left[\int_{\text{vis}} \tau''_{\lambda,G}(\lambda)\rho''_{\lambda,\text{BP}}(\lambda)\tau''_{\lambda,\text{shield}}(\lambda) i'_{\lambda,\text{source}}(\lambda)\,d\lambda + \int_{\text{vis}} \tau''_{\lambda,G}(\lambda)\rho''_{\lambda,\text{LQ}}(\lambda,\lambda_{\text{LQ}})\tau''_{\lambda,\text{shield}}(\lambda) i'_{\lambda,\text{source}}(\lambda)\,d\lambda\right] \tag{11}$$

Downloaded 06 Dec 2010 to 193.140.21.150. Redistribution subject to ASME license or copyright; see http://www.asme.org/terms/Terms_Use.cfm

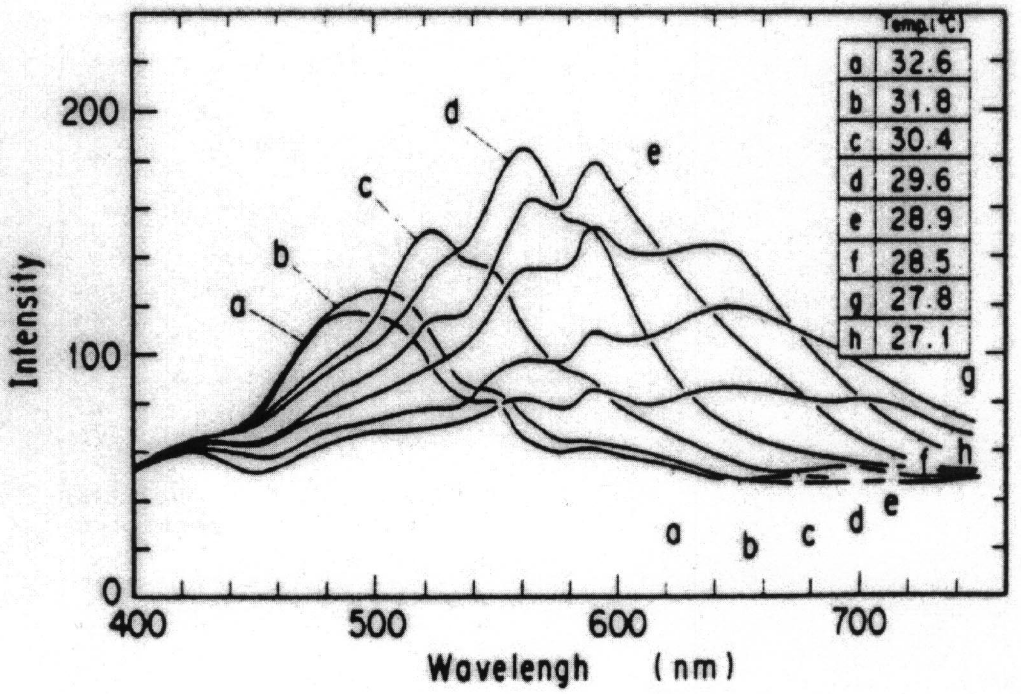

Fig. 5 Spectral characteristics of a (27–35°C) microencapsulated liquid crystal (from Akino et al. [11])

$$B(\lambda_{\mathrm{LQ}}) = \mathrm{Gain}^{*}\mathrm{BGain}^{*}\left[\int_{\mathrm{vis}} \tau''_{\lambda,B}(\lambda)\rho''_{\lambda,\mathrm{BP}}(\lambda)\tau''_{\lambda,\mathrm{shield}}(\lambda)i'_{\lambda,\mathrm{source}}(\lambda)d\lambda + \int_{\mathrm{vis}} \tau''_{\lambda,B}(\lambda)\rho''_{\lambda,\mathrm{LQ}}(\lambda,\lambda_{\mathrm{LQ}})\tau''_{\lambda,\mathrm{shield}}(\lambda)i'_{\lambda,\mathrm{source}}(\lambda)d\lambda\right] \quad (12)$$

The red, green, and blue components can be combined to calculate hue [from Eq. (1)] as follows:

$$\mathrm{Hue}(\lambda_{\mathrm{LQ}}) = \arctan\left[\frac{\sqrt{3}(G(\lambda_{\mathrm{LQ}}) - B(\lambda_{\mathrm{LQ}}))}{2R(\lambda_{\mathrm{LQ}}) - G(\lambda_{\mathrm{LQ}}) - B(\lambda_{\mathrm{LQ}})}\right] \quad (13)$$

Therefore the hue-temperature calibration is a function of the:

(1) Spectral characteristics of the light source
(2) Transmissivity of the UV filter (if used)
(3) Reflectivity of both the background and the liquid crystals
(4) Transmissivity of the R, G, and B filters
(5) Gain settings
(6) Relationship between temperature and wavelength.

Theoretical Model

Physical models for each of these six components will be described and then combined into the overall theoretical model.

Spectral Characteristics of the Light Source. Six light sources are considered, representing those commonly used in TLC work and those with the flattest possible spectrum. The light sources include a theoretically flat spectrum, a tungsten filament bulb (3200 K), a SoLux tungsten–halogen based bulb (4700 K), a cool white fluorescent bulb (4100 K), a cool white fluorescent bulb with a UV filter, and a Vita-Lite full spectrum fluorescent bulb (5500 K). The color temperature (or correlated color temperature) listed for each of these sources refers to the temperature of a black body whose X and Y coordinates on the CIE (International Commission on Illumination) chromaticity diagram most nearly match those of the light source. The normalized spectral distributions of these lights are shown in Fig. 2.

The tungsten source represents the standard illuminant A, defined by the CIE and has an emissive power distribution very close to that of a blackbody radiating at 2930 K with a relatively high red output and a relatively low blue output. The SoLux lamp is a tungsten–halogen based lamp which uses a unique filament/surface reflectivity arrangement to reduce the red output from that of a tungsten bulb and produce a flatter spectral distribution over the visible region. The SoLux is specially designed to have minimal UV output and is quoted as having 58% lower thermal emission than a standard tungsten–halogen light source (ergo its use in museums). The cool white fluorescent bulb has a high yellow/green output and, as with all the fluorescent bulbs, exhibits spikes associated with the spectral lines of the mercury vapor used to cause the phosphors to fluoresce. The UV filter surrounding the cool white fluorescent bulb basically eliminates all radiation below 380 nm and also reduces the yellow/green output resulting in a flatter spectrum from that of the original cool white bulb. The Vita-Lite bulb uses additional rare earth phosphors resulting in a flatter spectral distribution from that of the other fluorescent bulbs. Unfortunately, this flatter spectrum leads to an increased UV output over standard fluorescent bulbs and it has been suggested that the rare earth red phosphors may degrade faster than the other phosphors causing the spectral output to change over time.

Transmissivity of UV Filter. One of the disadvantages of fluorescent bulbs is the high UV output. UV radiation is known to cause damage to liquid crystals [8]. A Spectrum 574 filter, from Spectracom Technologies Corporation, was used in both the experimental and theoretical work presented here. This filter eliminates UV and slightly reduces the amount of radiation in the green/yellow region. When used with a cool white fluorescent

Downloaded 06 Dec 2010 to 193.140.21.150. Redistribution subject to ASME license or copyright; see http://www.asme.org/terms/Terms_Use.cfm

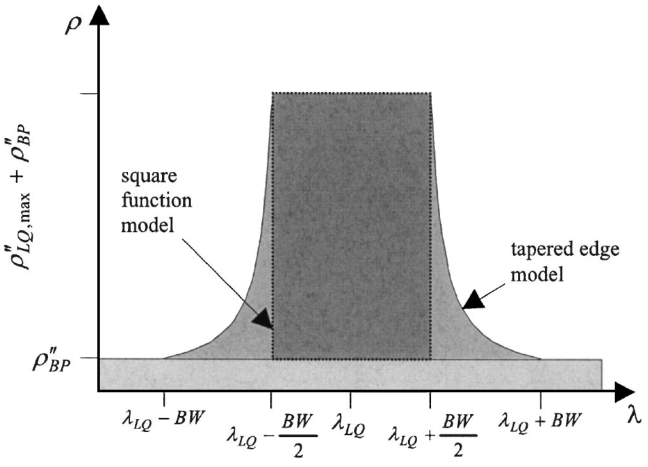

Fig. 6 Square function and tapered edge surface reflectivity models

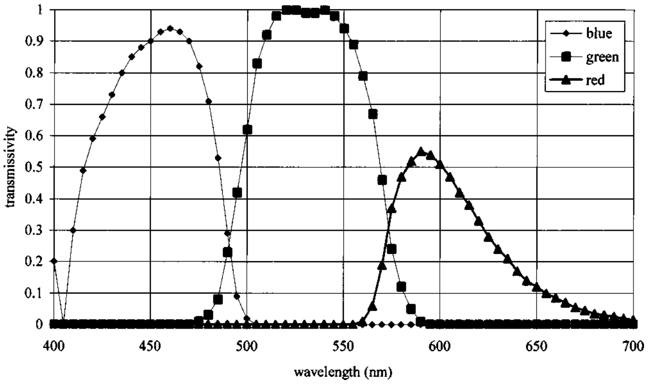

Fig. 7 Estimates of the R, G, and B filter spectral transmissivities for the camera used in the present work

bulb, which characteristically has a higher output in the green/yellow region than other regions of the visible spectrum, a flatter spectrum results.

Reflectivity of the Object Surface. There are two separate sources of reflection from the object surface: the background reflection and the liquid crystal reflection. If it were possible to isolate the liquid crystal, such that the only light reflected came from it, then this illumination study would be greatly simplified and much less informative. Unfortunately it is not possible to isolate the liquid crystal in this way. Reflections from the background paint, liquid crystal binder material, and microencapsulation material will also reflect a portion of the incident light causing a shift in the hue calibration (or attenuation) towards this background hue.

Cooper et al. [9] states, "The black substrate insures that all light transmitted through the liquid crystal film is absorbed and, therefore, is not reflected to compete with the desired signal." This is an oversimplification, and a common misconception is that the background reflection has little effect on the color-temperature relation. Zhu and Hieftje [10] achieved a peak reflected intensity 40 times larger than the background value, however the liquid crystal used in their work was nonencapsulated and was illuminated by a He–Ne laser which limited the background reflection to a narrow band of wavelengths. With microencapsulated TLC's illuminated by broad spectrum sources it is more common to obtain a peak intensity to background intensity ratio of 2 or 3 to 1 (e.g., Wang et al. [4], Akino et al. [11] Fig 5, Camci et al. [3]), although, Farina et al. [1], using an arrangement of polarizing filters, obtained ratios on the order of 15 to 1. Syson et al. [12], acknowledge that the reflection from a TLC coated surface includes contributions from the black paint undercoat and from the nonliquid-crystal constituents of the coating; however, they state that the reflection can be approximated by a monochromatic spike plus a background component.

There is a wide variation in reflectivities listed for various black paints in the literature. Siegel and Howell [13], Holman [14], and Incropera and DeWitt [15] list normal total solar absorptivities for black coatings ranging from 0.88 to 0.97. Since $\rho = 1 - \alpha$ for opaque diffuse surfaces, solar reflectivities, and therefore reflectivities in the visible region, for black paints should fall in the range 0.03–0.12. It is not known what the reflectivities of the binder or vinyl encapsulating materials are and the effect of these, along with the black paint are combined into the term $\rho''_{\lambda,\mathrm{BP}}(\lambda)$.

Thermochromic liquid crystals reflect a band of wavelengths due to a complex interaction of several individual effects including birefringence, optical activity, circular dichroism and Bragg scattering [16]. Hallcrest [16] describes the spectral reflectivity for a hypothetical TLC as a square function over a finite band of wavelengths. Syson et al. [12] provide a depiction of the reflected spectrum and suggest that it is well described by a monochromatic spike. The spectral reflectivity can actually be significantly more complicated than this. When the liquid crystal material is near a surface, the orientation of the molecules can be affected. Figure 3(*a*) shows the spectral reflection coefficient for a chiral nematic liquid crystal for a semi-infinite slab and for a finite slab [17]. The side undulations shown in Fig. 3(*b*) are rarely observed in practice due to inhomogeneities and the spectral reflection usually takes on more of a bell shaped curve (see Fig. 4 taken from [18]). This figure also shows that in general, the shape of the spectral reflectivity curve is not constant, and in fact it varies as a function of temperature for a particular liquid.

This behavior applies to a liquid crystal made up of a single compound. To obtain a liquid crystal substance with a particular color play start temperature and bandwidth it is usually necessary to mix compounds. For example the Hallcrest microencapsulated R24C5W/C-17 liquid crystal used in much of the work presented here is made up of five different compounds [19]. These mixtures can result in significantly more complicated spectral reflectivities as shown by Akino et al. [11]. They evaluated the spectral characteristics of a broad-band microencapsulated liquid crystal (temperature range 27–35°C) at 8 different temperatures by measuring the intensity of reflected light passing through 18 different narrow bandpass filters spanning the visible spectrum. Their results, in Fig. 5 show the highly nonuniform nature of the TLC reflectivity in peak intensity, in reflectivity bandwidth and in symmetry.

Two different reflectivity models have been considered in the current study. In each model the background reflectivity is assumed to be constant over wavelength with a value ρ''_{BP}. The difference between the two models lies in how the liquid crystal reflectivity is modeled (Fig. 6).

The first TLC reflectivity model consists of a square function model in which the liquid crystal reflectivity is represented by a square function with a constant reflectivity of $\rho''_{\mathrm{LQ,max}}$ over the reflected bandwidth (BW) and a reflectivity of 0 otherwise.

$$\rho''_{\lambda,\mathrm{LQ}}(\lambda,\lambda_{\mathrm{LQ}}) = \begin{cases} \rho''_{\mathrm{LQ,max}} & \lambda_{\mathrm{LQ}} - \dfrac{\mathrm{BW}}{2} < \lambda < \lambda_{\mathrm{LQ}} + \dfrac{\mathrm{BW}}{2} \\ 0 & \text{otherwise} \end{cases} \tag{14}$$

The second model, includes tapered edges which follow a logarithmic decay from $\rho''_{\mathrm{LQ,max}}$ to 0 over a distance of BW/2. For a prescribed bandwidth the liquid crystal reflectivity is given by

Downloaded 06 Dec 2010 to 193.140.21.150. Redistribution subject to ASME license or copyright; see http://www.asme.org/terms/Terms_Use.cfm

$$\rho''_{\lambda,\mathrm{LQ}}(\lambda,\lambda_{\mathrm{LQ}}) = \rho''_{\mathrm{LQ,max}} {}^* \frac{1}{9} \begin{cases} 10^{2^*[\lambda-(\lambda_{\mathrm{LQ}}-\mathrm{BW})]/\mathrm{BW}} - 1 & \lambda_{\mathrm{LQ}} - \mathrm{BW} < \lambda < \lambda_{\mathrm{LQ}} - \dfrac{\mathrm{BW}}{2} \\ 9 & \lambda_{\mathrm{LQ}} - \dfrac{\mathrm{BW}}{2} < \lambda < \lambda_{\mathrm{LQ}} + \dfrac{\mathrm{BW}}{2} \\ 10^{2^*[(\lambda_{\mathrm{LQ}}+\mathrm{BW})-\lambda]/\mathrm{BW}} - 1 & \lambda_{\mathrm{LQ}} + \dfrac{\mathrm{BW}}{2} < \lambda < \lambda_{\mathrm{LQ}} + \mathrm{BW} \\ 0 & \text{otherwise} \end{cases} \tag{15}$$

In each of these models, the bandwidth is held constant over the active range of wavelengths (or temperatures).

Telephone conversations with Hallcrest representatives have suggested that 20% of the incident light with a wavelength within the bandwidth is reflected. This is not useful here, however, because the amount of radiation reflected by the TLC to a particular pixel will depend not only on the reflectivity of the TLC but also the amount of TLC present in the area sensed by the pixel, which can vary significantly between surfaces [8]. Referring back to Eq. (3), the reflected radiant intensity was given by the product of the incident radiant intensity and the reflectivity of the surface. Since we are interested in the relative amounts of R, G, and B that a pixel in the CCD will sense, not only is the reflectivity of the TLC of concern, but so is the ratio of area covered by TLC material to the total area. The black paint, or background, is assumed to cover the remaining area. Microscopic examination of a typical TLC coated surface indicated that TLC coverage on the order of 50% of the surface area, or less, is not uncommon. The radiant intensity of the reflected energy from the TLC is therefore modified to include a coverage factor (CF) that may be on the order of 50%. Accounting for these approximations, Eq. (10) takes the form

$$\begin{aligned} R(\lambda_{\mathrm{LQ}}) = \mathrm{Gain}^*\mathrm{RGain}^* \Bigg[&\int_{\mathrm{vis}} \tau''_{\lambda,R}(\lambda)\rho''_{\lambda,\mathrm{BP}}\tau''_{\lambda,\mathrm{shield}}(\lambda) i'_{\lambda,\mathrm{source}}(\lambda)d\lambda \\ &+ \int_{\mathrm{vis}} \tau''_{\lambda,R}(\lambda) CF \rho''_{\lambda,\mathrm{LQ}}(\lambda,\lambda_{\mathrm{LQ}})\tau''_{\lambda,\mathrm{shield}}(\lambda) i'_{\lambda,\mathrm{source}}(\lambda)d\lambda \Bigg] \end{aligned} \tag{16}$$

where the reflectivities of the background and liquid crystal can be combined into the ratio

$$\rho''_{\mathrm{ratio}} = \frac{\rho''_{\mathrm{BP}}}{\mathrm{CF}\rho''_{\mathrm{LQ,max}}} \tag{17}$$

resulting in

$$\begin{aligned} R(\lambda_{\mathrm{LQ}}) = {} & \mathrm{Gain}^*\mathrm{RGain}^*\mathrm{CF}^*{\rho''_{LQ,\mathrm{max}}}^* \\ & \times \Bigg[\int_{\mathrm{vis}} \tau''_{\lambda,R}(\lambda)\rho''_{\mathrm{ratio}}\tau''_{\lambda,\mathrm{shield}}(\lambda) i'_{\lambda,\mathrm{source}}(\lambda)d\lambda \\ & + \int_{\mathrm{vis}} \tau''_{\lambda,R}(\lambda) \frac{\rho''_{\lambda,LQ}(\lambda,\lambda_{\mathrm{LQ}})}{\rho''_{\mathrm{LQ,max}}} \tau''_{\lambda,\mathrm{shield}}(\lambda) i'_{\lambda,\mathrm{source}}(\lambda)d\lambda \Bigg] \end{aligned} \tag{18}$$

The green and blue components are modified similarly. The term $\rho''_{\lambda,\mathrm{LQ}}(\lambda,\lambda_{\mathrm{LQ}})/\rho''_{\mathrm{LQ,max}}$ takes on a value of 0 or 1 for the square function and can take on values within this range for the tapered edge model.

Transmissivity of R, G, and B Filters. The spectral transmissivity curves for the R, G, and B filters used in common CCD cameras are shown in Fig. 7. It is notable that the red and blue transmissivities are both zero from about 500 nm to 560 nm. This means that for an "ideal" TLC reflection (i.e., an infinitesimal bandwidth) there should be no change in hue within this range; the hue should be that of pure green or 0.33 if the background is white (or gray). The fact that this behavior does not occur in practice will be a subject of discussion in the Results.

Gain Settings. R & B gain settings can each be adjusted from −128 to 127 independently. The gain value applies an equivalent percentage increase/decrease to the nominal, R and B gain setting of zero. This can be used, for example, to white balance the camera. By adjusting only the R & B, the relative magnitude of all three outputs R, G, and B can be controlled.

The overall gain setting increases all three components proportionally and was included for completeness. It has no effect on hue since either addition of a constant to or multiplication of a constant by each of the R, G, and B components has no net effect on hue [see Eq. (1)].

Wavelength-Temperature Relation. Experimental calibrations are specified in terms of temperature, requiring the model to be in terms of temperature for direct comparison. Hallcrest [16] suggests that for a typical TLC, the peak reflected wavelength and the temperature are inversely related. The relation

$$T = \frac{a}{\lambda + b} + c \tag{19}$$

has been used, where b is found iteratively by solving the expression

$$0 = T_3 - T_2 + \frac{T_1 - T_2}{\dfrac{1}{\lambda_1 + b} - \dfrac{1}{\lambda_2 + b}} \left(\frac{1}{\lambda_2 + b} - \frac{1}{\lambda_3 + b} \right) \tag{20}$$

and a and c are calculated in turn

$$a = \frac{T_1 - T_2}{\dfrac{1}{\lambda_1 + b} - \dfrac{1}{\lambda_2 + b}} \qquad c = T_1 - \frac{a}{\lambda_1 - b} \tag{21}$$

in which (T_1,λ_1), (T_2,λ_2), and (T_3,λ_3) represent three ordered pairs associated with the R, G, and B peaks.

Numerical Method. Calculations were performed in MATLAB. Spectral data for each of the light sources and filters were specified at 5 nm increments from 300 nm to 800 nm. This provides 100 nm on each side of the CCD filter limits to accommodate bandwidths of up to 200 nm for the square function reflectivity model and 100 nm for the tapered edge model. Each of the sources, including the cool white fluorescent/filter combination, was normalized to a maximum value of 1.0. For each source, the trapezoid method was used to integrate the background contribution for each of the R, G, and B components resulting in a single value for each,

Downloaded 06 Dec 2010 to 193.140.21.150. Redistribution subject to ASME license or copyright; see http://www.asme.org/terms/Terms_Use.cfm

$$R_{\text{background}} = \rho''_{\text{ratio}} \int_{300}^{800} \tau''_{\lambda,R}(\lambda)^{*} i'_{\lambda,i}(\lambda)\, d\lambda. \tag{22}$$

For each source, an array of liquid crystal contributions was calculated, also using the trapezoid rule, for each of the R, G, and B components as a function of wavelength

$$R_{\text{LQ}}(\lambda_{\text{LQ}}) = \int_{300+\text{BW}}^{800-\text{BW}} \tau''_{\lambda,R}(\lambda)^{*} \frac{\rho''_{\lambda,\text{LQ}}(\lambda,\lambda_{\text{LQ}})}{\rho''_{\text{LQ,max}}} {}^{*} i'_{\lambda,i}(\lambda)\, d\lambda \tag{23}$$

The respective background value, which is a constant for each light source, was added to each of these arrays producing R, G, and B components.

$$R(\lambda_{\text{LQ}}) = R_{\text{LQ}}(\lambda_{\text{LQ}}) + R_{\text{background}} \tag{24}$$

Correction factors were applied to the red and blue components to more closely relate theoretical background values to the experimental values. It is believed that the majority of this is due to camera electronics, although some of this offset may also be due to factors including nonconstant background reflectivity over wavelengths, coarseness of the illumination source data or other model approximations. The CCD camera used in the experimental portion of this study has color temperature settings of 3200 K and 5600 K. These two settings simply apply two different sets of red and blue gains to the signal. The 3200 K setting assumes that a tungsten bulb is being used, which is high in red, and therefore reduces the red component and increases the blue component to produce more uniform R, G, and B values when viewing a white or gray surface. The 5600 K setting assumes that sunlight is being used and adjusts the red and blue signals to obtain more uniform R, G, and B values when a white or gray surface is illuminated with sunlight. The 5600 K setting was used in these experiments, however, it is unknown what other modifications are made on the R, G, and B signals within the camera after leaving the CCD array. To account for the variation between the model and the experimental data the multipliers R_{mult} and B_{mult} are used on the red and blue components, respectively.

$$R_{\text{mult}} = \text{mean}\left(\frac{\overline{R}_{\text{BP,experimental}}}{\overline{G}_{\text{BP,experimental}}} \frac{G_{\text{BP,model}}}{R_{\text{BP,model}}} \right)_{\text{source}}$$

$$B_{\text{mult}} = \text{mean}\left(\frac{\overline{B}_{\text{BP,experimental}}}{\overline{G}_{\text{BP,experimental}}} \frac{G_{\text{BP,model}}}{B_{\text{BP,model}}} \right)_{\text{source}} \tag{25}$$

The term $\overline{R}_{\text{BP,experimental}}$ is an average of the 5 lowest-temperature red component data points for each source, all of which are well below the onset of color play. The experimental green and blue background components are determined similarly. Since each of the experimental tests were performed without changing any of the camera settings, there is assumed to be a single pair of red and blue multipliers that are applied to every light source configuration. These two multipliers are averages of the multipliers determined from each of the 5 light sources for red and blue, respectively. These multipliers are then applied to the red and blue arrays.

$$R(\lambda_{\text{LQ}}) = R^{*}_{\text{mult}} R(\lambda_{\text{LQ}})$$

$$B(\lambda_{\text{LQ}}) = B^{*}_{\text{mult}} B(\lambda_{\text{LQ}}) \tag{26}$$

A Macbeth color checker was considered as a means of performing this correction. The corrections determined from the Macbeth color checker (2.36 and 1.17 for red and blue, respectively) were very close to those from the experimental background (2.45 and 1.30 for red and blue, respectively). The slight variation was most likely due to differences in the spectral reflectivity between the background and the Macbeth color checker. Use of the experimental background was chosen over the Macbeth to incorporate the nongray background into the correction, resulting in better agreement between experimental data and the model.

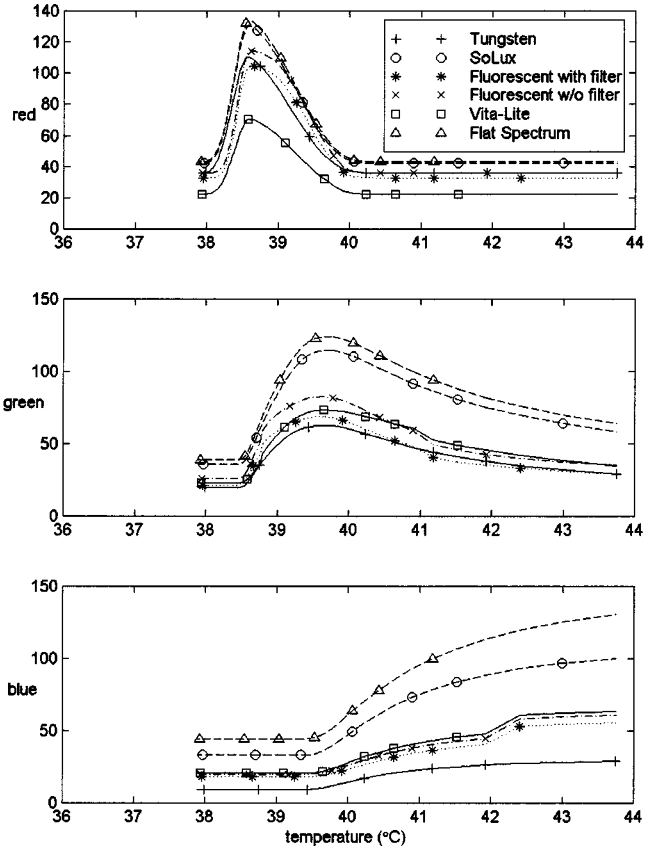

Fig. 8 Theoretical RGB output vs temperature (untapered model)

An overall multiplier RGB_{mult} was then determined for each source to normalize the background green for each model to its respective experimental background green. This simply represents using a source with the same average radiant intensity in the model as in the experiment, allowing for a more meaningful comparison. Since the radiant intensity of each light source is different, it is reasonable to use a different multiplier for each of the sources. This multiplier was applied to each of the R, G, and B components for a particular source and does not effect the hue distribution.

$$\text{RGB}_{\text{mult}} = \frac{\overline{G}_{\text{BP,experimental}}}{G_{\text{BP,model}}} \tag{27}$$

Once again, the experimental value is an average of the 5 lowest-temperature green component data points for each source, all of which are well below the onset of color play. These overall multipliers were then applied to each of the red green and blue arrays for each source.

$$R(\lambda_{\text{LQ}}) = \text{RGB}^{*}_{\text{mult}} R(\lambda_{\text{LQ}})$$

$$G(\lambda_{\text{LQ}}) = \text{RGB}^{*}_{\text{mult}} G(\lambda_{\text{LQ}})$$

$$B(\lambda_{\text{LQ}}) = \text{RGB}^{*}_{\text{mult}} B(\lambda_{\text{LQ}}) \tag{28}$$

Hue was then calculated by using MATLAB's RGB2HSV function [which gives results nearly identical to those of Eq. (1)].

Untapered TLC Reflectivity Model Results

Theoretical red, green, and blue data vs temperature results for the untapered (see square edged in Fig. 6) TLC reflectivity model are shown in Fig. 8. The hue is shown in Fig. 9. These theoretical

Downloaded 06 Dec 2010 to 193.140.21.150. Redistribution subject to ASME license or copyright; see http://www.asme.org/terms/Terms_Use.cfm

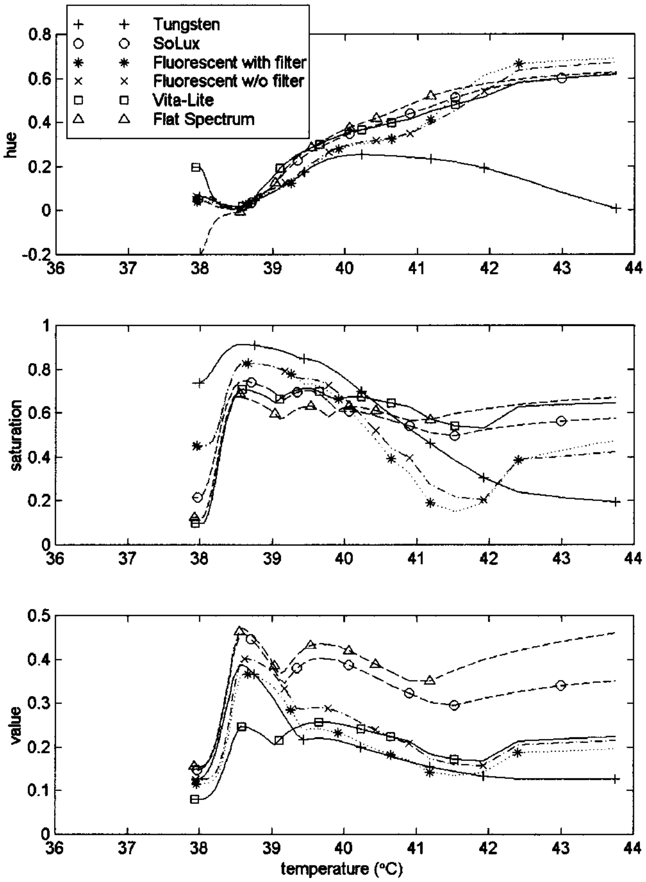

Fig. 9 Theoretical HSV output vs temperature (untapered model)

results show remarkably similar behavior to the experimental data in Part 1. The five separate items in the model discussed earlier were varied to achieve these results. To correct for camera electronics, multipliers of 2.45 and 1.30 were applied to the red and blue components respectively so that the relative magnitude of the red, green and blue background components would more closely match the experimental data. Overall multipliers of 1.4901, 1.2124, 2.6662, 2.6018, 2.4422, and 1.2124 were applied to the RGB data for the six light sources, respectively, to approximate illumination intensity levels comparable to the experimental sources. The overall multiplier for the theoretically flat spectrum, for which there is no experimental data, was set equal to the smallest of the other five to achieve a comparable magnitude. The temperature-wavelength relation was adjusted so that the peaks in the model R, G, and B components lined up with those from the experimental results [Eqs. (19)–(21)]. The wavelengths at which the peaks occur in the model depend slightly on the bandwidth and those associated with the optimum bandwidth (discussed later) were used. Finally the reflectivity ratio, ρ''_{ratio}, and liquid crystal bandwidth, BW, were varied to achieve a comparable shape and to force the peak magnitudes close to those of the experimental data. The optimum combination of reflectivity ratio and bandwidth was chosen such that

(1) The peak values for R, G, and B were close to those from the experimental results.
(2) The shapes of the red, green, blue, hue, saturation and value curves were similar to those from the experimental results.

In general, increasing the bandwidth causes the curves to widen, localized phenomena such as fluorescent spikes to diminish and the peak magnitudes to increase. Increasing the reflectivity ratio causes the R, G, B and value curves to reduce in magnitude when holding the background value constant. When the bandwidth is small, on the order of 20 nm, the spikes from the fluorescent sources are quite noticeable. Since the spikes have never been observed during experimentation, the bandwidth was chosen above this value. When the bandwidth increases above 100 nm (the width of the R, G, and B filters) the R, G, and B peaks begin to plateau. When the reflectivity ratio is low, below 0.2, the magnitude of the RGB peaks become very high and the relatively small contribution of background reflection caused the hue curves to collapse close to one another. When the reflectivity ratio is high, above 0.6, the relatively large contribution of background reflection causes the hue curves for all the sources to behave similar to that of the tungsten source becoming severely attenuated to the background hue values. Behle et al. [5] investigated the effect of TLC coating thickness on the hue-temperature characteristics. They used three different thicknesses and their results showed an increase in attenuation to the background hue as the coating became thinner (i.e., as the reflectivity ratio became higher). An optimum combination of reflectivity ratio and bandwidth for the current study has been chosen through iteration to be 0.45 and 90 nm, respectively.

One of the areas of poor agreement between the model and experimental results is the temperature at which color play begins for each of the components. The experimental RGB results in Part 1 indicate that color play begins in a gradual fashion starting at about 37.5°C for each of the three components. However the results from the theoretical model in Fig. 8 shows a more abrupt onset of color play for each of the three components and also shows this onset to begin at increasing temperatures for the Red, Green, and Blue components, respectively.

The theoretical HSV data in Fig. 9 exhibits all the same characteristics described in the experimental data. In addition this includes data for the theoretically flat spectrum which offers the highest distribution of value, the most uniform saturation and the hue curve with the least infection over the useful range—all desired properties.

Tapered TLC Reflectivity Model Results

Two ways of making the green and blue components of the model begin their color play at lower temperatures are to modify the temperature-wavelength relations, or to modify the liquid crystal reflectivity model. Modifying the temperature-wavelength relations, so that color play for all three components are at about the same temperature, has the negative effect of changing the temperature at which the peaks occur which is unreasonable. There are several different ways in which the liquid crystal reflectivity model can be modified:

(1) the square function bandwidth can be increased or decreased;
(2) the square function bandwidth can be increased or decreased unsymmetrically;
(3) the square function bandwidth can be increased or decrease either symmetrically or unsymmetrically as a function of wavelength;
(4) the bandwidth and amount of taper can be increased or decrease either symmetrically or unsymmetrically as a function of wavelength.

Cases (1)–(3) will cause some or all the RGB components to plateau and is unreasonable. Case (4) seems to have the potential for offering an explanation but results in a more complicated model.

A new set of calculations for a single tapered model, in which tapered edges were added to the optimum reflectivity ratio/bandwidth model chosen above (0.45/90 nm) were performed. The R, G, and B curves for this case are shown in Fig. 10. Adding taper to the reflectivity model had the expected effects of lowering

Downloaded 06 Dec 2010 to 193.140.21.150. Redistribution subject to ASME license or copyright; see http://www.asme.org/terms/Terms_Use.cfm

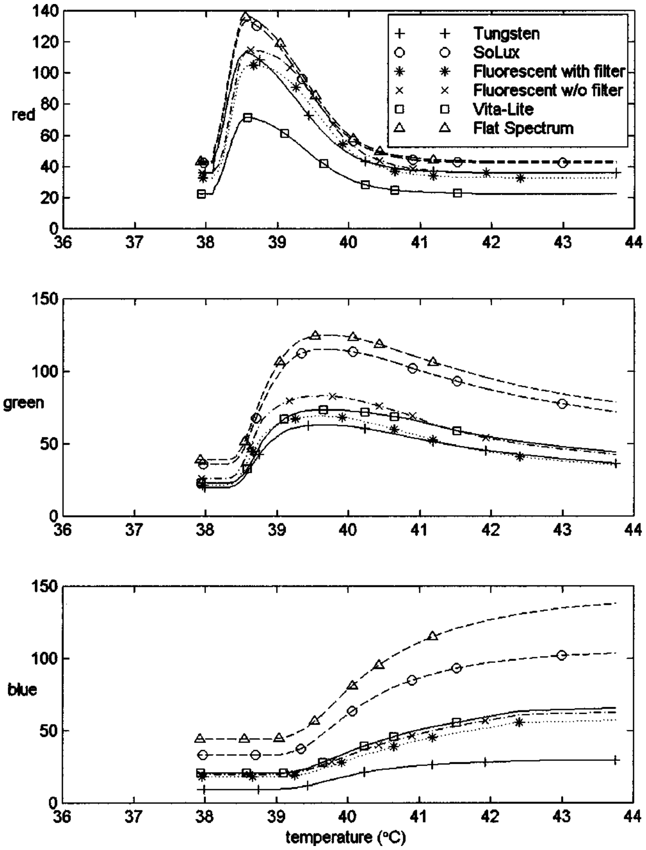

Fig. 10 Theoretical RGB output vs temperature (tapered model)

the temperature at which color play began (by 0.0, 0.2, and 0.4°C for the R, G, and B components, respectively) and causing a more gradual onset of color play. Further refinement of the liquid crystal reflectivity model would likely lead to an improved overall model, however, the number of possible reflectivity models is exhaustive and pursuit of a better model would lead away from the simplicity of the current model. Akino et al. [11] showed that the spectral reflectivity of a TLC coated surface does in fact have a highly varying taper and bandwidth as a function of temperature (Fig. 5).

The HSV data for the tapered liquid crystal reflectivity model shows similar behavior to the untapered model.

Summary and Conclusions

A theoretical model of a thermochromic liquid crystal imaging system has been developed. The model accounts for the spectral characteristics of the illumination source, the TLC coated surface, and the CCD imaging camera. The purpose of this theoretical model was to offer a more in-depth understanding of the factors involved in liquid crystal thermography, to describe the effects that various illumination sources have on a TLC hue-calibration, and to understand better the merits of the spectral distributions of various illumination sources. Regardless of the start temperature shortcoming, the model has served its purpose, describing the relative shapes of the hue saturation and value curves through the useful range and showing inflections, which correspond well to the experimental data.

Two reflectivity models for the liquid crystal were used: a square model and a tapered model. The main discrepancy between the TLC reflectivity models used and the experimental results is the temperature at which the R, G, and B components begin to increase from their background values. Experimentally, the three begin to increase at approximately the same temperature, although the rate of increase is greatest for the red and smallest for the blue. For the model to exhibit this same characteristic the taper length of the TLC reflectivity would have to extend toward the blue side (lower wavelengths) at each temperature and the magnitude of the reflectivity at lower wavelengths would be smallest at low temperatures and increase with temperature. This is precisely the behavior that Akino et al. [11] found. The common belief that selective reflection from a surface coated with a microencapsulated TLC is approximated by a monochromatic spike (e.g., Syson [12]) or occurs over a very narrow range of wavelengths is too simplistic.

Nomenclature

H, hue = hue (color) level in HSV color-space [Eq. (1)]
R or red = red component from RGB color-space
B or blue = blue component from RGB color-space
G or green = green component from RGB color-space
S or saturation = saturation (redness/pinkness) level in HSV color-space
V or value = brightness level in HSV color-space
i = radiant intensity
λ = wavelength
τ = transmissivity
ρ = reflectivity
Rgain, BGain = red and blue gain settings in the CCD camera
Gain = gain setting in the CCD camera
α = absorptivity
BW = bandwidth of wavelengths over which liquid crystal substance reflects incident light
CF = coverage factor to account for the fact that TLC microcapsules do not cover the entire surface
T = temperature

Subscripts

λ = specular quantity
i = incident
shield = UV shield
source = denotes specific illumination source
ref = reflected
LQ = liquid crystal or liquid crystal contribution
R = red component
vis = visible range of wavelengths
BP = black paint or background
max = maximum value
ratio = ratio of background to liquid crystal
background = background contribution
mult = multiplier used to adjust R and B values for theoretical imaging model to experimental values
exp or experimental = experimental value
model = value from theoretical imaging model

Superscripts

$'$ = unidirectional quantity
$''$ = bidirectional quantity

Acronyms

TLC = thermochromic liquid crystal
CNLC = chiral nematic liquid crystal
UV = ultraviolet
CCD = charge-coupled device
CIE = International Commission on Illumination

Downloaded 06 Dec 2010 to 193.140.21.150. Redistribution subject to ASME license or copyright; see http://www.asme.org/terms/Terms_Use.cfm

References

[1] Farina, D. J., Hacker, J. M., Moffat, R. J., and Eaton, J. K., 1994, "Illuminant Invariant Calibration of Thermochromic Liquid Crystals," Exp. Therm. Fluid Sci., **9**, pp. 1–12.

[2] Hay, J. L, and Hollingsworth, D. K., 1996, "A Comparison of Trichromic Systems for Use in the Calibration of Polymer-Dispersed Thermochromic Liquid Crystals," Exp. Therm. Fluid Sci., **12**, pp. 1–12.

[3] Camci, C., Kim, K., and Hippensteele, S. A., 1992, "A New Hue Capturing Technique for the Quantitative Interpretation of Liquid Crystal Images used in Convective Heat Transfer Studies," ASME J. Turbomach., **114**, pp. 765–775.

[4] Wang, Z., Ireland, P. T., and Jones, T. V., 1995, "An Advanced Method of Processing Liquid Crystal Video Signals from Transient Heat Transfer Experiments," ASME J. Turbomach., **117**, pp. 184–189.

[5] Behle, M., Schulz, K., Leiner, W., and Fiebig, M., 1996, "Color-Based Image Processing to Measure Local Temperature Distributions by Wide-Band Liquid Crystal Thermography," *Applied Scientific Research*, Kluwer Academic, Dordrecht, Vol. 56, No. 2–3, pp. 113–143.

[6] Billmeyer, F. W., 1967, "Optical Aspects of Color, Part 1–Introduction," Opt. Spectra **1**, pp. 59–63.

[7] Siegel, R., and Howell, J. R., 1992, *Thermal Radiation Heat Transfer*, 3rd ed., Hemisphere Publishing Corporation.

[8] Anderson, M. R., 1999, "Thermochromic Liquid Crystal Thermography: Hysteresis, Illumination and Imaging System Effects, Image Processing and Applications," Ph.D. dissertation, University of California, Davis.

[9] Cooper, T. E., Field, R. J., and Meyer, R. J., 1975, "Liquid-Crystal Thermometry and Its Application to the Study of Convective Heat Transfer," ASME J. Heat Transfer, **97**, pp. 442–450.

[10] Zhu, C., and Hieftje, G. M., 1989, "A New Liquid-Crystal-Based Fiber-Optic Temperature Sensor," Appl. Spectrosc., **43**, 1333–1336.

[11] Akino, N., Kunugi, T., Ichimiya, K., Mitsushiro, K., and Ueda, M., 1989, "Improved Liquid-Crystal Thermometry Excluding Human Color Sensation," ASME J. Heat Transfer, **111**, No. 4, pp. 558–565.

[12] Syson, B. J., Pilbrow, R. G., and Owen, J. M., 1996, "Effect of Rotation of Thermochromic Liquid Crystal," Int. J. Heat Fluid Flow, **17**, pp. 491–499.

[13] Siegel, R., and Howell, J. R., 1992, *Thermal Radiation Heat Transfer*, 3rd ed., Hemisphere Publishing Corporation.

[14] Holman, J. P., 1986, *Heat Transfer*, 6th ed., McGraw-Hill, NY.

[15] Incropera, F. P., and Dewitt, D. P., 1996, *Fundamentals of Heat and Mass Transfer*, 4th ed., Wiley, New York.

[16] Hallcrest Inc., 1991, *Handbook of Thermochromic Liquid Crystal Technology*, Sales Literature, Hallcrest Inc., Glenview, IL.

[17] Coles, H., 1998, "Chiral Nematics: Physical Properties and Applications," *Handbook of Liquid Crystals Vol. 2A: Calamitic Liquid Crystals*, Demus, J., Goodby, J., Gray, G. W., Spiess, H.-W., Vill, V., eds., Wiley–VCH, Weinheim (Federal Republic of Germany), pp. 335–409.

[18] Ennulat, R. D., 1971, "The Selective Light Reflection by Planar Textures," Mol. Cryst. Liq. Cryst., **13**, pp. 337–355.

[19] Harwood, S., 1999, Telephone Conversations April 1999, Organic Chemist at Hallcrest Inc., Glenview, Illinois.

Downloaded 06 Dec 2010 to 193.140.21.150. Redistribution subject to ASME license or copyright; see http://www.asme.org/terms/Terms_Use.cfm

The Effect of Support Grid Design on Azimuthal Variation in Heat Transfer Coefficient for Rod Bundles

Mary V. Holloway

Timothy A. Conover

Heather L. McClusky

Donald E. Beasley
Fellow, ASME

Department of Mechanical Engineering,
Clemson University,
Clemson, SC 29634

Michael E. Conner
Westinghouse Nuclear Fuel,
5801 Bluff Rd.,
Columbia, SC 29250

Support grids are an integral part of nuclear reactor fuel bundle design. Features, such as split-vane pairs, are located on the downstream edge of support grids to enhance heat transfer and delay departure from nucleate boiling in the fuel bundle. The complex flow fields created by these features cause spatially varying heat transfer conditions on the surfaces of the rods. Azimuthal variations in heat transfer for three specific support grid designs, a standard grid, split-vane pair grid, and disc grid, are measured in the present study using a heated, thin film sensor. Normalized values of the azimuthal variations in Nusselt number are presented for the support grid designs at axial locations ranging from 2.2 to 36.7 D_h*. Two Reynolds numbers,* $Re=28{,}000$ *and* $Re=42{,}000$ *are tested. The peak-to-peak azimuthal variation in normalized Nusselt number is largest just downstream of the support grids and decreases to a minimum value by the end of the grid span. A comparison of the azimuthal heat transfer characteristics between the support grids indicates distinctive results for each type of support grid design tested. The split-vane pair grid exhibits the largest peak-to-peak variation in azimuthal heat transfer of +30% to −15% just downstream of the grid at 2.2* D_h*. The disc grid has the most uniform azimuthal heat transfer distribution with a peak-to-peak value of ±4% for all axial locations tested.* [DOI: 10.1115/1.1863274]

Introduction

Nuclear fuel bundles that constitute the core for pressurized water reactors (PWRs) consist of parallel rods that are held in a fixed array by support grids. The flow of pressurized water along the rods provides the cooling for the rods during reactor operation. In addition to supporting the rods in the bundle, the support grids also affect the heat transfer and fluid flow characteristics in the rod bundle. Heat transfer enhancing features are often attached to the downstream edge of the support grids to improve the heat transfer performance of the rod bundle. One commonly implemented feature is a split-vane pair located on the downstream edge of the support grid and placed at the center of the flow area between four adjacent rods. Such vane pairs alter the flow field in two important ways, by creating a swirling flow and enhancing mixing among the parallel channels formed by the rods. The interconnected, parallel channels that are formed by rod bundles and the support grids are an exceedingly complex geometry for flow and heat transfer. Figure 1 presents a schematic diagram of a rod bundle assembly, and illustrates a subchannel, the flow area between four adjacent rods. Three support grid designs, shown in Fig. 2, are examined in the present study. For all of the support grid designs, features formed out of the grid strap hold the rods on a constant pitch in the rod bundle. A support grid having no flow enhancing features, termed a ‘‘standard’’ or ‘‘egg-crate’’ grid, is tested and serves as a basis for comparison for support grids having flow and heat transfer enhancing features. In addition, support grids with two different types of flow enhancing features, a disc and a split-vane pair, are tested. The disc support grid, shown in Fig. 2(*b*) has blunt disc blockages attached to the downstream edge of the support grid. The disc blockages are circular and have a 5.8 mm diameter. The split-vane pair support grid, shown in Fig. 2(*c*), has split-vane pairs attached to the downstream edge of the support grid. The vane orientation makes an approximately 30° angle with the axial flow direction. The split-vane pairs have left−right and up−down alternating vane patterns as indicated in Fig. 2(*c*). Flow enhancing features may be loosely characterized as streamlined or blunt, with the split-vane pair and the disc clearly representing these two classes.

Both single-phase and subcooled nucleate boiling heat transfer are important in pressurized water reactor operation. The power produced by the reactor core is limited in order to maintain the surface of the rods below the departure from nucleate boiling limit during different core transients including accident scenarios. In addition, the integrity of the fuel rods can be compromised if the local temperature on the surface of the rod is too large. For example, corrosion rates are larger at higher temperatures. Therefore, larger and more uniform values of the single-phase, local heat transfer coefficient on the rods yield increased performance, while preventing potential damage to the fuel rods that results from areas of increased temperature.

Several previous investigations have examined the azimuthal variations in wall temperature or Nusselt number in rod bundles. Dingee and Chastain [1] investigated heat transfer in rod bundles without support grids. Experiments were conducted on a square array rod bundle and a triangular array rod bundle. Each rod bundle configuration consisted of nine rods. Electrical current was passed through all nine rods to achieve resistance heating of the rods. The rods were cooled using pressurized water with Prandtl numbers of 1.18 and 1.75. The primary objective of this work was to measure fully developed Nusselt numbers. The experimental uncertainty of the measured Nusselt numbers was ±8%. Azimuthal variations in Nusselt number were observed to be less than the experimental uncertainty. Kidd et al. [2] investigated the azimuthal temperature variations and local heat transfer coefficients downstream of standard support grids in a fully heated rod bundle. The rod bundle consisted of seven rods arranged on a hexagonal array and heated using resistance heating. Air was used as the working fluid. Peak-to-peak variations in azimuthal Nusselt num-

---

Contributed by the Heat Transfer Division for publication in the JOURNAL OF HEAT TRANSFER. Manuscript received January 6, 2004; revision received December 16, 2004. Review conducted by: A. F. Emery.

Copyright © 2005 by ASME

Downloaded 06 Dec 2010 to 193.140.21.150. Redistribution subject to ASME license or copyright; see http://www.asme.org/terms/Terms_Use.cfm

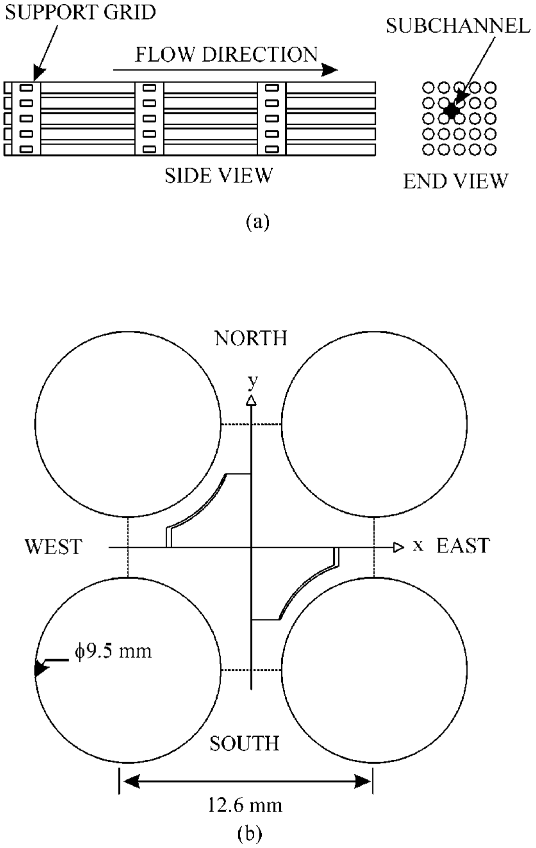

Fig. 1 (***a***) **Schematic diagram of 5×5 rod bundle assembly** (***b***) **Details of subchannel with split-vane pair**

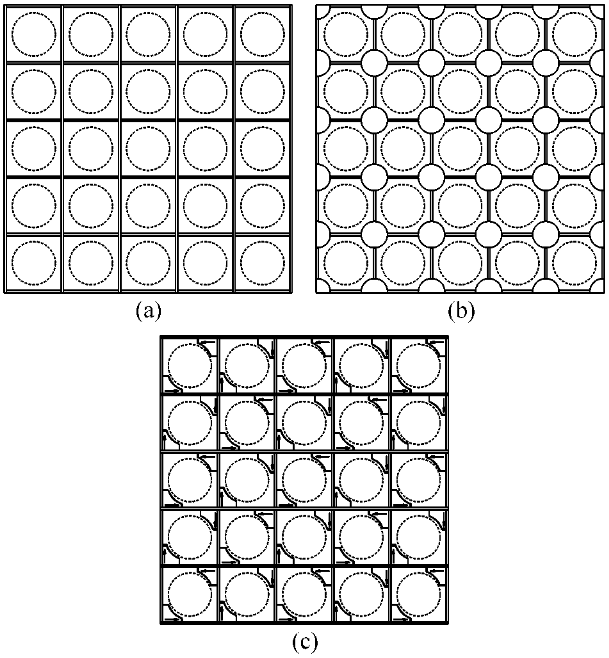

Fig. 2 Representative drawings of support grid designs for (***a***) **standard grid,** (***b***) **disc grid, and** (***c***) **split-vane pair grid.**

ber were approximately ±5% of the average Nusselt number at an axial location of two hydraulic diameters downstream of a standard support grid. In addition, Kidd et al. [2] developed a correlation for the azimuthally averaged heat transfer development downstream of a standard support grid in a rod bundle. This correlation was based on the Reynolds number and the axial distance downstream of a standard support grid in the rod bundle.

Marek and Rehme [3] investigated the heat transfer both within and immediately upstream and downstream of a standard support grid. The three-rod triangularly arrayed bundle was cooled with air. The rods in the bundle were directly heated using resistance heating. Local rod temperatures were measured to obtain heat transfer data. Azimuthal variations in the Nusselt number near the support grid were within ±5% of the circumferentially averaged Nusselt number at the corresponding axial location. A correlation for the maximum Nusselt number in the support grid region of a rod bundle was developed based on the blockage ratio (ratio of the projected area of the support grid to the open flow area in the rod bundle) of the standard support grid and the fully developed Nusselt number in the rod bundle.

Guellouz and Tavoularis [4] investigated azimuthal variations in heat transfer for a scaled model representing an outside segment of a 37-rod hexagonally arrayed reactor core. Air was the working fluid in the experiment. The 12.9:1 scaled model consisted of five rods. Three rods represented an outer segment of the hexagonal array. This outer segment of rods was surrounded by the test section wall on one side and by two interior rods on the other side. The central rod in the outer row was instrumented and positioned to determine the effect of spacing (between both the test section wall and adjacent rods) on azimuthal heat transfer variations. A small sector of the instrumented rod (corresponding to approximately 6.5 deg) was heated using a cartridge heater. The instrumentation was designed to determine the azimuthal sensitivity of the heat transfer coefficient rather than the absolute value of heat transfer coefficient that would be obtained from a fully heated rod bundle. Mean and fluctuating fluid temperature measurements were also obtained in this experiment. Results indicated that the heat transfer coefficient was a minimum adjacent to the narrow rod gaps and a maximum adjacent to the open flow regions in the rod bundle.

A limited number of studies have investigated local rod temperature and local, azimuthally averaged heat transfer downstream of a support grid with vane pairs. De Crecy [5] experimentally determined both the rod location in the array and azimuthal position on the rod for the initial occurrence of departure from nucleate boiling (DNB) downstream of a support grid with split-vane pairs. A 5×5 square array rod bundle cooled with water was used in the investigation. All rods in the bundle were heated using resistance heating. Results indicated that for rod bundles with standard support grids, DNB typically occurred first on the central rod in the bundle at an azimuthal location adjacent to the rod gaps. For support grids with split-vane pairs, DNB occurred first on one of the nine central rods in the rod bundle. In addition, the azimuthal location on the rod surface of the DNB occurrence appeared to be randomly distributed. Single-phase experiments were conducted to calculate a subchannel mixing coefficient based on the rod surface temperatures. These single-phase experiments [5] identified a subchannel mixing coefficient for the split-vane pair grid design that was approximately ten times greater than the mixing coefficient for a standard support grid design. Yao et al. [6] proposed a correlation for the local heat transfer development downstream of a support grid with vane pairs. Since no experimental heat transfer measurements downstream of a split-vane pair grid design were available, Yao et al. [6] incorporated information from fundamental research in decaying, swirling flow in a pipe to develop their correlation. The correlation developed for flow downstream of a split-vane pair modeled the effects of swirling flow in rod bundle subchannels based on the spatial decay rate of the angular momentum of swirling pipe flow reported by Kreith and Sonju [7].

Holloway et al. [8] investigated the local, azimuthally averaged heat transfer development downstream of support grid designs with flow-enhancing features. Support grids with vane pairs as

Downloaded 06 Dec 2010 to 193.140.21.150. Redistribution subject to ASME license or copyright; see http://www.asme.org/terms/Terms_Use.cfm

well as circular disc flow-enhancing features were investigated. A 5×5 square array rod bundle with water as the working fluid was used in the investigation. Pressure drop measurements across the support grids were documented for standard, split-vane pair, and disc grids. The measurements indicated that the disc grid had the largest pressure loss coefficients. The standard support grids had the lowest pressure loss coefficients. The split-vane pair support grids, with the streamlined vanes, had pressure loss coefficients in between those of the disc grid and the standard support grids with no flow-enhancing features. Heat transfer measurements were obtained by heating a small portion of a single rod in the bundle using a cartridge heater inserted concentrically into the instrumented rod. A general heat transfer correlation based on fundamental physics was developed for flow downstream of support grid designs with flow-enhancing features. Results indicated that the circumferentially averaged heat transfer downstream of a support grid with flow-enhancing features could be characterized based on the pressure losses associated with the flow-enhancing features attached to the support grid. No previous experimental investigations reporting azimuthal heat transfer variations downstream of support grids with flow-enhancing features were identified in the open literature.

Previous investigations have examined the natural mixing that occurs between closely spaced rod bundles (see [9] for a review). Flow pulsations through the rod gaps of neighboring subchannels have been identified for closely spaced rod bundles in numerous investigations. Some key results will be discussed here. Hooper and Rehme [10] found that for a fixed rod gap spacing, the frequency of the flow pulsations, as identified based on spectra of the velocity fluctuations, increased linearly with the Reynolds number. Moller [11], found that the nondimensional frequency, presented in terms of the Strouhal number, was a function of the relative gap width. Wu and Trupp [12] confirmed that the Strouhal number was a function of the relative gap width. Guellouz and Tavoularis [13,14] documented the structure of turbulent flow for W/D ratios ranging from 1.05 to 1.35. Flow pulsations were identified for each gap width tested. Krauss and Meyer [15] documented the quasi-periodic frequencies present in both velocity and fluid temperature measurements, which indicate that the flow pulsations and heat transfer through the rod gap are closely related. The flow conditions in all of these investigations were in the fully developed flow region, far downstream of any rod support structures. As far as is known, no investigation on the presence of flow pulsations downstream of different types of support grid designs separated by a short span ($\sim 40\, D_h$) has been published in the open literature. Therefore, the exact nature and existence of these flow pulsations for the rod bundle geometry investigated in the present study is not known. However, forced mixing due to the increased turbulence and large-scale flow structures created by the support grid designs is expected to have a much larger effect on the resulting convective heat transfer from the surface of the rods.

The present experimental investigation examines the azimuthal variations in heat transfer in a rod bundle downstream of various types of support grids. A 5×5 square array rod bundle, representing a portion of a full-scale 17×17 square array rod bundle, is the model rod bundle used in the present investigation. The support grids used in the model rod bundle assemblies are constructed from interior straps of the 17×17 support grid designs. The rod diameter and pitch as well as the axial spacing of the support grids in the rod bundle assembly are consistent with those in a full-scale 17×17 rod bundle. New support grid designs are typically benchmarked using a 5×5 (or similar reduced array) rod bundle. Results from benchmark tests are used to develop heat transfer and mass exchange correlations for the 17×17 rod bundle assemblies. In addition, required DNB testing of new support grid designs is performed on the reduced size array.

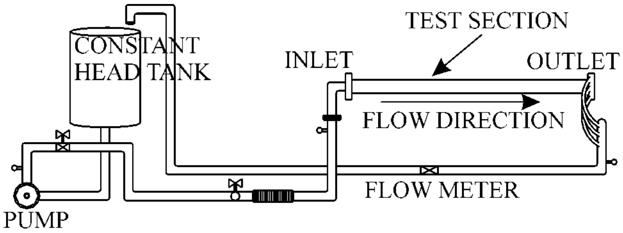

Fig. 3 Drawing of experimental facility.

In the present study, a heated, thin film sensor is implemented to obtain measurements of the azimuthal variations in heat transfer downstream of the three distinct support grid designs. Since only a small portion of the instrumented rod is heated, the measurement technique is similar in concept to that developed in [4]. Reynolds numbers (based on the hydraulic diameter of the central subchannel) of 28,000 and 42,000 are investigated. These Reynolds numbers are an order of magnitude lower than those occurring in the core of a nuclear reactor. However, comparison of experimental particle image velocimetry (PIV) measurements at $\mathrm{Re}=28{,}000$ [16,17] with computational fluid dynamics (CFD) results at in-core conditions downstream of a split-vane pair grid design indicates similar flow structures for both Reynolds numbers. In addition, the heat transfer enhancement in swirling flow is strongly dependent on the intensity of the swirl and only weakly dependent on the axial Reynolds number [18]. Since the flow structures present at $\mathrm{Re}=28{,}000$ are similar to those for in-core flow conditions, the trends in azimuthal heat transfer variation observed at the lower Reynolds numbers can be extended to those at in-core conditions. Azimuthal variations in Nusselt number were obtained for the central rod in the bundle. Axial locations ranging from 2.2 to 36.7 D_h are examined.

Experimental Facility and Measurements

Experimental Facility. Figure 3 shows a schematic drawing of the closed-loop experimental facility that is used in the present study. The flow loop uses water as a working fluid and consists of a constant head tank, heat exchanger, variable speed pump, flow straightener, test section, and flowmeter. The Lexan test section accommodates a square-arrayed 5×5 rod bundle. The test section height and length are 65 mm and 1.64 m, respectively. The rod bundle is constructed using 9.5 mm rods that are supported on a 12.6 mm pitch. Thus, the P/D ratio for the rod bundle is 1.33. The hydraulic diameter, D_h, of a single subchannel is 11.78 mm. Three grids are used to assemble the bundle and are placed on a span of 508 mm. The first grid is located 90 mm downstream of the test section inlet.

Local measurements of the variation in the heat transfer coefficient around the circumference of the central rod in the bundle are acquired at axial locations of 25.4–432 mm (2.2–36.7 D_h) downstream of the third grid. Measurements are obtained for axial velocities of 2.4 and 3.7 m/s and a bulk water temperature (T_b) of 20°C. The corresponding Reynolds numbers, based on hydraulic diameter, are $28{,}000 \pm 1200$ and $42{,}000 \pm 1700$. Full discussion of the flow loop can be found in [8].

Thin Film Sensor. The azimuthal variation in heat transfer coefficient is measured using a rod instrumented with a locally heated sensor. Figures 4 and 5 show a schematic drawing and a photograph of the sensor. The polycarbonate body of the sensor is 9.5 mm in diameter and is 54 mm long. A resistance heater (thin film of Hastings alloy) was flush mounted on the surface of the sensor to provide local heating at the surface of the sensor. The resistance heater is 0.013 mm thick, 1.6 mm wide, 28.6 mm long, and provides local heating to a 20 deg sector of the surface of the sensor. As shown in Fig. 4, a groove milled into the surface of the sensor accommodates the resistance heater. Figure 5 shows a photograph of the thin film resistance heater embedded on the surface of the sensor. The surface of the resistance heater is in direct contact with the water in the test section, and is heated using a

Downloaded 06 Dec 2010 to 193.140.21.150. Redistribution subject to ASME license or copyright; see http://www.asme.org/terms/Terms_Use.cfm

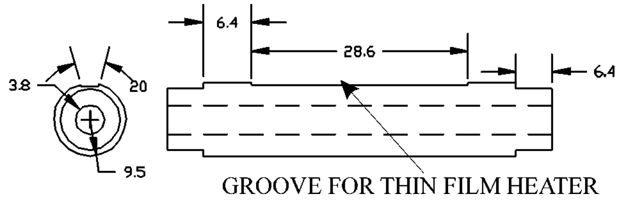

Fig. 4 Drawing of thin film azimuthal heat transfer sensor (Dimensions in mm)

direct current power supply. An E-type thermocouple and an Omega digital panel meter are used to measure the temperature directly beneath the resistance heater. The Omega digital panel meter has a measurement resolution of 0.01°C. The measurement system was calibrated from 10°C to 50°C and the uncertainty in temperature measurement based on a root-sum-square method of combining measurement error and the calibration error ($t_{\nu,95}Syx$) was ± 0.50°C. The thermocouple provided an accurate measure of the sensor surface temperature due to the small thickness of the resistance heater. High-frequency resolution in temperature fluctuations was not a goal of the present investigation. As such, the present experimental technique provides time-averaged heat transfer measurements around the circumference of the instrumented rod.

Experimental Measurements. The central rod instrumented with the thin film sensor is moveable. The remaining 24 rods are fixed at the inlet and outlet of the test section. The central moveable rod could be rotated about its axis and translated in a direction parallel to its axis. A protractor fixed to the rod provided measurement of the azimuthal position of the sensor; the resolution of the protractor was 1 deg and the uncertainty in the azimuthal position was $\pm 2°$. Figure 6 indicates the location of the instrumented rod as well as the angular coordinate orientation for the azimuthal locations tested.

The local heat transfer coefficient, h_θ, is calculated from the power and temperature measurements as

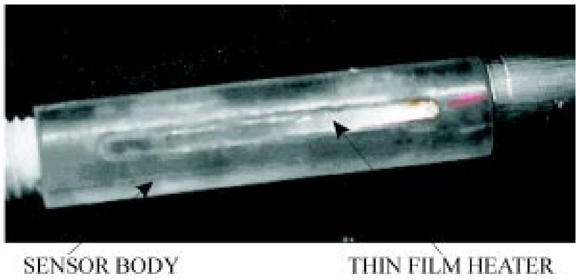

Fig. 5 Photograph of thin film azimuthal heat transfer sensor

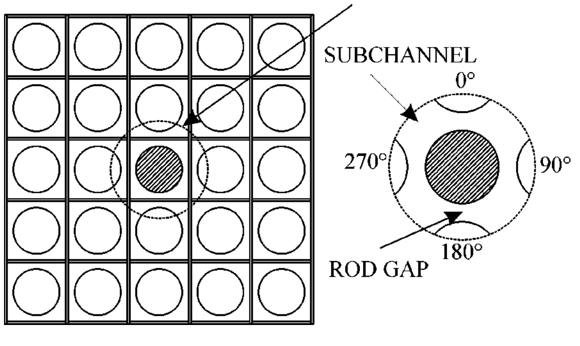

Fig. 6 Details of instrumented rod location

$$h_\theta=\frac{q}{A_{\mathrm{eff}}(T_\theta-T_b)} \tag{1}$$

In addition, the local Nusselt number is defined as

$$\mathrm{Nu}_\theta=\frac{h_\theta D_h}{k} \tag{2}$$

The local azimuthal variation in the normalized Nusselt number at a specific angular position was determined by measuring the surface temperature of the heater and the bulk fluid temperature

$$\frac{Nu_\theta(z)-\overline{Nu_\theta(z)}}{\overline{Nu_\theta(z)}}=\frac{(T_\theta-T_b)^{-1}-\overline{(T_\theta-T_b)^{-1}}}{\overline{(T_\theta-T_b)^{-1}}} \tag{3}$$

where $\overline{(T_\theta-T_b)^{-1}}$ represents the average of the inverse of the temperature difference between the rod and the bulk fluid for a given axial location. The bulk fluid temperature was measured before and after acquiring each data set at each axial location. The power input to the resistance heater was 7 W and was determined by measurement of the resistance and the voltage. The nominal resistance of the heater was 0.25 Ω. The power was selected to provide a temperature difference ($T_\theta-T_b$) ranging from 4°C to 10°C. The measurements obtained using this sensor for a specific angular position represent the heat transfer averaged over a 20 deg sector of the rod surface and over the 28.6 mm length. The measurement at a given axial location was obtained in a small time period to avoid drift in the power supply and thermocouple reference junction compensation. The bias error inherent in expressing an absolute value of local heat transfer is removed due to the normalization procedure described in Eq. (3). Therefore, the contribution of uncertainty in the local Nusselt number due to precision error (rather than absolute error) was estimated based on a Kline McClintock sensitivity approach

$$u_{Nu_\theta}=\sqrt{\left(u_q\frac{\partial \mathrm{Nu}_\theta}{\partial q}\right)^2+\left(u_{T_\theta}\frac{\partial \mathrm{Nu}_\theta}{\partial T_\theta}\right)^2+\left(u_{T_b}\frac{\partial \mathrm{Nu}_\theta}{\partial T_b}\right)^2} \tag{4}$$

with typical error contributions to the precision uncertainty as listed below.

u_q	± 0.17 W
$u_{T\theta}$	± 0.25°C
u_{Tb}	± 0.25°C

The measurements of hydraulic diameter, area, and fluid conductivity are assumed to be constant, and therefore, have zero contribution to the precision error of the Nusselt number. The uncertainty of the azimuthal variation in Nusselt number is $\pm 4\%$. This uncertainty claim is supported by repeatability measurements obtained during the experiment.

Previous research on conduction losses in similar heat flux probes (for example, [19]), indicate that as convective conditions at the surface of the probe increase, the amount of energy conducted into the body of the sensor will decrease. In order to quantify the conduction losses through the polycarbonate body of the sensor for the given flow conditions, a two-dimensional (2D) conduction model was investigated using FLUENT software. Convection heat transfer coefficients ranging from 12,500 to 30,000 W/m^{2}K were investigated. This resulted in temperature differences between the surface of the sensor and the bulk fluid ranging from approximate 5°C to 12°C. For the range of conditions examined, the convective heat transfer from the surface of the thin film sensor was 96–98% of the total energy generated by the thin-film sensor. Since the convective conditions in the present study result in negligible conduction losses to the sensor body, the effective area can be assumed constant and equal to the sensor area for all flow conditions.

Downloaded 06 Dec 2010 to 193.140.21.150. Redistribution subject to ASME license or copyright; see http://www.asme.org/terms/Terms_Use.cfm

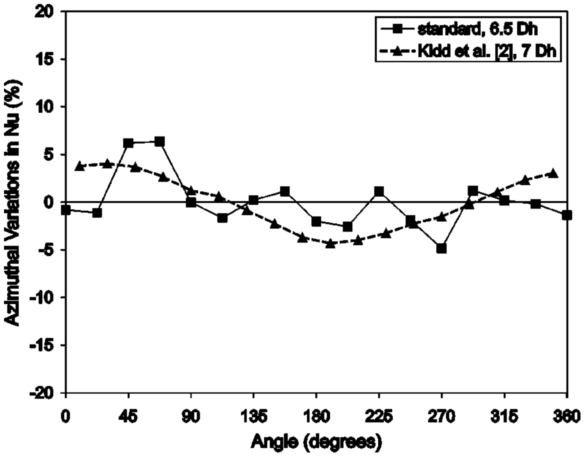

Fig. 7 Azimuthal variations in Nusselt number comparison with Kidd et al. [2]

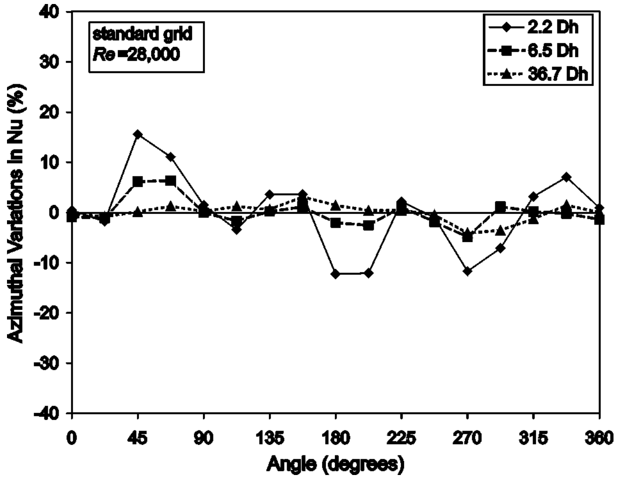

Fig. 8 Azimuthal variations in Nusselt number for standard grid

The temperature field that arises in the model rod bundle is different than that in a fully-heated bundle or reactor core. Hydrodynamic conditions are similar, but the thermal boundary layer on the rod is not developed; therefore, the measurements obtained using the thin film sensor are most closely related to the local magnitude of the shear stress on the rod surface. The variations of shear stress indicated by the sensor may be directly compared to those obtained from a fully heated case. This further motivates normalization of the results and allows interpretation of the present measurements in terms of heat transfer. Hay and West [20] and Guellouz and Tavoularis [4] employed a similar normalization procedure. Major flow features, whether impingement, separation, or flow acceleration, will have similar effects in either case.

Results and Discussion

Azimuthal variations in heat transfer downstream of a standard support grid design and support grid designs with disc and split-vane pair flow and heat transfer enhancing features have been acquired using the thin film sensor. Axial locations ranging from 2.2 to 36.7 D_h were investigated downstream of each of the support grid designs. Data are presented in the form of normalized variation in Nusselt number, Eq. (3), to allow direct comparison of the data obtained from different support grid designs.

The standard support grid design is a baseline case for comparison of azimuthal variations in support grids with flow-enhancing features. Azimuthal variations in heat transfer downstream of a standard support grid design are shown in Figs. 7 and 8. Note that the normalized azimuthal variation in Nusselt number, as defined in Eq. (3), is presented on the ordinate axes. The data points in the figures indicate individual measurement locations, with connecting lines through the data points included to provide distinction between each series included in the data plots. Figure 7 provides a comparison between measurements obtained downstream of the standard support grid using the thin film sensor in the present study and data obtained from the fully heated rod bundle study of Kidd et al. [2]. The data of [2] was obtained at Re=50,000 and at an axial location of 7.0 D_h while the data from the present study was obtained at Re=42,000 and 6.5 D_h. Heat transfer variations were measured around an outer rod of the seven rod hexagonally arrayed bundle in [2], so differences in the location of peak heat transfer are expected. Figure 7 indicates that the magnitude of azimuthal variations in heat transfer measured by the present experimental technique is consistent with that measured using a different measurement technique by Kidd et al. [2]. Based on previous investigations of azimuthal heat transfer [2,3], the variation in heat transfer downstream of a standard support grid design is expected to be on the order of ±5% for a hexagonally arrayed rod bundle. Data obtained using the thin film sensor confirm this result for a square arrayed rod bundle.

Figure 8 presents the azimuthal variations in Nusselt number downstream of the standard support grid at three axial locations for Re=28,000. The largest peak-to-peak variation in Nusselt number occurs just downstream of the standard support grid at 2.2 D_h. These azimuthal variations are attributed to increased turbulence, boundary layer destruction (surface renewal), and local flow acceleration caused by the support grid. The maximum azimuthal heat transfer variation of +16% occurs at an angle of 45 deg (adjacent to the subchannel flow area as shown in Fig. 6) while the minimum variation of −12% occurs at an angle of 180 deg (adjacent to the rod gap as shown in Fig. 6). As the flow develops in the streamwise direction, the peak-to-peak value of the azimuthal heat transfer variation decreases. At 36.7 D_h, where the flow is expected to be hydrodynamically fully developed, the peak-to-peak azimuthal variation in Nusselt number is within ±4%. A comparison between the data obtained at Re=42,000 (Fig. 7) and Re=28,000 for 6.5 D_h (Fig. 8) indicates the same general behavior for both Reynolds numbers tested. These similarities were documented for each of the support grid designs tested. As such, the lower Reynolds number case, Re=28,000, will be the focus for the remainder of the discussion.

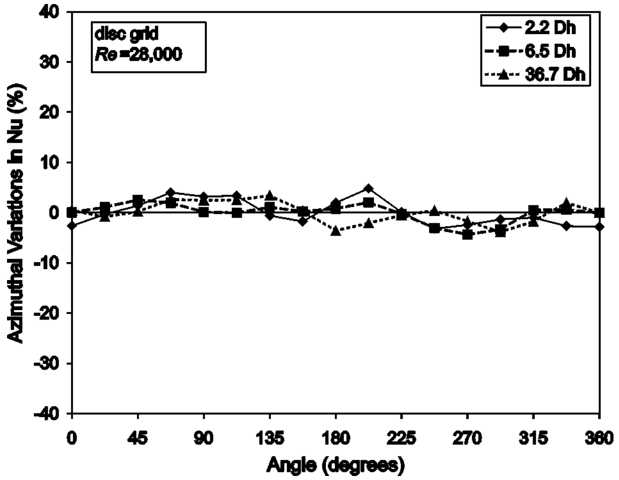

Fig. 9 Azimuthal variations in Nusselt number for disc grid

Downloaded 06 Dec 2010 to 193.140.21.150. Redistribution subject to ASME license or copyright; see http://www.asme.org/terms/Terms_Use.cfm

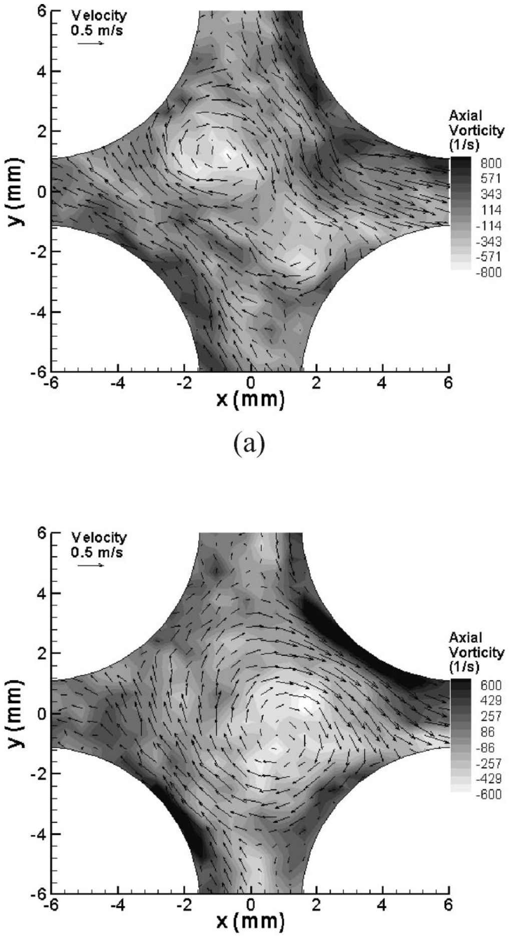

(a)

(b)

Fig. 10 Lateral velocity and axial vorticity downstream of split-vane pair grid [17] for (*a*) 2.8 D_h and (*b*) 6.3 D_h

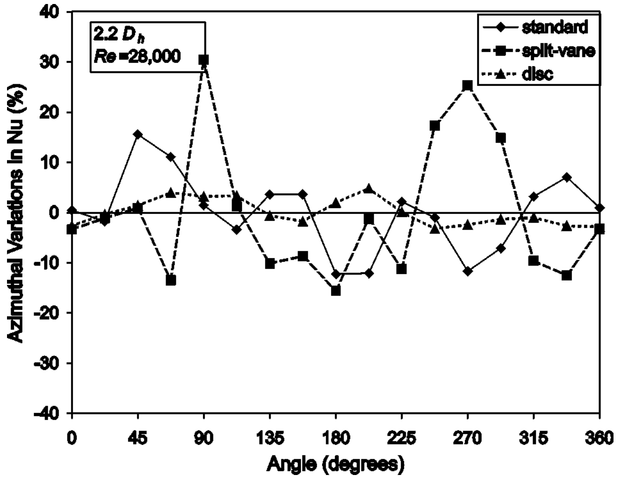

Fig. 12 Azimuthal variations in Nusselt number for 2.2 D_h

The azimuthal variations in the Nusselt number downstream of the disc grid design are documented for three axial locations at Re=28,000 in Fig. 9. The peak-to-peak azimuthal variation in the Nusselt number is within ±4% for all axial locations downstream of the disc grid. The azimuthal variation in the Nusselt number for all of the axial locations are comparable to the fully developed value obtained from the standard grid design at 36.7 D_h. The large peak-to-peak variations in the Nusselt number measured just downstream of the standard grid at 2.2 D_h are not observed just downstream of the disc grid.

The complex flow field downstream of support grids with split-vane pairs has been documented in several previous investigations. An investigation of the axial velocity downstream of split-vane pair grid design [21] indicates that just downstream of the support grid, the axial velocity is lowest in the center of the subchannel and highest in the center of the rod gaps. As the flow develops, the axial velocity profile returns to that of the fully developed profile with higher axial velocities in the center of the subchannel and lower axial velocities in the center of the rod gaps. McClusky et al. [16] documented a swirling flow structure, consistent with a Lamb–Oseen vortex, in the lateral flow field downstream of a single split-vane pair in a rod bundle subchannel. The swirling flow structure was found to migrate within the subchannel. In addition, the decay rate of the angular momentum was documented. McClusky et al. [17] presented lateral velocity fields for several subchannels downstream of a split-vane pair grid design. Integral measures of the lateral velocity field indicate that differences in lateral flow structures are present in each subchannel. Figure 10 presents lateral velocity and axial vorticity fields obtained using particle image velocimetry (PIV) downstream of a typical split-vane pair support grid as presented in [17]. Two axial

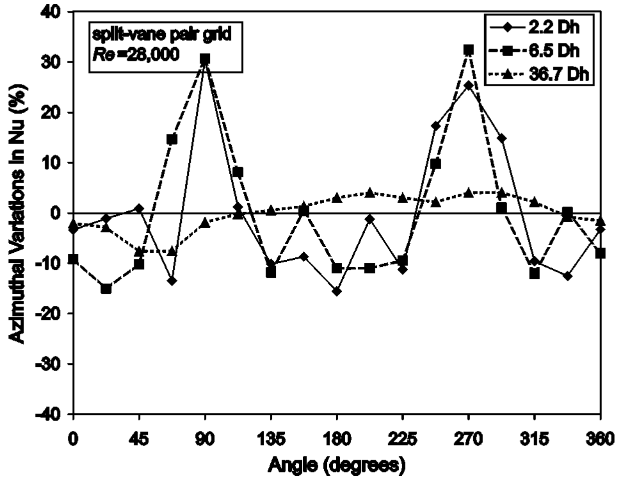

Fig. 11 Azimuthal variations in Nusselt number for split-vane pair grid

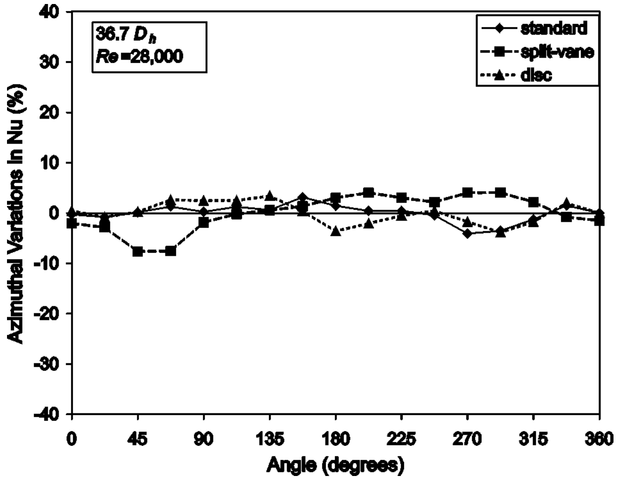

Fig. 13 Azimuthal variations in Nusselt number for 36.7 D_h

Downloaded 06 Dec 2010 to 193.140.21.150. Redistribution subject to ASME license or copyright; see http://www.asme.org/terms/Terms_Use.cfm

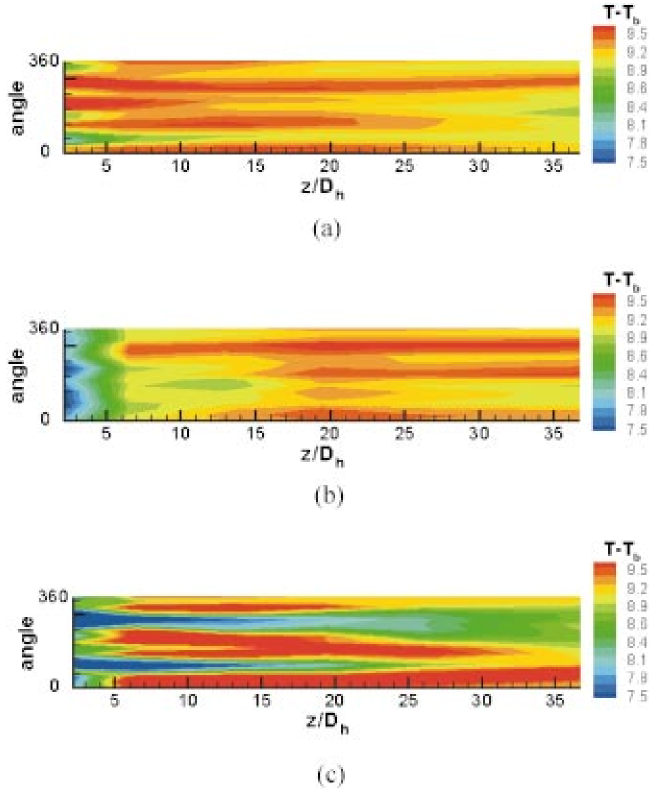

(a)

(b)

(c)

Fig. 14 (Color) Contour plots of temperature difference ($T - T_b$) at Re=28,000 for (*a*) standard grid, (*b*) disc grid, and (*c*) split-vane pair grid

locations, 2.8 D_h and 6.3 D_h, are presented. As shown in Fig. 10, two vortices shed from the vane tips are present at 2.8 D_h while a single vortex is present at an axial location of 6.3 D_h. The single vortex was documented in the subchannel for axial locations up to 25.5 D_h. However, the relative magnitude of the lateral velocities decreases with increasing distance from the support grid. Figure 10 also indicates differences in the lateral rod gap flows present in the subchannel. For example, the east rod gap in Figs. 10(*a*) and 10(*b*) has strong lateral velocities leaving the subchannel area. In contrast, the north and south rod gaps have smaller lateral velocities with some recirculation in the rod gaps. In addition, separation regions around portions of the rods are typically observed downstream of split-vane pair grid designs. A separation region is located on the southeast rod in Figs. 10(*a*) and 10(*b*). The axial velocity distributions and information on the complex lateral flow structure downstream of a split-vane pair support grid are useful in interpreting the azimuthal heat transfer variations obtained in the present investigation.

Figure 11 presents the azimuthal variation in Nusselt number downstream of a split-vane pair grid design for three axial locations at Re=28,000. At axial locations of 2.2 D_h and 6.5 D_h there are large peak-to-peak variations in the azimuthal Nusselt numbers. At these axial locations, the maximum azimuthal variation in Nusselt number is +30% while the minimum azimuthal variation is −15%. The maximum Nusselt number occurs at locations on the rod adjacent to the rod gaps (90 deg and 270 deg). The minimum azimuthal Nusselt number variation is observed at several azimuthal locations. As the flow develops in the streamwise direction, the peak-to-peak azimuthal variation diminishes. At 36.7 D_h, the azimuthal variations in Nusselt number range from +4% to −7.6%. The complex flow behavior downstream of split-vane pair grid designs, such as flow separation from the rod and axial velocity deficits, contributes to large variations in azimuthal Nusselt number.

Comparisons between the three support grid designs tested are presented in Figs. 12 and 13 for 2.2 D_h and 36.7 D_h, respectively. As shown in Fig. 12, the azimuthal variations in Nusselt number for the split-vane pair grid design are the largest at a location just downstream of the support grid. The circumferentially averaged Nusselt number at 2.2 D_h is larger for the split-vane pair grid than the standard grid design [8]. However, there are also larger variations in Nusselt number around the circumference of the rod. The disc grid produces the most uniform azimuthal Nusselt number distribution. At 2.2 D_h, the disc grid exhibits the largest average Nusselt number compared to the other support grid designs tested [8]. A disadvantage of the disc grid is the large pressure drop associated with the blunt discs. Figure 13 indicates that at 36.7 D_h the azimuthal variations in Nusselt number have similar magnitudes and behavior for the three support grid designs.

Figure 14 presents contour plots of the temperature difference, $T_\theta - T_b$, for the standard grid, disc grid, and split-vane pair grid for the range of axial locations measured in the present investigation. Regions of high temperature difference, called hot spots, form at localized angular positions for all three support grid designs. However, the axial location that the hot spots appear, as well as the axial development of the hot spots, is dependent on the type of support grid. For comparison with the current measurement technique, a temperature distribution obtained downstream of a split-vane pair grid design using computational fluid dynamics (CFD) is presented in Fig. 15 [22].

The CFD simulation [22] consisted of a two-subchannel model with periodic boundary conditions. The predicted temperature distribution for a central rod in a 5×5 rod bundle is obtained from the portion of the rod surfaces highlighted in Fig. 15. The 0° reference angle used in Fig. 15 is not the same as the orientation used in the present investigation (shown in Fig. 6). In Fig. 15, the angle of the rod location is represented by the horizontal axis and the axial distance downstream of the support grid is plotted on the vertical axis. A constant heat flux is applied at the surface of the rods; therefore, the bulk temperature of the fluid is increasing with axial distance downstream of the grid. In addition, the CFD simulates the thermal conditions in the core of a pressurized water reactor, which has significantly higher heat fluxes from the rod walls than the heated film sensor used in the present investigation. Therefore, a qualitative comparison between the trends in temperature (and not the absolute temperatures) of measurements made with the heated film sensor, Fig. 14(*c*), and the CFD simulation, Fig. 15 is appropriate. Two main regions of elevated surface temperature, or hot spots, are identified in both of these figures. The two hot spots merge into a single hot spot at approximately 30 D_h (353 mm downstream of the strap). A comparison between these figures indicates that the measurement technique utilized in the present study, which provides azimuthal variations that are averaged over a 20 deg angle of the rod surface, provides a good representation of the variations in temperature (or Nusselt number) that occur in a fully heated rod bundle at in-core conditions. In addition, comparisons between CFD predictions of the velocity and temperature fields [22] and the present measurements of the azimuthal heat transfer variations suggest that regions of lower magnitude total velocity that are associated with lateral flow structures are the primary contributor to regions of decreased Nusselt number.

Conclusions

The azimuthal variations in heat transfer downstream of several rod bundle assemblies have been quantified. Three different support grid designs were investigated. A standard support grid design provided a benchmark comparison with previous investigations. In addition, the standard support grid was used as a baseline case for comparison with the disc grid and split-vane pair grid designs. For the standard and split-vane pair grid designs, the peak-to-peak variation of heat transfer was largest at the measure-

Downloaded 06 Dec 2010 to 193.140.21.150. Redistribution subject to ASME license or copyright; see http://www.asme.org/terms/Terms_Use.cfm

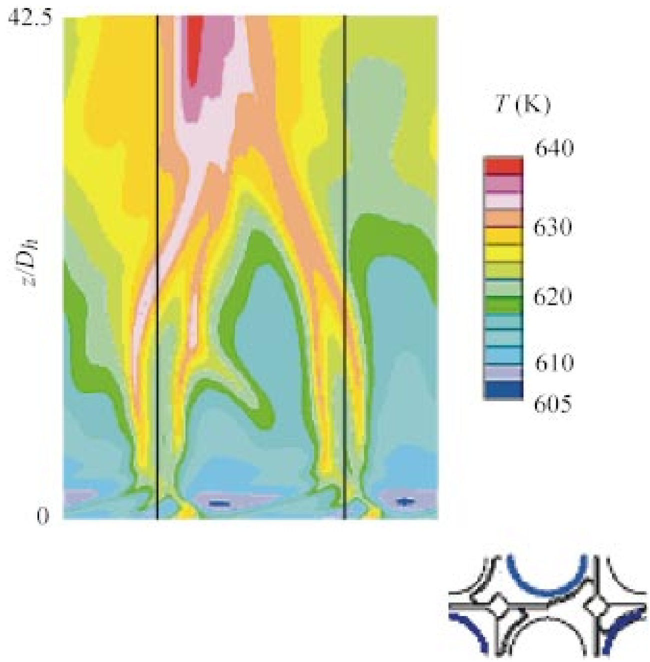

Fig. 15 (**Color**) **Temperature distribution for split-vane pair grid obtained from CFD** [**22**]

ment location just downstream of the grid. The peak-to-peak variation decreased with distance downstream of the grid.

For the standard grid, azimuthal variations in heat transfer ranged from +16% to −12% at 2.2 D_h, and decreased to +8% to −4% by 6.5 D_h. Split-vane pairs cause enhanced circumferentially average heat transfer, but also have the largest peak-to-peak variations (+30% to −15%) of the grid designs tested. These variations did not decay rapidly in the downstream direction, but persisted well past 10 hydraulic diameters downstream of the support grid. Such large variations are a result of the interaction between the lateral and streamwise flow structures that result in regions of total velocity deficit at the surface of the rods. The disc grid has enhanced circumferentially averaged heat transfer just downstream of the grid that is achieved with a large pressure drop. However, peak-to-peak variations of ±4% were observed at all axial locations. The results of the present study provide data on the variation in heat transfer that occurs on the surfaces of rods in heated rod bundles, and highlight the trends in the azimuthal variations that occur for different types of support grid designs. The azimuthal heat transfer distribution on the rod surface can be incorporated with other important design factors in the development of future support grid designs.

Nomenclature

A_{eff} = effective area
D = rod diameter
D_h = hydraulic diameter
h_θ = heat transfer coefficient
k = thermal conductivity
$\overline{\mathrm{Nu}}_\theta$ = average Nusselt number at an axial location
Nu_θ = local Nusselt number
P = rod pitch
Re = Reynolds number
T_θ = rod surface temperature
T_b = bulk fluid temperature
q = power
u = uncertainty
W = wall-to-rod distance
z = axial coordinate direction

References

[1] Dingee, D. A., and Chastain, J. W., 1956, ''Heat Transfer from Parallel Rods in Axial Flow,'' *Reactor Heat Transfer Conference of 1956*, TID-7529 (Pt. 1), Book 2, pp. 462–501.
[2] Kidd, G. J., Hoffman, H. W., and Stelzman, W. J., 1968, ''The Temperature Structure and Heat Transfer Characteristics of an Electrically Heated Model of a Seven-Rod Cluster Fuel Element,'' ASME paper 68-WA/HT-33.
[3] Marek, J., and Rehme, K., 1979, ''Heat Transfer in Smooth and Roughened Rod Bundles Near Spacer Grids,'' *Proceedings of the ASME Winter Annual Meeting Dec 2–7*, 1979, pp. 163–170.
[4] Guellouz, M. S., and Tavoularis, S., 1992, ''Heat Transfer in Rod Bundle Subchannels with Varying Rod-Wall Proximity,'' Nucl. Eng. Des., **132**, pp. 351–366.
[5] de Crecy, F., 1994, ''The Effect of Grid Assembly Mixing Vanes on Critical Heat Flux Values and Azimuthal Location in Fuel Assemblies,'' Nucl. Eng. Des., **149**, pp. 233–241.
[6] Yao, S. C., Hochreiter, L. E., and Leech, W. J., 1982, ''Heat-Transfer Augmentation in Rod Bundles Near Grid Spacers,'' J. Heat Transfer, **104**, pp. 76–81.
[7] Kreith, F., and Sonju, O. K., 1965, ''The Decay of a Turbulent Swirl in a Pipe,'' J. Fluid Mech., **22**, Part 2, pp. 257–271.
[8] Holloway, M. V., McClusky, H. L., Beasley, D. E., and Conner, M. E., 2003, ''The Effect of Support Grid Features on Local, Single-Phase Heat Transfer Measurements in Rod Bundles,'' J. Heat Transfer, **126**, pp. 43–53.
[9] Rehme, K., 1992, ''The Structure of Turbulence in Rod Bundles and the Implications on Natural Mixing Between the Subchannels,'' J. Heat Transfer, **35**, pp. 567–581.
[10] Hooper, J. D., and Rehme, K., 1984, ''Large-scale Structural Effects in Developed Turbulent Flow Through Closely-Spaced Rod Arrays,'' J. Fluid Mech., **145**, pp. 305–337.
[11] Moller, S. V., 1991, ''On Phenomena of Turbulent Flow Through Rod Bundles,'' Exp. Therm. Fluid Sci., **4**, pp. 25–35.
[12] Wu, X., and Trupp, A. C., 1993, ''Experimental Study on the Unusual Turbulence Intensity Distributions in Rod-to-Wall Gap Regions,'' Exp. Therm. Fluid Sci., **6**, pp. 360–370.
[13] Guellouz, M. S., and Tavoularis, S., 2000, ''The Structure of Turbulent Flow in a Rectangular Channel Containing a Cylindrical Rod-Part 1: Phase-averaged Measurements,'' Exp. Therm. Fluid Sci., **23**, 59–73.
[14] Guellouz, M. S., and Tavoularis, S., 2000, ''The Structure of Turbulent Flow in a Rectangular Channel Containing a Cylindrical Rod-Part 2: Reynolds-averaged Measurements,'' Exp. Therm. Fluid Sci., **23**, 75–91.
[15] Krauss, T., and Meyer, L., 1996, ''Characteristics of Turbulent Velocity and Temperature in a Wall Channel of a Heated Rod Bundle,'' Exp. Therm. Fluid Sci., **12**, pp. 75–86.
[16] McClusky, H. L., Holloway, M. V., Beasley, D. E., and Conner, M. E., 2002, ''Development of Swirling Flow in a Rod Bundle Subchannel,'' J. Fluids Eng., **124**, pp. 747–755.
[17] McClusky, H. L., Holloway, M. V., Conover, T. A., Beasley, D. E., Conner, M. E., and Smith, III, D. L., 2003, ''Mapping of the Lateral Flow Field in Typical Subchannels of a Support Grid with Vanes,'' J. Fluids Eng., **125**, pp. 987–996.
[18] Dhir, V. K., and Chang, F., 1992, ''Heat Transfer Enhancement Using Tangential Injection,'' ASHRAE Trans., **98**, pp. 383–390.
[19] Beasley, D. E., and Figliola, R. S., 1988, ''A Generalized Analysis of a Local Heat Flux Probe,'' J. Phys. E, **21**, pp. 316–322.
[20] Hay, N., and West, P. D., 1975, ''Heat Transfer in Free Swirling Flow in a Pipe,'' J. Heat Transfer, **97**, Series C, No. 3, pp. 411–416.
[21] Yang, S. K., and Chung, M. K., 1998, ''Turbulent Flow Through Spacer Grids in Rod Bundles,'' J. Fluids Eng., **120**, pp. 786–791.
[22] Conner, M. E., Smith, L. D. III., Paramonov, D. V., Liu, B., and Dzodzo, M., 2003, ''Understanding and Predicting the Flow Field in a Reactor Core,'' Proceedings of the ENS TopFuel 2003/ANS LWR Fuel Performance Meeting, 2003 Topfuel conference, INFORUM GmbH, March 16–19, Wurzburg, Germany.

Downloaded 06 Dec 2010 to 193.140.21.150. Redistribution subject to ASME license or copyright; see http://www.asme.org/terms/Terms_Use.cfm

A. Barletta
Mem. ASME
e-mail: antonio.barletta@mail.ing.unibo.it

S. Lazzari
e-mail: stefano.lazzari@mail.ing.unibo.it

Università di Bologna,
Dipartimento di Ingegneria Energetica,
Nucleare e del Controllo Ambientale (DIENCA),
Laboratorio di Montecuccolino,
Via dei Colli, 16,
I-40136 Bologna, Italy

Forced and Free Flow in a Vertical Annular Duct Under Nonaxisymmetric Conditions

The combined forced and free flow in a vertical annular duct is studied under the hypothesis of steady-state parallel laminar flow. The Boussinesq approximation is invoked and the viscous dissipation is considered as negligible. The thermal boundary conditions are such that axial symmetry does not occur and temperature does not change in the axial direction. The dimensionless local balance equations are solved analytically by means of the Fourier series expansion method. The analytical expressions of the dimensionless temperature field, of the dimensionless velocity field, and of the Fanning friction factor are obtained. [DOI: 10.1115/1.1863277]

Keywords: Mixed Convection, Annular Duct, Nonaxisymmetric Boundary Conditions, Analytical Method, Fourier Series

Introduction

Several technical papers on forced and free convection in ducts with annular cross section have been published in the last three decades. Shah and London [1], for instance, have provided a wide description of the main results available in the literature for the case of laminar flow forced convection. Many are also studies concerning mixed convection in annular ducts. Among the analytical studies on this subject, Rokerya and Iqbal [2] have analyzed the effect of viscous dissipation on fully developed mixed convection in a vertical annular duct. More recently, mixed convection in a vertical annulus has been studied by Kou and Huang [3] with reference to a duct filled with a porous medium, and by Barletta [4] with reference to power law fluids. Among the numerical studies about mixed convection in vertical annular ducts, Aung et al. [5] have considered the entrance region for the case of a fluid with temperature variable properties, while Tsou and Gau [6] have analyzed how important changes of the fluid properties may influence the temperature field, the Nusselt number, and the friction factor in the case of low wall heating rates. It must be pointed out that most of the studies on mixed convection refer to axisymmetric boundary conditions even if, in practice, this is sometimes a nonrealistic assumption. In fact, there are several technical cases in which the duct wall temperature and the duct wall heat flux depend on the azimuthal angular coordinate. In the design of heat exchangers where special flow configurations such as cross flow occur, nonuniform circumferential wall temperature distributions arise. Moreover, absence of axial symmetry in the thermal boundary conditions may occur in the thermal control of ducts for transport of water, gas, or hydrocarbons that are partially buried either in the soil or in a wall. With reference to the case of mixed convection in circular ducts, first Reynolds [7] and later Choi and Choi [8] have considered thermal boundary conditions that do not fulfill axial symmetry. Recently, Barletta et al. [9] have analytically studied the free and forced convection in a vertical tube subjected to a wall temperature that is uniform along the axial direction and is an arbitrary function of the angular coordinate. With reference to annular ducts, Sutherland and Kays [10] have studied the forced convection regime for either laminar or turbulent flow. They considered wall heat flux distributions that are uniform in the axial direction but nonaxisymmetric.

In the present paper, the fully developed and steady-state laminar mixed convection in a vertical duct with annular cross section is studied. Nonaxisymmetric thermal boundary conditions such that temperature does not change in the axial direction are considered. The Boussinesq approximation is invoked and the average temperature in the duct section is chosen as the reference temperature. Moreover, the effect of viscous dissipation is considered as negligible. The local momentum and energy balance equations are written in a dimensionless form and solved analytically by employing the Fourier series expansions of both the temperature field and the velocity field. The analytical expressions of the dimensionless temperature field, of the dimensionless velocity field, and of the Fanning friction factor are determined. It is shown that the governing dimensionless parameters are the ratio between the Grashof number Gr and the Reynolds number Re, as well as the ratio between the inner radius and the outer radius of the duct. To illustrate the general solution, two particular cases are considered: first, the case of an annular duct with the outer wall isothermal and the inner wall half adiabatic and half subjected to a uniform heat flux distribution. Then, the opposite case of an annulus with the inner wall isothermal and the outer wall half adiabatic and half subjected to a uniform heat flux distribution is analyzed. Finally, for both cases, the threshold values of the ratio Gr/Re for the onset of flow reversal are determined as a function of the duct aspect ratio.

Technical Interest of Buoyancy-Induced Flow with No Axial Fluid Heating

The class of thermal boundary conditions considered in the present paper include all of the cases such that the temperature field does not change in the axial direction. This constraint implies that, in the fully developed region, the heat transfer in the fluid is due to pure conduction and no convection in the streamwise direction occurs. Several authors [4,11–15] have analyzed mixed convection problems under the same constraint. Obviously, the practical interest of thermal boundary conditions that do not yield a net fluid heating in the streamwise direction does not rely on the possibility to enhance the heat transfer of the fluid. In fact, if the fluid does not experience a net streamwise heating or cooling, the heat transfer coefficient coincides with that of pure conduction. However, even if the buoyancy does not influence the fluid temperature distribution, it can significantly change both the velocity distribution and the value of the Fanning friction factor. Strong modifications of the velocity distribution occur when flow reversal phenomena arise, i.e., when there exist regions in the duct where the fluid velocity has a direction opposite to the mean flow. Under

---

Contributed by the Heat Transfer Division for publication in the JOURNAL OF HEAT TRANSFER. Manuscript received November 13, 2004; revision received November 25, 2004. Review conducted by: V. Dhir.

Copyright © 2005 by ASME

Downloaded 06 Dec 2010 to 193.140.21.150. Redistribution subject to ASME license or copyright; see http://www.asme.org/terms/Terms_Use.cfm

conditions of flow reversal, the influence of buoyancy on the value of the friction factor can be very important. In these cases, the head loss in the duct becomes quite different from that evaluated for isothermal flow. This effect has been pointed out, for instance, in [4] with reference to an annular duct with axisymmetric thermal boundary conditions and in [15] with reference to a rectangular duct. Buoyancy-induced changes of head losses in ducts can have interesting applications in the regulation of flow rates in ducts. Indeed, by adjusting the thermal boundary conditions of the fluid, and hence the buoyancy effect, one can increase or decrease the head loss in the duct, thus producing a "thermal pump" behavior, if head losses decrease, or a "thermal valve" behavior, if head losses increase.

Description of the Problem

With reference to Fig. 1, let us consider a vertical duct with annular cross section. Let the inner and outer radiuses be R_1 and R_2, respectively. The steady-state laminar flow of a Newtonian fluid is considered. Moreover, let the flow be parallel to the X-axis, so that the velocity vector $\mathbf{U}$ can be expressed as $\mathbf{U}=U\mathbf{X}$. By employing the Boussinesq approximation, $\mathbf{U}$ is a solenoidal field and, as a consequence, $\partial U/\partial X=0$. Therefore, the flow is fully developed and $U=U(R,\vartheta)$.

If a linear equation of state is considered and the average fluid temperature T_0 in a duct cross section is chosen as the reference temperature [16], the momentum balance equations along X, R, and ϑ can be written as

$$-\frac{\partial P}{\partial X}+\varrho_0 g\beta(T-T_0)+\mu\left(\frac{\partial^2 U}{\partial R^2}+\frac{1}{R}\frac{\partial U}{\partial R}+\frac{1}{R^2}\frac{\partial^2 U}{\partial \vartheta^2}\right)=0, \tag{1}$$

$$-\frac{\partial P}{\partial R}=0, \tag{2}$$

$$-\frac{1}{R}\frac{\partial P}{\partial \vartheta}=0, \tag{3}$$

where ρ_0 is the fluid mass density evaluated for $T=T_0$, and $P=p+\varrho_0 gX$ is the difference between the pressure and the hydrostatic pressure. Equations (2) and (3) show that P depends only on X.

Let the thermal boundary conditions be such that there is no net fluid heating in the axial direction, i.e., $\partial T/\partial X=0$. Therefore, $T=T(R,\vartheta)$, so that both the reference temperature T_0 and $\mathrm{d}P/\mathrm{d}X$ result to be constants.

If one considers the effect of viscous dissipation as negligible, one can write the energy balance equation as

$$\frac{\partial^2 T}{\partial R^2}+\frac{1}{R}\frac{\partial T}{\partial R}+\frac{1}{R^2}\frac{\partial^2 T}{\partial \vartheta^2}=0. \tag{4}$$

Equations (1) and (4) can be written in the following dimensionless form:

$$\frac{\mathrm{Gr}}{\mathrm{Re}}t+\lambda+4(1-\gamma)^2\left(\frac{\partial^2 u}{\partial r^2}+\frac{1}{r}\frac{\partial u}{\partial r}+\frac{1}{r^2}\frac{\partial^2 u}{\partial \vartheta^2}\right)=0, \tag{5}$$

$$\frac{\partial^2 t}{\partial r^2}+\frac{1}{r}\frac{\partial t}{\partial r}+\frac{1}{r^2}\frac{\partial^2 t}{\partial \vartheta^2}=0, \tag{6}$$

where

$$t=\frac{T-T_0}{\Delta T},\quad u=\frac{U}{U_0},$$

$$r=\frac{R}{R_2},\quad \gamma=\frac{R_1}{R_2},\quad \lambda=-\frac{4(R_2-R_1)^2}{\mu U_0}\frac{\mathrm{d}P}{\mathrm{d}X},$$

$$\mathrm{Re}=\frac{2(R_2-R_1)U_0}{\nu},\quad \mathrm{Gr}=\frac{8g\beta\Delta T(R_2-R_1)^3}{\nu^2}. \tag{7}$$

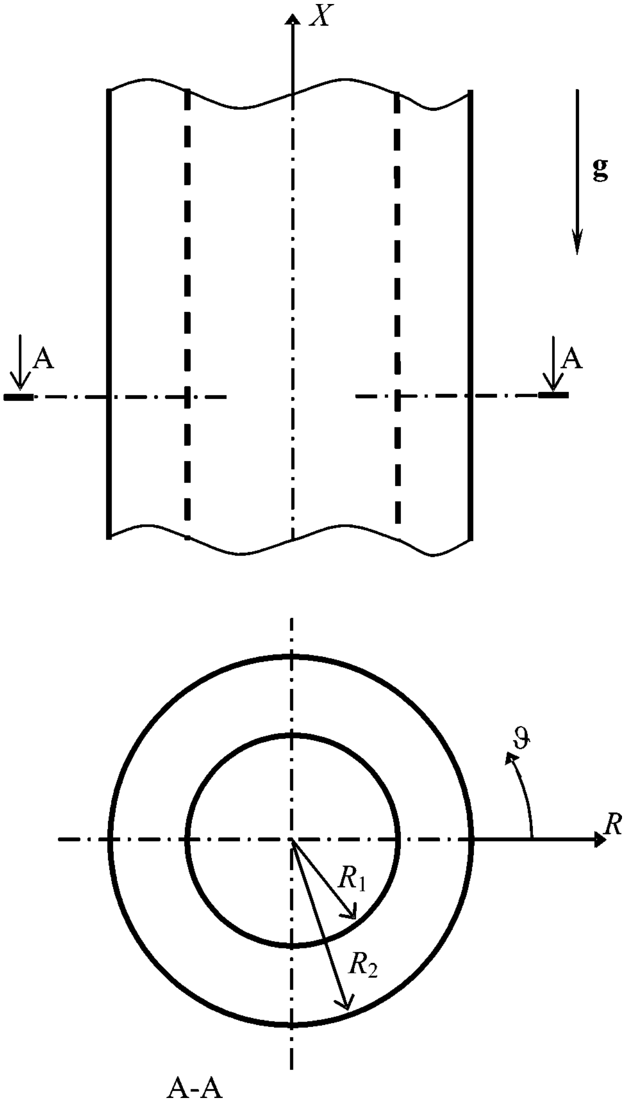

Fig. 1 Vertical annular duct and coordinate axes

In Eq. (7), U_0 is the average velocity in a duct section and ΔT is a reference temperature difference. Obviously, since $U=U(R,\vartheta)$, U_0 is a constant. Let us assume ΔT to be a positive quantity, so that positive values of Gr/Re imply positive values of U_0 (upward flow), while negative values of Gr/Re imply negative values of U_0 (downward flow).

The dimensionless no-slip conditions at the walls are

$$u(\gamma,\vartheta)=0,\quad u(1,\vartheta)=0. \tag{8}$$

Finally, if one writes the expressions of T_0 and U_0 in a dimensionless form, one obtains the following constraints on the dimensionless fields $t(r,\vartheta)$ and $u(r,\vartheta)$:

$$\int_0^{2\pi}\mathrm{d}\vartheta\int_\gamma^1 \mathrm{d}r\,t\,r=0, \tag{9}$$

$$\int_0^{2\pi}\mathrm{d}\vartheta\int_\gamma^1 \mathrm{d}r\,u\,r=\pi(1-\gamma^2). \tag{10}$$

Analytical Solution

As shown by Eqs. (5) and (6), one can first determine the dimensionless temperature field and then the dimensionless velocity

Downloaded 06 Dec 2010 to 193.140.21.150. Redistribution subject to ASME license or copyright; see http://www.asme.org/terms/Terms_Use.cfm

field. Moreover, since the function $t(r,\vartheta)$ is continuous for $\gamma \leqslant r < 1$ and $0 \leqslant \vartheta < 2\pi$, it can be expanded as a Fourier series with respect to the variable ϑ, as follows:

$$t(r,\vartheta)=\frac{a_0(r)}{2}+\sum_{n=1}^{\infty}\left[a_n(r)\sin(n\vartheta)+b_n(r)\cos(n\vartheta)\right]. \tag{11}$$

If one substitutes Eq. (11) in Eq. (6), one has

$$\frac{1}{2}\left(\frac{\mathrm{d}^2a_0}{\mathrm{d}r^2}+\frac{1}{r}\frac{\mathrm{d}a_0}{\mathrm{d}r}\right)+\sum_{n=1}^{\infty}\left[\left(\frac{\mathrm{d}^2a_n}{\mathrm{d}r^2}+\frac{1}{r}\frac{\mathrm{d}a_n}{\mathrm{d}r}-\frac{n^2}{r^2}a_n\right)\sin(n\vartheta) + \left(\frac{\mathrm{d}^2b_n}{\mathrm{d}r^2}+\frac{1}{r}\frac{\mathrm{d}b_n}{\mathrm{d}r}-\frac{n^2}{r^2}b_n\right)\cos(n\vartheta)\right]=0. \tag{12}$$

The unknown function $a_0(r)$ can be determined by means of Eqs. (9) and (12). In fact, if one integrates Eq. (12) with respect to ϑ in the range $[0,2\pi]$ and then takes into account the constraint given by Eq. (9), one obtains

$$a_0(r)=\left[\frac{2(1-\gamma^2)}{1-\gamma^2+2\gamma^2\ln\gamma}\ln r+1\right]A_0, \tag{13}$$

where A_0 is an integration constant.

On the other hand, the unknown functions $a_n(r)$ and $b_n(r)$ can be determined by multiplying Eq. (12), respectively, by $\sin(m\vartheta)$ and $\cos(m\vartheta)$, where m is an arbitrary positive integer, and then integrating with respect to ϑ in the range $[0,2\pi]$. By employing the orthogonality relations of trigonometric functions, one obtains the following expressions:

$$a_n(r)=A_n^{(1)}r^n+A_n^{(2)}r^{-n}, \tag{14}$$

$$b_n(r)=B_n^{(1)}r^n+B_n^{(2)}r^{-n}, \tag{15}$$

where $A_n^{(1)}$, $A_n^{(2)}$, $B_n^{(1)}$, and $B_n^{(2)}$ are integration constants. By means of Eqs. (13)–(15), Eq. (11) becomes

$$t(r,\vartheta)=\left[\frac{2(1-\gamma^2)}{1-\gamma^2+2\gamma^2\ln\gamma}\ln r+1\right]\frac{A_0}{2}+\sum_{n=1}^{\infty}\left[(A_n^{(1)}r^n+A_n^{(2)}r^{-n})\sin(n\vartheta)+(B_n^{(1)}r^n+B_n^{(2)}r^{-n})\cos(n\vartheta)\right], \tag{16}$$

which represents the dimensionless temperature distribution in a duct section. The integration constants that appear in Eq. (16) are determined by the thermal boundary conditions.

The dimensionless velocity distribution can be obtained in a similar way. In fact, the function $u(r,\vartheta)$ is continuous for $\gamma \leqslant r < 1$ and $0 \leqslant \vartheta < 2\pi$, so that it can be expanded as a Fourier series with respect to the variable ϑ, as follows

$$u(r,\vartheta)=\frac{c_0(r)}{2}+\sum_{n=1}^{\infty}\left[c_n(r)\sin(n\vartheta)+h_n(r)\cos(n\vartheta)\right]. \tag{17}$$

By substituting Eqs. (16) and (17) in Eq. (5), one obtains

$$\begin{aligned}&\frac{1}{2}(1-\gamma)^2\left(\frac{\mathrm{d}^2c_0}{\mathrm{d}r^2}+\frac{1}{r}\frac{\mathrm{d}c_0}{\mathrm{d}r}\right)+\frac{\lambda}{4} + \frac{A_0}{8}\frac{\mathrm{Gr}}{\mathrm{Re}}\left[\frac{2(1-\gamma^2)}{1-\gamma^2+2\gamma^2\ln\gamma}\ln r+1\right]\\ &+\sum_{n=1}^{\infty}\left[(1-\gamma)^2\left(\frac{\mathrm{d}^2c_n}{\mathrm{d}r^2}+\frac{1}{r}\frac{\mathrm{d}c_n}{\mathrm{d}r}-\frac{n^2}{r^2}c_n\right)+\frac{1}{4}\frac{\mathrm{Gr}}{\mathrm{Re}}(A_n^{(1)}r^n+A_n^{(2)}r^{-n})\right]\sin(n\vartheta)\\ &+\sum_{n=1}^{\infty}\left[(1-\gamma)^2\left(\frac{\mathrm{d}^2h_n}{\mathrm{d}r^2}+\frac{1}{r}\frac{\mathrm{d}h_n}{\mathrm{d}r}-\frac{n^2}{r^2}h_n\right)+\frac{1}{4}\frac{\mathrm{Gr}}{\mathrm{Re}}(B_n^{(1)}r^n+B_n^{(2)}r^{-n})\right]\cos(n\vartheta)=0.\end{aligned} \tag{18}$$

Moreover, by substituting Eq. (17) in Eq. (8), one obtains

$$\frac{c_0(\gamma)}{2}+\sum_{n=1}^{\infty}\left[c_n(\gamma)\sin(n\vartheta)+h_n(\gamma)\cos(n\vartheta)\right]=0, \tag{19}$$

$$\frac{c_0(1)}{2}+\sum_{n=1}^{\infty}\left[c_n(1)\sin(n\vartheta)+h_n(1)\cos(n\vartheta)\right]=0. \tag{20}$$

The unknown functions $c_0(r)$, $c_n(r)$, and $h_n(r)$ can be determined by multiplying Eqs. (18)–(20), respectively, by 1, $\sin(m\vartheta)$, and $\cos(m\vartheta)$, where m is an arbitrary positive integer, and then integrating with respect to ϑ in the range $[0,2\pi]$. By employing the orthogonality relations of trigonometric functions, one obtains the following expressions:

$$\begin{aligned}c_0(r)=&\left\{(1-r^2)\ln\gamma\left[(1-\gamma^2)\left(2\lambda-A_0\frac{\mathrm{Gr}}{\mathrm{Re}}\right)+2\gamma^2\ln\gamma\left(2\lambda+A_0\frac{\mathrm{Gr}}{\mathrm{Re}}\right)\right]\right.\\ &\left.-(1-\gamma^2)\ln r\left[(1-\gamma^2)\left(2\lambda-A_0\frac{\mathrm{Gr}}{\mathrm{Re}}\right)+2\ln\gamma\left(2\gamma^2\lambda+A_0\frac{\mathrm{Gr}}{\mathrm{Re}}r^2\right)\right]\right\}\\ &\times\left[16\ln\gamma(1-\gamma)^2(1-\gamma^2+2\gamma^2\ln\gamma)\right]^{-1},\end{aligned} \tag{21}$$

$$\begin{aligned}c_1(r)=&\frac{\mathrm{Gr}}{\mathrm{Re}}\{(1-r^2)[A_1^{(1)}(r^2-\gamma^2)(1-\gamma^2)+4A_1^{(2)}\gamma^2\ln\gamma]\\ &-4A_1^{(2)}r^2(1-\gamma^2)\ln r\}[32r(1-\gamma)^3(\gamma+1)]^{-1},\end{aligned} \tag{22}$$

$$\begin{aligned}c_n(r)=&\frac{\mathrm{Gr}}{\mathrm{Re}}\{A_n^{(1)}(n-1)[r^{2n}(1-r^2)-\gamma^{2n}(1-\gamma^2)\\ &+(\gamma r)^{2n}(r^2-\gamma^2)]+A_n^{(2)}(n+1)[\gamma^{2n}-\gamma^2+r^2(1-\gamma^{2n})\\ &-r^{2n}(1-\gamma^2)]\}\times[16r^n(n^2-1)(1-\gamma)^2(1-\gamma^{2n})]^{-1}\\ &\text{for } n>1,\end{aligned} \tag{23}$$

$$\begin{aligned}h_1(r)=&\frac{\mathrm{Gr}}{\mathrm{Re}}\{(1-r^2)[B_1^{(1)}(r^2-\gamma^2)(1-\gamma^2)+4B_1^{(2)}\gamma^2\ln\gamma]\\ &-4B_1^{(2)}r^2(1-\gamma^2)\ln r\}[32r(1-\gamma)^3(\gamma+1)]^{-1},\end{aligned} \tag{24}$$

$$\begin{aligned}h_n(r)=&\frac{\mathrm{Gr}}{\mathrm{Re}}\{B_n^{(1)}(n-1)[r^{2n}(1-r^2)-\gamma^{2n}(1-\gamma^2)\\ &+(\gamma r)^{2n}(r^2-\gamma^2)]+B_n^{(2)}(n+1)[\gamma^{2n}-\gamma^2+r^2(1-\gamma^{2n})\\ &-r^{2n}(1-\gamma^2)]\}\times[16r^n(n^2-1)(1-\gamma)^2(1-\gamma^{2n})]^{-1}\\ &\text{for } n>1.\end{aligned} \tag{25}$$

Then, Eq. (10) can be used in order to determine the value of the parameter λ. Indeed, Eqs. (10), (17), and (21) yield

$$\lambda=\lambda^{(1)}(\gamma)+\frac{\mathrm{Gr}}{\mathrm{Re}}\lambda^{(2)}(\gamma)A_0, \tag{26}$$

where

$$\lambda^{(1)}(\gamma)=\frac{32(1-\gamma)^2\ln\gamma}{1-\gamma^2+(1+\gamma^2)\ln\gamma}, \tag{27}$$

Downloaded 06 Dec 2010 to 193.140.21.150. Redistribution subject to ASME license or copyright; see http://www.asme.org/terms/Terms_Use.cfm

$$\lambda^{(2)}(\gamma)=\frac{2(1-\gamma^2)^2+(1-\gamma^4-4\gamma^2\ln\gamma)\ln\gamma}{4(1-\gamma^2+2\gamma^2\ln\gamma)[1-\gamma^2+(1+\gamma^2)\ln\gamma]}. \tag{28}$$

On account of Eqs. (17) and (21)–(28), the dimensionless velocity distribution can be expressed as

$$u(r,\vartheta)=u^{(1)}(r)+\frac{\mathrm{Gr}}{\mathrm{Re}}u^{(2)}(r,\vartheta), \tag{29}$$

where

$$u^{(1)}(r)=\frac{2[(1-r^2)\ln\gamma-(1-\gamma^2)\ln r]}{1-\gamma^2+(1+\gamma^2)\ln\gamma} \tag{30}$$

$$\begin{aligned}u^{(2)}(r,\vartheta)=A_0\{&(1-\gamma^2)[1-\gamma^4-4r^2(1-\gamma^2)-4r^2\ln\gamma\\&+4\gamma^2\ln\gamma(1-r^2)]\ln r-(1-r^2)(1-4\gamma^2+3\gamma^4\\&-4\gamma^4\ln\gamma)\ln\gamma\}\times\{64(1-\gamma)^2(1-\gamma^2+2\gamma^2\ln\gamma)\\&\times[1-\gamma^2+(1+\gamma^2)\ln\gamma]\}^{-1}+\sum_{n=1}^{\infty}[C_n(r)\sin(n\vartheta)\\&+H_n(r)\cos(n\vartheta)].\end{aligned} \tag{31}$$

In Eq. (31), $C_n(r)$ and $H_n(r)$ are given by

$$C_n(r)=\frac{\mathrm{Re}}{\mathrm{Gr}}c_n(r),\quad H_n(r)=\frac{\mathrm{Re}}{\mathrm{Gr}}h_n(r). \tag{32}$$

It can be observed that the term $u^{(1)}(r)$ represents the dimensionless velocity distribution for the forced convection regime. In fact, on account of Eqs. (29)–(32), in the limit of forced convection, i.e., for Gr/Re→0, $u(r,\vartheta)$ tends to $u^{(1)}(r)$. Moreover, let us define a modified dimensionless velocity $u^*(r,\vartheta)$ as

$$u^*(r,\vartheta)=\frac{\mathrm{Re}}{\mathrm{Gr}}u(r,\vartheta)=\frac{\nu U(R,\vartheta)}{4g\beta\Delta T(R_2-R_1)^2}. \tag{33}$$

Then, it can be observed that the term $u^{(2)}(r,\vartheta)$ represents the modified dimensionless velocity distribution for the natural convection regime. In fact, on account of Eqs. (29)–(33), in the limit of purely buoyancy-driven flow, i.e., for Gr/Re→∞, $u^*(r,\vartheta)$ tends to $u^{(2)}(r,\vartheta)$.

As is well known, the Fanning friction factor f is defined as

$$f=\frac{2\tau_w}{\varrho_0U_0^2}, \tag{34}$$

where the average wall shear stress τ_w is given by

$$\tau_w=\frac{\mu}{2\pi(R_1+R_2)}\left(R_1\int_0^{2\pi}\frac{\partial U}{\partial R}\bigg|_{R=R_1}\mathrm{d}\vartheta-R_2\int_0^{2\pi}\frac{\partial U}{\partial R}\bigg|_{R=R_2}\mathrm{d}\vartheta\right). \tag{35}$$

By means of Eqs. (7), (34) and (35), one obtains

$$f\,\mathrm{Re}=\frac{2(1-\gamma)}{\pi(1+\gamma)}\left(\gamma\int_0^{2\pi}\frac{\partial u}{\partial r}\bigg|_{r=\gamma}\mathrm{d}\vartheta-\int_0^{2\pi}\frac{\partial u}{\partial r}\bigg|_{r=1}\mathrm{d}\vartheta\right). \tag{36}$$

If one integrates both sides of Eq. (5) with respect to r and ϑ on the whole annular cross section, one is led to the expression

$$\lambda\pi(1+\gamma)+4(1-\gamma)\left(-\gamma\int_0^{2\pi}\frac{\partial u}{\partial r}\bigg|_{r=\gamma}\mathrm{d}\vartheta+\int_0^{2\pi}\frac{\partial u}{\partial r}\bigg|_{r=1}\mathrm{d}\vartheta\right)=0. \tag{37}$$

Equations (36) and (37) yield the relation

$$f\,\mathrm{Re}=\frac{\lambda}{2}. \tag{38}$$

To summarize, the solution obtained in this section shows that the buoyancy forces do not affect the dimensionless temperature distribution. On the other hand, the dimensionless velocity distribution, the dimensionless pressure drop parameter λ, and the Fanning friction factor f depend on Gr/Re.

In the following sections, the general solution obtained above will be applied to a couple of special cases. In particular, the examples refer to thermal boundary conditions in which one wall is isothermal and the other wall is half adiabatic and half subjected to a uniform heat flux distribution.

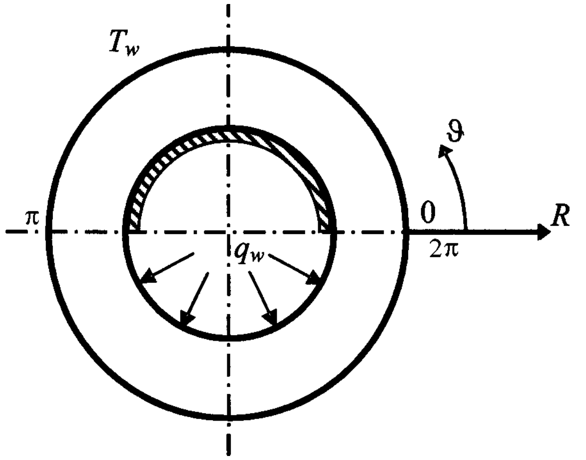

Fig. 2 First example: section of the annular duct with prescribed thermal boundary conditions

First Example

With reference to Fig. 2, let us consider the case of an annular duct with the outer wall isothermal and the inner wall half adiabatic and half subjected to a uniform inward heat flux distribution. The thermal boundary conditions can be expressed as

$$-\frac{\partial T}{\partial R}\bigg|_{R=R_1}=\frac{q_w}{k}F(\vartheta), \tag{39}$$

$$T(R_2,\vartheta)=T_w, \tag{40}$$

where q_w is a positive arbitrary inward heat flux at the inner wall, T_w is a positive arbitrary temperature at the outer wall, and $F(\vartheta)$ is a step function defined as

$$\begin{aligned}&F(\vartheta)=0\ \text{ if }\ 0<\vartheta<\pi,\\&F(\vartheta)=1\ \text{ if }\ \pi<\vartheta<2\pi.\end{aligned} \tag{41}$$

By defining the quantities

$$\Delta T=\frac{R_1q_w}{k},\quad t_w=\frac{T_w-T_0}{\Delta T}, \tag{42}$$

on account of Eqs. (7) and (42), Eqs. (39) and (40) can be written in the following dimensionless form:

$$-\frac{\partial t}{\partial r}\bigg|_{r=\gamma}=F(\vartheta), \tag{43}$$

$$t(1,\vartheta)=t_w. \tag{44}$$

Equations (16), (43), and (44) yield

$$A_0=-\frac{\gamma(1-\gamma^2+2\gamma^2\ln\gamma)}{2(1-\gamma^2)}, \tag{45}$$

$$A_n^{(1)}=\frac{[1-(-1)^n]\gamma^{1+n}}{n^2\pi(1+\gamma^{2n})},\quad A_n^{(2)}=-A_n^{(1)}, \tag{46}$$

Downloaded 06 Dec 2010 to 193.140.21.150. Redistribution subject to ASME license or copyright; see http://www.asme.org/terms/Terms_Use.cfm

$$B_n^{(1)}=0=B_n^{(2)}, \tag{47}$$

$$t_w=\frac{A_0}{2}. \tag{48}$$

On account of Eqs. (16) and (45)–(47), the dimensionless temperature distribution is

$$t(r,\vartheta)=-\frac{\gamma}{4}\left(1+2\ln r+\frac{2\gamma^2\ln\gamma}{1-\gamma^2}\right)-\frac{2}{\pi}\sum_{n=1}^{\infty}\frac{[1-r^{2(2n-1)}]\gamma^{2n}\sin[(2n-1)\vartheta]}{(2n-1)^2r^{2n-1}[1+\gamma^{2(2n-1)}]}. \tag{49}$$

On the other hand, as a consequence of Eqs. (22)–(25), (31), (32), and (45)–(47), the buoyancy-induced dimensionless velocity term $u^{(2)}$ can be easily evaluated.

On account of Eqs. (26)–(28), (38), and (45), one obtains the following expression of the Fanning friction factor:

$$f\,\mathrm{Re}=\frac{16(1-\gamma)^2\ln\gamma}{1-\gamma^2+(1+\gamma^2)\ln\gamma}-\frac{\mathrm{Gr}}{\mathrm{Re}}\,\frac{\gamma[2(1-\gamma^2)^2+(1-4\gamma^2\ln\gamma-\gamma^4)\ln\gamma]}{16[(1-\gamma^2)^2+(1-\gamma^4)\ln\gamma]}. \tag{50}$$

It can be observed that, for upward flow, there exists a positive real number $(\mathrm{Gr/Re})_{FRup}$ such that flow reversal occurs when $\mathrm{Gr/Re}>(\mathrm{Gr/Re})_{FRup}$. As can be easily verified by plotting the dimensionless temperature distribution $t(r,\vartheta)$ for a fixed value of γ, the fluid is hotter close to the internal wall, for $\vartheta=3\pi/2$, and cooler close to the external wall, for $\vartheta=\pi/2$. Therefore, for $\mathrm{Gr/Re}=(\mathrm{Gr/Re})_{FRup}$, the first derivative of $u(r,\vartheta)$ evaluated for $r=1$ and $\vartheta=\pi/2$ vanishes, so that

$$\left(\frac{\mathrm{Gr}}{\mathrm{Re}}\right)_{FRup}=-\left.\frac{\mathrm{d}u^{(1)}}{\mathrm{d}r}\right|_{r=1}\left(\left.\frac{\partial u^{(2)}}{\partial r}\right|_{r=1,\vartheta=\pi/2}\right)^{-1}. \tag{51}$$

Similarly, for downward flow, flow reversal occurs when $\mathrm{Gr/Re}<(\mathrm{Gr/Re})_{FRdw}$, where

$$\left(\frac{\mathrm{Gr}}{\mathrm{Re}}\right)_{FRdw}=-\left.\frac{\mathrm{d}u^{(1)}}{\mathrm{d}r}\right|_{r=\gamma}\left(\left.\frac{\partial u^{(2)}}{\partial r}\right|_{r=\gamma,\vartheta=3\pi/2}\right)^{-1}. \tag{52}$$

Obviously, $(\mathrm{Gr/Re})_{FRdw}$ is a negative real number. By means of Eqs. (51) and (52), one can evaluate both $(\mathrm{Gr/Re})_{FRup}$ and $(\mathrm{Gr/Re})_{FRdw}$, namely,

$$\left(\frac{\mathrm{Gr}}{\mathrm{Re}}\right)_{FRup}=\frac{2(1-\gamma^2+2\ln\gamma)}{1-\gamma^2+(1+\gamma^2)\ln\gamma}\times\left\{\frac{\gamma^2[1-\gamma^4+4\gamma^2\ln\gamma]}{8\pi(1-\gamma)^3(1+\gamma)(1+\gamma^2)}+\frac{\gamma[(3-\gamma^2)(1-\gamma^2)^2+2\ln\gamma(1+2\gamma^2-3\gamma^4+4\gamma^4\ln\gamma)]}{128(1-\gamma)^3(1+\gamma)[1-\gamma^2+(1+\gamma^2)\ln\gamma]}+\frac{1}{8\pi(1-\gamma)^2}\sum_{n=2}^{\infty}(-1)^n\frac{\gamma^{2(1+3n)}[(n-1)\gamma^2-n]+\gamma^{2(n+2)}[1-n(1-\gamma^2)]}{n(n-1)(2n-1)(\gamma^4-\gamma^{8n})}\right\}^{-1}, \tag{53}$$

$$\left(\frac{\mathrm{Gr}}{\mathrm{Re}}\right)_{FRdw}=\frac{2(1-\gamma^2+2\gamma^2\ln\gamma)}{\gamma[1-\gamma^2+(1+\gamma^2)\ln\gamma]}\times\left\{-\frac{\gamma^2(3-4\gamma^2+\gamma^4+4\ln\gamma)}{8\pi(1-\gamma)^3(1+\gamma)(1+\gamma^2)}-\frac{1-5\gamma^2+7\gamma^4-3\gamma^6-2\gamma^2\ln\gamma(3-2\gamma^2-\gamma^4+4\ln\gamma)}{128(1-\gamma)^3(\gamma+1)[1-\gamma^2+(1+\gamma^2)\ln\gamma]}+\frac{1}{8\pi(1-\gamma)^2}\sum_{n=2}^{\infty}(-1)^n\frac{(n-1)\gamma^{2(1+4n)}-n\gamma^6+\gamma^{2(1+2n)}[1+4n(n-1)(1-\gamma^2)]}{n(n-1)(2n-1)^2(\gamma^4-\gamma^{8n})}\right\}^{-1}. \tag{54}$$

Since the series that appear in Eqs. (53) and (54) have a fast convergence, the values of $(\mathrm{Gr/Re})_{FRup}$ and $(\mathrm{Gr/Re})_{FRdw}$ can be determined with six-digit accuracy by means of less than 500 terms. In Table 1, the values of $(\mathrm{Gr/Re})_{FRup}$ and $(\mathrm{Gr/Re})_{FRdw}$ are reported for some values of γ.

A drawing of the regions of flow reversal in the plane (γ, Gr/Re) is given in Fig. 3. It can be easily proved that, either for upward flow or downward flow, both in the limiting case $\gamma\to 0$ and in the limiting case $\gamma\to 1$, the threshold values $(\mathrm{Gr/Re})_{FRup}$ and $(\mathrm{Gr/Re})_{FRdw}$ tend to infinity, i.e., flow reversal never occurs.

Table 1 First example: threshold values of the ratio Gr/Re for the onset of flow reversal

γ	$(\mathrm{Gr/Re})_{FR\,up}$	$(\mathrm{Gr/Re})_{FR\,dw}$
0.1	3129.51	−1797.14
0.2	1463.78	−771.415
0.3	970.208	−505.825
0.4	775.387	−410.277
0.5	710.355	−384.613
0.6	732.284	−406.222
0.7	849.159	−481.876
0.8	1142.49	−661.746
0.9	2082.91	−1228.95

Moreover, on account of Eq. (50), one can conclude that negative values of the dimensionless pressure drop parameter λ and of $f\,\mathrm{Re}$ can hardly be reached. In fact, one can conclude that in order to obtain $\lambda<0$ (and $f\,\mathrm{Re}<0$), one should consider values of Gr/Re greater than 7000, i.e., values exceedingly high, probably characterized by flow instability.

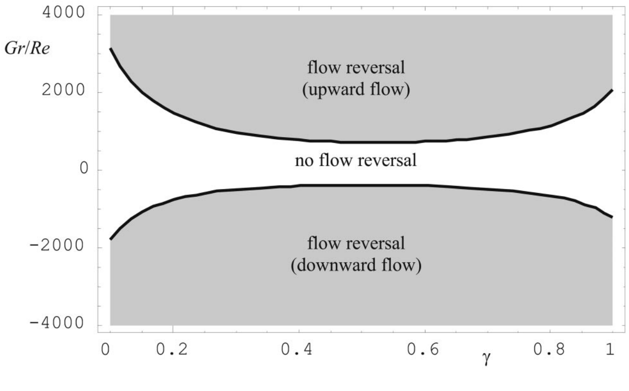

Fig. 3 Flow reversal regions as a function of γ

Downloaded 06 Dec 2010 to 193.140.21.150. Redistribution subject to ASME license or copyright; see http://www.asme.org/terms/Terms_Use.cfm

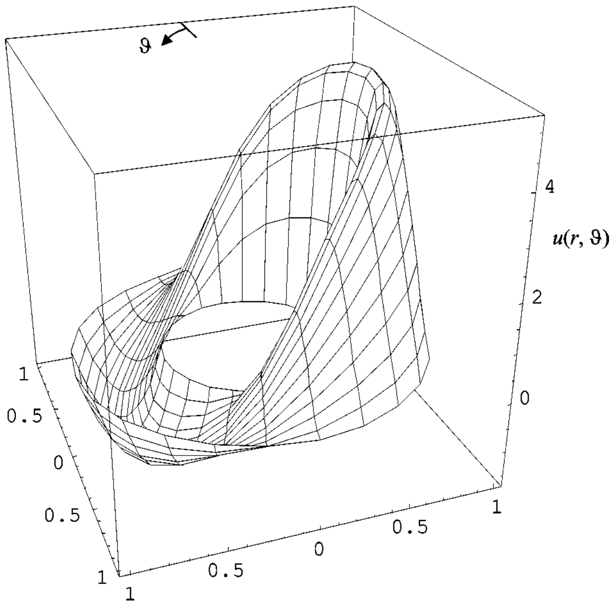

Fig. 4 Three-dimensional plot of the dimensionless velocity distribution $u(r,\vartheta)$, for $\gamma=0.5$ and Gr/Re=1500

In Fig. 4, the dimensionless velocity distribution $u(r,\vartheta)$ is plotted for $\gamma=0.5$ and Gr/Re=1500, i.e., for the case of upward flow. The figure reveals that, for the considered value of Gr/Re, which is greater than $(\mathrm{Gr/Re})_{FRup}$, strong deformations with respect to the isothermal velocity distribution occur. In particular, negative values of u are present in the region where the fluid is cooler (flow reversal).

Second Example

Let us consider an annular duct with the inner wall isothermal and the outer wall half adiabatic and half subjected to a uniform inward heat flux distribution (see Fig. 5). The thermal boundary conditions are expressed as

$$T(R_1,\vartheta)=T_w, \tag{55}$$

$$\left.\frac{\partial T}{\partial R}\right|_{R=R_2}=\frac{q_w}{k}F(\vartheta). \tag{56}$$

By defining the quantities

$$\Delta T=\frac{R_2 q_w}{k}, \quad t_w=\frac{T_w-T_0}{\Delta T}, \tag{57}$$

on account of Eqs. (7) and (57), Eqs. (55) and (56) can be written in the following dimensionless form:

$$t(\gamma,\vartheta)=t_w, \tag{58}$$

$$\left.\frac{\partial t}{\partial r}\right|_{r=1}=F(\vartheta). \tag{59}$$

Equations (16), (58), and (59) yield

$$A_0=\frac{1-\gamma^2+2\gamma^2\ln\gamma}{2(1-\gamma^2)}, \tag{60}$$

$$A_n^{(1)}=\frac{-1+(-1)^n}{n^2\pi(1+\gamma^{2n})}, \quad A_n^{(2)}=-\gamma^{2n}A_n^{(1)}, \tag{61}$$

$$B_n^{(1)}=B_n^{(2)}=0, \tag{62}$$

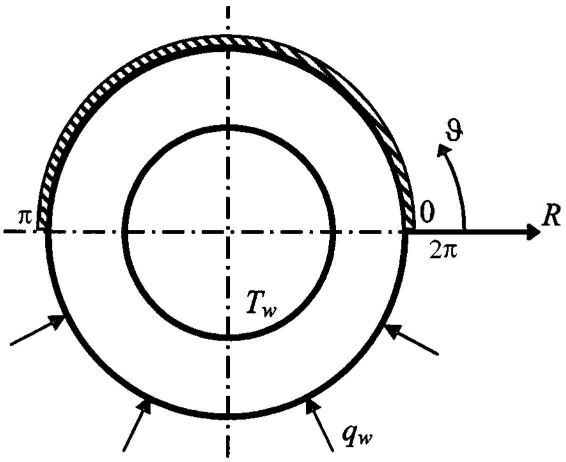

Fig. 5 Second example: section of the annular duct with prescribed thermal boundary conditions

$$t_w=\frac{1-\gamma^2+2\ln\gamma}{4(1-\gamma^2)}. \tag{63}$$

On account of Eqs. (16) and (60)–(62), the dimensionless temperature distribution is

$$t(r,\vartheta)=\frac{1}{4}\left(1+2\ln r+\frac{2\gamma^2\ln\gamma}{1-\gamma^2}\right)-\frac{2}{\pi}\sum_{n=1}^{\infty}\frac{[r^{2(2n-1)}-\gamma^{2(2n-1)}]\sin[(2n-1)\vartheta]}{(2n-1)^2r^{2n-1}[1+\gamma^{2(2n-1)}]}. \tag{64}$$

By employing Eqs. (22)–(25), (31), (32), and (60)–(62), the buoyancy-induced dimensionless velocity term $u^{(2)}$ can be easily obtained.

As a consequence of Eqs. (26)–(28), (38), and (60), the Fanning friction factor is given by

$$f\,\mathrm{Re}=\frac{16(1-\gamma)^2\ln\gamma}{1-\gamma^2+(1+\gamma^2)\ln\gamma}+\frac{\mathrm{Gr}}{\mathrm{Re}}\,\frac{2(1-\gamma^2)^2+(1-4\gamma^2\ln\gamma-\gamma^4)\ln\gamma}{16[(1-\gamma^2)^2+(1-\gamma^4)\ln\gamma]}. \tag{65}$$

As in the example discussed in the preceding section, for upward flow, there exists a positive real number $(\mathrm{Gr/Re})_{FRup}$ such that flow reversal occurs when $\mathrm{Gr/Re}>(\mathrm{Gr/Re})_{FRup}$. On account of Eq. (29), one obtains

$$\left(\frac{\mathrm{Gr}}{\mathrm{Re}}\right)_{FRup}=-\left.\frac{\mathrm{d}u^{(1)}}{\mathrm{d}r}\right|_{r=\gamma}\left(\left.\frac{\partial u^{(2)}}{\partial r}\right|_{r=\gamma,\vartheta=\pi/2}\right)^{-1}. \tag{66}$$

Moreover, for downward flow, there exists a negative real number $(\mathrm{Gr/Re})_{FRdw}$ such that flow reversal occurs when $\mathrm{Gr/Re}<(\mathrm{Gr/Re})_{FRdw}$. Indeed, for $\mathrm{Gr/Re}=(\mathrm{Gr/Re})_{FRdw}$, the first derivative of $u(r,\vartheta)$, evaluated for $r=1$ and $\vartheta=3\pi/2$, vanishes, so that

$$\left(\frac{\mathrm{Gr}}{\mathrm{Re}}\right)_{FRdw}=-\left.\frac{\mathrm{d}u^{(1)}}{\mathrm{d}r}\right|_{r=1}\left(\left.\frac{\partial u^{(2)}}{\partial r}\right|_{r=1,\vartheta=3\pi/2}\right)^{-1}. \tag{67}$$

By employing Eqs. (66) and (67), the threshold values of Gr/Re for the onset of flow reversal in the case of upward flow and downward flow are, respectively, given by

Downloaded 06 Dec 2010 to 193.140.21.150. Redistribution subject to ASME license or copyright; see http://www.asme.org/terms/Terms_Use.cfm

$$\left(\frac{\mathrm{Gr}}{\mathrm{Re}}\right)_{FRup}=\frac{2(1-\gamma^2+2\gamma^2\ln\gamma)}{\gamma[1-\gamma^2+(1+\gamma^2)\ln\gamma]}\times\left\{-\frac{1-\gamma^4+4\gamma^2\ln\gamma}{8\pi(1-\gamma)^3(1+\gamma)(1+\gamma^2)}+\frac{1-5\gamma^2+7\gamma^4-3\gamma^6-2\gamma^2(3-2\gamma^2-\gamma^4+4\ln\gamma)\ln\gamma}{128\gamma(1-\gamma)^3(1+\gamma)[1-\gamma^2+(1+\gamma^2)\ln\gamma]}\right.$$
$$\left.-\frac{1}{8\pi(1-\gamma)^2}\sum_{n=2}^{\infty}(-1)^n\frac{\gamma^{6n}[(n-1)\gamma^2-n]+\gamma^{2(n+1)}[1-n(1-\gamma^2)]}{n(n-1)(2n-1)(\gamma^4-\gamma^{8n})}\right\}^{-1}, \tag{68}$$

$$\left(\frac{\mathrm{Gr}}{\mathrm{Re}}\right)_{FRdw}=\frac{2(1-\gamma^2+2\ln\gamma)}{1-\gamma^2+(1+\gamma^2)\ln\gamma}\times\left\{-\frac{1-4\gamma^2+3\gamma^4-4\gamma^4\ln\gamma}{8\pi(1-\gamma)^3(1+\gamma)(1+\gamma^2)}-\frac{3-7\gamma^2+5\gamma^4-\gamma^6+2(1+2\gamma^2-3\gamma^4+4\gamma^4\ln\gamma)\ln\gamma}{128(1-\gamma)^3(1+\gamma)[1-\gamma^2+(1+\gamma^2)\ln\gamma]}\right.$$
$$\left.+\frac{1}{8\pi(1-\gamma)^2}\sum_{n=2}^{\infty}(-1)^n\frac{(n-1)\gamma^4-n\gamma^{8n}+\gamma^{2(1+2n)}[\gamma^2-4n(n-1)(1-\gamma^2)]}{n(n-1)(2n-1)^2(\gamma^4-\gamma^{8n})}\right\}^{-1}. \tag{69}$$

The series that appear in Eqs. (68) and (69) have a fast convergence, so that 500 terms are usually enough to get six-digit accurate results. In Table 2, the values of $(\mathrm{Gr/Re})_{FRup}$ and $(\mathrm{Gr/Re})_{FRdw}$ are reported for some values of γ.

In Fig. 6, a drawing of the flow reversal states in the (γ, Gr/Re) plane is presented. This figure reveals that flow reversal conditions are gained for values of $|\mathrm{Gr/Re}|_{FR}$ that become smaller as γ decreases. In Fig. 7, the states with negative values of λ (and, as a consequence, also of f Re) are represented in the plane (γ, Gr/Re). This figure shows that negative values of λ may occur for $\gamma \lesssim 0.5$.

In Fig. 8, the dimensionless velocity distribution $u(r,\vartheta)$ is plotted for $\gamma=0.5$ and $\mathrm{Gr/Re}=500$, i.e., for a case of upward flow. The figure shows that, for the considered value of Gr/Re, which is greater than $(\mathrm{Gr/Re})_{FRup}$, strong deformations of the Poiseuille dimensionless velocity profile occur. Namely, values of u higher than 2 take place in the hotter parts of the duct, while negative values of u are present close to the cooler parts of the wall (flow reversal).

Table 2 Second example: threshold values of the ratio Gr/Re for the onset of flow reversal

γ	$(\mathrm{Gr/Re})_{FR\,up}$	$(\mathrm{Gr/Re})_{FR\,dw}$
0.1	152.095	−93.6228
0.2	149.998	−100.664
0.3	165.379	−112.748
0.4	196.080	−132.594
0.5	248.029	−164.728
0.6	335.641	−218.069
0.7	491.829	−312.398
0.8	811.581	−504.711
0.9	1772.21	−1081.46

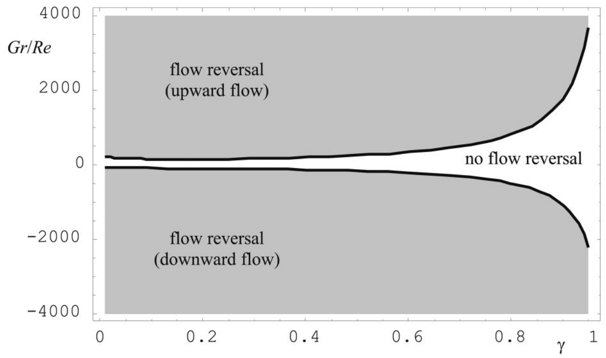

Fig. 6 Flow reversal regions as a function of γ

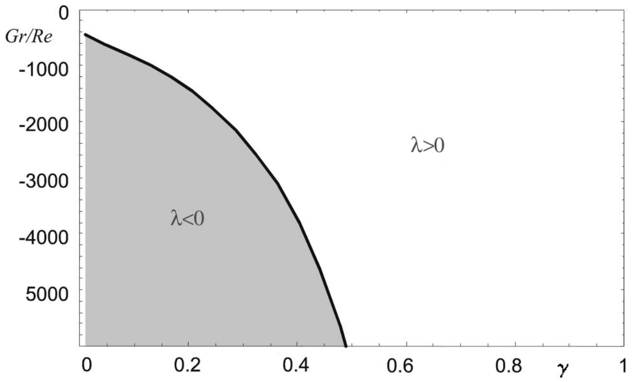

Fig. 7 Regions of positive and/or negative values of the dimensionless pressure drop parameter λ

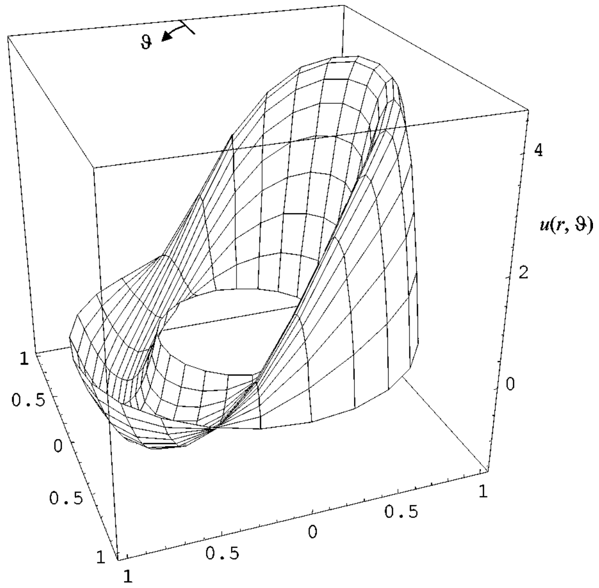

Fig. 8 Three-dimensional plot of the dimensionless velocity distribution $u(r,\vartheta)$, for $\gamma=0.5$ and $\mathrm{Gr/Re}=500$

Downloaded 06 Dec 2010 to 193.140.21.150. Redistribution subject to ASME license or copyright; see http://www.asme.org/terms/Terms_Use.cfm

Conclusions

The steady laminar mixed convection of a Newtonian fluid in a vertical annular duct subjected to nonaxisymmetric thermal boundary conditions has been studied under the hypotheses of parallel and fully developed flow. The Boussinesq approximation has been employed and the effect of viscous dissipation has been considered as negligible. The momentum and energy balance equations have been solved analytically by means of a Fourier series method. Moreover, the dimensionless pressure drop parameter and the Fanning friction factor have been determined.

The solution shows that, except for the dimensionless temperature field, either the dimensionless velocity distribution or the dimensionless pressure drop parameter or the Fanning friction factor are influenced by the buoyancy effect. Moreover, it has been shown that for any given value of the duct aspect ratio, there exists a threshold value of the ratio between the Grashof number and the Reynolds number for the onset of flow reversal. These threshold values have been evaluated analytically both for upward flow and for downward flow.

Finally, the general solution has been applied to a couple of special cases such that one wall is kept isothermal and the other wall is half adiabatic and half subjected to a uniform inward heat flux distribution. In particular, the second example refers to an annular duct with an internal isothermal wall and an external wall half adiabatic and half heated with a uniform heat flux. In this case, regimes with negative pressure drops in the streamwise direction may occur for downward flow provided that the aspect ratio γ is sufficiently small.

Nomenclature

A_0, $A_n^{(1)}$, $A_n^{(2)}$ = integration constants
$a_0(r)$, $a_n(r)$, $b_n(r)$ = functions that appear in the temperature Fourier expansion
$B_n^{(1)}$, $B_n^{(2)}$ = integration constants
$C_n(r)$, $H_n(r)$ = functions defined in Eq. (32)
$c_0(r)$, $c_n(r)$, $h_n(r)$ = functions that appear in the velocity Fourier expansion
$F(\vartheta)$ = step function defined in Eq. (41)
f = Fanning friction factor
$\mathbf{g}$ = gravitational acceleration, m/s^2
g = magnitude of gravitational acceleration, m/s^2
Gr = Grashof number
k = thermal conductivity, W/(mK)
m, n = positive integers
P = difference between the pressure and the hydrostatic pressure, Pa
p = pressure, Pa
q_w = arbitrary inward wall heat flux, W/m^2
R = radial coordinate, m
r = dimensionless radial coordinate
Re = Reynolds number
T = temperature, K
t = dimensionless temperature
T_0 = average temperature in a duct section, K
T_w = arbitrary wall temperature, K
t_w = arbitrary dimensionless wall temperature
U = X component of the fluid velocity, m/s
u = dimensionless velocity
$u^{(1)}$ = forced convection dimensionless velocity
$u^{(2)}$ = buoyancy-induced dimensionless velocity
u^* = modified dimensionless velocity
$\mathbf{U}$ = fluid velocity, m/s
U_0 = average velocity in a duct section, m/s
$\mathbf{X}$ = unit vector parallel to the X-axis
X = axial coordinate, m

Greek Symbols

β = volumetric coefficient of thermal expansion, K^{-1}
γ = aspect ratio of the duct
ΔT = reference temperature difference, K
ϑ = angular coordinate, rad
λ = dimensionless pressure drop
$\lambda^{(1)}$ = forced convection dimensionless pressure drop
$\lambda^{(2)}$ = buoyancy-induced dimensionless pressure drop
μ = dynamic viscosity, Pa s
ν = kinematic viscosity, m^2/s
ϱ = mass density, kg/m^3
ϱ_0 = mass density for $T=T_0$, kg/m^3
τ_w = average wall shear stress, Pa

Subscripts

1 = internal wall
2 = external wall
dw = downward flow
up = upward flow
FR = onset of flow reversal

References

[1] Shah, R. K., and London, A. L., 1978, *Laminar Flow Forced Convection in Ducts*, T. F. Irvine and J. P. Hartnett, eds., Academic Press, New York.
[2] Rokerya, M. S., and Iqbal, M., 1971, "Effects of Viscous Dissipation on Combined Free and Forced Convection Through Vertical Concentric Annuli," Int. J. Heat Mass Transfer, **14**, pp. 491–495.
[3] Kou, H. S., and Huang, D. K., 1997, "Fully Developed Laminar Mixed Convection Through a Vertical Annular Duct Filled With Porous Media," Int. Commun. Heat Mass Transfer, **24**, pp. 99–110.
[4] Barletta, A., 2000, "Combined Forced and Free Flow of a Power-Law Fluid in a Vertical Annular Duct," Int. J. Heat Mass Transfer, **43**, pp. 3673–3686.
[5] Aung, W., Moghadam, H. E., and Tsou, F. K., 1991, "Simultaneous Hydrodynamic and Thermal Development in Mixed Convection in a Vertical Annulus With Fluid Property Variations," ASME J. Heat Transfer, **113**, pp. 926–931.
[6] Tsou, F. K., and Gau, C., 1992, "Wall Heating Effects in Mixed Convection in Vertical Annulus With Variable Properties," J. Thermophys. Heat Transfer, **6**, pp. 273–276.
[7] Reynolds, W. C., 1960, "Heat Transfer to Fully Developed Laminar Flow in a Circular Tube With Arbitrary Circumferential Heat Flux," ASME J. Heat Transfer, **82**, pp. 108–112.
[8] Choi, D. K., and Choi, D. H., 1994, "Developing Mixed Convection Flow in a Horizontal Tube Under Circumferentially Non-Uniform Heating," Int. J. Heat Mass Transfer, **37**, pp. 1899–1913.
[9] Barletta, A., Lazzari, S., and Zanchini, E., 2003, "Laminar Mixed Convection in a Vertical Circular Duct With a Perimetrally Variable Wall Temperature," *Proc. 6th ASME-JSME Thermal Engineering Joint Conference*, Hawaii, ASME, New York.
[10] Sutherland, W. A., and Kays, W. M., 1964, "Heat Transfer in an Annulus With Variable Circumferential Heat Flux," Int. J. Heat Mass Transfer, **7**, pp. 1187–1194.
[11] Aung, W., and Worku, G., 1986, "Theory of Fully Developed Combined Convection Including Flow Reversal," ASME J. Heat Transfer, **108**, pp. 485–488.
[12] Lavine, A. S., 1988, "Analysis of Fully Developed Opposing Mixed Convection Between Inclined Parallel Plates," Waerme-Stoffuebertrag., **23**, pp. 249–257.
[13] Hamadah, T. T., and Wirtz, R. A., 1991, "Analysis of Laminar Fully Developed Mixed Convection in a Vertical Channel With Opposing Buoyancy," ASME J. Heat Transfer, **113**, pp. 507–510.
[14] Patel, N., and Ingham, D. B., 1994, "Analytic Solutions for the Mixed Convection Flow of Non-Newtonian Fluids in Parallel Plate Ducts," Int. Commun. Heat Mass Transfer, **21**, pp. 75–84.
[15] Barletta, A., 2001, "Analysis of Flow Reversal for Laminar Mixed Convection in a Vertical Rectangular Duct With One or More Isothermal Walls," Int. J. Heat Mass Transfer, **44**, pp. 3481–3497.
[16] Barletta, A., and Zanchini, E., 1999, "On the Choice of the Reference Temperature for Fully-Developed Mixed Convection in a Vertical Channel," Int. J. Heat Mass Transfer, **42**, pp. 3169–3181.

Downloaded 06 Dec 2010 to 193.140.21.150. Redistribution subject to ASME license or copyright; see http://www.asme.org/terms/Terms_Use.cfm

O. B. Adeyinka
Ph.D. Candidate

G. F. Naterer
Professor

Department of Mechanical and Industrial Engineering,
University of Manitoba,
Winnipeg, Manitoba, R3T 2N2, Canada

Particle Image Velocimetry Based Measurement of Entropy Production With Free Convection Heat Transfer

Local entropy production rates are determined from a numerical and experimental study of natural convection in an enclosure. Numerical predictions are obtained from a control-volume-based finite element formulation of the conservation equations and the Second Law. The experimental procedure combines methods of particle image velocimetry and planar laser induced fluorescence for measured velocity and temperature fields in the enclosure. An entropy based conversion algorithm in the measurement procedure is developed and compared with numerical predictions of free convection in the cavity. The predicted and measured results show close agreement. A measurement uncertainty analysis suggests that the algorithm postprocesses velocities (accurate within ±0.5%) to give entropy production data, which is accurate within ±8.77% near the wall. Results are reported for free convection of air and water in a square cavity at various Rayleigh numbers. The results provide measured data for tracking spatial variations of friction irreversibility and local exergy losses. [DOI: 10.1115/1.1863272]

1 Introduction

Free convection heat transfer in enclosures occurs in various engineering systems. For example, cooling of microelectronic assemblies involves natural convection. Heating/ventilation in buildings, heat transfer between panes of glass in double-pane windows, solar collectors, and gas-filled cavities surrounding a nuclear reactor core are other examples. This paper considers the practical significance of entropy production during free convection heat transfer.

Although the physical processes of free convection have been widely documented in the literature, fewer studies have considered the related importance of thermal irreversibilities in such applications. A specified rate of heat transfer can be achieved, but with varying levels of fluid irreversibilities, depending on the surface area and temperature difference across which heat transfer occurs. For example, convective cooling of a microelectronic assembly entails free convection from the heat sink, but pressure losses with forced convection occur with air flow past internal components. In this instance, each unit of entropy produced (or exergy destroyed) leads to a corresponding unit of heat flow which is desired to be removed, but cannot be removed due to entropy production. This entropy production leads to pressure losses and kinetic energy dissipated to internal energy, which works against the desired objective of component cooling.

Previous studies have shown that numerical solutions involving free convection in an enclosure can be successfully obtained by finite differences, finite volumes or finite elements [1–4]. The buoyancy term depends on the local temperature, thereby requiring coupled solutions with the energy equation. Benchmark solutions provide useful data regarding validation of predictive models for variations of flow patterns and heat transfer [1].

In contrast to conservation equations, the Second Law of Thermodynamics involves an inequality. It offers a useful way of characterizing energy conversion through entropy production of fluid irreversibilities. It has been shown that the Second Law can serve to optimize the design of thermal, fluid, and energy systems [5–9]. An analytical approach involves derivation of a functional expression for the entropy generation in a thermofluid process. The extrema of this functional expression, which guarantees a minimum entropy production, is then determined by methods of differential calculus.

However, analytical methods are often limited to simplified geometries. Related advances in computational methods over the past few decades have calculated the entropy production, after postprocessing of the predicted flow fields. Moore and Moore [10,11] developed a numerical model of mean entropy production in turbulent flow. Based on this model, Drost and White [12] predicted the local rate of entropy production associated with a fluid jet impinging on a heated wall. Kramer-Bevan [13] presented a derivation of the time-averaged entropy production equation, with a closure based on the small thermal turbulence model.

Other numerical procedures have predicted entropy generation for mixed convection in a vertical channel with transverse fin arrays [14], laminar and turbulent flow through a smooth duct [15–18], radial flow in concentric cylindrical annuli with relative rotation [19] and diffuser geometries [9]. Entropy based models have also been applied to optimization in applications involving natural convection in an inclined enclosure [20,21], irreversibilities at the onset of natural convection in a rectangular cavity [22], and laminar natural convection over a heated rotating cylinder [23]. In contrast to these past studies, this paper develops a procedure for measuring such local production rates, thereby providing a useful tool for validating past numerical predictions.

Although particle image velocimetry (PIV) and planar laser induced fluorescence (PLIF) techniques are conventional experimental techniques, their application to entropy production analysis has not been developed previously (to our knowledge). Unlike velocity or temperature, the measurement of entropy production cannot be performed directly, so algorithms for experimental postprocessing of measured quantities are needed. Past experimental PIV/PLIF studies have been reported for whole-field measurements of velocity and temperature of water in free convection [24,25]. Adeyinka and Naterer [9,26] show that postprocessing of the spatial velocity gradients characterizes the flow irreversibilities, while establishing entropy production as a derived experimental quantity.

Contributed by the Heat Transfer Division of ASME for publication in the JOURNAL OF HEAT TRANSFER. Manuscript received April 1, 2004; revision received November 23, 2004. Review conducted by: J. M. Khodadadi.

Copyright © 2005 by ASME

Downloaded 06 Dec 2010 to 193.140.21.150. Redistribution subject to ASME license or copyright; see http://www.asme.org/terms/Terms_Use.cfm

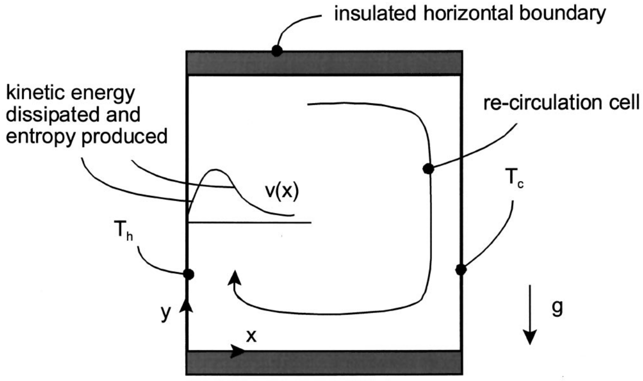

Fig. 1 Problem schematic

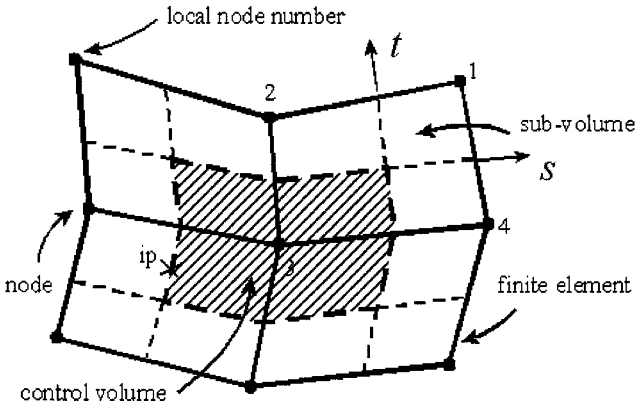

Fig. 2 Definitions of finite element and control volume

In this paper, an experimental technique is developed for deriving entropy production data, particularly involving free convection heat transfer. Attention is focused on entropy production due to fluid friction. The experimental study involves natural convection of water in a square cavity. This paper represents a study of whole-field, nonintrusive measurements for postprocessing of spatial entropy production rates (to our knowledge). The measured data are compared to numerical simulations for verification purposes. The numerical solutions also provide certain quantitative information regarding detailed analysis of the measured entropy production field.

Optimization of thermofluid systems has been performed previously with various techniques, i.e., (i) estimation of the theoretical ideal operating conditions of a proposed design (called EA: exergy analysis), (ii) minimization of the lost available work or entropy generation by design modifications (EGM: entropy generation minimization). In this paper, the developed experimental technique of entropy production measurement would be useful in both EA and EGM methods. In addition to measured data for validation of past predictive models, the entropy production data could be used to determine local variations of exergy destruction and energy availability losses. In this way, the diagnostic tool would allow designers to target problem areas of thermofluid systems, characterized by high entropy production.

2 Numerical Formulation

Consider free convection within a square enclosure, as depicted in Fig. 1. It is assumed that the cavity is sufficiently wide in the direction perpendicular to the plane of Fig. 1, so the buoyancy-induced fluid motion is considered to be two dimensional. The conservation equations for steady, incompressible, laminar two-dimensional flow of a Newtonian fluid can be expressed in tensor notation as follows [27]:

$$\frac{\partial}{\partial x_j}(\rho u_j)=0 \tag{1}$$

$$\frac{\partial}{\partial x_j}(\rho u_j u_i)=-\frac{\partial p}{\partial x_i}+\frac{\partial}{\partial x_j}\left(\mu\frac{\partial u_i}{\partial x_j}\right)+(\rho-\rho_0)g_i \tag{2}$$

$$\frac{\partial}{\partial x_j}(\rho u_j T)=\frac{\partial}{\partial x_j}\left(\frac{k}{c_p}\frac{\partial T}{\partial x_j}\right) \tag{3}$$

where ρ is the density and u_i and x_i are the Cartesian velocity components and coordinate directions, respectively. Also, g_i is the component of the gravity acceleration vector in the x_i direction. The last term in Eq. (2) represents the buoyancy force, according to the Boussinesq approximation. Variations of temperature affect the change of density in the Boussinesq approximation of Eq. (2), as the buoyancy term becomes the thermal expansion coefficient multiplied by g_i and the local temperature difference. Thermophysical properties are considered as isotropic and independent of temperature, except density in the buoyancy term. Changes of thermal conductivity and specific heat with temperature over the relatively small temperature differences in this paper are considered to have negligible impact on the predicted results.

The temperatures of the hot and cold vertical walls are T_h and T_c, respectively. The top and bottom walls are insulated. The solution of the discrete equations for velocity, pressure, temperature and entropy is obtained with a control-volume finite element method (CVFEM) and a physical influence scheme (PINS) of convective upwinding [27]. PINS obtains the integration point value of the scalar by a local approximation of the governing equations at the integration point. The upwinding procedure accounts for transient, pressure, and source terms, when calculating the convected variable at the integration point.

A schematic of the finite element and control volume discretization is illustrated in Fig. 2. The domain is subdivided into linear, quadrilateral finite elements. The grid is arranged in a collocated manner, so that velocity components, pressure, temperature, and entropy are obtained at nodes located at every element corner. The finite element model uses a local (s,t) coordinate system, when calculating shape functions and other element properties (see Fig. 2). A local numbering scheme (ranging from 1 to 4) is adopted within each element, so the finite element equations can be developed locally and independently of the mesh configuration.

Following a conventional assembly procedure for the finite elements, the local node equations are assembled into the global system of equations involving global nodes. This assembly procedure yields a banded matrix of coefficients. A direct banded solver is used to solve this algebraic set of equations. An entropy balance is applied over the "effective" control volume, as defined by all subvolumes from elements surrounding a particular node in the mesh. Each element is subdivided into four sub-control volumes, with internal subcontrol-volume boundaries coincident with the local coordinate surfaces defined by $s=0$ and $t=0$ (see Fig. 2). Further details of the numerical formulation for the conservation and entropy transport equations are outlined in Refs. [27–29].

The entropy balance for an open system may be written as

$$\dot{P}_s=\frac{\partial S}{\partial t}+\frac{\partial F_j}{\partial x_j}\geqslant 0 \tag{4}$$

where the entropy per unit volume and entropy flux are given by

$$S=\rho s \tag{5}$$

and

$$F_j=\rho u_j s+\frac{q_j}{T} \tag{6}$$

Using the continuity equation, Eq. (4) can be rewritten as

Downloaded 06 Dec 2010 to 193.140.21.150. Redistribution subject to ASME license or copyright; see http://www.asme.org/terms/Terms_Use.cfm

$$\rho \frac{Ds}{Dt} = -\frac{\partial}{\partial x_j}\left(\frac{q_j}{T}\right) + \dot{P}_s \qquad (7)$$

where D/Dt is the total (substantial) derivative and $\dot{P}_s$ is the entropy production rate. The specific entropy, s, can be expressed in terms of temperature using the Gibbs equation. Equation (7) represents the entropy transport equation. In this form, the rate of entropy accumulation in the control volume is balanced by the net convection of entropy, entropy transport associated with heat flow and a non-negative entropy production. When combined with the Gibbs equation, the entropy transport equation provides a way of calculating the local entropy generation.

Alternatively, the entropy production can be computed by [5]:

$$\dot{P}_s = \frac{k}{T^2}\left(\frac{\partial T}{\partial x_j}\frac{\partial T}{\partial x_j}\right) + \frac{\mu \Phi}{T} \geqslant 0 \qquad (8)$$

where Φ is the viscous dissipation arising from velocity gradients in the fluid motion. In Eq. (8), Fourier's Law has been used for the thermal term, while Φ can be expanded in terms of spatial velocity gradients.

Based on these models, Eq. (8) becomes a positive definite expression for the entropy generation rate, since it can be expressed as a sum of squared terms. It must balance the expression determined from the transient entropy derivative and entropy flux in Eq. (4). In the following section, local entropy production rates will be measured based on the positive definite formulation of Eq. (8). These measurements will be obtained with combined PIV and PLIF.

3 Experimental Design and Measurement Procedure

Flow irreversibilities can be measured indirectly from spatial gradients of velocity in the positive-definite equation of entropy production, Eq. (8). Experimental techniques involving PIV and PLIF methods offer certain advantages over standard methods of anemometry for entropy related experimental analysis [30]. They provide a whole-field method, while allowing nonintrusive and time-varying measurements of the instantaneous velocity and temperature fields. This section addresses a need to gain physical data regarding the detailed structure of available energy losses throughout a flow field. Since the PIV and PLIF techniques provide whole-field data regarding the velocity and temperature fields, these methods can address the objective by measuring local variations of the entropy production rates.

In planar laser induced fluorescence, molecules and atoms emit light in a de-excitation process induced by absorption of a photon of higher energy. The local fluorescence intensity, I, varies with intensity of excitation light, I_e, concentration of the fluorescent dye, C, quantum efficiency as a function of temperature, ϕ, and the molar absorptivity, ε, i.e.:

$$I = f I_e \varepsilon C \phi(T) \qquad (9)$$

where f is a factor corresponding to the optical setup. For a known concentration and excitation energy, the quantum energy decreases with higher temperatures. This dependence is the basis for PLIF temperature measurements. The temperature is determined from Eq. (9) as follows:

$$T - T_{\mathrm{ref}} = \frac{\Delta I}{f I_e \varepsilon C \Delta \phi} \qquad (10)$$

The experimental setup involved planar laser induced fluorescence for measurering temperatures within the test cell, as well as particle image velocimetry for velocity measurements (see Figs. 3 and 4). The test cell was assembled with front, back, top, and bottom plexiglass walls and heat exchangers controlling the sidewall temperatures.

The optical configuration for the PIV/PLIF setup consists of a light source [New Wave gemini Nd: yttritium-aluminum-garnet (YAG) pulsed laser], light sheet optics, fluorescent dye for PLIF (Rhodamine B), tracer particles for PIV (5 μm polyamide particles), and charge coupled device (CCD) cameras (Dantec HiSense cameras, 1280×1024 pixels, 24 bit). The camera and image capturing systems detect particle images and fluorescent images successively at two different instants. The wavelength of the fluorescence emitted from the PLIF dye is longer than the wavelength of the reflected laser light. An optical filter is attached to the front of the camera for the florescence image to cut off reflected light from the PIV particles. The camera operated at 30 Hz, while permitting measurements of about 20 frames per second. The temperatures were recorded after steady-state conditions were reached in both velocity and temperature fields. Temporal uncertainties were considered to have unnoticeable effects on the measurements.

The Rayleigh number was controlled by adjusting fluid temperatures into the aluminum heat exchanger sidewalls. The test cell cross section (39×39 mm) was designed for laminar free convection. The test cell depth is 59 mm. Heat losses from front and back sides of the cavity may lead to velocity variations in the x_3 direction. However, the depth was designed to minimize these three-dimensional variations of thermal and flow fields along the plane of symmetry [31]. Two holes on the top walls were needed to fill and drain the liquid during experiments. Water at a known temperature was circulated between each aluminum heat exchanger from two NESLAB temperature baths (RTE140 bath/circulator). The temperature difference between the inlet and outlet of the aluminum cross-flow exchanger was approximately 0.9°C. In the flow loop, the cooling water was circulated by a pump between the water and heat exchangers. The temperature of the outer surface of the aluminum heat exchanger was approximately equal to the temperature of the circulating water.

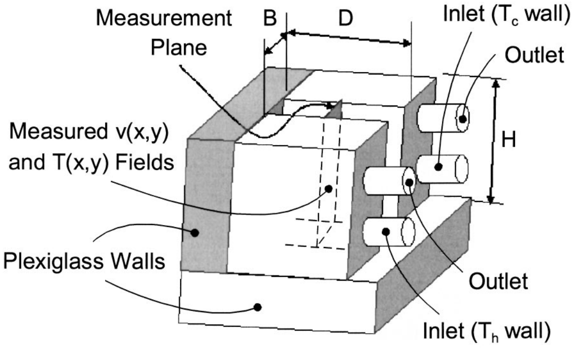

Fig. 3 Test Cell ($B=H=39$ mm; $D=59$ mm)

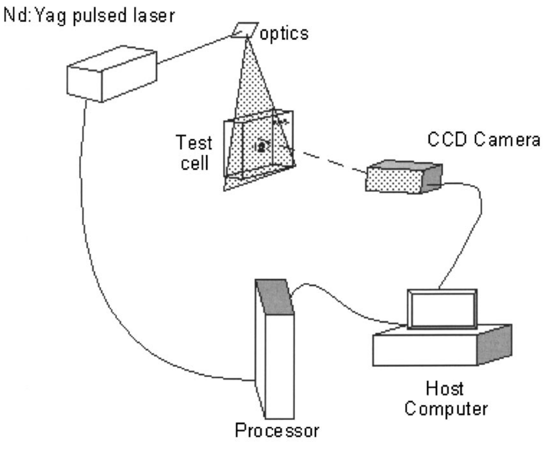

Fig. 4 Experimental setup

Downloaded 06 Dec 2010 to 193.140.21.150. Redistribution subject to ASME license or copyright; see http://www.asme.org/terms/Terms_Use.cfm

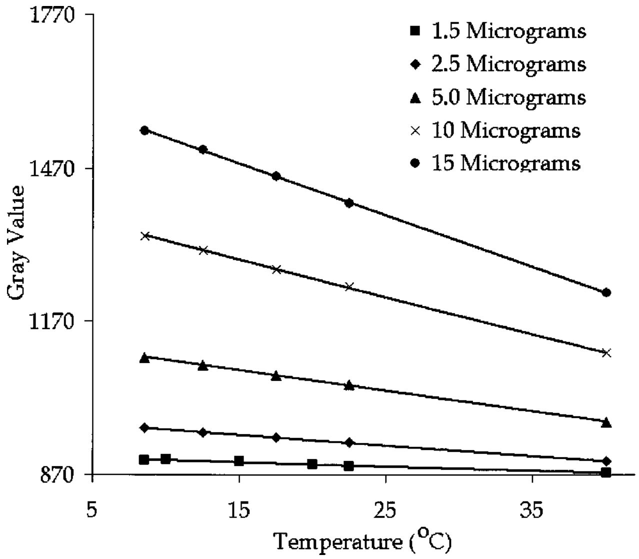

Fig. 5 Gray values in PLIF measurements

Calibration experiments for the PLIF method were performed in the cavity. Distilled water was circulated and seeded with a solution of Rhodamine B at a known concentration and temperature. The cavity was illuminated from above at the vertical plane of symmetry by a Nd:YAG pulsed laser. A Dantec Hisense CCD camera captured the sequence of image maps. The first step in the calibration procedure is to find the optimal concentration resulting in the maximum temperature resolution with low absorption phenomena. The variations of gray values at various concentration levels are shown in Fig. 5 (note: spatial gradient of gray value with temperature represents the PLIF resolution). The corresponding absorption, A is calculated from

$$A = e^{-l\eta_{\mathrm{Rhod}}C} \tag{11}$$

where η_{Rhod} is the extinction coefficient of Rhodamine B in water and l is the optical path length. In Fig. 5, The temperature resolution is maximum for a concentration of 15 μg/L. The final calibration used approximately 89% of the concentration at which the slope of the temperature vs. intensity resolution graph is maximum, i.e., $C_0 = 0.89 \times C_{\max} = 13.5$ μg/L.

The calibration maps the response at every pixel of the camera to varying temperature, laser energy levels and concentration. Equation (10) is then used to determine the response of the camera to temperature and laser energy. Values of temperature at discrete locations in the measurement domain are obtained using the calibration map. The PLIF software (Dantec Dynamics) used in this study includes several methods for advanced analysis of the PLIF results. Statistical averages are available to establish whole-field statistics on the LIF data acquired. Optimization methods are used to enhance the signal to noise ratio and precision, thereby giving an absolute temperature accuracy of $\pm 0.6°$C.

A single CCD camera was used to capture both PLIF and PIV images. The optical filters for each measurement were switched to permit sequential measurements. The PIV images were postprocessed by a fast Fourier-transform based cross-correlation scheme (FlowManager, Dantec Dynamics). The 1280×1024 pixel PIV image plane of the camera was divided into 32×32 pixel subregions with 50% overlap, in order to give a spatial resolution of 0.7 mm based on the whole cavity. The PIV processor was operated in a single frame mode with 100 ms delay time between successive frames to yield optimal raw velocity data. The PLIF images were resampled by a calibration map with a spatial resolution corresponding to the velocity map.

The measured velocity vectors are displayed by the PIV software over a discrete grid. Then, the local rates of entropy production are determined by spatial differencing of Eq. (8) over the discrete grid. Let $\boldsymbol{u}(i,j)$ and $\boldsymbol{v}(i,j)$ denote the velocity vector components at grid position (i,j). Equation (8) yields the following representation of the entropy production rate for two-dimensional flows:

$$\begin{aligned}\dot{P}_s = {} & \frac{k}{T(i,j)^2}\left[\frac{T(i+1,j)-T(i-1,j)}{\Delta x}\right]^2 \\ & + \frac{k}{T(i,j)^2}\left[\frac{T(i,j+1)-T(i,j-1)}{\Delta y}\right]^2 \\ & + \frac{\mu}{T(i,j)}\left[\frac{u(i,j+1)-u(i,j-1)}{\Delta y} + \frac{v(i+1,j)-v(i-1,j)}{\Delta x}\right]^2 \\ & + 2\,\frac{\mu}{T(i,j)}\left\{\left[\frac{u(i+1,j)-u(i-1,j)}{\Delta x}\right]^2 \right. \\ & \left. + \left[\frac{v(i,j+1)-v(i,j-1)}{\Delta y}\right]^2\right\}\end{aligned} \tag{12}$$

In Eq. (12), Δx and Δy refer to the PIV grid spacing in the x and y directions, respectively. In this paper, thermophysical properties are assumed to be uniform.

4 Results and Discussion

Accuracy of the numerical formulation of predicting entropy production in this study has been tested previously with problems involving both heat transfer and fluid flow [9,26,28]. In this section, the algorithm is applied to a natural convection problem and compared with benchmark data [1] and measured data. Water was used as the working fluid in the experiments, while air was used in the numerical simulations for benchmarking purposes. The CVFEM formulation is validated for the velocity and temperature data of de Vahl Davies and the entropy production results obtained for the natural convection of air are compared with previous studies. Figure 6 shows predicted velocity and isotherm patterns for Rayleigh numbers of 10^3, 10^4, 10^5, and 10^6. The velocity vectors are shown on a 40×40 grid for easy visualization. The flow structure shows close agreement with contour maps obtained in previous studies [1].

At low Rayleigh numbers in Fig. 6, the flow is nearly symmetrical about the center point. As the Rayleigh number increases, the recirculation becomes more elliptical and eventually separates into two zones at $\mathrm{Ra} = 10^5$. The boundary layer becomes thinner, with the recirculation zones moving closer to the wall at $\mathrm{Ra} = 10^6$. The temperature profile is nearly linear at the lowest Rayleigh number (10^3). As the Rayleigh number increases, convection becomes increasingly significant and the profiles show a progressive departure from linearity. The contours flatten as Ra increases, with the highest temperature gradients closer to the wall. This characteristic arises due to increasing vertical buoyancy-induced motion of the fluid.

Predictions of the average Nusselt number, maximum horizontal velocity on the vertical midplane, $U_{\max}$, and the maximum vertical velocity in the horizontal midplane of the cavity, $V_{\max}$, and their locations are given in Table 1 for Rayleigh numbers of 10^3, 10^4, 10^5, and 10^6 with the 80×80 grid. The x and y coordinates are normalized with respect to the cavity width, L. Also, the velocities are normalized by a diffusion velocity, i.e., $k/(c_p L)$.

As illustrated in Fig. 7, convergence towards the same grid independent value with the present numerical formulation and the finite difference formulation of de Vahl Davies [1] can be observed when the mesh is refined. The grid size has been normalized by the width of the cavity. The Nusselt number represents the ratio of the heat flux across the cavity to the heat flux that would result from pure conduction. Since the formulation is conservative, the heat flux across the cavity was determined as the average heat flux at the hot and cold walls of the cavity. The calculation of

Downloaded 06 Dec 2010 to 193.140.21.150. Redistribution subject to ASME license or copyright; see http://www.asme.org/terms/Terms_Use.cfm

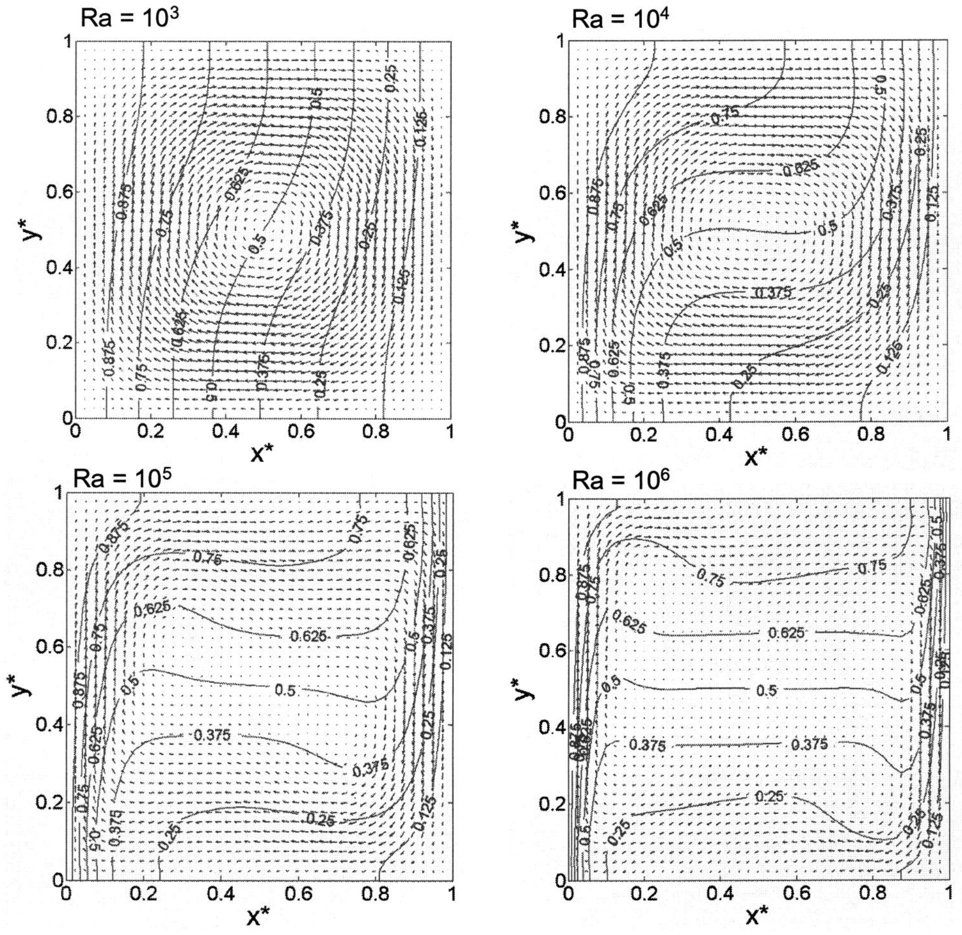

Fig. 6 Predicted temperatures and velocities at varying Rayleigh numbers

Nu is performed by finding temperature gradients at the subcontrol volume level for all boundary elements. In order to ascertain the accuracy of the numerical formulation, velocity components and temperatures are monitored at a reference location ($x=0.2, y=0.4$) and recorded for different grid sizes at Rayleigh Numbers of 10^3, 10^4, and 10^5. The velocities and temperatures converge towards the grid independent values as the mesh is refined. A Richardson extrapolation for second order schemes was used, i.e.:

$$\phi=\phi_i+\frac{1}{3}(\phi_i-\phi_{i-1}) \tag{13}$$

Based on this extrapolation, the grid independent value and the percentage error associated with each grid size were determined. When these errors are plotted against the grid spacing on a logarithmic scale in Fig. 8, all curves indicate a slope of 2, thereby suggesting second order accuracy of the numerical formulation.

Table 1 Comparisons with benchmark solution of de Vahl Davis [1]

	U_{max}	y-position	V_{max}	x-position	Nu
	Ra = 10^3				
Predicted	3.63068	0.8125	3.69075	0.175	1.12411
Benchmark	3.649	0.813	3.697	0.178	1.118
	Ra = 10^4				
Predicted	16.2295	0.825	19.616	0.125	2.2527
Benchmark	16.178	0.823	19.617	0.119	2.243
	Ra = 10^5				
Predicted	35.1589	0.85	68.6567	0.0625	4.52037
Benchmark	34.73	0.855	68.59	0.066	4.519
	Ra = 10^6				
Predicted	64.805	0.85	220.016	0.0375	8.8312
Benchmark	64.63	0.85	219.36	0.0379	8.8

Downloaded 06 Dec 2010 to 193.140.21.150. Redistribution subject to ASME license or copyright; see http://www.asme.org/terms/Terms_Use.cfm

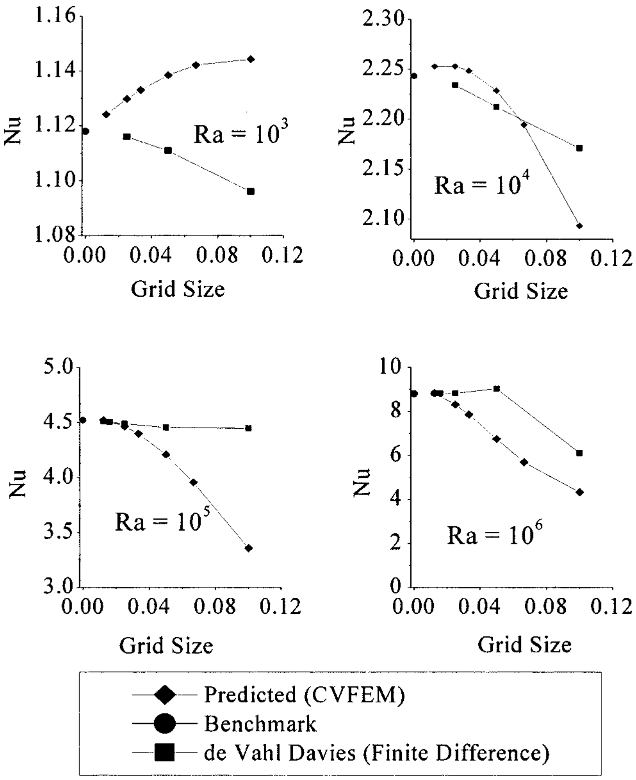

Fig. 7 Predicted average Nusselt numbers at varying grid sizes and Rayleigh numbers

The flow field behavior as Ra increases shows close agreement with the benchmark solution of de Vahl Davis [1]. The results presented for comparison purposes in the remaining figures were obtained with the finest grid.

In Fig. 6 at higher Rayleigh numbers, the temperature field is skewed about the center of the cavity with hot fluid drifting closer to the cold wall. The temperature field is flattened with the hottest fluid at the top left region of the cavity. This temperature distribution suggests an increasing magnitude of buoyancy effects along the vertical cold surface of the enclosure. Stronger convection closer to this wall leads to higher velocities. This observation is consistent with results obtained previously by Hamady and Lloyd [32]. Comparisons show similar temperature stratification in both numerical and experimental data.

The predicted entropy generation due to friction irreversibilities at Rayleigh numbers of 10^3 and 10^6 (laminar regime; $\mathrm{Pr}=0.71$) is shown in Figs. 9(*a*)–9(*b*), respectively. The predicted results show close agreement with previous studies of Baytas [21]. At the low Rayleigh number ($\mathrm{Ra}=10^3$), the entire flow field contributes to entropy production. But at $\mathrm{Ra}=10^6$, these irreversibilities occur predominantly near the sidewalls. Also, the maximum values occur near the center points along the sidewalls. At these locations, the near-wall velocities and their spatial gradients are highest, while adverse pressure gradients contribute to flow deceleration when the fluid approaches the corners of the cavity.

At the low Rayleigh number (10^3), comparable entropy production rates are observed along both horizontal and vertical walls, since comparable fluid accelerations are observed at those locations. But higher buoyancy along the side walls leads to greater differences of fluid acceleration and entropy production at the higher Rayleigh number (10^6). Entropy production depends on both temperature difference (between wall and fluid) and heat transfer rate. Thus, higher entropy production is often undesirable in free convection problems, since a higher temperature difference (i.e., additional input power to maintain this difference) is needed to maintain a fixed rate of heat transfer between the fluid and wall.

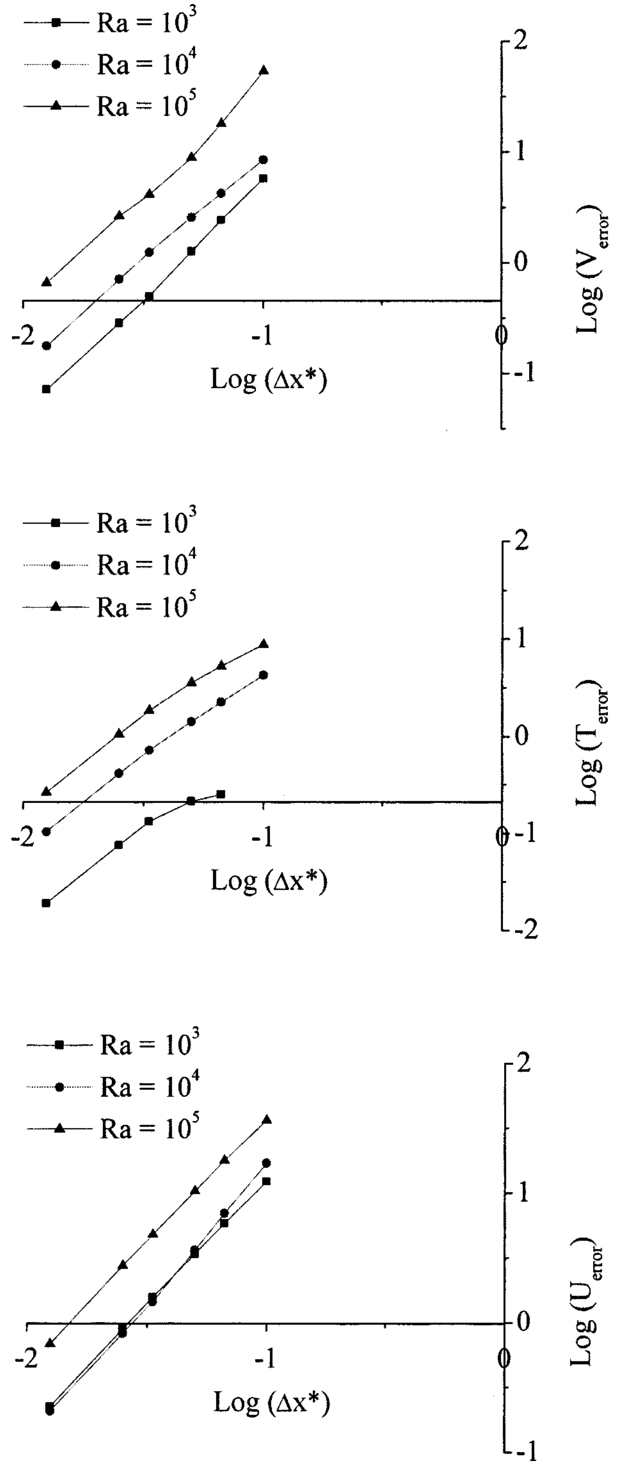

Fig. 8 Predicted temperatures and velocities at varying Rayleigh numbers

In the remaining figures, a second case of free convection is considered with a working fluid of water ($\mathrm{Pr}=8.06$). The hot and cold walls are maintained at 20 and 10°C, respectively, thereby yielding a Rayleigh number of 5.35×10^6. Measurement uncertainties of both velocity and entropy production data are outlined in the appendix.

The spatial resolution of measurements was approximately 0.1 mm, but measured velocities could be obtained within a distance

Downloaded 06 Dec 2010 to 193.140.21.150. Redistribution subject to ASME license or copyright; see http://www.asme.org/terms/Terms_Use.cfm

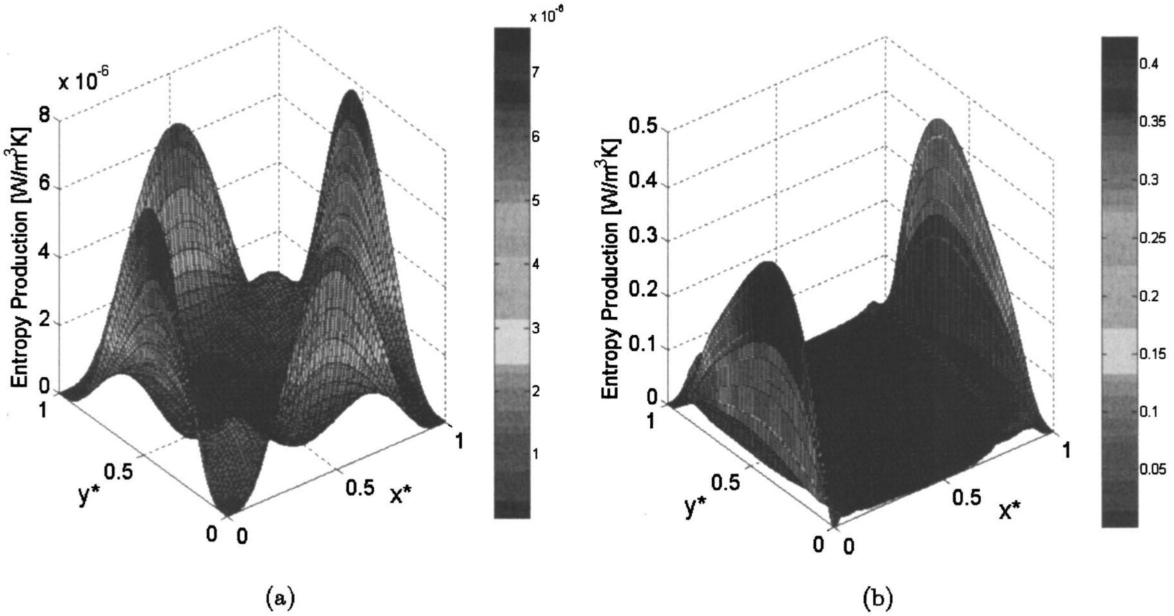

Fig. 9 Predicted entropy production at Rayleigh numbers of (a) 10^3 and (b) 10^6

of 0.2 mm from the wall. The total measurement uncertainty of measured velocities was about ±0.5% (see Appendix). Table 1 indicates similar accuracy in the numerical analysis, as the measured velocities and Nusselt numbers generally agree within ±1% of the benchmark solution at varying Rayleigh numbers. In this regard, velocity errors appear to have similar effects on the reported experimental and predicted rates of entropy production.

Surface plots of U-velocity values across the entire cavity are shown in Fig. 10. These results also show close agreement between predicted and measured results. The maximum horizontal velocity occurs near the top corner of the cold wall. Unlike fluid flow of air at Pr=0.71, where the maximum U-velocity is closer to the hot wall in the top corner of the cavity, the predicted and measured results in Fig. 10 (Pr=8.06; water) exhibit a maximum magnitude closer to the top corner of the cold wall. Buoyancy induced acceleration of fluid up the hot wall leads to an adverse pressure gradient and velocity change, when the fluid is redirected horizontally near that corner. This momentum exchange involves a balance between fluid inertia and forces imparted by pressure, friction, and fluid buoyancy. The frictional resistance of the fluid along the wall increases, when the momentum diffusion rate exceeds the energy diffusion rate (Pr>1). This affects the overall

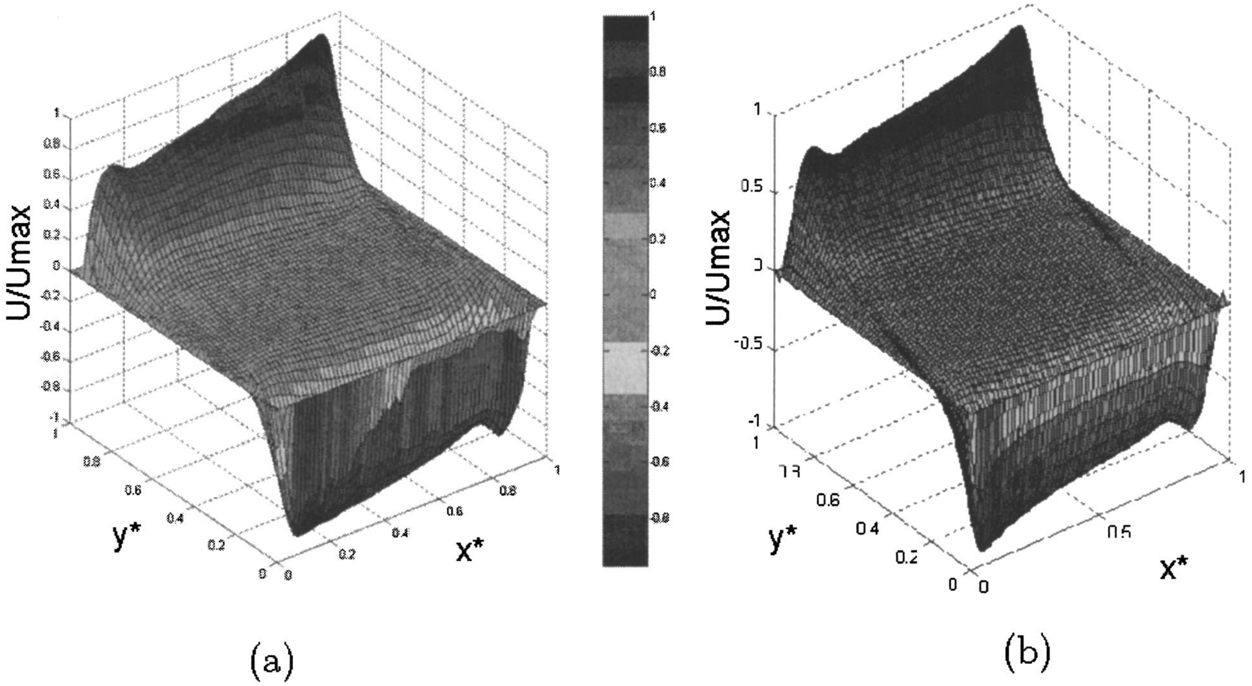

Fig. 10 (a) Predicted and (b) measured U-velocities (Ra=5.35×10^6, Pr=8.06)

Downloaded 06 Dec 2010 to 193.140.21.150. Redistribution subject to ASME license or copyright; see http://www.asme.org/terms/Terms_Use.cfm

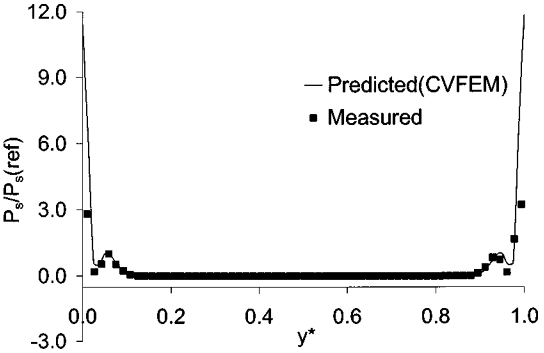

Fig. 11 Entropy production on horizontal mid-plane (Ra $=5.35\times10^6$, Pr$=8.06$)

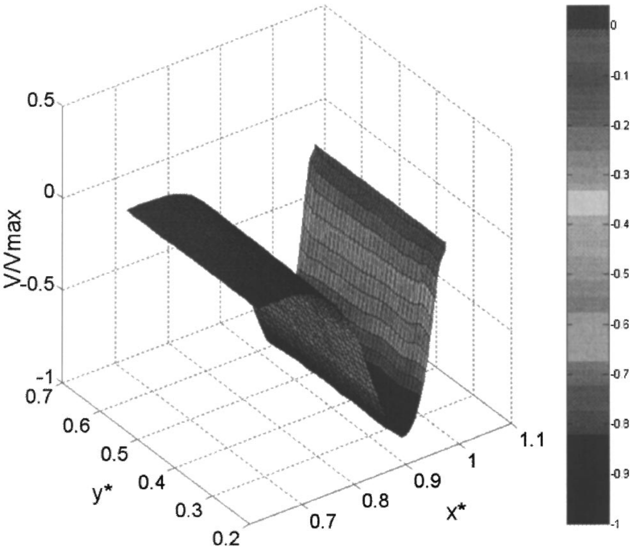

Fig. 13 Near-wall measured V-velocity (Ra$=5.35\times10^6$, Pr $=8.06$)

momentum balance on the fluid, thereby altering pressure gradients near the top corners of the cavity and changing the trends of maximum fluid velocity for air ($\Pr<1$) and water ($\Pr>1$). Also, the distance of this maximum velocity point from the wall changes at different Prandtl numbers. Past similarity solutions of free convection along a vertical wall have confirmed that the point of maximum velocity moves closer to the wall at higher Prandtl numbers (see Ref. [27]).

Postprocessing of the measured velocity results yields the spatial variation of entropy production throughout the cavity. Figure 11 shows the predicted and measured entropy production along the horizontal midplane. The peak values occur at the vertical walls, corresponding to the locations of largest spatial gradients of velocity. The measured data properly indicate that entropy production decreases to nearly zero at a point near the wall where the velocity reaches a peak value. This occurs due to the zero gradient of streamwise velocity, but a slight variation of cross-stream velocity at that location yields some entropy production.

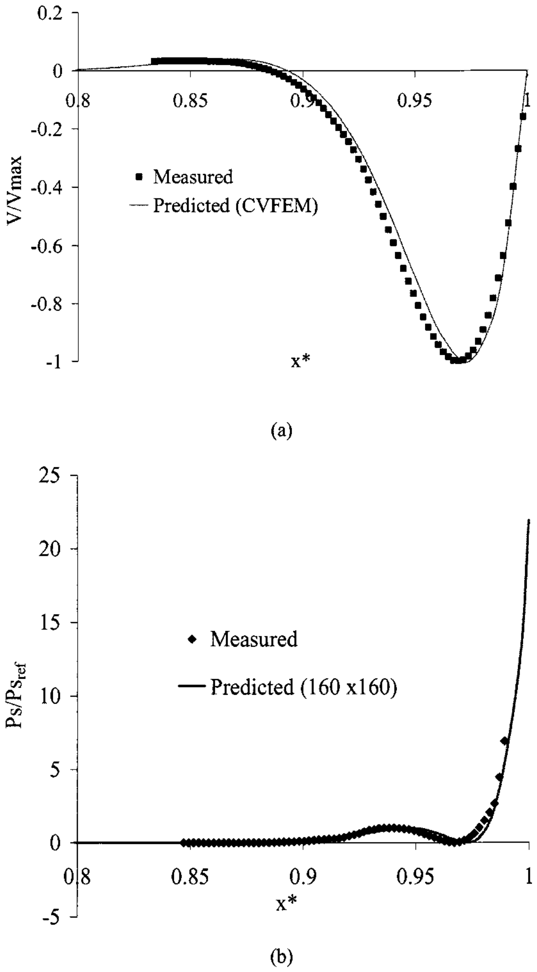

(a)

(b)

Fig. 12 Near-wall measurements on horizontal mid-plane (Ra $=5.35\times10^6$, Pr$=8.06$): (a) V-velocity (b) entropy production

Then, entropy production increases to a local maximum and decreases back to approximately zero at further distances from the wall. The local peak value occurs past the local velocity peak, where the decreasing velocity produces a relatively high entropy production rate. In Fig. 10, the entropy production is a minimum in the center of the cavity, where the stagnation point of the recirculation cell is observed. Experimental and predicted entropy production rates agree closely except close to the wall, due to certain limitations of PIV technology, i.e., camera resolution, particle seeding, and light reflection issues. These limitations and other uncertainties, including both bias and precision errors, lead to about $\pm0.5\%$ accuracy of measured velocities and $\pm8.77\%$ accuracy of resulting entropy production data near the wall (see Appendix).

Figures 12–14 show near-wall measurements of V-velocity and entropy production in the midregion of the cavity at the cold wall. In Fig. 12, the maximum velocity occurs close to the wall and approaches zero near the midpoint of the cavity, due to the stagnation point of the recirculation cell. The measured maximum U and V components of velocity are 0.611 mm/s and 1.69 mm/s, respectively. The predicted maximum U and V components of velocity are 0.632 mm/s and 1.89 mm/s, respectively. Although efforts were taken to minimize heat losses from the top, bottom, front, and backwalls, any losses may have affected thermal buoyancy, thereby yielding lower measured velocities, as compared with the numerical predictions.

Close agreement between predicted and measured velocities near the wall are important, since near-wall spatial gradients of velocity are needed for the entropy production calculations. Although PIV technology is limited by camera resolution and particle tracing of small-scale structures near the wall, the experiments successfully measured velocity and derived entropy production at very close proximity to the wall (see Figs. 12(*a*) and 12(*b*)). In particular, a resolution of 0.2 mm was achieved in the wall region between $0.65\leqslant x^*\leqslant1$ and $0.35\leqslant y^*\leqslant0.7$. Such near-wall accuracy becomes particularly significant for turbulent flows.

Downloaded 06 Dec 2010 to 193.140.21.150. Redistribution subject to ASME license or copyright; see http://www.asme.org/terms/Terms_Use.cfm

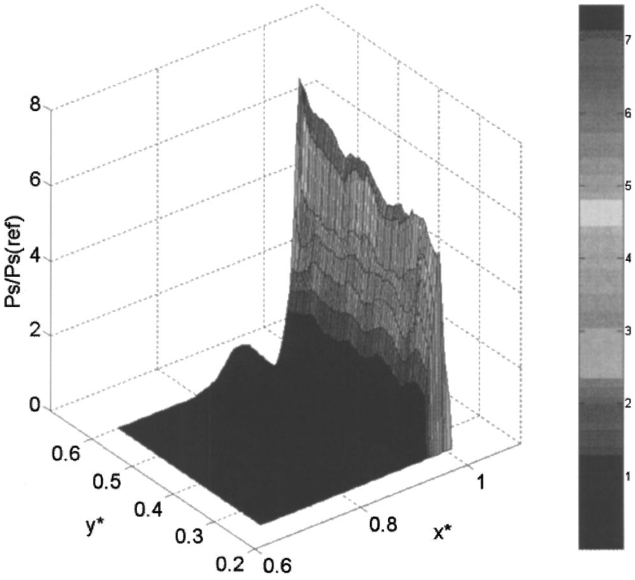

Fig. 14 Near-wall measured entropy production (Ra=5.35 ×10^6, Pr=8.06)

Since measured velocities with PIV are estimated over finite grids, the statistical analysis of turbulence data is influenced by a low-pass filter [33]. For this reason, conventional dissipation rate approximations would be limited in conventional PIV data analysis. Sheng et al. [34] viewed the resolution of finite scales by the PIV method, similarly to the large eddy simulation approach. The authors have devised a large eddy PIV method to use full-field velocity data and estimate the dissipation rate. The large eddy PIV method does not preclude the possibility of obtaining high resolution velocity measurements, where the detailed turbulent structures are captured [35]. However, it provides a useful estimate of the turbulent dissipation rate, in regions where the dynamic range of velocity measurements captured by PIV, is limited by the spatial resolution.

Figures 13 and 14 illustrate the quality of the experimental data in a representative subregion of the cavity. Such data can have valuable utility and add knowledge in engineering technologies involving free convection. For example, the placement of components in a microelectronic assembly could be modified, based on knowledge regarding high entropy production regions, in order to maximize thermal effectiveness of convective cooling. Another example is free convection between double-pane windows, whereby entropy production data can add insight regarding convective cell breakdown. Other applications include free convection in solar collectors and thermal processing of materials.

The measurement procedure is considered to be a useful diagnostic tool for identifying local flow losses, so that energy conversion devices can be redesigned locally around regions of highest entropy production. It is viewed that the current developments provide a useful basis, from which future advances can extend the method to more complex flows, such as turbomachinery, heat exchangers, or microelectronics cooling problems. Naterer and Camberos [36] have given a comprehensive historical review regarding how predictions of entropy production and exergy losses have exhibited considerable practical utility in such applications. In these technologies, local values of both friction and thermal components of entropy production can be mapped to detect key areas that require a design modification.

5 Conclusions

An experimental technique for measuring entropy production of laminar free convection has been presented. Measured velocities and temperatures are obtained with PIV and PLIF, respectively. Postprocessing of these results entails spatial gradients of velocity, which contribute to friction irreversibilities and entropy production. An experimental apparatus is constructed with free convection of water between differentially heated walls of a square cavity. A pulsed laser light sheet illuminates a cross-sectional plane of the cavity, so that two-dimensional profiles of velocity and temperature can be obtained. The peak value of entropy production occurs at the wall. A local maximum is measured close to the wall, due to a local velocity peak and zero spatial gradient of streamwise velocity component. The measurement procedure and data have been successful in characterizing whole-field entropy production rates. Such measurements provide a useful tool for evaluating local exergy losses, thereby contributing to local redesign of system components for higher overall energy efficiency.

Acknowledgment

This work was supported by a research grant from the Natural Sciences and Engineering Research Council of Canada to G.F.N., as well as a University of Manitoba Graduate Fellowship (O.B.A.). Also, infrastructure support from CFI (Canada Foundation for Innovation) and WED (Western Economic Diversification) is gratefully acknowledged.

Nomenclature

c_p = specific heat (J/kg K)
g = gravitational acceleration (m/s^2)
k = thermal conductivity (W/mK)
p = pressure (Pa)
Ra = Rayleigh Number=$g\beta\Delta TL^3/\nu\alpha$
Pr = Prandtl Number=ν/α
$\dot{P}_s$ = entropy production rate (W/m^3 K)
s = specific entropy (J/kg K)
t = time (s)
T = temperature (K)
q = heat flux (W/m^2)
u_i = components of velocity (m/s)
x,y = cartesian coordinates (m)
x^*,y^* = normalized position
U, V = velocity components (m/s)
h = Heat transfer coefficient (W/m^2 K)
B = width of cavity (m)
H = height of cavity (m)
D = depth of cavity (m)
Nu = Mean Nusselt number=hD/k

Greek

α = thermal diffusivity=k/ρc$_p$ (m^2/s)
β = coefficient of expansion
Φ = viscous dissipation function
ρ = density (kg/m^3)
μ = dynamic viscosity (kg/ms)
ν = kinematic viscosity (m^2/s)

Appendix—Measurement Uncertainties

Experimental uncertainties include errors arising in the PIV software, thermal bath, and others. Although all efforts were taken to minimize heat losses from the top/bottom walls, perfectly insulated boundaries are difficult to achieve in practice. Even small heat gains across these walls can have effects on the internal temperatures. In this appendix, measurement uncertainties are summarized based on the AIAA standard [37]. The total error consists of a bias component, B, plus a precision component, P. In the former case, the bias error of the measured velocity, U, is related to the elementary bias errors and sensitivity coefficients, i.e.:

$$B_U^2=\eta_{\Delta s}^2 B_{\Delta s}^2+\eta_{\Delta t}^2 B_{\Delta t}^2+\eta_{L_o}^2 B_{L_o}^2+\eta_{L_I}^2 B_{L_I}^2 \qquad (A\text{-}1)$$

Downloaded 06 Dec 2010 to 193.140.21.150. Redistribution subject to ASME license or copyright; see http://www.asme.org/terms/Terms_Use.cfm

where the sensitivity coefficients are defined as $\eta_\chi = \partial U/\partial \chi$. Also, Δt is the time interval between laser pulses, Δs is the particle displacement from the correlation algorithm, L_o is the width of the camera view in the object plane, and L_I is the width of the digital image. Assembling contributions for each source of bias error, a velocity bias error of 0.45% is obtained.

For the second component of error, the precision error measured from N samples is given by

$$P = \frac{t\sigma}{N} \tag{A-2}$$

In this equation, t is the confidence coefficient (equaling 2 for a 95% confidence interval) and σ is the standard deviation of the sample of N images. The standard deviation is given by

$$\sigma = \sqrt{\frac{1}{N-1}\sum_{k=1}^{N} (X_k - \overline{X})^2} \tag{A-3}$$

where the average quantity is defined by

$$\overline{X} = \frac{1}{N}\sum_{k=1}^{N} X_k \tag{A-4}$$

Calculated values of the standard deviation at the points of maximum velocity and near the wall are 0.5% and 1.2%, thereby yielding precision limits of 0.005% and 0.012%, respectively. As a result, the total uncertainties of measured velocity at these points are 0.45% and 0.5%, respectively.

Then, the data reduction equation for entropy production is written as

$$P_s = \frac{\mu}{T}\left\{\left(\frac{\Delta u_y}{\Delta y}\right)^2 + \left(\frac{\Delta v_x}{\Delta x}\right)^2 + \left(\frac{\Delta u_x}{\Delta x}\right)^2 + \left(\frac{\Delta v_x}{\Delta y}\right)^2\right\} \tag{A-5}$$

Using a similar procedure as applied previously for the bias and precision errors of measured velocity, the total error of measured entropy production becomes

$$\varepsilon_{P_s}^2 = \eta_T^2\varepsilon_T^2 + \eta_{\Delta U}^2\varepsilon_{\Delta U}^2 + \eta_{\Delta y}^2\varepsilon_{\Delta y}^2 \tag{A-6}$$

This equation gives a total uncertainty of measured entropy production to be 8.77% at $X = 0.985L$ and $Y = 0.46L$ with a velocity resolution of 0.2 mm. This error estimate represents a maximum error bound within the 95% confidence interval.

References

[1] De Vahl Davis, G., 1983, ''Natural Convection of Air in a Square Cavity: A Benchmark Solution,'' Int. J. Numer. Methods Fluids, **3**, pp. 249–264.

[2] Hortmann, M., Peric, M., and Scheuerer, G., 1990, ''Finite Volume Multigrid Predictions for Laminar Natural Convection: Benchmark Solution,'' Int. J. Numer. Methods Fluids, **11**, pp. 189–207.

[3] Lightstone, M. F., and Collins, W. M., 1994, ''Simulation of Natural Convection of Air in a Square Cavity Using the GOTHIC Thermohydraulic Code,'' Proceedings of the CNA/CNS Annual Conference, Montreal, Canada, June 5–8.

[4] Ismail, K. A. R., and Scalon, V. L., 2000, ''A Finite Element Free Convection Model for the Side Wall Heated Cavity,'' Int. J. Heat Mass Transfer, **43**, pp. 1373–1389.

[5] Bejan, A., 1996, *Entropy Generation Minimization: The Method of Thermodynamic Optimization of Finite-Time Systems and Finite-Time Processes*, CRC Press, Boca Raton, FL.

[6] Poulikakos, D., and Bejan, A., 1982, ''A Fin Geometry for Minimum Entropy Generation in Forced Convection,'' Trans. ASME, **104**, pp. 616–623.

[7] Zubair, S. M., Kadaba, P. V., and Evans, R. B., 1987, ''Second-Law-Based Thermoeconomic Optimization of Two-phase Heat Exchangers,'' ASME J. Heat Transfer, **109**, pp. 287–294.

[8] Bejan, A., 1979, ''A Study of Entropy Generation in Fundamental Convective Heat Transfer,'' Trans. ASME, **101**, pp. 718–725.

[9] Adeyinka, O. B., and Naterer, G. F., 2002, ''Predictive Entropy Production and Measurement with Particle Image Velocimetry (PIV) for Recirculating Flows,'' AIAA/ASME 8th Joint Thermophysics and Heat Transfer Conference, AIAA Paper-2002-3090, St. Louis, M., June.

[10] Moore, J., and Moore, J. G., 1983, ''Entropy Production Rates from Viscous Flow Calculations Part I-A Turbulent Boundary Layer Flow,'' ASME Gas Turbine Conference, ASME Paper 83-GT-70, Phoenix.

[11] Moore, J., and Moore, J. G., 1983, ''Entropy Production Rates from Viscous Flow Calculations Part II—Flow in a Rectangular Elbow,'' ASME Gas Turbine Conference, ASME Paper 83-GT-71, Phoenix.

[12] Drost, M. K., and White, M. D., 1991, ''Numerical Predictions of Local Entropy Generation in an Impinging Jet,'' ASME J. Heat Transfer, **113**, pp. 823–829.

[13] Kramer-Bevan, J. S., 1992, ''A Tool for Analysing Fluid Flow Losses,'' M.Sc. thesis, University of Waterloo.

[14] Cheng, C. H., Ma, W. P., and Huang, W. H., 1994, ''Numerical Predictions of Entropy Generation for Mixed Convective Flows in a Vertical Channel with Transverse Fin Arrays,'' Int. J. Heat Mass Transfer, **21**, pp. 519–530.

[15] Sahin, A. Z., 2000, ''Entropy Generation in Turbulent Liquid Flow Through a Smooth Duct Subjected to Constant Wall Temperature,'' Int. J. Heat Mass Transfer, **43**, pp. 1469–1478.

[16] Sahin, A. Z., 2002, ''Entropy Generation and Pumping Power in a Turbulent Fluid Flow Through a Smooth Pipe Subjected to Constant Heat Flux,'' Exergy, An International Journal, **2**, pp. 314–321.

[17] Demirel, Y., 1999, ''Irreversibility Profiles in a Circular Couette Flow of Temperature Dependence Materials,'' Int. Commun. Heat Mass Transfer, **26**, pp. 75–83.

[18] Mahmud, S., and Fraser, R. A., 2002, ''Thermodynamic Analysis of Flow and Heat Transfer Inside Channel with Two Parallel Plates,'' Exergy, An International Journal, **2**, pp. 140–146.

[19] Mahmud, S., and Fraser, R. A., 2002, ''Analysis of Entropy Generation Inside Concentric Cylinder Annuli With Relative Rotation,'' Int. J. Therm. Sci., **42**, pp. 513–521.

[20] Baytas, A. C., 1997, ''Optimization in an Enclosure for Minimum Entropy Generation in Natural Convection,'' J. Non-Equilib. Thermodyn., **22**(2), pp. 145–155.

[21] Baytas, A. C., 2000, ''Entropy Generation for Natural Convection in an Inclined Porous Cavity,'' Int. J. Heat Mass Transfer, **43**, pp. 2089–2099.

[22] Megherbi, M., Abbassi, H., and Brahim, A. B., 2003, ''Entropy Generation at the Onset of Natural Convection,'' Int. J. Heat Mass Transfer, **46**(18), pp. 3441–3450.

[23] Abu-Hijleh, B. A., and Heilen, W. N., 1999, ''Entropy Generation Due to Laminar Natural Convection Over a Heated Rotating Cylinder,'' Int. J. Heat Mass Transfer, **42**, pp. 4225–4233.

[24] Meyer, K. E., Larsen, P. S., Guillard, F., and Westergaard, C. H., 2002, ''Temperature and Velocity Fields in Natural Convection by PIV and LIF,'' 11th International Symposium on Application of Laser Techniques to Fluid Mechanics, Lisbon, Portugal, July.

[25] Coolen, M. C. J., Kieft, R. N., Rindt, C. C. M., and Van Steenhoven, A. A., 1999, ''Application of 2-D LIF Temperature Measurement in Water using a Nd:YAG Laser,'' Exp. Fluids, **27**, pp. 420–426.

[26] Adeyinka, O. B., 2002, ''Entropy and Second Law Optimization in Computational Thermofluids with Laser Based Measurements.,'' M.Sc. thesis, University of Manitoba.

[27] Naterer, G. F., 2002, *Heat Transfer in Single and Multiphase Systems*, CRC Press, Boca Raton, FL.

[28] Adeyinka, O. B., and Naterer, G. F., 2002, ''Apparent Entropy Difference with Heat and Fluid Flow Irreversibilities,'' Numer. Heat Transfer, Part B, **42**, pp. 411–436.

[29] Schneider, G. E., 1988, ''Elliptic Systems: Finite Element Method I,'' in *Handbook of Numerical Heat Transfer*, W. J. Minkoycz, E. M. Sparrow, G. E. Schneider, and R. H. Pletcher, eds., J Wiley, New York.

[30] Westerweel, J., 2002, ''Introduction to PIV,'' Dantec Dynamics website: www.dantecmt.com June.

[31] Mallinson, G. D., and De Vahl Davis, G., 1977, ''Three Dimensional Natural Convection in a Box: A Numerical Study,'' J. Fluid Mech., **83**(1), pp. 1–31.

[32] Hamady, F. J., and Lloyd, J. R., 1989, ''Study of Local Convection Heat Transfer in an Inclined Enclosure,'' Int. J. Heat Mass Transfer, **32(9)**, pp. 1697–1708.

[33] *FlowMap Particle Image Velocimetry Instrumentation: Installation and User Guide*, Dantec Dynamics, Demark, 1998.

[34] Sheng, J., Meng, H., and Fox, R. O., 2000, ''A Large Eddy PIV Method for Turbulence Dissipation Rate Estimation,'' Chem. Eng. Sci., **55**, pp. 4423–4434.

[35] Liu, Z. C., Landreth, C. C., Adrain, R. J., and Hanratty, T. J., 1991, ''High Resolution Measurement of Turbulent Structure in a Channel with Particle Image velocimetry,'' Exp. Fluids, **10**, pp. 301–312.

[36] Naterer, G. F., and Camberos, J. A., 2003, ''Entropy and the Second Law in Fluid Flow and Heat Transfer Simulation,'' AIAA Journal of Thermophysics and Heat Transfer, **17**(3), pp. 360–371.

[37] AIAA-Standard-S017-1995, 1995, ''*Assessment of Experimental Uncertainty with Application to Wind Tunnel Testing*,'' American Institute of Aeronautics and Astronautics, Washington, DC.

Downloaded 06 Dec 2010 to 193.140.21.150. Redistribution subject to ASME license or copyright; see http://www.asme.org/terms/Terms_Use.cfm

Minh Vuong Pham
Ph.D. Student

Frédéric Plourde
Senior CNRS Scientist

Son Doan Kim
Professor

Laboratoire d'Etudes Thermiques,
Ecole Nationale Supérieure de Mécanique et
d'Aérotechnique,
Téléport 2,
1 Avenue Clément Ader,
BP 40109,
86961 Futuroscope Cedex, France

Three-Dimensional Characterization of a Pure Thermal Plume

Pure thermal plumes have been investigated by two-dimensional (2D) and three-dimensional (3D) particle imaging velocimetry (PIV) techniques. While classical plume features have been checked out, time-dependent analysis allows one to clearly detect contraction and expulsion phases which are mainly driven by turbulent structure behavior. Balance of momentum equation demonstrates the link between stronger structures and expulsion-contraction motion mainly dominated by plume engulfment during contraction phases. A ratio of 3 between entrained mass flow rate during contraction and expulsion phases has been estimated. A new method, never previously applied to pure thermal plume, allows one to accurately characterize entrainment mechanism and for the first time, the latter renders it possible to estimate the entrainment coefficient all along the plume height, even close to the heating source. Moreover, entrainment coefficient is found to be 20% higher with direct method as opposed to the classical differential one widely used in the literature. Such a huge gap is found to be due to the fluctuating density and velocity part. Even through it markedly contributes to an enhanced entrainment mechanism, the role of fluctuation was generally overlooked in the previous works devoted to entrainment coefficient estimate. [DOI: 10.1115/1.1863275]

Introduction

Given the importance in the engineering field of natural flows in general and thermal plumes in particular, pure thermal plumes have been widely investigated from either a theoretical, experimental, or numerical point of views; dispersion and dilution of pollutants in the atmosphere, fire development, cooling towers and cumulus cloud may be listed just to mention a few examples of practical interest. Several key points have been specifically dealt with, such as laminar turbulence transition. For instance, Gebhart et al. [1] pointed out that turbulence is an event subsequent to the initial instability of a laminar flow and stated that perturbations in the plume can grow in amplitude; such a mechanism is then driven mainly by buoyancy. Quick amplification is generally observed and such behavior is surely due to the absence of boundaries. According to Elicer-Cortes et al. [2], transition is governed by growth mechanisms of linear disturbances at the beginning and nonlinear ones far away from the plume source. To depict the turbulent region, Morton et al. [3] developed an analytical approach, still valid today, enabling one to characterize temperature and velocity distributions inside the plume. Such analytical development was based on the entrainment concept initially introduced by Taylor [4]. This concept states mainly that a turbulent buoyant element expands at the expense of the quiescent surrounding fluid through entrainment of exterior fluid. Morton et al. [3] established that the entrainment velocity is proportional to the vertical velocity, and that such a proportional coefficient is a constant. Experiments were conducted in order to estimate this coefficient, which still constitutes a challenge. Ricou and Spalding [5] directly measured entrainment in a turbulent jet by surrounding the latter with a porous cylindrical-walled chamber; air was injected through the wall until pressure in the chamber was uniform and atmospheric so that entrainment was satisfactorily performed. Such a technique induces strong uncertainties and because of the fragile plume feature, one cannot carry out this kind of measurement without greatly disturbing flow field behavior. To characterize plume development and also to check out entrainment theory, measurements in thermal plumes have been carried out with hotwires and laser Doppler anemometry (LDA). For instance, George et al. [6] performed measurements of temperature and velocity in an axisymmetric turbulent buoyant plume and measurements were carried out with two-wire probes allowing temperature-velocity correlations. Shabbir and George [7] performed a comprehensive set of hot-wire measurements of a round buoyancy jet in which vertical and lateral velocity components were determined and results show satisfactory agreement with the expected similarity scaling. In addition, Papanicolau and List [8] and Dehmani et al. [9], to quote just a few, performed measurement of velocities using the laser Doppler anemometer technique and obtained vertical and lateral velocity distributions. Such measurements provide confirmation of the theoretical development [3]. Recently, integral methods have been also implemented by Agrawal and Prasad [10] in order to derive similarity solutions for several quantities of pronounced interest, such as cross-stream velocity, Reynolds stresses and diffusivity of momentum and heat. The cross-stream velocity profiles show that axisymmetric plumes experience an outflow near the axis and an inflow far away from it. Agrawal and Prasad [10] also showed that the entrainment velocity should not in general be equated to the product of the entrainment coefficient and the centerline velocity. Brahimi et al. [11] estimated the α entrainment coefficient by measuring average velocity field with LDA. As far as we know, the particle image velocimetry (PIV) has not yet been used to characterize thermal plume development. However, such a technique has been successively employed by Han and Mungal [12] in turbulent jets and a direct method for the entrainment coefficient was tested. Such measurements enable one to directly and accurately investigate entrainment properties of nonreacting and reacting jets.

In addition to entrainment characterization, it is important to stress that recent numerical works were dedicated to thermal buoyant jets and that due to significant improvement in computing science and continuous increase of computer efficiency, light has been shed on the role of vortex dynamics in plume development. Recently, Zhou et al. [13] reported on the turbulence characterization in a forced plume from large-eddy simulation; a fair comparison between numerical and experimental data was achieved. Agreement was reached in the mean fields as well as in the fluc-

---

Contributed by the Heat Transfer Division for publication in the JOURNAL OF HEAT TRANSFER. Manuscript received September 1, 2004; revision received November 24, 2004. Review conducted by: J. H. Lienhard V.

Copyright © 2005 by ASME

Downloaded 06 Dec 2010 to 193.140.21.150. Redistribution subject to ASME license or copyright; see http://www.asme.org/terms/Terms_Use.cfm

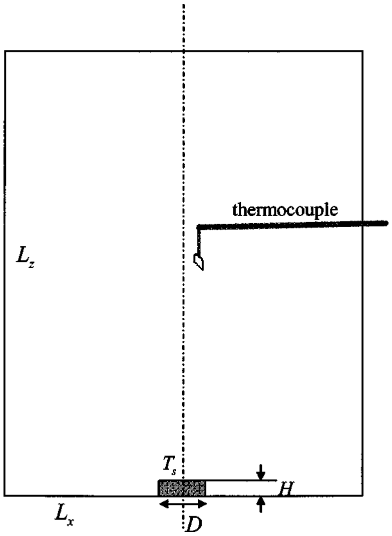

Fig. 1 Schematic of thermal plume experiment

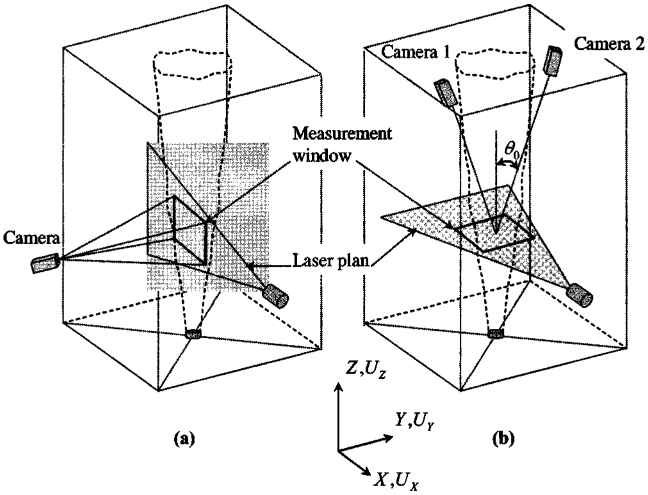

Fig. 2 Measurement setup using (*a*) classical 2D PIV technique and (*b*) stereoscopic PIV technique

tuating fields. For instance, the energy spectrum for fluctuating fields contains a $-5/3$ and -3 power-law in the inertial-convective and inertial-diffusive ranges and highlights the ability of large-eddy simulation to capture the whole turbulent flow field behavior. Moreover, Basu and Narimsha [14] performed simulations of heated and nonheated jets, and they clearly demonstrated that enhancement of vorticity, due to vortex stretching, favors intense structures that tend to attract fluid from the quiescent environment. Thus, correlation between large structures and entrainment has been demonstrated but no experimental evidence may be found in the literature of pure plume development. Agrawal and Prasad [15,16] provided recently spatial filtering of PIV data in a self-similar axisymmetric turbulent jet in order to exhibit the role of large vortices which tend to organize themselves. Actually, such links require three-dimensional computations to depict structure development in the plume while no works have yet been devoted to plume analysis through PIV measurements or through stereoscopic PIV measurements either. Actually, stereoscopic measurement is a promising way of measuring the three velocity components which facilitates assessment of turbulent intensity as well as structures involved in the flow.

The aim of the present study is to characterize the three-dimensional behavior of a pure thermal plume and to address its behavior in time so as to depict the role of structures in the entrainment mechanism. In addition, a direct technique has been tested to measure the α entrainment coefficient along the plume axis which as far as we know has never been done in the past.

Experiment Setup and Measurement Technique

Experimental Setup. The heating source is made up of a metallic disk with a D diameter of 0.1 m and a thickness of 0.02 m. The heat is provided by a heating resistance wire which is located directly inside the metallic disk. A regulated A.C. of 1 KVA supplied electric power and was able to keep the disk temperature at a constant level of $T_S=400°\text{C}$. As shown in Fig. 1, the heating source was located in a large enclosure of $2\,\text{m}\times 2\,\text{m}\times 2.5\,\text{m}$ filled with air and such an enclosure was assumed to be large enough to provide nonconfined conditions for the plume. Stratification in the enclosure will be addressed later in this part but first, it is noteworthy that the disk was mounted above the enclosure floor at a 0.01 m height to help the plume to establish. Actually, even such a limited distance is large enough to concentrate fluid flow around the disk and to ensure stabilization of the plume development. Moreover, such an artifact was widely used in the past in the study of thermal plume. For instance, Elicer-Cortés et al. [2] performed their analysis with a flat disk located at 0.3 m above the floor. On the contrary, Guillou and Doan-Kim [17] performed an experimental setup which was flushed mounted at the ground level of the enclosure but the shape of the heating source was a sphere portion ensuring the stabilizing development of pure thermal plumes.

As just mentioned, a strong dependency between plume development and its surrounding environment requires actual control of the latter. Thus, the enclosure in which the plume develops was integrated in a larger room of $6\,\text{m}\times 6\,\text{m}\times 6\,\text{m}$ which was equipped with an air conditioning system and its temperature was kept at a constant level of 20°C. It is very important to control the plume environment because of temperature stratification, which may greatly change plume flow development. For instance, Beuther and George [18] and Dehmani et al. [19] showed that only a slight stratification level in the ambient fluid generates a significant loss or gain of the buoyancy force. In order to check out the stratification in our own enclosure, temperature in the immediate environment of the plume was regularly controlled by an Al–Cr thermocouple of 12.7 μm diameter. In accordance with the whole temperature acquisition system, temperature measurement errors were found to be less than 0.01°C. The thermocouple was fixed on a (3D) traverse system allowing the latter to determine height-wise temperature profile. The traverse system resolution is equal to 1 mm. In our setup, a 0.4°C/m was found as temperature stratification and in conjunction with established criteria [18], such a stratification level is not strong enough to directly interact and alter plume flow field development. Thus, one can consider that our experimental setup may help us to study plume development in a semi-infinite open domain. Two of the main lateral walls were optical Plexiglas in order to investigate the flow by optical measurement methods.

Measurement Techniques. In order to measure the flow field velocity, particle imaging velocimetry technique (PIV) was used and we also performed 2D as well as 3D stereoscopic PIV measurements. For both of these measurements, Hamamatsu Hisence cameras provided 1024×1280 pixel resolution pictures. Each pixel was sized 6.7×6.7 μm and a pair of images was recorded at a 9.0 Hz rate. To illuminate the flow field, a 50 mJ frequency doubled Ng-Yag laser was set up in synchronization with cameras. The laser plane was oriented in accordance with the type of measurement (2D or 3D) as shown in Fig. 2.

In the 2D configuration, only one camera was necessary and was equipped with a 28 mm lens, and it focused a plane at a 1.0 m interval. The plane of measurement was then approximately $25\,\text{cm}\times 30\,\text{cm}$. The time delay between two consecutive pictures

Downloaded 06 Dec 2010 to 193.140.21.150. Redistribution subject to ASME license or copyright; see http://www.asme.org/terms/Terms_Use.cfm

was arbitrarily fixed according to the kind of measurement to carry out. A short time delay of about 2 ms was setup to determine the vertical velocities while on the contrary, a longer time delay (~20 ms) was necessary to select in order to accurately capture the radial component. Actually, the differing time delays are due to the expected vast differences in axial and radial velocity magnitudes. It is true that measuring entrainment velocities in the plume surrounding require particular attention given the fact that radial displacements are equivalent to 2 up to 4 pixels compared to the bias error of PIV. On the contrary, long time delays are not adapted to axial velocities ranging from 20 to 30 pixels and no correlations are accessible with a regular interrogation zone. With a view window of 26 cm × 30 cm, the interrogation zone is set to 32 × 32 pixels using 50% overlapping, which corresponds to a 63 × 79 vector resolution in the *XZ* plane.

For the 3D stereoscopic velocity measurements, two cameras were installed as shown in Fig. 2(*b*). The laser sheet was located so as to create a horizontal plane perpendicular to the vertical axis. The two cameras were located at 1 m from the laser plane to obtain 30 cm × 30 cm of window measurement. Each camera was positioned at a certain angle from the normal measurement plane in order to obtain a stereo view of the plane depending on the laser sheet orientation. Alkislar [20] estimated that errors are minimized when θ_0 ranges from 30 deg to 60 deg. In the present study, θ_0 has been arbitrarily fixed at 30 deg and camera calibration routines are necessary before performing measurements that integrate and account for perspective distortion arising from the skewed orientation of the cameras. After processing images from each camera, data had to be processed so as to evaluate the third velocity component perpendicular to the laser sheet plane. Equations governing transformation of images and data processing from the two different views yielding a three-dimensional velocity field are put forward by Alkislar [20]. Measurements of the velocity field were carried out in several sections corresponding to different vertical heights in moving cameras and laser sheet. At each plane, over 200 s were necessary in order to acquire 800 instantaneous velocity fields at a rate of 4.0 Hz.

Velocity measurements through PIV method necessitate seeding the flow with small droplets which scatter the laser light and it matters to lay emphasis on the pronounced accuracy of this high-tech process. When estimating the method's degree of precision, one may first list the potential sources of error: Influence of dynamic-particles, processing errors, systematic errors introduced by the effect of temperature gradient including beam steering and image distortion. Concerning error linked to particle dynamic, the latter is due to slip velocity between the particle and the fluid and may be estimated through the *St* Stockes number estimation. This relates the τ_p characteristic particle response time versus the τ_f time scale of the flow variation. For $St \ll 1$, one can consider that particles indeed follow the fluid motions to be measured. All of our measurements were performed by using glycerin particles originating in a smoke generator and it is assumed that the diameter particle range is 5–10 μm. According to the diameter, density, and velocity level of the flow, one can assume that the bias due to dynamic-particles is around 0.2%. To estimate processing errors, we took a picture as reference while a second one was created by introducing a previously known displacement throughout the complete first one. Then, one may just have to compare the PIV estimation with regard to the introduced displacement. The processing errors are due algorithm and may be estimated as 0.1 pixels that correspond to 1.8% error for a standard 32 × 32 interrogation window size cross-correlation. The beam steering error is linked to the index of refraction change due to the density variation in thermal plume but along with image distortion effects, such an error may be considered negligible [21].

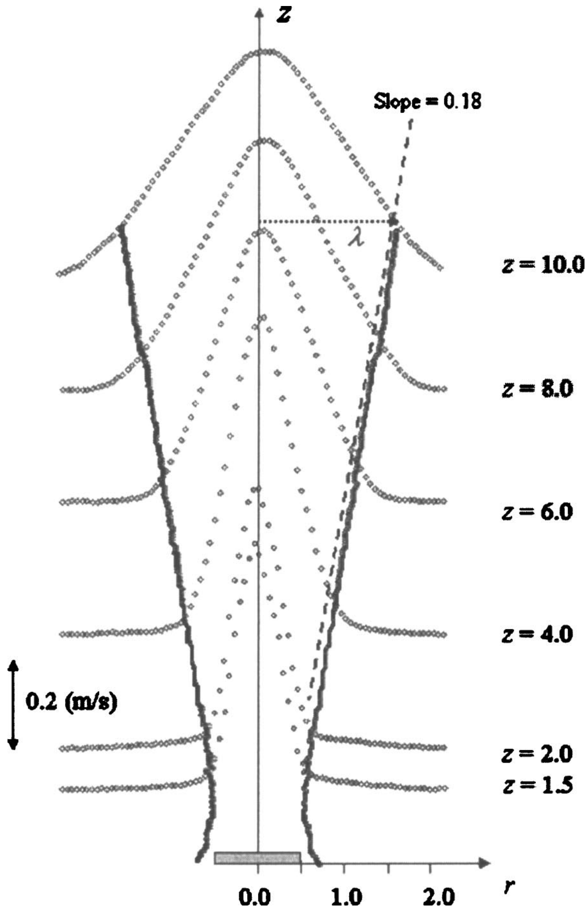

Fig. 3 Radial profiles of the $\overline{U_z}$ mean axial velocity component and λ plume width change with regard to *z*

Thermal Plume Characterization

Mean and Fluctuating Velocity Fields. As already mentioned in the Introduction, particle imaging velocimetry has not yet been used to depict plume flow field development. However, the technique allows us to instantaneously measure two or even three velocity components when using stereoscopic PIV technique and it may likewise be an excellent way to assess structure development as well as velocity fluctuation correlations. One of the first steps is to depict plume flow field through such measurements in order to validate the technique used with regard to results available in the literature. Figure 3 presents the $\overline{u_z}$ mean axial velocity profiles along a lateral direction at given heights above the source. It appears obvious that profiles obtained in the vicinity of the heating source, see for instance, at $z = 1.5$ and 2.0, have a pointed shape while the farther they are from the source, the more profiles become larger and fit a Gaussian distribution. Such a trend is typical in a plume study when the flow field organizes towards a fully developed turbulent way; velocity profiles fit a well-known self-similar region. Figure 4 allows one to clearly observe such a region in which the axial velocity profile is normalized by its maximum value reached close to the plume axis. And then, above $z = 4.0$, the whole vertical velocity profile satisfactorily corresponds to a Gaussian law:

$$\overline{u_z}(r,z)=\overline{u_{z,c}}e^{-B\varepsilon^2}$$

The constant value *B* obtained with our results is comparable with values reported by Shabbir and George [7] and Chen and Rodi [22]. Figure 3 also presents the λ normalized plume width change (in round point line) and such a parameter has been estimated through momentum balance as:

Downloaded 06 Dec 2010 to 193.140.21.150. Redistribution subject to ASME license or copyright; see http://www.asme.org/terms/Terms_Use.cfm

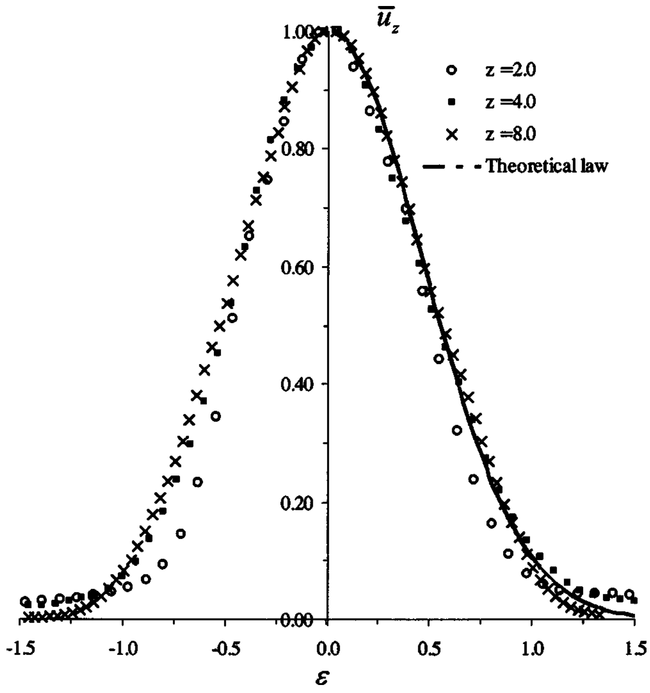

Fig. 4 Normalized radial profiles of the $\overline{u}_z$ mean axial velocity component

$$\lambda^2 = \frac{2\left(\int_0^\infty \overline{u}_z r dr\right)^2}{\int_0^\infty \overline{u}_z^2 r dr}$$

The change of the λ normalized plume first decreases up to a minimum value close to $z=1.5$ and from this point, increases with regard to z. Such an evolution sheds light on plume restriction before its enlargement. Then, λ evolves linearly close to $z\sim3.0$; such linear change is in agreement with the theoretical point of view [3] and its linear slope is found to be equal to 0.18, while in the literature, authors [7,8,23] focused upon reported values in the 0.14–0.18 range. To show how plume develops, mean axial velocity is often taken as a reference and its normalized change is reported in Fig. 5. Mean axial velocity is normalized by its highest value reached at $z=3.5$. Figure 5 clearly puts forward that $\overline{u}_{z,c}/\overline{u}_{z,\max}$ follows a $-1/3$ power law for $z\geqslant4.0$ with $\overline{u}_{z,c}z^{1/3}=A_1$, where the A_1 value is found to be equal to 1.26 approximately and is in agreement with values reported in previous works [8]. Evolution of the $\overline{u}_{z,c}/\overline{u}_{z,\max}$ normalized centerline velocity is significant because plume is assumed to be fully turbulent when the $-1/3$ power law is followed. Thus, it is a convenient way of precisely locating the laminar–turbulent transition and such transition occurs close to $z\sim4.0$.

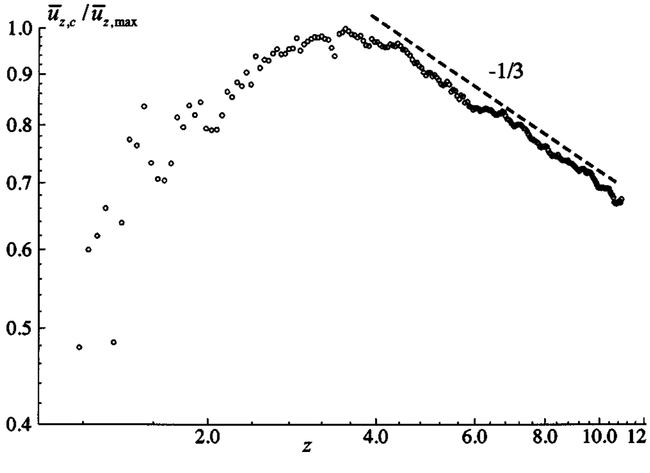

Fig. 5 Change of the normalized $\overline{u}_{z,c}/\overline{u}_{z,\max}$ mean axial velocity component along the geometrical axis

After describing the average flow field development and confirming that the well-known laws are followed, we likewise focused on higher statistical orders to determine how the turbulent plume behaves. With this in mind, the radial profiles of the axial, radial, and circumferential root-mean-square velocities are plotted in Fig. 6. It is noticeable in Fig. 6(*a*) that $\sqrt{\overline{u_z'^2}}/\overline{u}_{z,c}$ reveals off-axis maxima of 25%; such value is in agreement with those found in the literature [8,24]. Concerning the radial and tangential fluctuating activity shown in Figs. 6(*b*) and 6(*c*), profile shape as well as the intensities reached are similar, maximum levels being smaller than those obtained in the vertical flow field. Moreover, one of the advantages of measuring plume velocity with a stereoscopic method is the possibility of plotting the *It* turbulent intensity without any particular assumption (see Fig. 6(*d*)). *It* profiles also reveal off-axis maxima of about 34% and are not altered above $z\geqslant4.0$. Figure 7 allows researchers to spatially depict the fluctuating flow field behavior. In particular, several maps at different heights in the plume clearly underline that its development occurs symmetrically with regard to the plume geometrical axis as well as off-axis maximum location. Nevertheless, it is true that the greater z, the more the maximum location of *It* is close to the axis; this is due to the homogeneity process driven by turbulence. Finally, it is important to emphasize that the levels reached by *It* are significant in the vicinity of the heating source as shown in Fig. 7(*b*). To do this, we use the 2D PIV and *It* was computed assuming that the radial and circumferential fluctuation levels were similar. In addition, Fig. 7(*b*) compares *It* magnitudes obtained by 2D PIV and 3D PIV measurements. Actually, *It* rises up to 60% for $z\leqslant1.0$ and decreases sharply for higher z locations and reaches a constant value of approximately 34%. It must likewise be underlined that such high intensities in the fluctuating field close to the source are linked to severe perturbations in the area in which fluid flow develops.

Vortex Structure Development. Thermal plume structure has been fully investigated by characterizing its expansion, Gaussian axial velocity distributions in radial direction, power $-1/3$ law axial centerline velocity in vertical direction, and turbulent intensity as well. However, it is helpful to bear in mind that tracking instantaneous turbulent structure will help us to fully understand the flow field development, but we still need to describe structures in such flows. Moreover, previous experimental studies did not use techniques allowing them to detect structures in the plume development. However, there are several studies in the literature dedicated to plume flow field visualization. Morton et al. [3] as well as Turner [23] were the first to carry out plume visualization, and the hypothesis of coherent structures inside the plume development was convincingly put forward. Recently, Zinoubi et al. [24] performed a plume visualization allowing for the demonstration of three different regions lengthwise in the plume. One of the regions is mainly driven by plume contraction while above the latter, the appearance of small structures is detected and the existence of these turbulent structures leads to uniform flow field behavior. Due to recent improvement in computing science, Zhou et al. [13] depicted flow field behavior and structure changes through a large eddy simulation technique. Similarly to Zhou's approach, we have characterized instantaneous structures by estimating the ω_θ azimuthal vorticity field. Figures 8(*a*) and 8(*b*) show instantaneous ω_θ maps in the r-z plane passing through the geometrical plume axis at two different time steps. Figure 8 mainly focuses on a region close to the heating source ($z\leqslant3.0$).

Downloaded 06 Dec 2010 to 193.140.21.150. Redistribution subject to ASME license or copyright; see http://www.asme.org/terms/Terms_Use.cfm

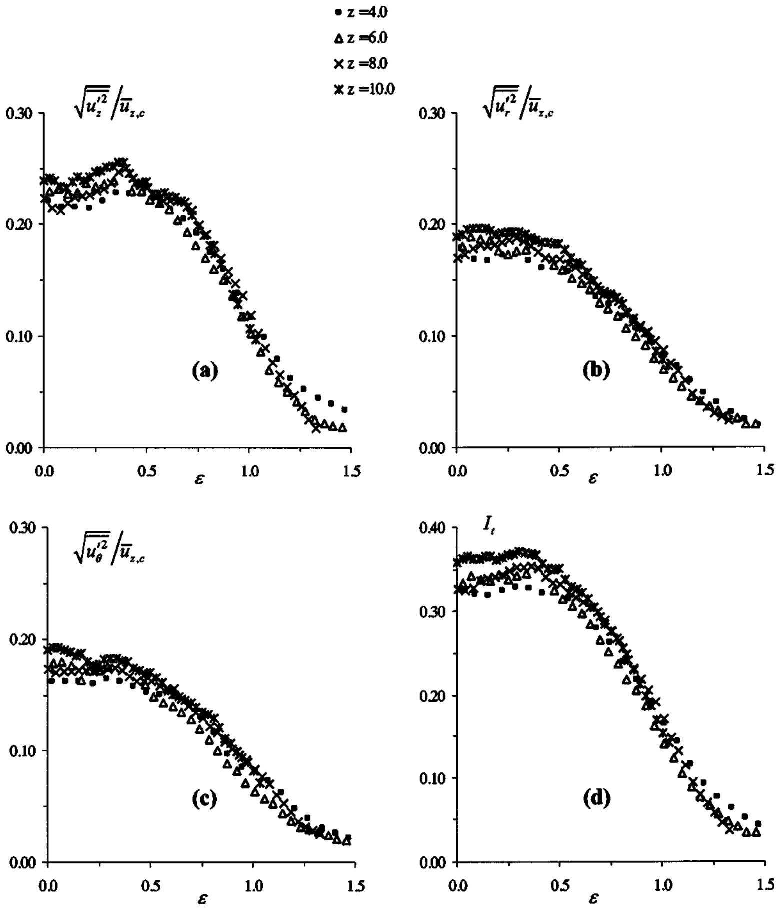

Fig. 6 Radial profiles of mean turbulent intensities: (*a*) Vertical velocity turbulent intensity, (*b*) radial velocity turbulent intensity, (*c*) circumferential velocity turbulent intensity, (*d*) I_t velocity turbulent intensity

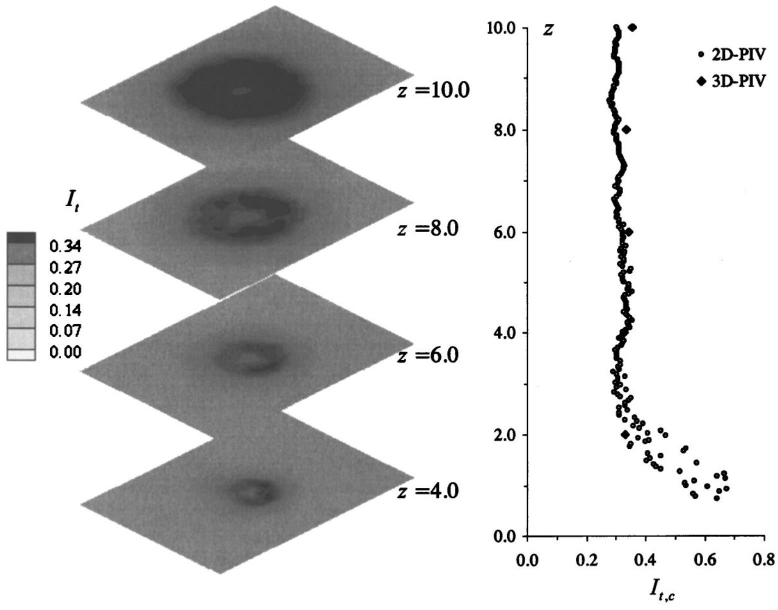

(a) (b)

Fig. 7 Mean turbulent intensity distribution: (*a*) Contour I_t in several planes, (*b*) variation of I_t along the geometrical axis

Downloaded 06 Dec 2010 to 193.140.21.150. Redistribution subject to ASME license or copyright; see http://www.asme.org/terms/Terms_Use.cfm

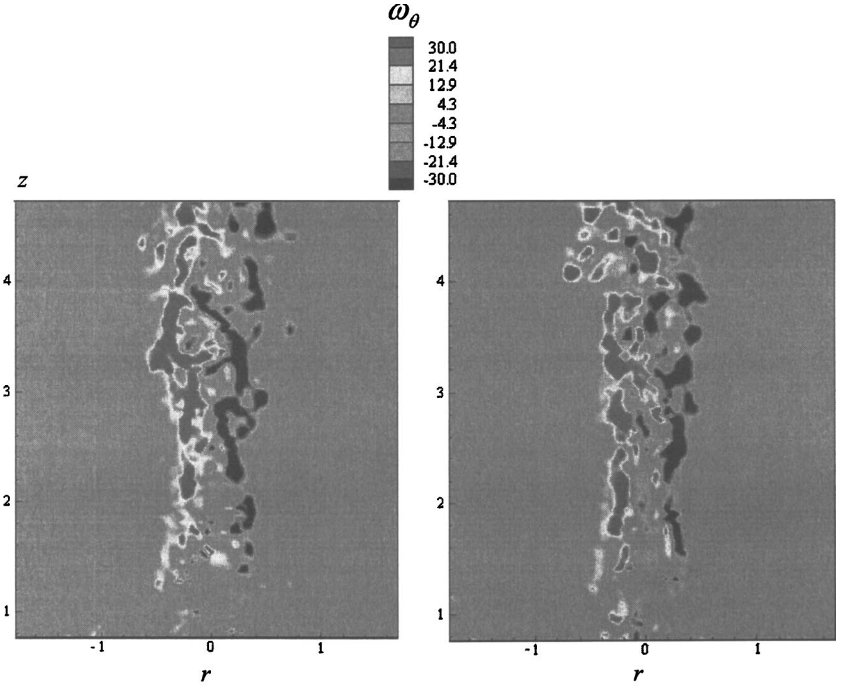

(a) (b)

Fig. 8 Contour of instantaneous circumferential vorticity field close to the heating source

The time delay between two maps is equal to 0.5 s and the latter corresponds to the highest rate available for our system. Such pictures allow one to clearly distinguish two different regions. First of all, vorticity does not change drastically with regard to t for $z \leqslant 3.0$ and it corresponds to spatial restriction phase of the plume. Second and contradictory to the first region, structures develop rapidly and change from one picture to the other for $z \geqslant 3.0$. This is confirmed in Fig. 9, which shows some maps obtained at higher z positions $(3.5 \leqslant z \leqslant 8.5)$. It is important to underline that in this region, the plume develops instantaneously with an oscillating motion at different distances from its axis. Such oscillations may enhance mixture mechanisms driven by large structures and then increase diffusion from large structures to small structures.

In addition, an interesting feature may be evoked by following ω_θ changes in time (Fig. 9). Plume develops in conjunction with contraction and expulsion phases, which are linked to the instantaneous width of the plume. For instance, Fig. 9(*c*) reveals restrictions due to fresh air engulfment in the plume at $z=5.0$ which arises almost symmetrically. At the same time, plume is enlarged due to vortex structure concentration for $6.0 \leqslant z \leqslant 7.0$, which may try to expel fluid from the core to external environment of the plume. Such contraction and expulsion phenomena are more easily observed through stereoscopic PIV measurements since we measured in a parallel plane to the heating source surface (Fig. 10). As shown in Fig. 10(*a*), structures in such a plan expel fluid from the core to the immediate environment of the plume. Such motions may have a direct impact on entrainment induced by the buoyant arising forces. These explusions are highly localized and clearly enhanced by a stronger vorticity field. Such a point is not yet fully understood and only a few works have been devoted to the problem. For instance, Basu and Narimsha [14] reported simulations of turbulent jet subjected to local volumetric heating and their results clearly demonstrated that enhancement of vorticity, due to vortex stretching, favors intense structures that tend to attract fluid from the quiescent environment. From 3D measurement and while taking into account the surrounding of the plume during the two identified phases, i.e., contraction and repulsion phases, entrainment mass flux can be estimated and has been found to be equal to $\dot{m}_e = 0.0226$ and $\dot{m}_e = 0.0074$ in the contraction and repulsion phases, respectively. Although, as we will observe later, estimating entrainment flux is a very sensitive problem, a ratio of 3 has been put forward which clearly demonstrates that entrained mass flux is significantly more important during contraction phase than during expulsion phase.

To undertake the analysis of plume development, let us perform the budget analysis of the momentum equation at two different heights:

$$\underbrace{\bar{u}_z \frac{\partial \bar{u}_z}{\partial z}}_{vertical\ convection} + \underbrace{\bar{u}_r \frac{\partial \bar{u}_z}{\partial r}}_{radial\ convection} \approx \underbrace{-\frac{(\bar{\rho}-\rho_\infty)}{\bar{\rho}} g}_{buoyancy} - \underbrace{\frac{\partial(\overline{u_z'^2})}{\partial z}}_{vertical\ transport} \underbrace{-\frac{1}{r}\frac{\partial(r\overline{u_r' u_z'})}{\partial r}}_{radial\ transpot}$$

Due to thermal plume spreading, the *radial transport* and the *buoyancy* terms are relatively significant in the budget (Fig. 11). Nevertheless, one of the more interesting terms is the *radial convection* term. Actually, this is the only one which offers a significant different profile shape between $z=2.0$ and $z=5.0$. It is true that all the other terms, vertical convection, buoyancy, turbulent transports, have almost the same profile shape even if they are all more or less modulated in amplitude with regard to z. Close to the heating source, i.e. at $z=2.0$, $\overline{u_r}(d\overline{u_z}/dr)$ is always positive (see Fig. 11(*a*)). Because the vertical velocity gradients are always negative $(d\overline{u_z}/dr<0)$ due to its Gaussian distribution, it means

Downloaded 06 Dec 2010 to 193.140.21.150. Redistribution subject to ASME license or copyright; see http://www.asme.org/terms/Terms_Use.cfm

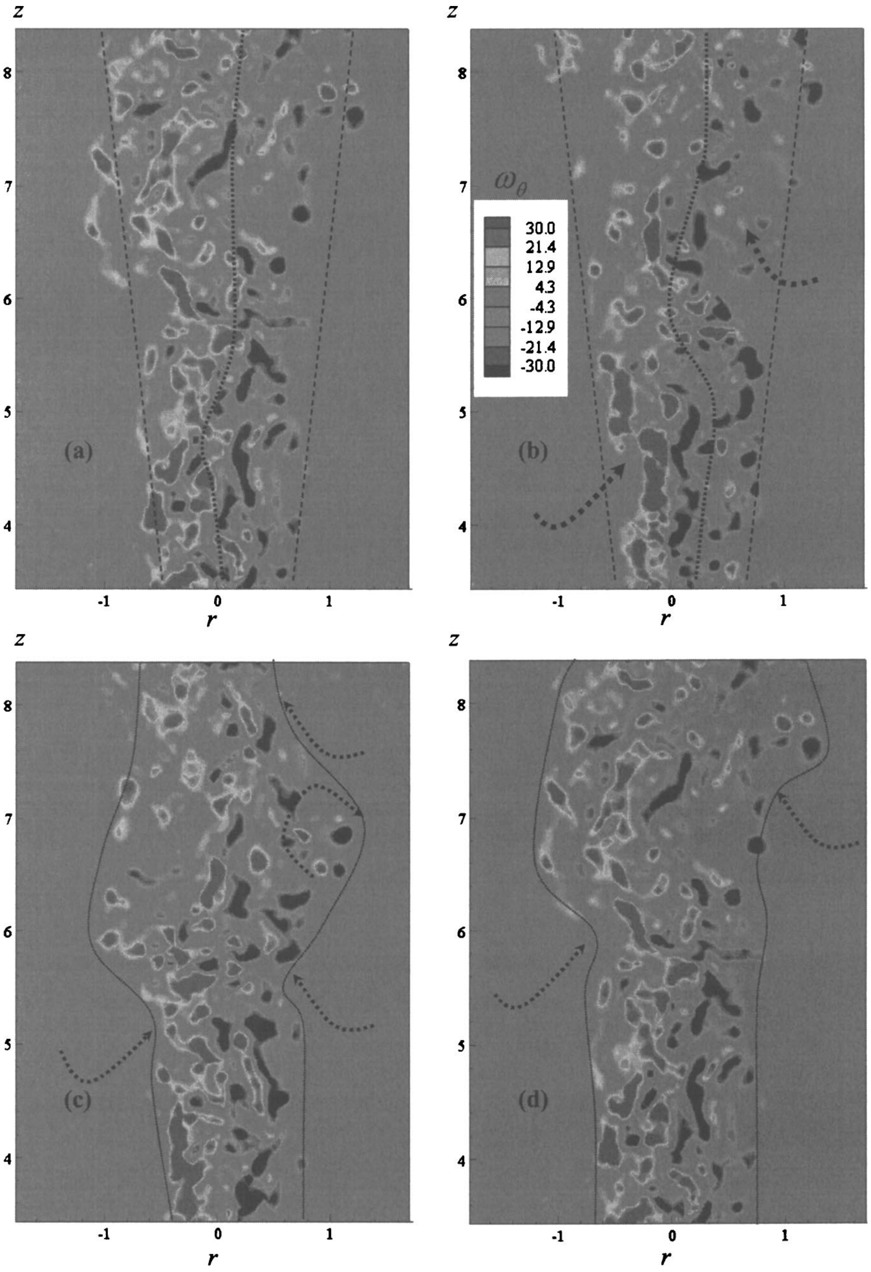

Fig. 9 Contour of instantaneous circumferential vorticity field far from the heating source

that the radial velocity is negative $\overline{u}_r < 0$. On the contrary, for $z \geqslant 4.0$, the $\overline{u}_r(d\overline{u}_z/dr)$ radial convection term in the Fig. 11(*b*) is positive for $r \geqslant 0.5$ and negative for $r \leqslant 0.5$. Such a sign change reveals a strong plume expansion in this area which occurs through large structure activities. These structures are also amplified through the expulsion–contraction motion mainly dominated by plume engulfment during contraction phases.

It is also important to stress that other budget terms clearly shed light on plume flow field behavior. Concerning the region close to the heating source (Fig. 11(*a*)), the thermal plume is mainly dominated by vertical convection and buoyancy. As expected, buoyancy plays a leading role because it induces the whole fluid motion. Due to thermal plume spreading, the vertical convection terms are also relatively significant in the budget. Actually, the effect of the heated source is strong enough to generate shear-layer development, as observed in the vorticity field; it may also favor a strong stretching mechanism of large-scale structures. On the contrary, Fig. 11(*b*) shows the budget profiles obtained at $z = 5.0$ in the plume turbulent region. Due to its spreading, the vertical convection as well as the buoyancy terms are no longer so dominant. Turbulence develops rapidly thereby enhancing interaction between large and small structures as observed in the vorticity field. Therefore, *radial transport* is the leading term in this region.

Plume Entrainment Mechanisms

Direct Measurement of Entrained Mass Flow Rate. As mentioned in the Introduction, one of our goals is to characterize entrainment induced by pure thermal plume development. To do so, it would be very interesting to directly measure the entrainment mass flow rate even if such a measurement is difficult to perform. To our knowledge, Ricou and Spalding [5] were the first to directly measure the entrainment flux of a turbulent jet by sur-

Downloaded 06 Dec 2010 to 193.140.21.150. Redistribution subject to ASME license or copyright; see http://www.asme.org/terms/Terms_Use.cfm

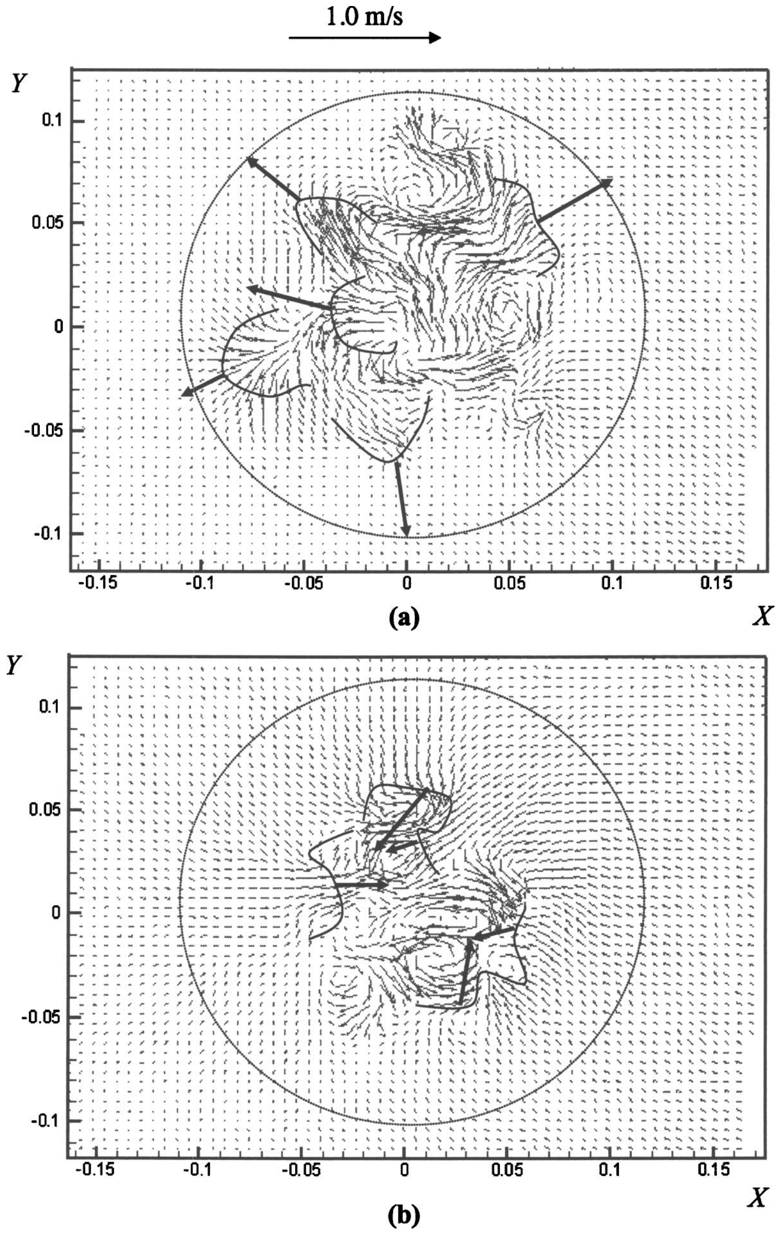

Fig. 10 Instantaneous velocity field of thermal plume obtained from stereoscopic PIV at $z=5.0$ during (*a*) expulsion phase and (*b*) contraction phase

rounding the latter with a porous-walled cylindrical chamber. The chamber was equipped for measuring the mass flow rate passing through the porous wall and feeding the core flow of the jet. Note that such an experimental setup cannot guarantee accurate measurements; moreover, it cannot be applied to jets in coflow configuration where the encroachment of the jet boundary is the leading mechanism of entrainment. Nor can it be applied to thermal plume, because the presence of porous walls would definitely modify pressure balance around the plume. Direct interaction with plume development and its entrainment would be enhanced. Thus, a second way for measuring the entrainment was more widely used [3] and is based mainly on mass balance. Entrained mass flow rate is actually estimated by tentatively calculating the difference of the whole mass flow rate between two plume sections as:

$$\dot{m}_e=\Delta\dot{m}=\dot{m}_2-\dot{m}_1$$

$$\text{with }\ \dot{m}=\int_0^\infty(\bar{\rho}\bar{u}_z+\overline{\rho' u_z'})2\pi r dr$$

Figure 12(*a*) schematically depicts the way to obtain such an estimate of the entrainment mass flow rate. It requires measurement of the density and axial velocity, but such a method is no longer a direct one. Moreover, the $\overline{\rho' u_z'}$ fluctuating quantity is very complex to determine. Let us add that when such a method is referred to, the average fluctuating part is generally overlooked in the mass flow rate balance. However, it is difficult to precisely determine the contribution of the fluctuating term because it requires simultaneous measurement of instantaneous fluid density (temperature) and velocity. Dibble et al. [25] estimated the contribution of the fluctuating term on the mass flux integral by measuring the average and fluctuating axial velocity component using LDV technique and the average and fluctuating density using Raleigh scattering in a hydrogen jet. Based on their findings, the ρ' and u'

Downloaded 06 Dec 2010 to 193.140.21.150. Redistribution subject to ASME license or copyright; see http://www.asme.org/terms/Terms_Use.cfm

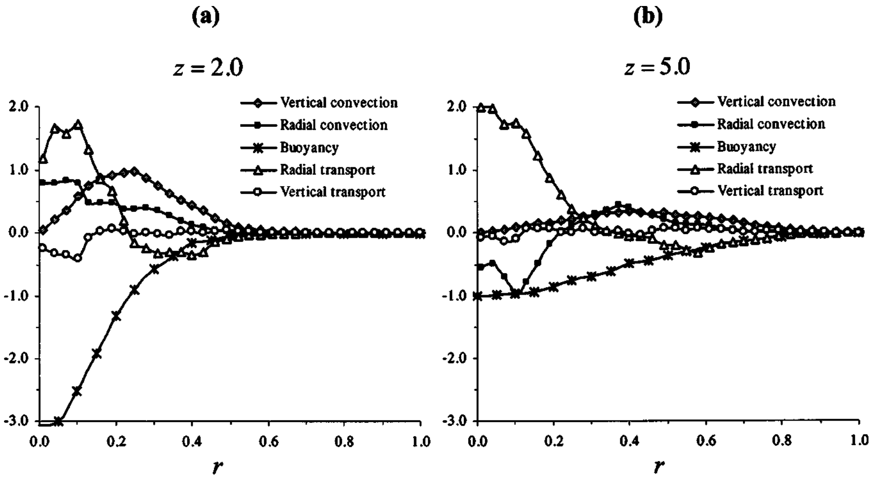

Fig. 11 Balance of mean momentum: (*a*) at $z=2.0$, (*b*) at $z=5.0$

fluctuations could contribute to an approximately 20% increase to mass flux obtained by considering only the average quantities. It is also important to stress that the measurements carried out by Diddle et al. [25] were not performed simultaneously so that the error due to neglecting the fluctuating term may be valid only if fluctuations are assumed to be correlated. To avoid these difficulties, a direct measurement method is required such as that of Ricou and Spalding [5] but without the physical structure that intrudes into the flow field.

In order to estimate the entrained mass flux without encountering such difficulties, a direct method has been carried out in studying reacting jets [12]. The basic idea consists in measuring the velocity outside of the plume; in that way, entrainment measurement is not potentially altered by the density fluctuations which exist inside the plume. This direct method was checked out on jets and validated by comparing it with results of previous measurements. As of now, pure thermal plume has not yet been characterized through such a method, which explains why we are focusing our attention on a direct technique. The entrained mass flux may be estimated directly as:

$$\dot{m}_e = \int_{z_1}^{z_2} \overline{\rho u_n}\, 2\pi r \,\frac{dz}{\cos\beta} = \rho_\infty \int_{z_1}^{z_2} \overline{u_n}\, 2\pi r \,\frac{dz}{\cos\beta}$$

in which u_n corresponds to the normal velocity component with respect to the plume boundary. In this way, entrained mass flux is calculated by integrating the inflow mass passing through the plume boundary. As long as plume evolves in a constant and known surrounding environment, the density involved in $\dot{m}_e$ equation remains at a constant level and no fluctuations arise in the momentum term. Nevertheless, such a method entails two major difficulties. First, border of the plume which limits the main ascendant flow field with the one providing laterally is not as at easy to establish, and accurately measuring small velocities in the plume surrounding environment is a difficult task. Second, such a border is tilted with regard to the z direction. Moreover, the choice of the β angle may introduce some bias in the direct technique measurements. That said, applying direct technique to reacting jets, change of β angle from 5 deg up to 15 deg may be considered as generating second-order errors in the entrained mass flow rate measurement [12]. And since no clear plume border definition has been established except the one given above, stating that the plume width is equal to $\lambda(z)$, it appears consistent to consider such a definition as well as the tilted angle obtained with the latter. From Fig. 3, the angle may be estimated as equal to 6 deg. It is also important to add that radial velocity component decays as $1/r$ by continuity. This is a key point which explains why direct measurement technique may be assumed to be not particularly dependent on plume border location: All around the plume, the ru_r term remains at a constant level. After that, the exact plume border location no longer figures as a predominant parameter in the accuracy of the direct method. As a result, accuracy when measuring velocities in the immediate surrounding of the plume becomes the key point to address.

To measure flow field velocity in and close to the plume, two different time delays between two images were employed. According to spatial resolution, a time delay of 2 ms was chosen to obtain velocity field inside the plume and Fig. 13(*a*) shows an example of velocity field in the r-z plane. A dashed line delimits in Fig. 13 the $\lambda(z)$ plume width. A longer interval, ten times higher, is required in order to precisely capture small displacements all around the plume width. Such a choice in the PIV parameters is essential in order to accurately measure these small velocity levels. As underlined in Fig. 13, such a long time delay

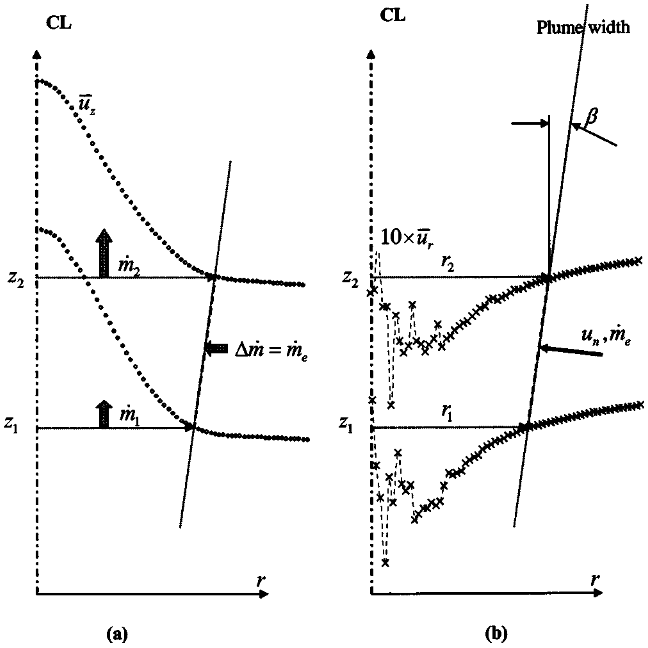

Fig. 12 Schematic of entrainment measurement: (*a*) Differential method, (*a*) direct method

Downloaded 06 Dec 2010 to 193.140.21.150. Redistribution subject to ASME license or copyright; see http://www.asme.org/terms/Terms_Use.cfm

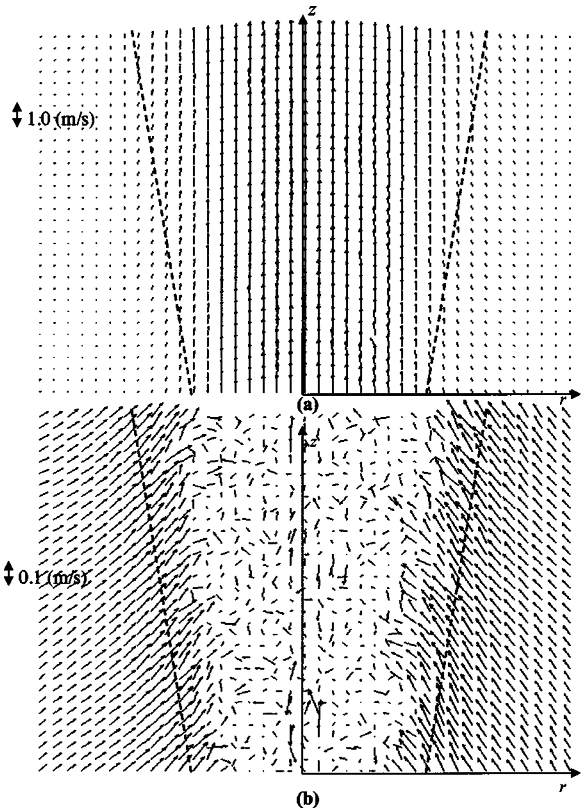

Fig. 13 Mean velocity from PIV using two different time intervals between images: (*a*) Short time of 2 ms and (*b*) long time of 20 ms

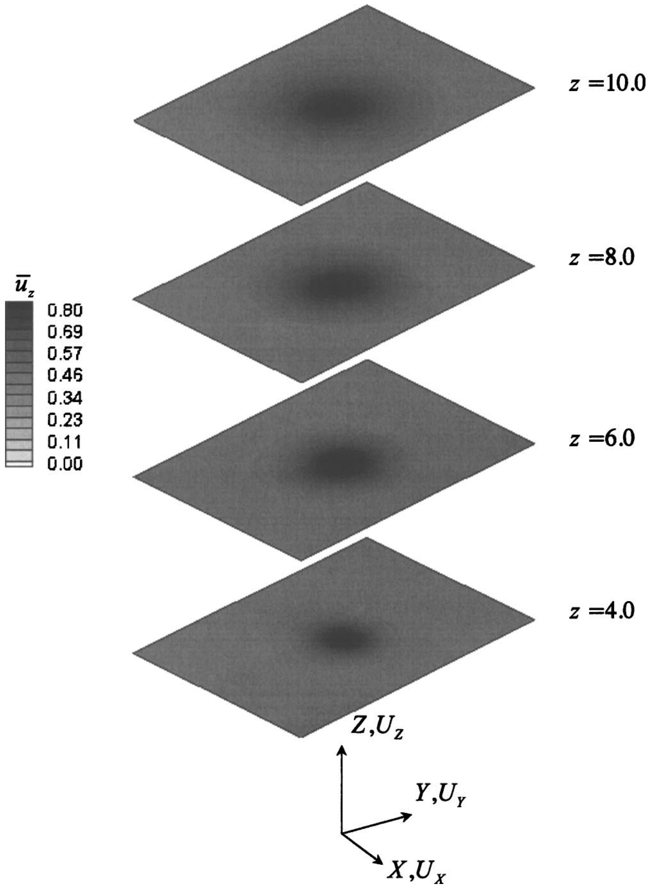

Fig. 14 Contour of mean vertical velocity obtained by the stereoscopic measurements

no longer effectively helps to correlate fluid motion in the plume. Consequently, in order to estimate entrained mass in the plume, one only needs velocity measurements in the r-z plane if we assume that the plume behaves axisymmetrically. Thanks to stereoscopic measurements, Fig. 14 presents mean velocity fields at several z levels in the x-y plane and this clearly demonstrates the circular behavior of the flow field. In fact, our measurements render direct entrained mass flow rate possible through 2D PIV measurements in r-z planes. In order to compare results obtained while using direct technique, we also computed the entrained mass flux through the differential technique introduced by Morton et al. [3]. As already mentioned, such a technique consists in calculating mass flow rate in the plume at two different heights; difference between the two mass flow rates corresponds to the entrained one. To do so, mean temperature is also measured and density may be deduced through the ideal gas law assumption. As velocity and density are not measured directly and instantaneously, the $\overline{\rho' u_z'}$ fluctuating part is not taken into account. Figure 15(*a*) shows the change of $\dot{m}$ mass flow rate with regard to z. From this $\dot{m}$ estimation, one can easily deduce the $\dot{m}_e$ entrained mass flow rate by the plume development by considering its difference between two locations. The change of $\dot{m}_e$ is presented in Fig. 15(*b*) and it allows one to compare results obtained by differential and direct techniques. First, one can observe that the main trend is similar with each of the two techniques; close to the heating source, i.e., $z \leqslant 2.0$, $\dot{m}_e$ increases rapidly to a maximum level and is also rapidly damped to a relative minimum level reached at $z = 2.0$ approximately. For $z \geqslant 2.0$, $\dot{m}_e$ increases almost linearly. In the laminar region, the flow organizes and is subjected to strong mixing, which may explain such drastic change in the $\dot{m}_e$ evolution; as soon as turbulent regime is established, the entrained mass flow rate evolves with regard to z. Second, significant differences between the two techniques used need to be emphasized. It is true that $\dot{m}_e$ determined by the differential technique offers abrupt variations which appear not to reveal physical mechanisms. Such method is based on a difference scheme, errors made in the $\dot{m}$ estimation may amplify those made in the $\dot{m}_e$ estimation. Moreover, and by far the most important point, the $\dot{m}_e$ entrained mass flux with the differential technique is on the average smaller than the one computed by the direct technique. This bias is linked to the fact that the fluctuating part cannot be considered in the differential technique which may be significant in plumes. Besides, $\dot{m}_e$ differences represent almost 15%–20% and such a huge difference may naturally affect the entrainment coefficient estimation. Finally, it is important to underline that shifting plume border of 50% provides only a change of less than 5% in the $\dot{m}_e$ estimation. Such a result clearly demonstrates that direct measurement technique is not linked to the arbitrary border location.

Entrainment Coefficient Assessment. According to the first theoretical step, entrainment has been defined as a ratio between the lateral velocity and the main ascendant one in order to describe the ability of plumes to displace their surroundings [3] and α entrainment coefficient has been first estimated as:

$$\alpha = -\frac{\overline{u_r}(\lambda)}{\overline{u_{z,c}}}$$

which can be written directly with regard to $\dot{m}_e$ entrained mass flow rate:

$$\alpha = \frac{\dot{m}_e}{\Delta z}\frac{1}{2\pi\rho_\infty\lambda\overline{u_{z,c}}}$$

Downloaded 06 Dec 2010 to 193.140.21.150. Redistribution subject to ASME license or copyright; see http://www.asme.org/terms/Terms_Use.cfm

Table 1 α **entrainment coefficient estimates available in the literature**

Authors	Configurations	α
Morton et al. [3]	Atmospheric plume	0.093
George et al. [6]	Hot jet	0.108
Dehmani et al. [9,19]	Turbulent axisymmetric plume	0.150

From this definition and taking into account the Gaussian shape for the vertical velocity profiles in the self-similar region, a relation allowing estimating the entrainment coefficient is easily established:

$$\lambda = \frac{6}{5}\alpha z$$

Table 1 lists the different values for α entrainment coefficient available in the literature. It is important to underline that most of the works listed applied a α modified entrainment coefficient definition. Actually, instead of relating entrained velocity estimated through $\dot{m}_e$ measurement to mean axial velocity component, researchers mainly prefer to refer to average velocity as:

$$\overline{u_{z,m}} = \frac{\int_0^\infty \overline{u_z}^2 2\pi r dr}{\int_0^\infty \overline{u_z} 2\pi r dr}$$

instead of $\overline{u_{z,c}}$ and in order to compare our results with available data in the literature, we compute α entrainment coefficient by using average ascendant velocity as reference velocity. One of our purposes is also to compare entrainment coefficient obtained with differential and direct techniques and Fig. 15 allows such a comparison. When α is computed through direct method, strong variations are observed close to the heating source. In this region, α reveals very high levels ranging from 0.2 to 0.6; such a region corresponds to thermal plume development that leads by dominating buoyancy forces as well as radial transport. Moreover, the average radial velocity is negative so that plume develops mainly by first concentrating hot fluid around its geometrical axis. While z increases, α is damped and tends rapidly towards a constant level of approximately 0.11. According to Table 1, such a level is included in the available literature range. Nevertheless, it clearly appears that direct technique introduces a significant improvement in the α entrainment coefficient determination. First and as one may think when studying the $\dot{m}_e$ data, the change of α with regard to z also involves unstable and unphysical variations close to the heating source region due to the measurement uncertainties when using differential method in this area. Second, one can observe significant variations as well for $z \geqslant 4.0$. Similarly to $\dot{m}_e$ data, the α entrainment coefficient is on the average smaller that the one computed by using direct technique. As already mentioned and thanks to accurate velocity measurements, direct technique allows one to evaluate the α entrainment coefficient without restrictive assumptions such as not taking into account the $\overline{\rho' u_z'}$ fluctuating quantity. In addition, such accurate measurements render it possible to assess the change of the α entrainment coefficient with regard to z. The differential method is only able to give an estimate of α in the self similarity region. In fact, most of the works dedicated to plume entrainment characterization only report an estimate and do not address its changes versus z. Moreover, the estimates available in the literature are generally inaccurate, which is no longer when using direct measurement technique.

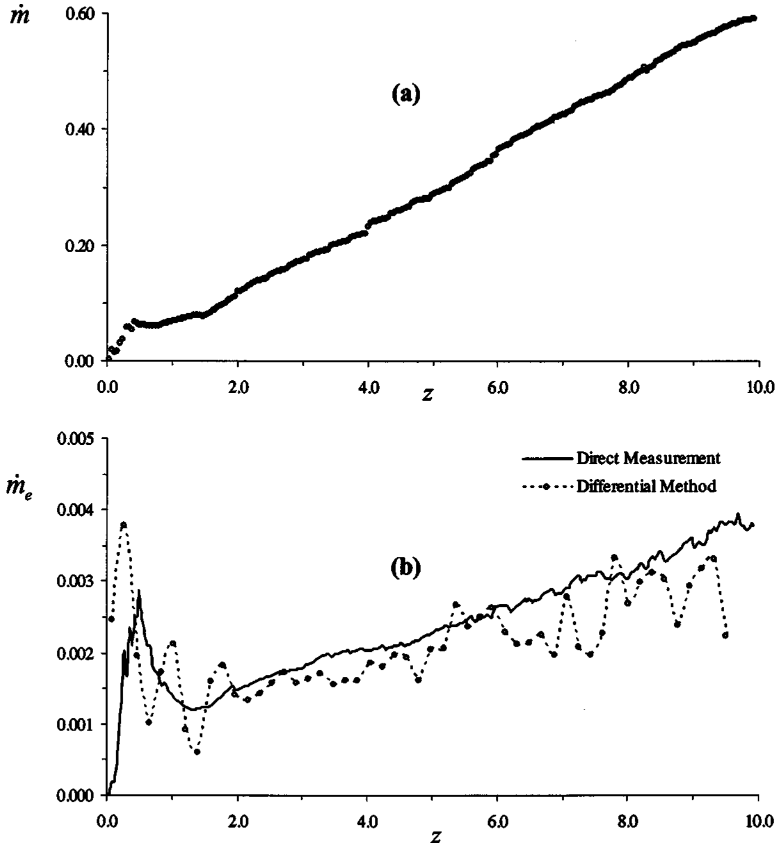

Fig. 15 **Variation of the flow rate along height: (*a*) Total flow rate, (*b*) entrained flow rate**

Downloaded 06 Dec 2010 to 193.140.21.150. Redistribution subject to ASME license or copyright; see http://www.asme.org/terms/Terms_Use.cfm

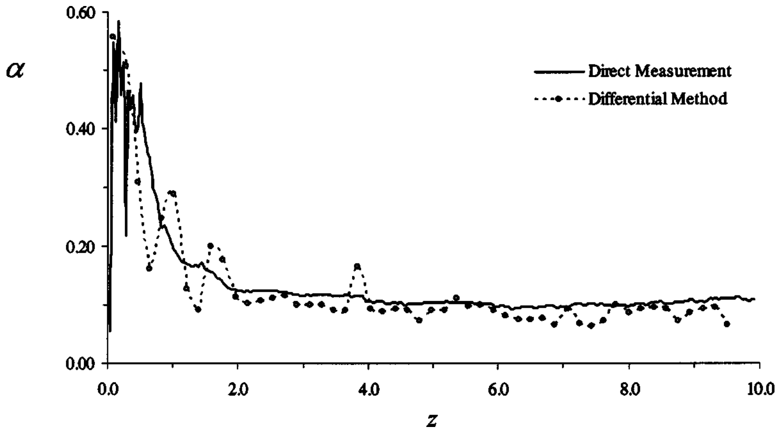

Fig. 16 Variation of entrainment coefficient along vertical axis

Conclusion

A pure turbulent thermal plume characterization has been performed using 2D and 3D stereoscopic measurements which enable researchers to depict its complex spatial development. It allows for clear detection of the laminar and turbulent development region of the plume. In accordance with the velocity field changes with time, contraction and repulsion phenomena arise. Contraction favors mass entrainment from the quiescent surroundings and vortex structure identification clearly demonstrate the role of such large structures in the entrainment mechanism. Even if the repulsion phase is not the driving one, the latter has been clearly identified and accounts for roughly only 20%–30% of the mass flow exchange entrainment. Our experimental results agree with numerical trends depicting the link between complex structure motions and entrainment. We strongly believe that future experiments should try to determine structure development in time in order to improve our understanding of their role in turbulent flow field.

Moreover, results allow one to accurately determine the entrainment coefficient. Firstly, axisymmetricity of the plume has been checked out through stereoscopic measurements; secondly, a direct measurement technique has been implemented and makes it possible to obtain the change of the entrainment coefficient along the *z* axis. By comparing such a technique with the classical mass balance usually performed in plumes and jets, results clearly show that close to the heating source, the differential technique provides no physical trend concerning the entrainment coefficient change, whereas far away from the source results are somewhat altered by noise and reveal average value smaller in the turbulent region than that obtained through a direct method. It is important to stress that the direct method is accurate because its principle consists in balancing mass flow rate in the plume surroundings and that it does not suffer from overly simplistic assumptions such as, for instance, neglecting the fluctuating part as is the case with the well-known differential technique.

Finally, such experimental measurements are highly promising and should help us in the near future to reach two main goals: (1) To better understand large structure role in complex flows and particularly on entrainment mechanisms; (2) to provide experimental data for validating turbulence models such as for instance large-eddy simulation. It is also important to underline that some unknown elements still exist in thermal plume such as for instance the rotation effects of the heating source on plume development and their consequences on entrainment and the interaction between several plumes.

Acknowledgment

The authors would like to warmly thank Dr. Christian TANGUY, from Dantec France Company, who helped us to carry out the experiments presented and provided us with his advice on stereoscopic measurements.

Nomenclature

B = Gaussian parameter
D = heating source diameter (m)
g = gravity acceleration in the z axial direction (ms^{-2})
H = disk height above the floor (m)
$I_t = \sqrt{\overline{u_r'^2} + \overline{u_\theta'^2} + \overline{u_z'^2}}/\overline{u}_{z,c}$
= turbulent intensity
$L_X \times L_Y \times L_Z$ = dimension of the enclosure (m)
$\dot{m}$ = nondimensional plume mass flow rate
$\dot{m}_e$ = nondimensional entrained mass flow
$St = \tau_p/\tau_f$ = Stockes number
R, θ, Z = Cylindrical co-ordinate system transformed from X, Y, Z
r, z = radial and axial co-ordinates scaled by D
T_s = heating source temperature (°C)
$\Delta T_s = T_s - T_\infty$
= characteristic temperature difference (°C)
T = temperature normalized by ΔT_s
$U_{\max}$ = maximum axial velocity (m/s)
U_x, U_y, U_z = Cartesian velocity components (m/s)
u_x, u_y, u_z = Cartesian velocity components normalized by $U_{\max}$
u_r, u_θ, u_z = cylindrical velocity components transformed from u_x, u_y, u_z
X, Y, Z = dimensional Cartesian co-ordinate (m)
x, y, z = nondimensional Cartesian co-ordinate normalized by D
Λ = plume radius estimated through mass balance (m)
$\lambda = \Lambda/D$ = normalized plume radius
α = entrainment coefficient
β = plume expansion angle (°)
$\varepsilon = R/\Lambda$ = nondimensional radius ratio
θ_0 = angle between view of camera and normal of measurement plane (°)
ρ = fluid density normalized by ρ_{REF}
ρ_{REF} = fluid density at T_∞ ($\mathrm{kg/m^3}$)
$\omega_\theta = \partial u_z/\partial r - \partial u_r/\partial z$
= normalized circumferential vorticity
τ_p = characteristic particle response time (s)
τ_f = characteristic time scale of flow (s)

Subscripts

c = geometrical axis location
s = heating source
∞ = referred to quiescent environment
max = referred to maximum value

Downloaded 06 Dec 2010 to 193.140.21.150. Redistribution subject to ASME license or copyright; see http://www.asme.org/terms/Terms_Use.cfm

References

[1] Gebhart, B., Jaluria, Y., Mahajan, R., Sammakia, 1988, *Buoyancy-induced Flows and Transport*, Textbook ed., Hemisphere Publishing Corporation, New York.

[2] Elicer-Cortes, J. C., Fuentes, J., Valencia, A., and Baudet, C., 2000, ''Experimental Study of Transition to Turbulence of a Round Thermal Plume by Ultrasound Scattering,'' Exp. J. Fluid Sci., **20**, pp. 137–149.

[3] Morton, B. R., Taylor, G., and Turner, J. S., 1956, ''Turbulent Gravitational Convection from Maintained and Instantaneous Sources,'' Proc. R. Soc. London, Ser. A, **A234**, pp. 1–24.

[4] Taylor, G. ''Dynamics of a Mass of Hot Gas Rising in Air,'' U.S. Atomic Energy Commission, MDDC-919, LADC-276, 1945.

[5] Ricou, F. P., and Spalding, D. B., 1961, ''Measurements of Entrainment by Axisymmetrical Turbulent Jets,'' J. Fluid Mech., **11**, pp. 21–32.

[6] George, W. K., Alpert, R. L., and Tamanini, F., 1977, ''Turbulence Measurements in an Axisymmetric Buoyant Plume,'' Int. J. Heat Mass Transfer, **20**, pp. 1145–1154.

[7] Shabbir, A., and George, W. K., 1994, ''Experiments on Round Turbulent Buoyant Plume,'' J. Fluid Mech., **275**, pp. 1–32.

[8] Papanicolaou, P. N., and List, E. J., 1988, ''Investigations of Round Vertical Turbulent Buoyant Jets,'' J. Fluid Mech., **195**, pp. 341–391.

[9] Dehmani, L., Doan-Kim, S., and Gbahoue, L., 1996, ''Turbulent Structure of an Axisymmetric Plume Penetrating a Strong Density Stratification,'' Int. J. Heat Fluid Flow, **17**, pp. 452–459.

[10] Agrawal, A., and Prasad, A. K., 2003, ''Integral Solution for the Mean Flow Profiles of Turbulent Jets, Plumes, and Wakes,'' J. Fluids Eng., **125**, pp. 813–822.

[11] Brahimi, M., Lamour, M., and Doan Kim, S., 1988, ''Champs moyens et fluctuants des panaches thermiques isolés ou en interaction,'' Rev. Gen. Therm., **315**, pp. 236–243.

[12] Han, D., and Mungal, M. G., 2001, ''Direct Measurement of Entrainment in Reacting–Nonreacting Turbulent Jets,'' Combust. Flame, **124**, pp. 370–386.

[13] Zhou, X., Luo, K. H., and Williams, J. J. R., 2001, ''Large-Eddy Simulation of a Turbulent Forced Plume,'' Eur. J. Mech. B/Fluids, **20**, pp. 233–254.

[14] Basu, A. J., and Narasimha, R., 1999, ''Direct Numerical Simulation of Turbulent Flows with Cloud-Like off Heating,'' J. Fluid Mech., **385**, pp. 199–228.

[15] Agrawal, A., and Prasad, A. K., 2002, ''Organizational Modes of Large-Scale Vortices in an Axisymmetric Turbulent Jet,'' Flow, Turbul. Combust., **68**, pp. 359–377.

[16] Agrawal, A., and Prasad, A. K., 2004, ''Evolution of a Turbulent Jet Subjected to Volumetric Heating,'' J. Fluid Mech., **511**, pp. 95–123.

[17] Guillou, B., and Doan-Kim, S., 1983, ''Etude Theorique du Développement d'un Panache Thermique a symétrie axiale-influence des propriétés thermo-physiques du fluide,'' Int. Commun. Heat Mass Transfer, **10**, pp. 101–109.

[18] Beuther, P. D. and George, W. K., 1982, ''The Turbulent Plume in a Stratified Environment,'' Proc. Natl Congr. Theor. and Appl. Mech., Cornell University, Ithaca, NY.

[19] Dehmani, L., Doan Kim, S., Gbahoue, L., and Rongère, F. X., 1996, ''Influence of a Strong Density Stratification Axisymmetric Plume,'' Exp. Fluids, **21**, pp. 170–180.

[20] Alkislar, M. B., Lourenco, L. M., and Krothapalli, A., 2000, ''Stereoscopic PIV Measurements of Screeching Supersonic Jet,'' J. Visualisation, **3**(**2**), pp. 135–143.

[21] Muñiz, L., ''Particle Image Velocimetry Studies of Turbulent Non-Premixed Flames,'' PhD thesis, Stanford University, Stanford, CA, 2000.

[22] Chen, C. J. and Rodi, W., 1980, *Vertical Turbulent Buoyant Jets*, Pergamon.

[23] Turner, J. S., 1969, ''Buoyant Plumes and Thermals,'' Annu. Rev. Fluid Mech., **1**, pp. 29–44.

[24] Zinoubi, J., Maad, R. B., and Belghith, A., 2004, ''Influence of The Vertical Source-Cylinder Spacing on The Interaction of Thermal Plume With a Thermosiphon Flow: An Experimental Study,'' Exp. Therm. Fluid Sci., **28**, pp. 329–336.

[25] Dibble, R. W., Schefer, R. W., Chen, J. Y. and Hartmann, V., 1987, ''Velocity and Density Measurements in a Turbulent Nonpremixed Flame with Comparison to Numerical Model Predictions,'' Sandia Report, SAND85-8233, UC-304.

Downloaded 06 Dec 2010 to 193.140.21.150. Redistribution subject to ASME license or copyright; see http://www.asme.org/terms/Terms_Use.cfm

Combined Influence of Mass and Thermal Stratification on Double-Diffusion Non-Darcian Natural Convection From a Wavy Vertical Wall to Porous Media

B. V. Rathish Kumar[1]
e-mail: bvrk@iitk.ac.in

Shalini Gupta

Parallel Computing Laboratory,
Department of Mathematics,
Indian Institute of Technology,
Kanpur, 208 016, India

In this study we analyze the combined influence of mass and thermal stratification on non-Darcian double-diffusive natural convection from a wavy vertical wall to a porous media. A finite difference scheme based on the Keller box approach is derived for the boundary layer equations resulting from the use of nonsimilarity transformation on the coupled nonlinear partial differential equations. Extensive numerical simulations are carried out to analyze the influence of wave amplitude a, Grashof number Gr^*, thermal stratification parameter S_T, concentration stratification parameter S_C, buoyancy ratio B, and Lewis number Le on the double-diffusive natural convection process. Increasing a and Gr^* or decreasing B is seen to favor the heat and mass transport in the porous region thereby reducing the heat and mass fluxes along the vertical heated surface. Increasing S_T or decreasing Le leads to an enhanced mass transfer process. Presence of surface waviness brings in a wavy pattern in the local heat and mass fluxes with decreasing magnitudes in the streamwise direction in the presence of stratification terms.

[DOI: 10.1115/1.1863258]

1 Introduction

Natural convection flow caused by the combined buoyancy effects of thermal and species diffusion in a saturated porous medium has applications in a number of areas, including geothermal fields, solar power collectors, dispersion of chemical contaminants, etc. The work related to the double-diffusive convection process in a porous medium is given by Nield and Bejan [1], Bejan and Khair [2], Angirasa et al. [3], Singh and Queeny [4], Nakayama and Hossain [5], and others. Several studies have been found to analyze the influence of the combined heat and mass transfer process by natural convection in a thermal and/or mass-stratified porous medium, owing to its wide applications, such as development of advanced technologies for nuclear waste management, hot dike complexes in volcanic regions for heating of ground water, separation process in chemical engineering, etc. Here stratified porous medium means that the ambient concentration of dissolved constituent and/or ambient temperature is not uniform and varies as a linear function of vertical distance from the origin. Angirasa et al. [6], Rathish Kumar et al. [7], El-Khatib and Prasad [8], Rathish Kumar and Shalini [9], and others analyzed the double-diffusion process in a thermal and/or mass-stratified porous medium by using analytical or numerical techniques. In these studies authors have carried out numerical computations based on full equations. Their results in the form of the streamlines, isotherms, and isoconcentration contours depicted the presence of boundary layers in flow, temperature, and concentration fields along the heated wall. Also, Takhar and Pop [10], Tewari and Singh [11], Rees and Lage [12], Rathish Kumar and Singh [13], among others, have studied the natural convection process in a thermally stratified porous medium.

In the present work we aim to solve the problem of non-Darcian double-diffusive natural convection in a thermal and mass-stratified fluid-saturated porous medium along a semi-infinite irregular-shaped surface, immersed vertically in the porous medium. Irregular surfaces are often used in many applications, such as heat transfer devices (flat-plate condensers in refrigerators, flat-plate solar collectors, cavity wall-insulating systems with surface nonuniformities) and grain stoage units, etc. In view of the complex pattern of the surface geometry, Yao [14] discussed a wavy-to-flat surface transformation, approximating the surface roughness by the sinusoidal waves. Later several authors, for example, Rees and Pop [15], Cheng [16], Rathish Kumar and Shalini [9], used the same transformation technique and studied the convection process in a fluid-saturated porous medium. In the geometric model of the domain, even when the number of waves per unit length is increased, boundary layers are seen mainly near the leading edge of the wavy wall, say, when $x \sim O(1)$. Several authors, such as Rees and Pop [15] and Cheng [16], have solved the problem based on boundary layer equations. Yao [14] also solved the natural convection problem along the wavy wall in the continuum fluid without any porous media based on boundary layer assumptions. In these studies authors assume that $x \sim O(1)$ so that the boundary layer concept becomes meaningflul. Also, for better modeling of the convection process, non-Darcy laws for momentum equation are found to be more appropriate. Related work can be found in Bejan and Poulikakos [17], Plumb and Huenefeld [18], Kumari et al. [19], Lai and Kulacki [20], among others.

We are using boundary layer assumptions to solve the problem of non-Darcian, double-diffusive natural convection caused by a vertical wavy surface in a fluid-saturated semi-infinite porous medium. Non-Darcy terms are used based on the Darcy-extended Forchheimer model, and the wavy nature of the surface is modeled by sinusoidal waves. We assume that the porous medium is mass and thermally stratified. Boundary layer analysis of such a thermally stratified model is feasible only at small and moderate thermal stratification levels when the thermal and species buoyancy forces are not opposing each other [6,21,22]. In the current study we attempt to understand the physics of the problem at

---

[1] Author to whom all correspondence should be addressed.

Contributed by the Heat Transfer Division of ASME for publication in the JOURNAL OF HEAT TRANSFER. Manuscript received by the Heat Transfer Division March 7, 2004; revision received November 20, 2004. Associate Editor: J. N. Chung.

Downloaded 06 Dec 2010 to 193.140.21.150. Redistribution subject to ASME license or copyright; see http://www.asme.org/terms/Terms_Use.cfm

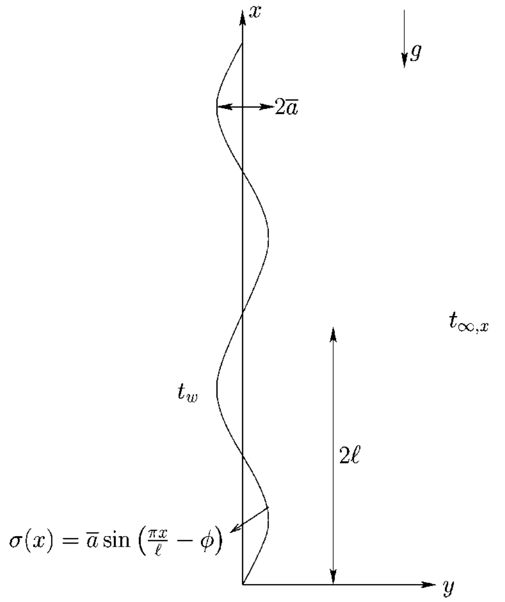

Fig. 1 Schematic diagram of the coordinate system with the boundary conditions

small and moderate thermal stratification levels when the two buoyancy forces are aiding each other. Since similarity arguments are not valid in dealing with thermally stratified fluid [6,21], we employ the local nonsimilarity technique, which has emerged as an alternate to similarity arguments at mild and moderate stratification levels. A wavy-to-flat surface transformation is used that is derived based on the scale analysis, and the resulting equations are simplified to boundary layer equations for asymptotically large Rayleigh numbers Ra. Resulting nonsimilar boundary layer equations are solved by an implicit finite difference scheme based on the Keller box approach [23]. The sparse linear system resulting from the finite difference analysis is solved in an optimal way following the Block tri-diagonal solver. Results are presented in terms of the local and average Nusselt and Sherwood number plots and stream function, temperature, and concentration contours.

2 Mathematical Formulation

As shown in Fig. 1, we consider a vertical wavy surface immersed in a fluid-saturated porous medium. The surface profile of the vertical wavy wall is approximated by the sinusoidal waves as

$$y=\sigma(x)=\overline{a}\sin\left(\frac{\pi x}{\ell}-\phi\right) \tag{1}$$

where $\overline{a}$, 2ℓ, and ϕ are the amplitude, wavelength, and phase, respectively, of the wavy surface. The vertical wavy surface is considered at constant temperature t_w and at constant mass concentration c_w of some constituent in the fluid. Sufficiently far from the vertical wall, temperature and concentration are considered as $t_{\infty,x}$ and $c_{\infty,x}$, respectively, where $t_{\infty,x}$ and $c_{\infty,x}$ are defined as

$$t_{\infty,x}=t_{\infty,0}+s_t x, \quad s_t=\frac{dt_{\infty,x}}{dx}$$

$$c_{\infty,x}=c_{\infty,0}+s_c x, \quad s_c=\frac{dc_{\infty,x}}{dx}$$

The two-dimensional, steady-state equations under the Boussinesq approximation and the Darcy-extended Forchheimer assumptions can be written as follows in terms of nondimensional variables:

$$(1+\mathrm{Ra}^{-1}\mathrm{Gr}^*Q)\nabla^2\Psi+\frac{\mathrm{Ra}^{-1}\mathrm{Gr}^*}{Q}\left[\left(\frac{\partial\Psi}{\partial X}\right)^2\frac{\partial^2\Psi}{\partial X^2}+2\frac{\partial\Psi}{\partial X}\frac{\partial\Psi}{\partial Y}\frac{\partial^2\Psi}{\partial X\partial Y}+\left(\frac{\partial\Psi}{\partial Y}\right)^2\frac{\partial^2\Psi}{\partial Y^2}\right]=\mathrm{Ra}\left(\frac{\partial T}{\partial Y}+B\frac{\partial C}{\partial Y}\right) \tag{2}$$

$$\frac{\partial^2 T}{\partial X^2}+\frac{\partial^2 T}{\partial Y^2}=\frac{\partial\Psi}{\partial Y}\frac{\partial T}{\partial X}+S_T\frac{\partial\Psi}{\partial Y}-\frac{\partial\Psi}{\partial X}\frac{\partial T}{\partial Y} \tag{3}$$

$$\frac{\partial^2 C}{\partial X^2}+\frac{\partial^2 C}{\partial Y^2}=\mathrm{Le}\left(\frac{\partial\Psi}{\partial Y}\frac{\partial C}{\partial X}+S_C\frac{\partial\Psi}{\partial Y}-\frac{\partial\Psi}{\partial X}\frac{\partial C}{\partial Y}\right) \tag{4}$$

with the boundary conditions $\Psi=0$, $T=1-S_T X$, $C=1-S_C X$ on $Y=\sigma(X)=\frac{a}{\pi}\sin(\pi X-\phi)$

$$\frac{\partial\Psi}{\partial Y}\to 0, \quad T\to 0, \quad C\to 0 \text{ as } Y\to\infty \tag{5}$$

where $Q=\sqrt{(\partial\Psi/\partial X)^2+(\partial\Psi/\partial Y)^2}$. The nondimensional variables are defined as follows:

$$X=\frac{x}{\ell}, \quad Y=\frac{y}{\ell}, \quad a=\frac{\overline{a}\pi}{\ell}, \quad \Psi=\frac{\overline{\Psi}}{\alpha}, \quad T=\frac{t-t_{\infty,x}}{t_w-t_{\infty,0}},$$

$$C=\frac{c-c_{\infty,x}}{c_w-c_{\infty,0}} \tag{6}$$

Other parameters have their usual meaning as defined in the nomenclature.

Using scale analysis we obtain the following transformation to transform the wavy surface to a flat surface:

$$\xi=X, \quad Y=\xi^{1/2}\mathrm{Ra}^{-1/2}\eta+\sigma(X)$$
$$\Psi=\mathrm{Ra}^{1/2}\xi^{1/2}f(\xi,\eta) \tag{7}$$

Substituting (7) into (2)–(5) and in the limiting case Ra$\gg$1, we obtain following transformed boundary layer equations:

$$(1+\sigma_\xi^2)\frac{\partial^2 f}{\partial\eta^2}+\mathrm{Gr}^*(1+\sigma_\xi^2)^{3/2}\frac{\partial}{\partial\eta}\left(\frac{\partial f}{\partial\eta}\right)^2=\frac{\partial T}{\partial\eta}+B\frac{\partial C}{\partial\eta} \tag{8}$$

$$(1+\sigma_\xi^2)\frac{\partial^2 T}{\partial\eta^2}+\frac{1}{2}f\frac{\partial T}{\partial\eta}=\xi\left(\frac{\partial f}{\partial\eta}\frac{\partial T}{\partial\xi}+S_T\frac{\partial f}{\partial\eta}-\frac{\partial f}{\partial\xi}\frac{\partial T}{\partial\eta}\right) \tag{9}$$

$$(1+\sigma_\xi^2)\frac{\partial^2 C}{\partial\eta^2}+\frac{1}{2}\mathrm{Le}f\frac{\partial C}{\partial\eta}=\xi\mathrm{Le}\left(\frac{\partial f}{\partial\eta}\frac{\partial C}{\partial\xi}+S_C\frac{\partial f}{\partial\eta}-\frac{\partial f}{\partial\xi}\frac{\partial C}{\partial\eta}\right) \tag{10}$$

with the boundary conditions

$$f=0, \quad T=1-S_T\xi, \quad C=1-S_C\xi \text{ on } \eta=0$$
$$\frac{\partial f}{\partial\eta}\to 0, \quad T\to 0, \quad C\to 0 \text{ as } \eta\to\infty. \tag{11}$$

Local and average Nusselt numbers at a vertical distance ξ are given, respectively, by

$$\frac{\mathrm{Nu}_\xi}{\mathrm{Ra}^{1/2}\xi^{1/2}}=-T'(\xi,0)(1+\sigma_\xi^2)^{1/2} \tag{12}$$

$$\frac{\mathrm{Nu}_m}{\mathrm{Ra}^{1/2}}=-\xi\frac{\displaystyle\int_0^\xi\frac{(1+\sigma_{\overline{X}}^2)T'(\overline{X},0)}{\overline{X}^{1/2}}d\overline{X}}{\displaystyle\int_0^\xi(1+\sigma_{\overline{X}}^2)^{1/2}d\overline{X}} \tag{13}$$

Similarly, local and average Sherwood numbers at a vertical distance ξ are given, respectively, as

Downloaded 06 Dec 2010 to 193.140.21.150. Redistribution subject to ASME license or copyright; see http://www.asme.org/terms/Terms_Use.cfm

$$\frac{\mathrm{Sh}_{\xi}}{\mathrm{Ra}^{1/2}\xi^{1/2}} = -C'(\xi,0)(1+\sigma_{\xi}^{2})^{1/2} \tag{14}$$

$$\frac{\mathrm{Sh}_m}{\mathrm{Ra}^{1/2}} = -\xi\,\frac{\displaystyle\int_0^{\xi}\frac{(1+\sigma_{\overline{X}}^{2})C'(\overline{X},0)}{\overline{X}^{1/2}}\,d\overline{X}}{\displaystyle\int_0^{\xi}(1+\sigma_{\overline{X}}^{2})^{1/2}d\overline{X}} \tag{15}$$

The resulting coupled nonlinear and nonsimilar partial differential equations (8)–(10) together with the boundary conditions (11) are solved by an implicit finite difference approach given by Keller and Cebeci [23]. At each fixed ξ, the iteration process is repeated to obtain an accuracy of 10^{-10}, using double-precision arithmetic throughout. For smaller Gr* (Gr*$\leqslant$10), $\eta=10$ is found to lie sufficiently out from the boundary layer (i.e., the entire boundary layer is covered within this η thickness; and the flow, temperature, and concentration properties have negligible change for further increase in η). For Gr*$>$10, maximum η length is adequately chosen as 30. Detailed investigations are carried out for grid selection. A uniform step size of 0.05 is used in the ξ direction, $0 \leqslant \xi \leqslant 10$ with a logarithmic grid having more concentrated points toward $\eta=0$, in the η direction. In Figs. 2(*a*) and 2(*b*), f values are shown for different grids at $\xi=0$ and $\xi=5$. The computational grid of size 200×500 for Gr*$\leqslant$10 and of size 200×1000 for Gr*$>$10 is found to be more than adequate for carrying out the detailed simulations.

3 Results and Discussion

The parameters that influence the double-diffusion natural convection process from a vertical wavy surface with the non-Darcian assumptions and with the heat and mass stratification conditions are as follows: (i) wave amplitude a, (ii) Grashof number Gr*, (iii) thermal and mass stratification parameters (S_T and S_C, respectively), (iv) Buoyancy ratio B, and (v) Lewis number Le. The influence of all these parameters is analyzed on the flow, temperature, and concentration properties. First, we validated our code by comparing the obtained local Nusselt and Sherwood number values with the similarity solution values of Bejan and Khair [2] at $\xi=0$ for various B and Le with $a=0$, Gr*$=0$, $S_T=0$, $S_C=0$, $\phi=0$ deg. Table 1 shows that the obtained results are in excellent agreement with those reported in [2]. Details of the further study are discussed in the following sections.

3.1 Influence of Wave Amplitude *a* on the Heat and Mass Transfer Process. The influence of increasing surface roughness on the heat and mass transfer process has been analyzed by comparing the local and average Nusselt and Sherwood number plots for varying a. In Figs. 3(*a*) and 3(*b*), local and average Nusselt number plots are presented for $0.0 \leqslant a \leqslant 0.5$ under the non-Darcian assumption, Gr*$=1$, with thermal and mass stratification conditions, $S_T=0.05$ and $S_C=0.025$, and with $B=2$, Le $=1$, $\phi=0$ deg. From Fig. 3(*a*), it can be observed that there is almost a periodic variation in local Nusselt number. The amplitude of these wavy curves of local Nu plots increases with increasing a. The magnitude of the local heat transfer rate depends on the slope of the wavy surface. It is mainly controlled by the stream motion induced by the buoyancy force parallel to the surface. For the portion of the wavy surface parallel to the gravitational force (i.e., at the trough and crest locations of the wavy surface), the heat transfer rate is larger. A fall in local Nu plots is observed with increasing ξ, owing to the presence of the thermal stratification parameter S_T. Figure 3(*b*) corresponds to the average Nu plots with varying a. With increasing surface roughness parameter a, a continuous fall in the average Nusselt number has been observed all along the wavy wall. Similar qualitative variations are also observed in local and average Sherwood number plots.

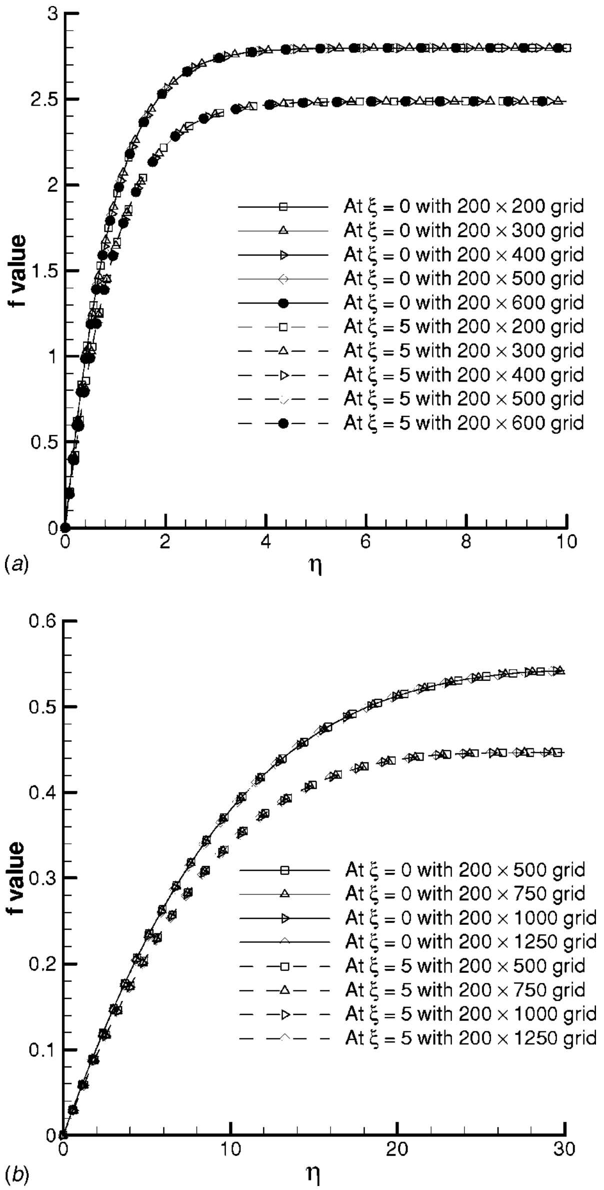

Fig. 2 Grid validation tests for various grids: (*a*) with Gr*=0, (*b*) with Gr*=1000 and with *a*=0.2, ϕ=0 deg, *B*=2, Le=1, S_T=0.05, and S_C=0.025

To further analyze the flow, temperature, and concentration variation in the entire region, $0 \leqslant \xi \leqslant 10$, $0 \leqslant \eta \leqslant 10$, f, T, and C contours are presented in Figs. 4(*a*)–4(*f*) corresponding to the parameter setting $a=0.0,0.5$, Gr*$=1$, $B=2$, Le$=1$, $S_T=0.05$, $S_C=0.025$, and $\phi=0$ deg. From these contours, one can observe that the presence of surface roughness brings in a wavy pattern. For large η, f contours get horizontal with almost zero f_η gradients, which depict a flow field with zero x component velocity and, thus, a reduced flow situation. With an increase in the surface roughness, flow is seen to get more intensified. In the corresponding T contours in Figs. 4(*c*) and 4(*d*), a plumelike structure with negative temperature values has been noted in the upper-right region for all values of wave amplitude. Temperature and concentration values are observed to be larger in the presence of surface roughness.

3.2 Influence of Grashof Number Gr* on the Heat and Mass Transfer Process. The influence of the presence of inertial forces on the double-diffusive natural convection process has

Downloaded 06 Dec 2010 to 193.140.21.150. Redistribution subject to ASME license or copyright; see http://www.asme.org/terms/Terms_Use.cfm

Table 1 Comparison of the local Nusselt and Sherwood numbers for $\xi=0$, $a=0$, Gr*$=0$, $S_T=0$, $S_C=0$

B	Le	Local Nusselt Number $((Ra\,\xi)^{-1/2}Nu_\xi)$		Local Sherwood Number $((Ra\,\xi)^{-1/2}Sh_\xi)$	
		Bejan & Khair [2]	Present Work	Bejan & Khair [2]	Present Work
4	1	0.992	0.9922	0.992	0.9922
4	4	0.798	0.7976	2.055	2.0548
4	10	0.681	0.6810	3.290	3.2896
4	100	0.521	0.5209	10.521	10.5191
2	1	0.769	0.7686	0.769	0.7686
2	2	0.710	0.7098	1.122	1.1222
2	4	0.650	0.6495	1.624	1.6243
2	6	0.618	0.6176	2.009	2.0088
2	8	0.597	0.5970	2.332	2.3324
2	10	0.582	0.5824	2.617	2.6170
2	100	0.490	0.4900	8.424	8.4226
0	1	0.444	0.4439	0.444	0.4439
0	4	0.444	0.4439	1.019	1.0191
0	10	0.444	0.4439	1.680	1.6802
0	100	0.444	0.4439	5.544	5.5440

been analyzed for a wide range of Grashof numbers ($0\leqslant$Gr*$\leqslant 10^4$), with $a=0.2$, $\phi=0$ deg, $B=2$, Le$=1$, $S_T=0.05$, and $S_C=0.025$. The local and average Nusselt number plots showing the heat fluxes along the wavy wall are presented in Figs. 3(*c*) and 3(*d*). From Fig. 3(*c*), it is observed that in the absence of inertial forces (i.e., with Gr*$=0$), the wavelength of the local heat flux variation is half that of the wavy surface. This is due to (i) the effect of diffusive forces [the first term in Eq. (8)], whose frequency is twice that of the wavy surface, and (ii) the alignment of the buoyancy forces with respect to the solid surface. Consequently, the local maxima of the local heat fluxes occur near the crests and troughs of the sinusoidal surface, where heat is convected away from the surface at a higher rate. In the presence of inertial forces, with Gr*$\neq 0$, in addition to the diffusive forces, the centrifugal forces [the second term in Eq. (8)] are also present and their combined influence again leads to an almost wavy pattern in the local heat flux distribution with wavelength half that of the wavy surface. From Fig. 3(*c*), it can also be noted that there is a drastic fall in local heat fluxes along the vertical wavy surface with increasing Gr*. For smaller Gr* ($0\leqslant$Gr*$\leqslant 1$), influence of thermal stratification term can be noted in the local heat flux curves as local heat transfer reduces significantly with increasing ξ. At larger Gr* (Gr*>1), the stratification term has only a marginal influence. At larger Gr*, heat fluxes seem to achieve a saturation level and there is no further significant reduction in the local heat fluxes as Gr* increases. The average Nusselt number plot in Fig. 3(*d*) shows a sharp raise in average heat fluxes along the wavy surface, for small values of Gr*. But for larger Gr*, there is only a slight increment in heat fluxes with increasing ξ, which implies that the thermal boundary layer (which is thin with Gr*$=0$) gets thicker as Gr* increases. Increasing Gr* shows an overall reduction in average heat flux values all along the wavy surface.

Streamlines, temperature, and concentration contours are presented in Figs. 5(*a*)–5(*i*) corresponding to Gr*$=0$, 1, 10^2 and $a=0.2$, $\phi=0$ deg, $B=2$, Le$=1$, $S_T=0.05$, and $S_C=0.025$. From the f contours in Figs. 5(*a*)–5(*c*), it can be observed that the almost-zero f_η-gradients region occurs farther away from the vertical wall as Gr* increases, thus depicting a flow intensification with increasing Gr*. From the corresponding T contours in Figs. 5(*d*)–5(*f*), one can observe the presence of a thin thermal boundary layer for Gr*$=0$, which gets thicker as Gr* increases. The extent of the region covered by the plumelike pattern, occurring in the top-right corner of the considered region, reduces as Gr* increases. With increasing Gr*, an enhancement in the temperature and concentration values has been observed.

3.3 Influence of Stratification Parameters S_T and S_C on the Heat and Mass Transfer Process. The effect of increasing the thermal stratification level has been analyzed on the double-diffusive natural convection process for a wide range of thermal stratification, $0.0\leqslant S_T\leqslant 0.1$, $a=0.2$, Gr*$=1$, $B=2$, Le$=1$, $\phi=0$ deg, $S_C=0.025$. Here it can be noted that fixing $S_T=0$ is equivalent to no stratification case (i.e., to the isothermal wall case), whereas $S_T=0.1$ shows that corresponding to the considered wall length ξ ($0\leqslant\xi\leqslant 10$), there is 100% variation in the temperature from $T=1$ at the lower end ($\xi=0$) to $T=0$ at the upper end ($\xi=10$) of the vertical surface. From the local and average Nusselt number plots in Figs. 3(*e*) and 3(*f*), one can observe that the local and average heat transfer decreases significantly with an increasing thermal stratification parameter S_T. Since at the lower end of the vertical wall (i.e., at $\xi=0$, due to the boundary condition $T=1-S_T\xi$) wall temperature is always 1, irrespective of the stratification parameter S_T, heat fluxes are equal at $\xi=0$ for all S_T. For all thermal stratification levels, local heat fluxes are seen to reduce as ξ increases. Also this reduction in local heat fluxes with ξ becomes more significant with an increment in the thermal

Downloaded 06 Dec 2010 to 193.140.21.150. Redistribution subject to ASME license or copyright; see http://www.asme.org/terms/Terms_Use.cfm

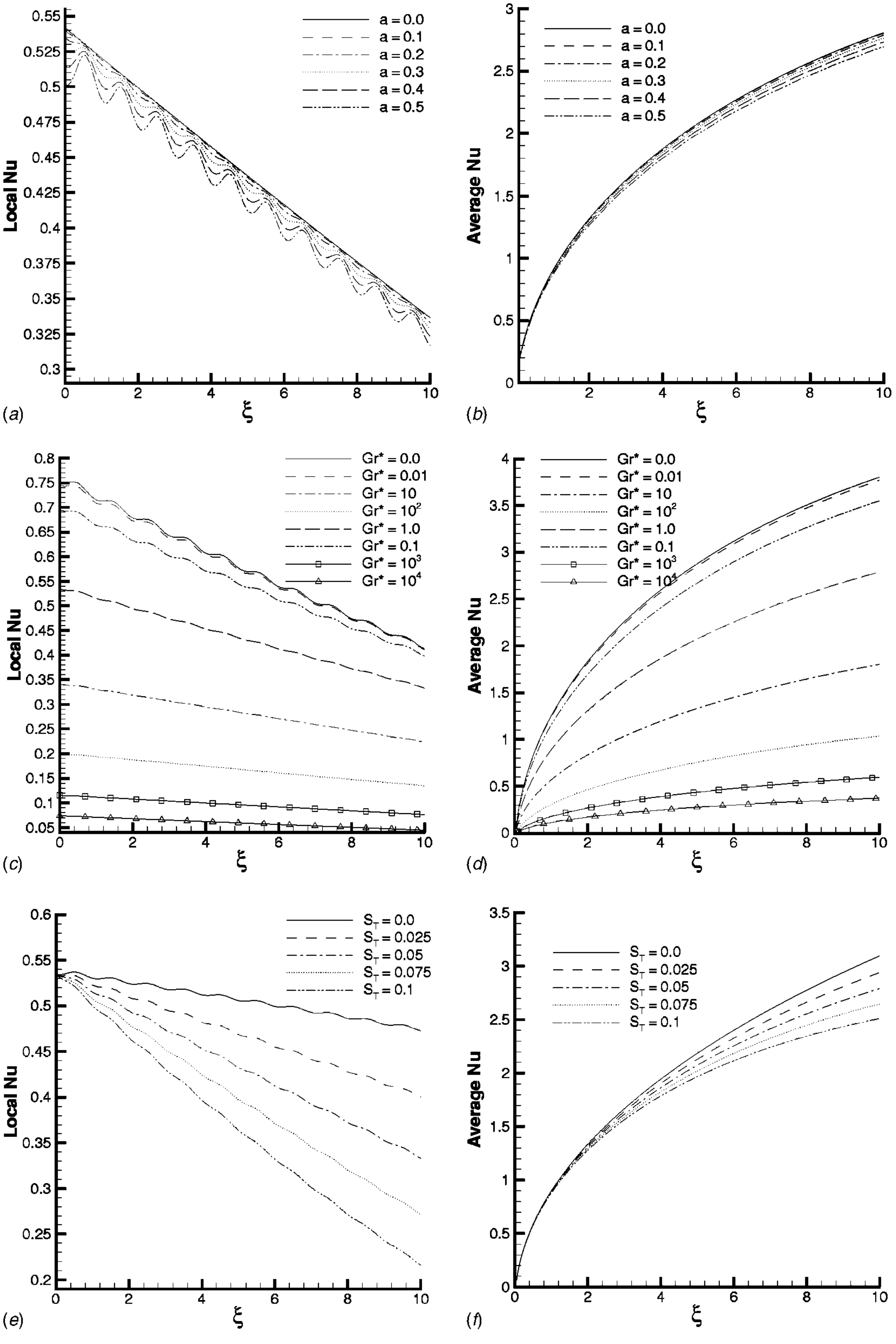

Fig. 3 Local Nusselt number plots with (*a*) varying *a*, (*b*) varying Gr*, (*c*) varying S_T and corresponding average Nusselt number plots are in (*b*), (*d*) and (*f*), respectively.

stratification parameter S_T. Both of these effects can be attributed to the reduction in wall temperature specified by the boundary condition $T=1-S_T\xi$. Though for the $S_T=0$ case there is no thermal stratification, the marginal fall in local Nu plot is due to the presence of mass stratification term S_C. The waviness in the local Nu plots disappears with increasing S_T and ξ. The reduction in the average Nusselt number plots in Fig. 3(*f*) depicts the increasing thickness of the thermal boundary layer with increasing S_T.

For the further investigations f, T, and C contours are traced

Downloaded 06 Dec 2010 to 193.140.21.150. Redistribution subject to ASME license or copyright; see http://www.asme.org/terms/Terms_Use.cfm

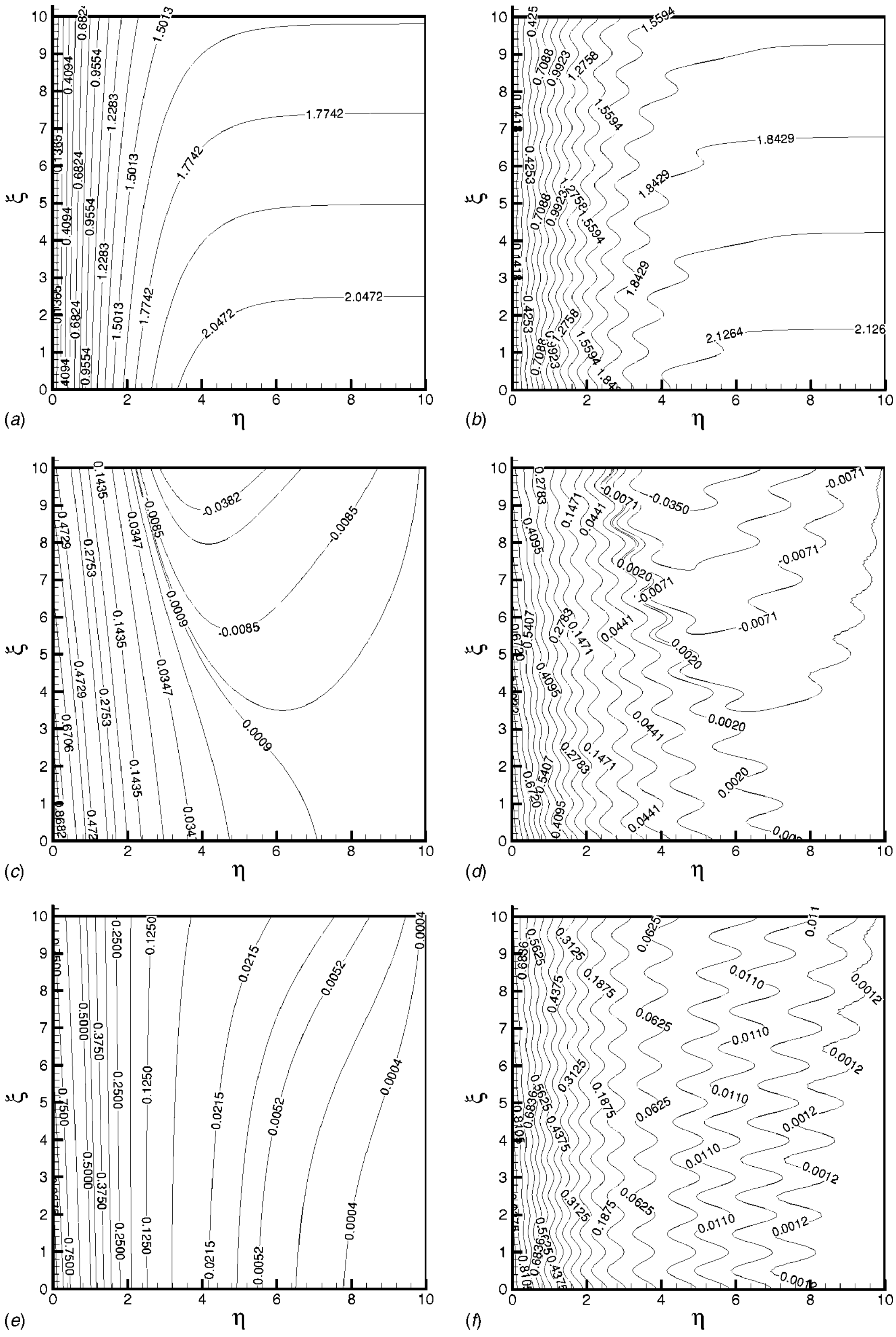

Fig. 4 ***f*** **contours for (*a*)** ***a*=0.0, (*b*)** ***a*=0.5 with ϕ=0 deg, *B*=2, Le=1, Gr*=1, S_T=0.05, and S_C=0.025, corresponding *T* and *C* contours are in (*c*) and (*d*) and in (*e*) and (*f*) respectively.**

corresponding to the parameter settings $a=0.2$, $\mathrm{Gr}^*=1$, $B=2$, $\mathrm{Le}=1$, $\phi=0$ deg, $S_C=0.025$, and $S_T=0.0,0.05,0.1$. It was observed from the f contours that the spatial location of η corresponding to almost zero f_η gradients shift to the left, with increasing S_T. In Fig. 6(*a*) corresponding to $S_T=0.0$, one can see that the isotherms, which are parallel to the vertical wall when η is small, slightly shift to the right in the upper region as η increases. This can be attributed to the influence of the mass stratification term present. Such a shift is not noted when both thermal and mass stratification values are zero. When S_T increases above 0.025, a

Downloaded 06 Dec 2010 to 193.140.21.150. Redistribution subject to ASME license or copyright; see http://www.asme.org/terms/Terms_Use.cfm

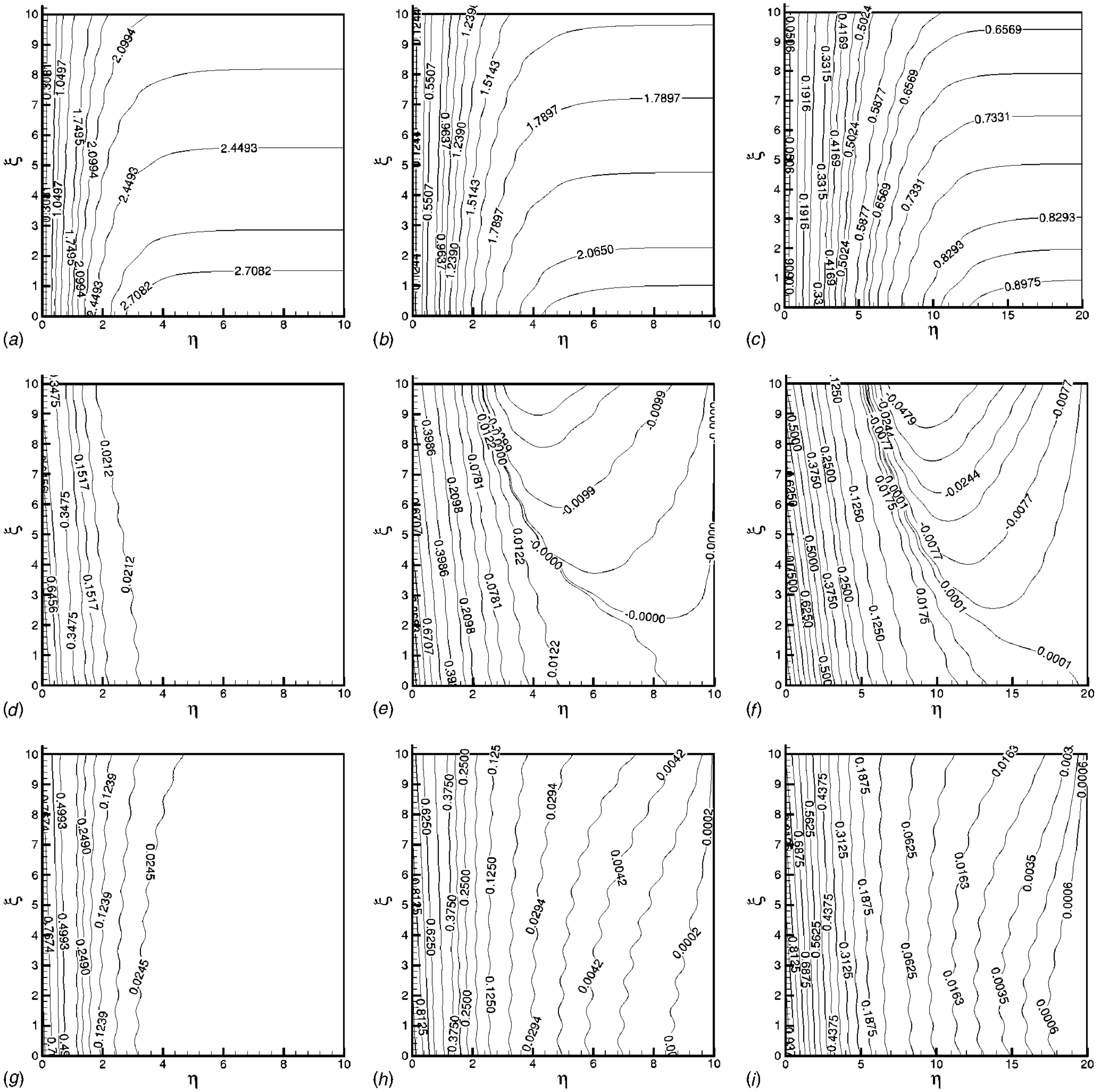

Fig. 5 ***f*-contours for (*a*) $Gr^*=0$, (*b*) $Gr^*=1$, (*c*) $Gr^*=10^2$ with $a=0.2$, $\phi=0$ deg, $B=2$, $Le=1$, $S_T=0.05$, and $S_C=0.025$, corresponding *T* and *C* contours are in (*d*)–(*f*) and in (*g*)–(*i*) respectively.**

cold region with a plumelike pattern emerges from the upper-right corner of the porous region. It has a zero temperature isotherm interface to the positive temperature zone adjacent to the wavy wall. With increasing value of S_T, the cold region with a plumelike structure gets dominantly enlarged, indicating a drastic reduction in the heat transfer. For the case $S_T=0.1$ [i.e. when the temperature of the upper end of the vertical surface ($\xi=10$) is zero], this thermal plumelike structure starts exactly from the upper-left corner and spreads up to the lower-right end thus covering most of the porous region. From the corresponding concentration contours in Figs. 6(*d*)–6(*f*) one can note that with an increasing thermal stratification level S_T, the spread of the species dissolved in the fluid shifts to the right in the top of the considered porous region. Similar features were observed by Angirasa et al. [6] in their study of aiding buoyancy forces (i.e., for $B>0$ in the presence of thermal stratification and with $S_C=0$).

Influence of increasing mass stratification level S_C is analyzed for $0.0\leqslant S_C\leqslant 0.05$, $a=0.2$, $\phi=0$ deg, $Gr^*=1$, $B=2$, $Le=1$ and $S_T=0.05$. It was observed from the local and average Nusselt number plots that an increasing mass stratification level results in a reduction in the heat flux magnitudes along the wavy surface. *f* contours have been traced with varying S_C, and they depict a reduction in the flow intensities. Interesting features are observed in the isotherms shown in Figs. 6(*g*)–6(*i*). Here the cold regions with the plumelike pattern, noted at low levels of concentration stratification, gradually vanish with increasing levels of concentration stratification. Isoconcentration contours show a reduction in the concentration level in the entire region with increasing S_C.

3.4 Influence of Buoyancy Ratio *B* on the Heat and Mass Transfer Process.

Influence of varying buoyancy ratio on heat

Downloaded 06 Dec 2010 to 193.140.21.150. Redistribution subject to ASME license or copyright; see http://www.asme.org/terms/Terms_Use.cfm

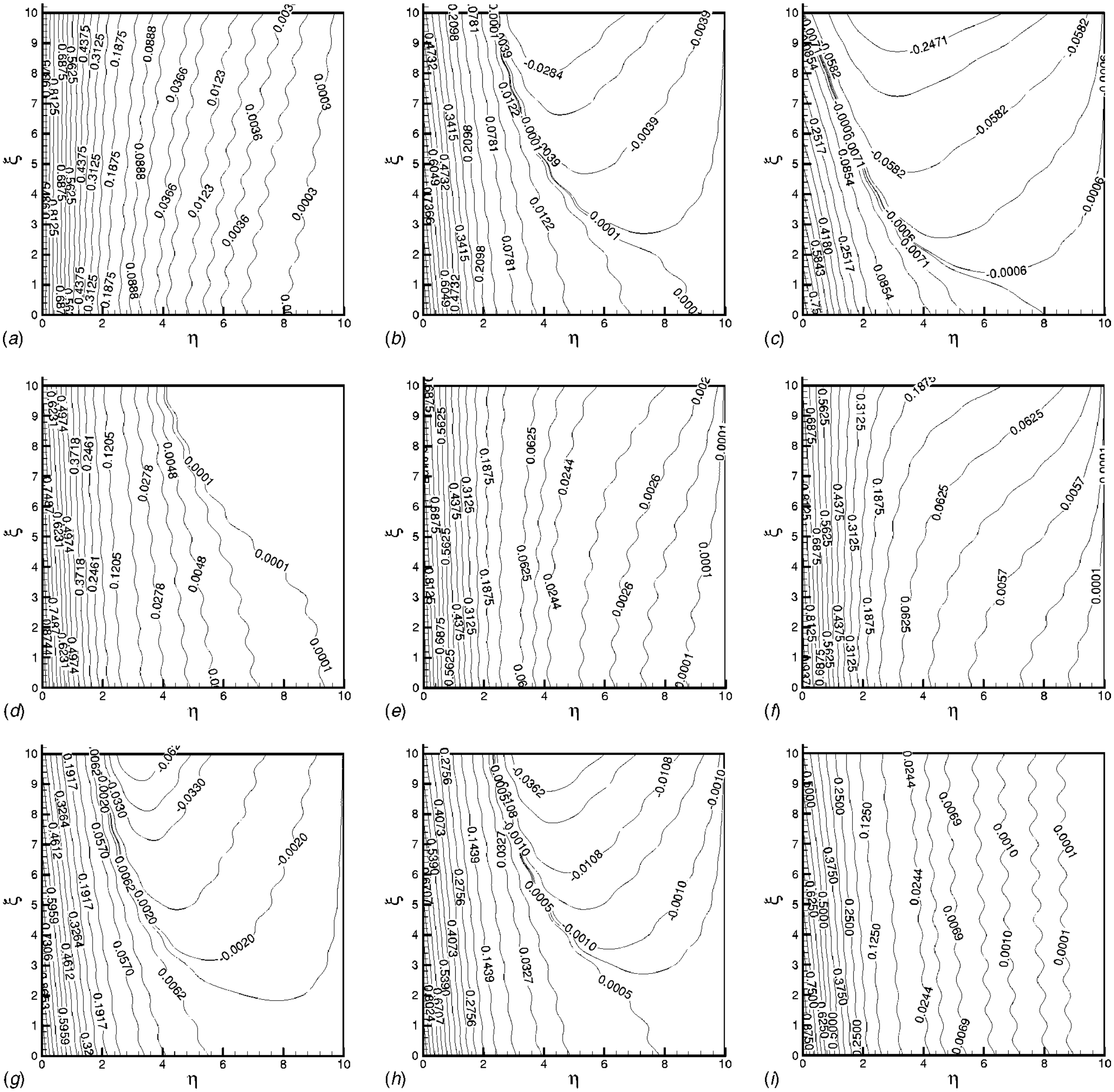

Fig. 6 T contours in (*a*)–(*c*) and C contours in (*d*)–(*f*) corresponding to $S_T=0.0$, 0.05, 0.1, respectively, with $a=0.2$, $\phi=0$ deg, $\mathrm{Gr}^*=1$, $B=2$, $\mathrm{Le}=1$, and $S_C=0.025$. T contours with varying S_C ($S_C=0.0$, 0.025, 0.05) are in (*g*)–(*i*) with other parameters fixed as $a=0.2$, $\phi=0$ deg, $\mathrm{Gr}^*=1$, $B=2$, $\mathrm{Le}=1$, and $S_T=0.05$.

and mass transfer has been studied by choosing $0 \leqslant B \leqslant 4$, $a=0.2$, $\phi=0$ deg, $\mathrm{Gr}^*=1$, $S_T=0.05$, and $S_C=0.025$. The magnitude of B indicates the relative strengths of the two buoyant forces, namely, concentration and thermal buoyancy forces, and its sign indicates the direction of these forces. For the case $B=0$, the flow is driven by the thermal buoyancy alone. In Figs. 7(*a*) and 7(*b*), local and average Nusselt number plots are presented for $0 \leqslant B \leqslant 4$. It is observed from both the plots that the heat fluxes along the wavy wall are smaller when only thermal buoyancy forces are present (i.e., for $B=0$.) With increasing B, both local and average Nusselt numbers increase along the wavy wall. Local heat fluxes become more wavy with increasing B, which shows that the surface undulations have more influence when the buoyancy ratio is higher.

It was observed from the streamlines that increasing B enhances the region that corresponds to the zero f_η gradients. The flow region, which covers almost the entire region for $B=0$ case, confines to the region $\eta<3$ for $B=4$. Isotherms presented in Figs. 8(*a*)–8(*c*), corresponding to $B=0$, 2, 4, show that the colder region with a plumelike structure in the isotherms increases in size with increasing B. Here one may also note that no plumelike structure is seen when $B=0$. Iso-concentration plots show the reduction of species concentration values with increasing B.

3.5 Influence of Lewis Number Le on the Heat and Mass Transfer Process.

To analyze the influence of increasing Lewis number on the double-diffusive natural convection process, local and average Nusselt and Sherwood number plots are presented in Figs. 7(*c*)–7(*f*) for the parameters setting $0.05 \leqslant \mathrm{Le} \leqslant 5$, $a=0.2$, $\phi=0$ deg, $\mathrm{Gr}^*=1$, $B=2$, $S_T=0.05$, and $S_C=0.025$. From Figs.

Downloaded 06 Dec 2010 to 193.140.21.150. Redistribution subject to ASME license or copyright; see http://www.asme.org/terms/Terms_Use.cfm

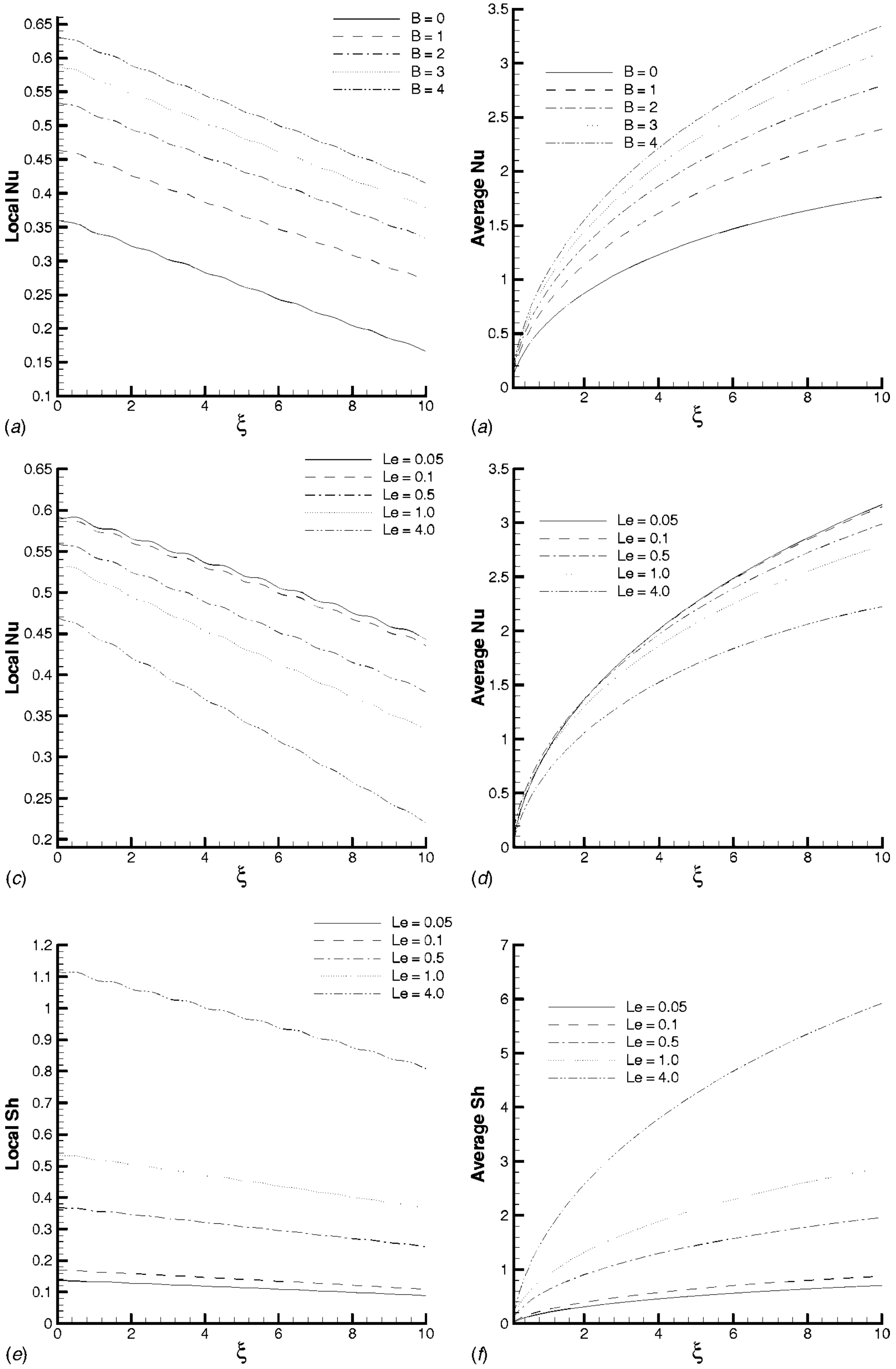

Fig. 7 Local Nusselt number plots with (*a*) varying *B*, (*c*) varying Le and corresponding average Nusselt number plots are in (*b*) and (*d*), local Sherwood number plots with varying Le in (*e*) and corresponding average Sherwood number plots in (*f*).

7(*c*) and 7(*e*), it can be observed that increasing Le reduces the heat fluxes along the vertical wavy surface, whereas it significantly enhances the mass fluxes along the wavy surface. The average Nusselt number in Fig. 7(*d*) decreases while the average Sherwood number in Fig. 7(*f*) increases all along the wavy surface with increasing Le.

For the further analysis of flow, temperature, and concentration properties in the entire region, streamlines, isotherms, and isoconcentration plots are drawn corresponding to the above-mentioned parameter setting. From the f contours, it was observed that with increasing Le, the region that corresponds to the zero f_η gradients increases, which supports a reduction in the flow region. Tempera-

Downloaded 06 Dec 2010 to 193.140.21.150. Redistribution subject to ASME license or copyright; see http://www.asme.org/terms/Terms_Use.cfm

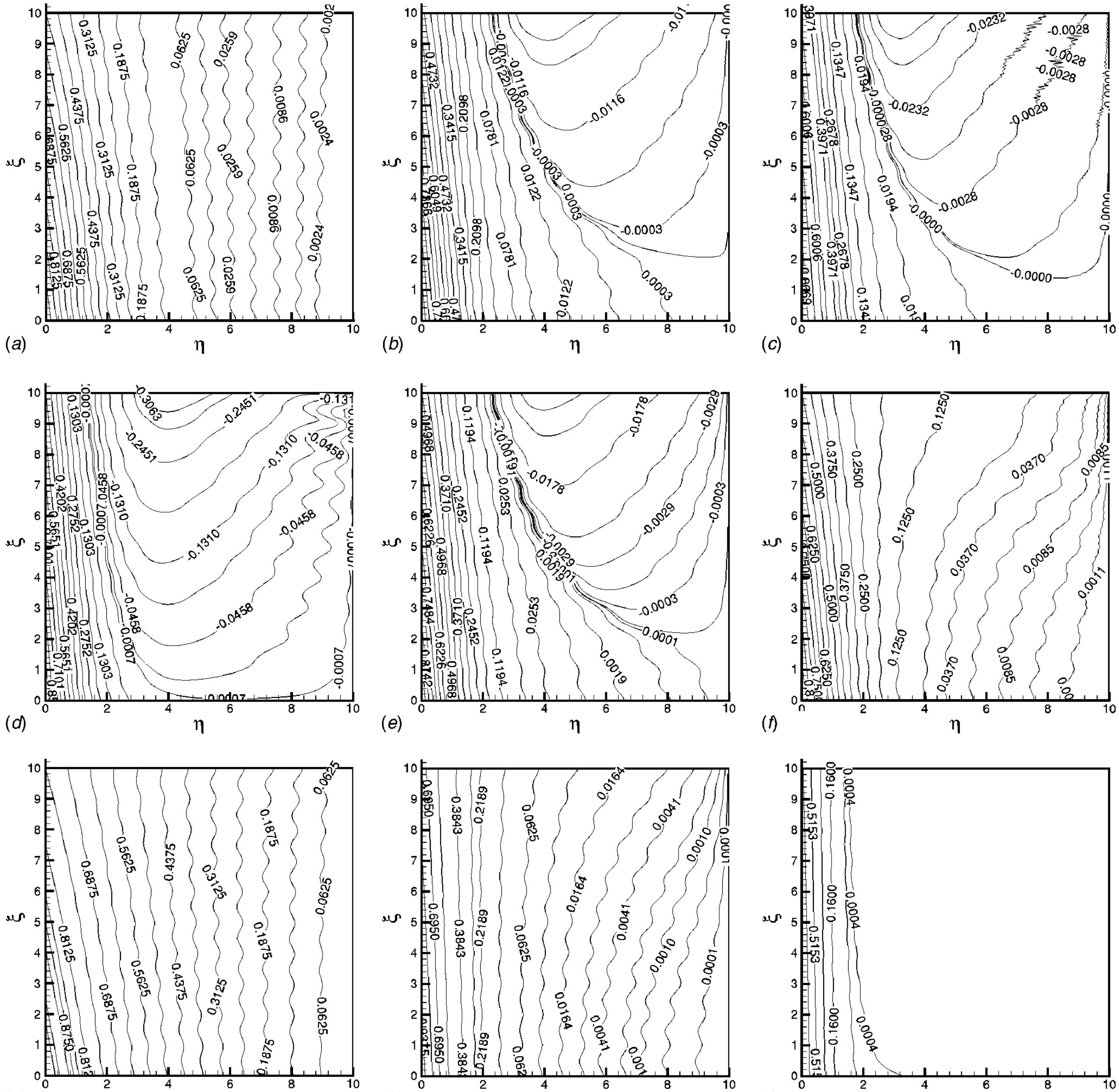

Fig. 8 ***T* contours for (*a*) $B=0$, (*b*) $B=2$, and (*c*) $B=4$ with $a=0.2$, $\phi=0$ deg, Gr*=1, Le=1, $S_T=0.05$, and $S_C=0.025$. *T* contours in (*d*)–(*f*) and *C* contours in (*g*)–(*i*) corresponding to Le=0.05, 1, 5, respectively, with $a=0.2$, $\phi=0$ deg, Gr*=1, $B=2$, $S_T=0.05$, and $S_C=0.025$.**

ture and concentration contours for Le=0.05, 1, 5 are presented in Figs. 8(*d*)–8(*i*). As Le being the ratio of thermal and mass diffusivity, an increase in Le shows greater thermal diffusive forces and a reduction in mass diffusive forces. From the isotherms and isoconcentration plots it is clear that increasing Le diffuses the heat in a larger region and confines the diffusion of the species to a smaller region. The plumelike structure covering almost the entire region in the temperature contour corresponding to Le=0.05 slowly disappears as Le increases, thus showing an enhancement in the heat transfer. From the concentration contours it is clear that as Le increases, the concentration of the species decreases and, for large Le, becomes almost zero in the entire region.

4 Conclusion

The combined influence of mass and thermal stratification together with a non-Darcian assumption, has been analyzed on double-diffusive natural convection from a wavy vertical wall to a porous media. Results obtained can be summarized as follows:

- An almost-periodic variation has been observed in the local Nu plots with a wavelength ℓ in the absence or presence of Gr*.
- Increasing a, Gr*, S_T, and S_C are seen to reduce the local and average Nu and Sh values, while increasing B enhances both. Increasing Le reduces the local and average heat transfer and significantly enhances the mass transfer along the wavy surface.
- Increasing thermal stratification increasingly limits the region to which heat is spread and the opposite is noted with increasing mass stratification.
- Increasing Gr* enhances the meaningful flow region, whereas increasing S_T, S_C, B, and Le are seen to confine this region.

Downloaded 06 Dec 2010 to 193.140.21.150. Redistribution subject to ASME license or copyright; see http://www.asme.org/terms/Terms_Use.cfm

- Increasing S_T favors the concentration transport to the porous region increasingly farther from the wavy wall, whereas increasing S_C leads to increasing confinement of the concentration spread region. Increasing both a and Gr* are observed to increase T and C values, whereas increasing B is seen to reduce both. Increasing Le enhances the temperature and reduces the species concentration values in the porous region.

Nomenclature

$\bar{a}$ = dimensional amplitude of the wavy surface
a = nondimensional amplitude of the wavy surface
B = buoyancy ratio $[=\beta_c(c_w-c_{\infty,0})/\beta_t(t_w-t_{\infty,0})]$
c = dimensional concentration of the dissolved species
C = nondimensional concentration of the dissolved species $[=(c-c_{\infty,x})/(c_w-c_{\infty,0})]$
C_f = dimensionless form drag constant [1] used in Gr* expression
D = diffusion coefficient of the species
f = nonsimilar stream function [Eq. (7)]
g = gravitational acceleration
Gr* = modified Grashof number $[=Kg\beta_t(t_w-t_{\infty,0})K'/\nu^2]$
K = permeability of the porous medium
K' = inertia coefficient used in Gr* expression $(=C_f K^{1/2})$
ℓ = wavelength parameter of the surface waves
Le = Lewis number $(=\alpha/D)$
Nu = Nusselt number
Ra = modified Rayleigh number $[=Kg\beta_t\ell(t_w-t_{\infty,0})/\alpha\nu]$
s_c = dimensional mass stratification term $(=dc_{\infty,x}/dx)$
s_t = dimensional thermal stratification term $(=dt_{\infty,x}/dx)$
S_C = nondimensional mass stratification term $\{=[1/(c_w-c_{\infty,0})]/(dc_{\infty,x}/dX)\}$
S_T = nondimensional thermal stratification term $\{=[1/(t_w-t_{\infty,0})]/(dt_{\infty,x}/dX)\}$
Sh = Sherwood number
t = dimensional temperature
T = nondimensional temperature $[=(t-t_{\infty,x})/(t_w-t_{\infty,0})]$
u,v = dimensional velocity components
x,y = dimensional Cartesian coordinates
X,Y = nondimensional Cartesian coordinates
$\prec$ = almost less than
$\succ$ = almost greater than

Greek Symbols

α = thermal diffusivity
β_c = coefficient of mass expansion $[=-(1/\rho)(\partial\rho/\partial c)_{P,t}]$
β_t = coefficient of thermal expansion $[=-(1/\rho)(\partial\rho/\partial t)_{P,c}]$
σ = sinusoidal wavy curve $[\sigma(X)=\frac{a}{\pi}\sin(\pi X-\phi)]$
ξ,η = transformed coordinate variables
ρ = fluid density
$\bar{\Psi}$ = dimensional stream function $(u=\partial\bar{\Psi}/\partial y, v=-\partial\bar{\Psi}/\partial x)$
Ψ = nondimensional stream function $(=\bar{\Psi}/\alpha)$
ν = kinematic viscosity
ϕ = phase of the wavy surface

Subscripts

$0,\infty$ = ambient points
P = pressure
w = evaluated at the wall
x = evaluated at point x

References

[1] Nield, D. A., and Bejan, A., 1998, *Convection in Porous Media*, Springer Verlag, New York.
[2] Bejan, A., and Khair, K. R., 1985, "Heat and Mass Transfer by Natural Convection in a Porous Medium," Int. J. Heat Mass Transfer, **28**(5), pp. 909–918.
[3] Angirasa, D., Peterson, G. P., and Pop, I., 1997, "Combined Heat and Mass Transfer by Natural Convection With Opposing Buoyancy Effects in a Fluid Saturated Porous Medium," Int. J. Heat Mass Transfer, **40**(12), pp. 2755–2773.
[4] Singh, P., and Queeny, O., 1997, "Free Convection Heat and Mass Transfer Along a Vertical Surface in a Porous Medium," Acta Mech., **123**, pp. 69–73.
[5] Nakayama, A., and Hossain, M. A., 1995, "An Integral Treatment for Combined Heat and Mass Transfer by Natural Convection in a Porous Medium," Int. J. Heat Mass Transfer, **38**(4), pp. 761–765.
[6] Angirasa, D., Peterson, G. P., and Pop, I., 1997, "Combined Heat and Mass Transfer by Natural Convection in a Saturated Thermally Stratified Porous Medium," Numer. Heat Transfer, Part A, **31**, pp. 255–272.
[7] Rathish Kumar, B. V., Singh, P., and Bansod, V. J., 2002, "Effect of Thermal Stratification on Double-Diffusive Natural Convection in a Vertical Porous Enclosure," Numer. Heat Transfer, Part A, **41**, pp. 421–447.
[8] El-Khatib, G., and Prasad, V., 1987, "Effects of Stratification on Thermal Convection in Horizontal Porous Layers With Localized Heating from Below," ASME J. Heat Transfer, **109**, pp. 683–687.
[9] Rathish Kumar, B. V., and Shalini, 2004, "Double-Diffusive Natural Convection Induced by a Wavy Surface in a Stratified Porous Medium," J. Porous Media, **7**(4), pp. 31–40.
[10] Takhar, H. S., and Pop, I., 1987, "Free Convection From a Vertical Flat Plate to a Thermally Stratified Fluid," Mech. Res. Commun., **14**(2), pp. 81–86.
[11] Tewari, K., and Singh, P., 1992, "Natural Convection in a Thermally Stratified Fluid Saturated Porous Medium," Int. J. Eng. Sci., **8**, pp. 1003–1007.
[12] Rees, D. A. S., and Lage, J. L., 1997, "The Effect of Thermal Stratification on Natural Convection in a Vertical Porous Insulation Layer," Int. J. Heat Mass Transfer, **40**(1), pp. 111–121.
[13] Rathish Kumar, B. V., and Singh, P., 1998, "Effect of Thermal Stratification on Free Convection in a Fluid-Saturated Porous Enclosure," Numer. Heat Transfer, Part A, **34**, pp. 343–356.
[14] Yao, L. S., 1983, "Natural Convection Along a Vertical Wavy Surface," ASME J. Heat Transfer, **105**, pp. 465–468.
[15] Rees, D. A. S, and Pop, I., 1994, "A Note on Free Convection Along a Vertical Wavy Surface in a Porous Medium," ASME J. Heat Transfer, **116**, pp. 505–508.
[16] Cheng, C. Y., 2000, "Natural Convection Heat and Mass Transfer Near a Vertical Wavy Surface with Constant Wall Temperature and Concentration in a Porous Medium," Int. Commun. Heat Mass Transfer, **27**(8), pp. 1143–1154.
[17] Bejan, A., and Poulikakos, D., 1984, "The Non Darcy Regime for Vertical Boundary Layer Natural Convection in a Porous Medium," Int. J. Heat Mass Transfer, **27**(5), pp. 717–722.
[18] Plumb, O. A., and Huenefeld, J. C., 1981, "Non-Darcy Natural Convection from Heated Surfaces in Saturated Porous Medium," Int. J. Heat Mass Transfer, **24**(4), pp. 765–768.
[19] Kumari, M., Pop, I., and Nath, G., 1985, "Non-Darcy Natural Convection from a Heated Vertical Plate in Saturated Porous Media with Mass Transfer," Int. Commun. Heat Mass Transfer, **12**, pp. 337–346.
[20] Lai, F. C., and Kulacki, F. A., 1987, "Non-Darcy Convection from Horizontal Impermeable Surfaces in Saturated Porous Media," Int. J. Heat Mass Transfer, **30**(10), pp. 2189–2192.
[21] Angirasa, D., and Srinivasan, J., 1992, "Natural Convection Heat Transfer From an Isothermal Vertical Surface to a Stable Thermally Stratified Fluid," ASME J. Heat Transfer, **114**, pp. 917–923.
[22] Johnson, C. H., and Cheng, P., 1978, "Possible Similarity Solutions for Free Convection Boundary Layers Adjacent to Flat Plates in Porous Media," Int. J. Heat Mass Transfer, **21**, pp. 709–718.
[23] Keller, H. B., and Cebeci, I., 1971, *Accurate Numerical Method for Boundary Layers—I, Two Dimensional Laminar Flows, Lecture Notes in Physics, 8*, Springer Verlag, New York.

Downloaded 06 Dec 2010 to 193.140.21.150. Redistribution subject to ASME license or copyright; see http://www.asme.org/terms/Terms_Use.cfm

A Novel Methodology for Thermal Analysis of a Composite System Consisting of a Porous Medium and an Adjacent Fluid Layer

Jung Yim Min

Sung Jin Kim

Department of Mechanical Engineering,
Korea Advanced Institute of Science and Technology,
Taejon, 305-701, Korea

An innovative methodology is presented for the purpose of analyzing fluid flow and heat transfer in a porous–fluid composite system, where the porous medium is assumed to have a periodic structure, i.e., solid and fluid phases repeat themselves in a regular pattern. With the present method, analytical solutions for the velocity and temperature distributions are obtained when the distributions in the adjacent fluid layer are allowed to vary in the directions both parallel and perpendicular to the interface between the porous medium and the adjacent fluid layer. The analytical solutions are validated by comparing them with the corresponding numerical solutions for the case of the ideal composite channel, and with existing experimental data. The present analytical solutions have a distinctive advantage in that they do not involve any unknown coefficients resulting from the previous interfacial conditions. Moreover, by comparing interfacial conditions derived from the present study with the stress- and flux-jump conditions developed by previous investigators, the unknown coefficients included in the stress- and flux-jump conditions are analytically determined and are shown to depend on the porosity, the Darcy number and the pore diameter. [DOI: 10.1115/1.1863273]

1 Introduction

A composite system, consisting of a porous medium and an adjacent fluid layer, is used in various engineering applications [1]. For example, a composite system can be found in the following applications: Drying processes, solid-matrix heat exchangers, electronics cooling, thermal insulation, heat pipes, nuclear reactors, and porous journal bearings. Due to the numerous applications, there have been many attempts to examine fluid-flow and heat-transfer characteristics in composite systems. For correct analysis of fluid flow and heat transfer in composite systems, imposition of appropriate conditions at the interface is very important. This is because interfacial conditions significantly affect final solutions for velocity and temperature distributions. For that reason, many investigators have proposed different types of interfacial conditions between the porous medium and the adjacent fluid layer, as summarized and compared in the work of Alazmi and Vafai [2].

The study on hydrodynamic interfacial conditions stems from the work of Beavers and Joseph [3]. They performed experiments and postulated that there exists a slip in velocity at the interface, i.e., the interfacial velocity is not equal to the Darcian velocity in the porous medium. Neale and Nader [4] pointed out that the slip in velocity occurred because Darcy's law was used inside the porous medium. They proposed continuous interfacial conditions for both velocity and shear stress which can be used when the Brinkman term is introduced into Darcy's law. Since then, many investigators [5–8] had accepted the use of continuous interfacial conditions to analyze fluid flow in composite channels until Nield [9] claimed that discontinuity occurs in shear stress at the interface. He claimed that continuity in shear stress is inappropriate at the interface while continuity in velocity is valid there. He pointed out that shear stress is continuous over the fluid (or pore) portion of the interface, but that this continuity breaks down over the solid (or matrix) portion of the interface. Recently, Ochoa-Tapia and Whitaker [10,11] presented a mathematical model for the so-called (shear) stress-jump condition based on the volume-averaging technique of momentum equations.

As for thermal interfacial conditions, most conditions found in the literature are proposed for the one-equation model in analyzing heat transfer through a porous medium [5,6,12–14]. The one-equation model is appropriate under the assumption of local thermal equilibrium. When this condition of local thermal equilibrium is far from reality, the one-equation model needs to be replaced with the two-equation model, which treats the fluid part and the solid part in the porous medium separately. The trend is moving toward using the two-equation model because in many practical engineering applications the fluid temperature deviates greatly from the solid temperature in a porous medium. Nevertheless, thermal interfacial conditions for the two-equation model have rarely been suggested. Recently, Ochoa-Tapia and Whitaker [15] have done a pioneering work by developing the so-called (heat) flux-jump conditions which can be used together with the continuous temperature condition over the fluid portion of the interface. However, the stress- and flux-jump conditions have an inherent problem; they involve unknown coefficients, which need to be fitted experimentally or numerically. The former involves the stress-jump coefficient β, and the latter includes the so-called boundary heat transfer coefficient, $h_{\beta\sigma}$. The practical use of the stress- and flux-jump conditions has been hampered due to insufficient information on these coefficients. To the authors' knowledge, there are only a few studies dealing with those coefficients, including the one in which Ochoa-Tapia and Whitaker [11] tried to determine β using the experimental data of Beavers and Joseph [3]. For that reason, in the study of Kuznetsov [12], arbitrary values for β were taken as if β was an independent parameter, even though it depends on the system characteristics.

The purpose of the present paper is to present a novel method for analyzing fluid flow and heat transfer in a porous–fluid composite system without invoking the above-mentioned unknown coefficients. In the proposed method, velocity and temperature profiles in the adjacent fluid layer are allowed to vary in the directions both parallel and perpendicular to the interface between

Contributed by the Heat Transfer Division of ASME for publication in the JOURNAL OF HEAT TRANSFER. Manuscript received February 5, 2004; revision received November 19, 2004. Review conducted by: V. Prasad.

Copyright © 2005 by ASME

Downloaded 06 Dec 2010 to 193.140.21.150. Redistribution subject to ASME license or copyright; see http://www.asme.org/terms/Terms_Use.cfm

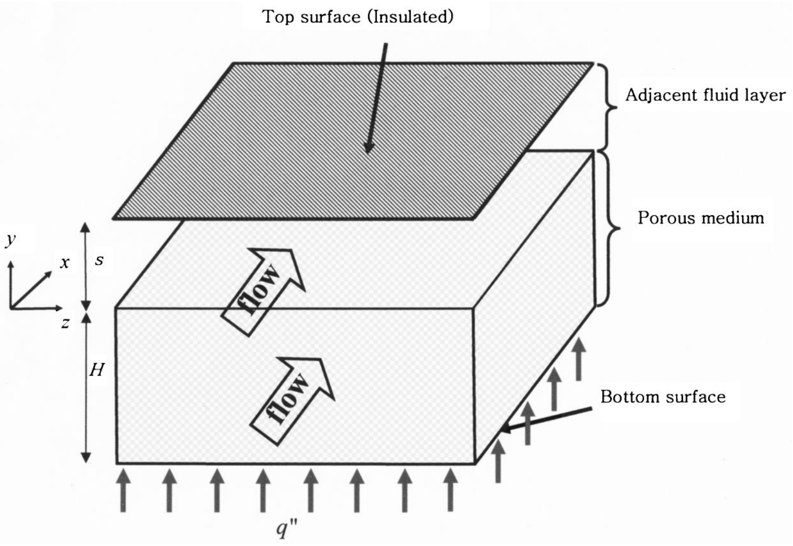

Fig. 1 Schematic of a composite system consisting of a porous medium and an adjacent fluid layer

the porous medium and the adjacent fluid layer, where solid and fluid phases repeat themselves in a regular pattern. Analytical solutions free from any unknown coefficients for velocity and temperature distributions are obtained for a homogeneous porous–fluid composite channel. The validity of the analytical solutions obtained from the present method is confirmed both numerically and experimentally. An ideal composite channel, which was previously used in the studies of Taylor [16] and Richardson [17], is introduced for numerical validation. In addition, the analytical solutions are validated by comparing them with the experimental data of Beavers and Joseph [3]. The interfacial conditions, derived from the continuities of shear stress and heat flux between two phases of the porous medium and the contacting fluid layer, bear a favorable comparison with the stress- and flux-jump conditions of Ochoa-Tapia and Whitaker [10,15]. Finally, through the comparison of the proposed interfacial conditions with the stress- and flux-jump conditions, we analytically determine the unknown coefficients appearing in the stress- and flux-jump conditions.

2 Mathematical Formulation

The problem under consideration in this paper is forced convective fluid flow and heat transfer in the composite channel occupied by a porous medium and an adjacent fluid layer. The porous medium is isotropic and homogeneous. In addition, the porous medium is assumed to have a periodic structure, i.e., its solid and fluid phases repeat themselves in a regular pattern, as shown in Fig. 1. The fluid is flowing uniformly parallel to the interface between the porous medium and the adjacent fluid layer (hereafter the porous–fluid interface) in the x-direction. The top surface of the channel ($y=s$) is insulated, and the bottom surface ($y=-H$) is uniformly heated. In analyzing the problem, the flow is assumed to be laminar and both hydrodynamically and thermally fully developed. All thermo-physical properties are assumed to be constant. For convenience of mathematical formulation, we introduce the following dimensionless parameters:

$$U=\frac{u}{H^2\left(-\frac{1}{\mu_f}\frac{dp}{dx}\right)},\quad \theta=\frac{T-T_w}{\frac{q''(H+s)}{k_f}},\quad Y=\frac{y}{H} \tag{1}$$

where U, u, H, p, μ_f, θ, T, q'', s, and k_f are dimensionless velocity, velocity, height of the porous medium, pressure, fluid viscosity, dimensionless temperature, temperature, uniform heat flux, thickness of the fluid layer, and fluid conductivity, respectively.

2.1 Velocity Distributions

2.1.1 Previous Approach with the Stress-Jump Condition The following equations, which are written in the dimensionless form with the parameters defined in Eq. (1), have been used in previous analyses for the porous medium and for the adjacent fluid layer [3–12].

In the porous medium ($-1\leqslant Y\leqslant 0^-$)

$$\frac{d^2\langle U\rangle_f}{dY^2}-\frac{\langle U\rangle_f}{Da}=-1 \tag{2}$$

$$\langle U\rangle_s=0 \tag{3}$$

In the adjacent fluid layer ($0^+\leqslant Y\leqslant S$)

$$\frac{d^2\langle U\rangle}{dY^2}=-1 \tag{4}$$

where $Da=K/\varepsilon H^2$. Also, $\langle\ \rangle_f$, and $\langle\ \rangle_s$ denote the volume-averaged values over the fluid phase and the solid phase of the porous medium, respectively. Similarly, $\langle\ \rangle$ denotes the volume-averaged value over the adjacent fluid layer. Equations (2)–(4) are averaged in the z-direction, and can be analytically solved by using the appropriate interfacial conditions at the porous–fluid interface. Several interfacial conditions are already reviewed in the Introduction section. Among them, the stress-jump condition along with the continuous velocity condition, suggested by Ochoa-Tapia and Whitaker [10], is given by

$$\left.\frac{d\langle U\rangle_f}{dY}\right|_{y=0^-}-\left.\frac{d\langle U\rangle}{dY}\right|_{y=0^+}=\frac{\beta}{\sqrt{\varepsilon Da}}U_i \tag{5}$$

$$\langle U\rangle_f\big|_{y=0^-}=\langle U\rangle_f\big|_{y=0^+} \tag{6}$$

where U_i is the superficial averaged velocity at the porous–fluid interface. The coefficient β appearing in the so-called stress-jump condition, Eq. (5), is an unknown coefficient. It should be fitted experimentally or numerically. To overcome the extra work in determining the unknown coefficient, we propose a method for obtaining an analytical solution for the velocity distribution without invoking the unknown coefficient.

2.1.2 Present Approach. The governing equations for the porous medium are the same as Eqs. (2) and (3). On the other

Downloaded 06 Dec 2010 to 193.140.21.150. Redistribution subject to ASME license or copyright; see http://www.asme.org/terms/Terms_Use.cfm

hand, instead of using Eq. (4), Eq. (7) is used as the governing equation for the adjacent fluid layer in this study.

In the adjacent fluid layer $(0^+ \leq Y \leq S)$

$$\frac{\partial^2 U}{\partial Z^2} + \frac{\partial^2 U}{\partial Y^2} = -1 \tag{7}$$

Here we should address the difference between the present method and the existing methods and the reason why we propose the present method. Previous investigators [4–12] used Eqs. (2)–(4) when they tried to analyze fluid flow in the composite system with proper interfacial conditions, such as the continuous velocity and stress conditions [4], and the stress-jump condition with the continuous velocity condition [10]. Many investigators had frequently used the continuous velocity and stress conditions in the past, but the stress-jump condition with the continuous velocity condition has recently been accepted as the most appropriate interfacial condition. However, the discontinuity in shear stress across the fluid portion of the interface is not familiar from a viewpoint of classical fluid mechanics. Physically speaking, there is no reason why there exists discontinuity in shear stress across the fluid portion of the interface. The problem arises due to the fact that the governing equation for the adjacent fluid layer, Eq. (4), does not allow a variation in the *z*-direction (direction parallel to the porous-fluid interface and perpendicular to the flow direction). In the porous medium, two average values for the velocity exist (at a fixed *y*): The average velocity in the solid phase is zero, and that in the fluid phase is nonzero. On the other hand, only one value for the velocity (at a fixed *y*) is associated with the one-dimensional momentum equation, Eq. (4). This mismatch in the number of dependent variables across the porous–fluid interface results in the claim that there exists a discontinuity in shear stress across the interface between the porous medium and the adjacent fluid layer [9]. We are trying to resolve this problem by using the two-dimensional equation, Eq. (7). With this equation, the velocity in the adjacent fluid layer is allowed to vary in the directions both parallel and perpendicular to the porous–fluid interface, i.e., the velocity in the adjacent fluid layer is expressed as a function of *y* and *z*. The two-dimensionality allows the velocity at the interface to be zero in the fluid layer contacting the solid phase of the porous medium and to have a finite value in the fluid layer contacting the fluid phase of the porous medium.

When a homogeneous porous–fluid composite channel having a porous medium with periodic structure (solid and fluid phases repeating in a regular pattern), is considered, velocity and temperature distributions along the interface vary periodically, as shown in Fig. 2(*a*). Along the interface, two representative values exist: The volume-averaged velocity for the fluid portion (a nonzero velocity, U_i/ε), and that for the solid portion (zero value). The periodic distribution can be mathematically expressed in terms of the Fourier cosine series as follows:

$$U(Z)|_{Y=0^+} = U_i\left[1 + 2\sum_{n=1}^{\infty} \frac{\sin(\varepsilon n\pi)}{\varepsilon n\pi}\cos\left(\frac{n\pi Z}{L}\right)\right] \tag{8}$$

where L is one-half of a period and related to half of the pore diameter D_p (the characteristic length of the fluid phase of the porous medium) as

$$L = \frac{D_p}{2\varepsilon} \tag{9}$$

The Fourier series not only represent the function on the given interval of $(-L, L)$ but also give the periodic extension outside of this interval. At the interface of the porous medium, the velocity condition for the fluid portion is

$$\langle U\rangle_f|_{Y=0^-} = U_i/\varepsilon \tag{10}$$

The no-slip conditions are satisfied on the bottom and the upper surfaces as follows:

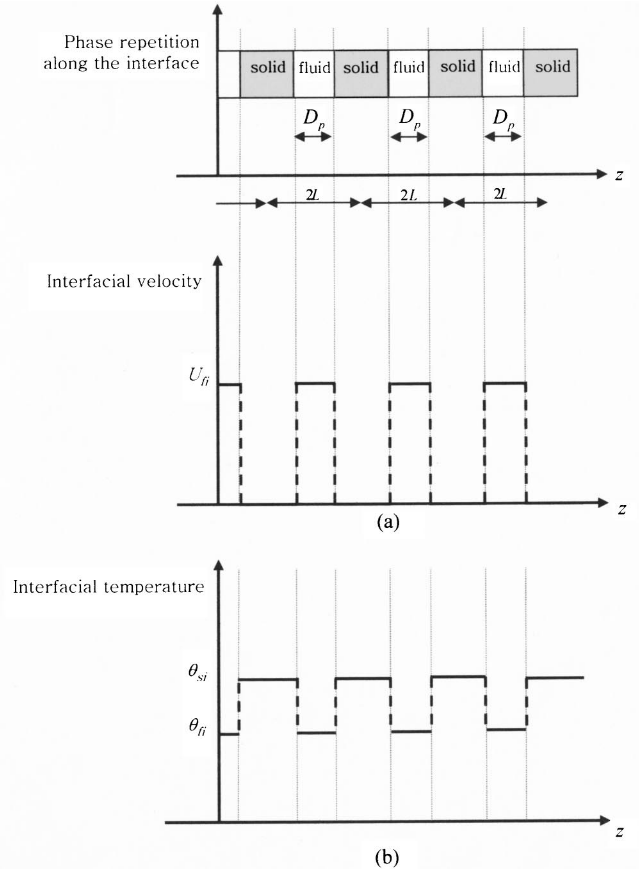

Fig. 2 Distributions of (*a*) velocity and (*b*) temperature along the porous–fluid interface

$$\langle U\rangle_f|_{Y=-1} = 0 \tag{11}$$

$$U|_{Y=S} = 0 \tag{12}$$

In addition, at the planes of symmetry, the velocity gradient is zero.

$$\left.\frac{\partial U}{\partial Z}\right|_{Z=0} = \left.\frac{\partial U}{\partial Z}\right|_{Z=L} = 0 \tag{13}$$

Here it is noted that another condition is required at the interface since the interfacial velocity U_i is not known. For mathematical convenience, the interfacial velocity is treated as a known quantity in this section and will be determined in the following section using another condition for shear stress at the fluid portion of the interface. By integrating Eq. (2) twice with Eqs. (10) and (11), the velocity distribution for the fluid phase in the porous medium becomes

$$\langle U\rangle_f = C_1 \cosh\left(\frac{Y}{\sqrt{Da}}\right) + C_2 \sinh\left(\frac{Y}{\sqrt{Da}}\right) + Da, \quad -1 \leq Y \leq 0^- \tag{14}$$

where $C_1 = U_i/\varepsilon - Da$ and $C_2 = C_1/\tanh(1/\sqrt{Da}) + Da/\sinh(1/\sqrt{Da})$.

By using the method of separation of variables, Eq. (7) is solved with Eqs. (8), (12), and (13) as

Downloaded 06 Dec 2010 to 193.140.21.150. Redistribution subject to ASME license or copyright; see http://www.asme.org/terms/Terms_Use.cfm

$$U=-\frac{1}{2}Y^2+\left(\frac{S}{2}-\frac{U_i}{S}\right)Y+U_i$$

$$+2U_i\sum_{n=1}^{\infty}C_n\sinh\left(\frac{n\pi(S-Y)}{L}\right)\cos\left(\frac{n\pi Z}{L}\right),\quad 0^+\leqslant Y\leqslant S \tag{15}$$

$$\text{where}\quad C_n=\frac{\sin(\varepsilon n\pi)}{\varepsilon n\pi\sinh\left(\frac{n\pi S}{L}\right)}.$$

2.2 Temperature Distributions. A treatment similar to the fluid flow analysis is employed for heat transfer in the porous–fluid composite system.

2.2.1 Previous Approach with the Flux-Jump Conditions. As the governing equations for the porous medium, the two-equation model is used without resorting to the local thermal equilibrium assumption. The two-equation model is written in the dimensionless form as

$$\frac{d^2\langle\theta\rangle_s}{dY^2}=\frac{H^2h_{sf}}{k_{se}}(\langle\theta\rangle_s-\langle\theta\rangle_f),\quad -1\leqslant Y\leqslant 0^- \tag{16}$$

$$\frac{d^2\langle\theta\rangle_f}{dY^2}+\frac{H^2h_{sf}}{k_{fe}}(\langle\theta\rangle_s-\langle\theta\rangle_f)=P\langle U\rangle_f\quad -1\leqslant Y\leqslant 0^- \tag{17}$$

where $P=[1/(1+S)]^2 1/U_m$. Note that the energy balance requirement [18]

$$\rho_f c_f u_m(H+s)\frac{\partial\langle T\rangle}{\partial x}=q'' \tag{18}$$

is used in reducing the right-hand side of Eq. (17). The volume-averaged governing equation for heat transfer in the adjacent fluid layer has been used as follows [5,6,12–14]:

$$\frac{\partial^2\langle\theta\rangle_f}{\partial Y^2}=PU,\quad 0^+\leqslant Y\leqslant S \tag{19}$$

Equations (16), (17), and (19) are solved with the following flux-jump conditions, suggested by Ochoa-Tapia and Whitaker [15],

$$k_{fe}\frac{d\langle\theta\rangle_f}{dY}\bigg|_{Y=0^-}=k_f\frac{d\langle\theta\rangle_f}{dY}\bigg|_{Y=0^+}-h_{\beta\sigma}H(\theta_{fi}-\theta_{si}) \tag{20}$$

$$k_{se}\frac{d\langle\theta\rangle_s}{dY}\bigg|_{Y=0^+}=h_{\beta\sigma}H(\theta_{fi}-\theta_{si}) \tag{21}$$

together with the temperature condition at the interface,

$$\theta_i=\theta_{fi} \tag{22}$$

where θ_{fi}, θ_{si}, and θ_i are dimensionless interfacial temperature of the fluid phase in the porous medium, that of the solid phase in the porous medium and that of the fluid phase in the adjacent fluid layer, respectively. Also, $h_{\beta\sigma}$, the so-called boundary heat transfer coefficient, is an unknown coefficient and needs to be determined in advance for closure. To resolve the same issue raised in the previous section, a method for obtaining an analytical solution for the temperature distributions without invoking the unknown coefficient is proposed in the following section.

2.2.2 Present Approach. The governing equations for the temperature distributions in the porous medium are identical to Eqs. (16) and (17). Just like in the fluid flow analysis, the two-dimensional energy equation is employed for the adjacent fluid layer.

$$\frac{\partial^2\theta}{\partial Z^2}+\frac{\partial^2\theta}{\partial Y^2}=PU,\quad 0^+\leqslant Y\leqslant S \tag{23}$$

Note that the temperature for the adjacent fluid layer is expressed as a function of y and z so that the temperature variation along the interface of the overlying fluid layer can be accounted for in the proposed method. Along the interface, the two representative values are periodically repeated, as shown in Fig. 2(*b*): One is a volume-averaged temperature over the solid portion and the other over the fluid portion along the interface. Using the same approach adopted above for fluid flow analysis, the interfacial temperature in the adjacent fluid layer is expressed in terms of the Fourier cosine series as

$$\theta(Z)|_{Y=0^+}=\varepsilon T_{fi}+(1-\varepsilon)T_{si}+2(T_{fi}-T_{si})\sum_{n=1}^{\infty}\frac{\sin(\varepsilon n\pi)}{n\pi}\cos\left(\frac{n\pi Z}{L}\right) \tag{24}$$

The continuity of temperature across the interface for the two phases of the porous medium is expressed, respectively, as follows:

$$\langle\theta\rangle_f|_{Y=0^-}=\theta_{fi},\quad \langle\theta\rangle|_{Y=0^-}=\theta_{si} \tag{25}$$

The boundary conditions on the bottom and upper surfaces are as follows:

$$\langle\theta\rangle_f|_{Y=-1}=0,\quad \langle\theta\rangle_s|_{Y=-1}=0 \tag{26}$$

$$\frac{\partial\theta}{\partial Y}\bigg|_{Y=S}=0 \tag{27}$$

In addition, at the planes of symmetry, the temperature gradient is zero.

$$\frac{\partial\theta}{\partial Z}\bigg|_{Z=0}=\frac{\partial\theta}{\partial Z}\bigg|_{Z=L}=0 \tag{28}$$

For a simple mathematical formulation, we introduce the following two variables [19],

$$\theta_1=\theta_s-\theta_f,\quad \theta_2=k_{se}\theta_s+k_{fe}\theta_f \tag{29}$$

With these two variables, Eq. (16) is rearranged as

$$\frac{d^2\theta_1}{dY^2}-A^2\theta_1=-P\langle U\rangle_f \tag{30}$$

where $A=\sqrt{H^2h_{sf}(1/k_{se}+1/k_{fe})}$.
Similarly, Eq. (17) is rearranged as

$$\frac{d^2\theta_2}{dY^2}=k_{fe}P\langle U\rangle_f \tag{31}$$

Integrating Eqs. (30) and (31) subject to Eqs. (25) and (26) yields

$$\theta_1=C_3\cosh(AY)+C_4\sinh(AY)+D_1\cosh\left(\frac{Y}{\sqrt{Da}}\right)+D_2\sinh\left(\frac{Y}{\sqrt{Da}}\right)+D_3 \tag{32}$$

$$\theta_2=k_fPDa\left\{C_1\cosh\left(\frac{Y}{\sqrt{Da}}\right)+C_2\sinh\left(\frac{Y}{\sqrt{Da}}\right)+\frac{\varepsilon Y^2}{2}\right\}+C_5Y+C_6 \tag{33}$$

where

$$D_1=\frac{P}{\varepsilon}C_1\bigg/\left(-\frac{1}{Da}+A^2\right),\quad D_2=\frac{P}{\varepsilon}C_2\bigg/\left(-\frac{1}{Da}+A^2\right),$$

$$D_3=\frac{PDa}{A^2}$$

Downloaded 06 Dec 2010 to 193.140.21.150. Redistribution subject to ASME license or copyright; see http://www.asme.org/terms/Terms_Use.cfm

$$D_4=\left[(-D_1-D_3)\cosh(A)+D_1\cosh\left(\frac{1}{\sqrt{Da}}\right)-D_2\sinh\left(\frac{1}{\sqrt{Da}}\right)+D_3\right]\Big/\sinh(A)$$

$$D_5=k_fPDa\left[C_1\cosh\left(\frac{1}{\sqrt{Da}}\right)-C_2\sinh\left(\frac{1}{\sqrt{Da}}\right)+\frac{\varepsilon}{2}-C_1\right]$$

$$C_3=\theta_{si}-\theta_{fi}-D_1-D_3$$

$$C_4=\frac{\theta_{si}-\theta_{fi}}{\tanh(A)}+D_4$$

$$C_5=k_{se}\theta_{si}+k_{fe}\theta_{fi}+D_5$$

$$C_6=k_{se}\theta_{s,i}+k_{fe}\theta_{f,i}-k_fPDaC_1$$

Finally, analytical solutions for the temperature distributions in the porous medium are obtained as

$$\theta_s=\frac{1}{k_{se}+k_{fe}}\left[k_{fe}\times\left\{C_3\cosh(AY)+C_4\sinh(AY)+D_1\cosh\left(\frac{Y}{\sqrt{Da}}\right)+D_2\sinh\left(\frac{Y}{\sqrt{Da}}\right)+D_3\right\}+k_fPDa\left\{C_1\cosh\left(\frac{Y}{\sqrt{Da}}\right)+C_2\sinh\left(\frac{Y}{\sqrt{Da}}\right)+\frac{\varepsilon Y^2}{2}\right\}+C_5Y+C_6\right] \tag{34}$$

$$\theta_f=\frac{1}{k_{se}+k_{fe}}\left[-k_{se}\times\left\{C_3\cosh(AY)+C_4\sinh(AY)+D_1\cosh\left(\frac{Y}{\sqrt{Da}}\right)+D_2\sinh\left(\frac{Y}{\sqrt{Da}}\right)+D_3\right\}+k_fPDa\left\{C_1\cosh\left(\frac{Y}{\sqrt{Da}}\right)+C_2\sinh\left(\frac{Y}{\sqrt{Da}}\right)+\frac{\varepsilon Y^2}{2}\right\}+C_5Y+C_6\right] \tag{35}$$

In addition, Eq. (23) is solved with Eqs. (24), (27), and (28) by the method of separation of variables to yield the temperature distribution in the adjacent fluid layer:

$$\theta=P\left[-\frac{Y^4}{24}+\left(\frac{S}{2}-\frac{U_i}{S}\right)\frac{Y^3}{6}+\frac{U_i}{2}Y^2-\left(\frac{S^3}{12}+\frac{U_iS}{2}\right)Y\right]+\varepsilon\theta_{fi}+(1-\varepsilon)\theta_{si}+\sum_{n=1}^{\infty}\left[PU_iC_n\frac{L}{n\pi}(S-Y)\cosh\left(\frac{n\pi(S-Y)}{L}\right)+A_n\cosh\left(\frac{n\pi(S-Y)}{L}\right)+B_n\sinh\left(\frac{n\pi(S-Y)}{L}\right)\right]\times\cos\left(\frac{n\pi Z}{L}\right) \tag{36}$$

where

$$B_n=-U_iC_n\left(\frac{L}{n\pi}\right)^2$$

$$A_n=\frac{1}{\cosh\left(\frac{n\pi S}{L}\right)}\left[2(\theta_{fi}-\theta_{si})\frac{\sin(\varepsilon n\pi)}{n\pi}-B_n\sinh\left(\frac{n\pi S}{L}\right)\right]$$

2.3 Determination of Interfacial Velocity and Temperature

So far, we have obtained the analytical solutions for velocity and temperature profiles with their values at the interface assumed to be known. In this section, we determine the interfacial values of velocity U_i and temperatures θ_{fi}, θ_{si}, and θ_i by applying the matching conditions of shear stress and heat flux at the porous–fluid interface. For this, conditions based on continuities of shear stress and heat flux across the interface between each phase of the porous medium and the adjacent fluid are applied. With the two-dimensional velocity and temperature distributions for the adjacent fluid layer employed in the present study, we can obtain the values of shear stress and heat flux over the fluid and solid portions of the interface, separately. Over the fluid portion of the interface, the continuity of shear stress at the interface between the fluid phase of the porous medium and the adjacent fluid layer is expressed as

$$\left.\frac{d\langle U\rangle_f}{dY}\right|_{Y=0-}=\frac{1}{D_p}\int_0^{D_p}\left.\frac{\partial U}{\partial Y}\right|_{Y=0+}dZ \tag{37}$$

Substituting Eqs. (14) and (15) into Eq. (37) yields the interfacial velocity as

$$U_{fi}=\frac{\frac{S}{2}+\sqrt{Da}\left[\frac{1}{\tanh(1/\sqrt{Da})}-\frac{1}{\sinh(1/\sqrt{Da})}\right]}{\frac{1}{\sqrt{Da}\tanh(1/\sqrt{Da})}+\frac{\varepsilon}{S}+\frac{2}{L}\sum_{n=1}^{\infty}\frac{\sin^2(\varepsilon n\pi)}{\varepsilon n\pi\tanh\left(\frac{n\pi S}{L}\right)}} \tag{38}$$

In a similar manner, continuities of heat flux at the interface between each of the solid and fluid phases of the porous medium and the adjacent fluid layer are expressed, respectively, as follows:

$$k_{fe}\left.\frac{d\langle\theta\rangle_f}{dY}\right|_{Y=0-}=\frac{1}{L}\int_0^{D_p}k_f\left.\frac{d\theta}{dY}\right|_{Y=0+}dZ \tag{39}$$

$$k_{se}\left.\frac{d\langle\theta\rangle_s}{dY}\right|_{Y=0-}=\frac{1}{L}\int_{D_p}^{L}k_f\left.\frac{d\theta}{dY}\right|_{Y=0+}dZ \tag{40}$$

Substituting Eqs. (34)–(36) into Eqs. (39) and (40) yields

$$\theta_{fi}=\frac{n_sm_c-m_sn_c}{m_fn_s-m_sn_f},\quad\text{and}\quad\theta_{si}=\frac{n_fm_c-m_fn_c}{m_sn_f-m_fn_s} \tag{41}$$

where

$$m_s=\frac{k_{se}}{k_{fe}+k_{se}}\left(k_{se}+\frac{A}{\tanh(A)}k_{fe}\right)+k_f(1-\varepsilon)\sum_{n=1}^{\infty}\frac{2\sin^2(\varepsilon n\pi)}{n\pi}\tanh\left(\frac{n\pi S}{L}\right)$$

Downloaded 06 Dec 2010 to 193.140.21.150. Redistribution subject to ASME license or copyright; see http://www.asme.org/terms/Terms_Use.cfm

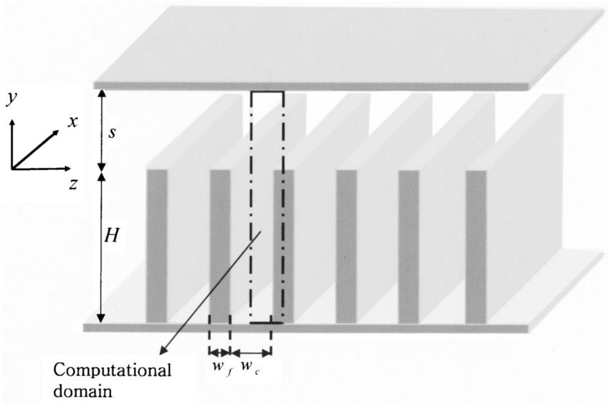

Fig. 3 Schematic diagram of the ideal composite channel

$$m_f=\frac{k_{se}}{k_{fe}+k_{se}}\left(k_{fe}-\frac{A}{\tanh(A)}k_{fe}\right)-k_f(1-\varepsilon)\sum_{n=1}^{\infty}\frac{2\sin^2(\varepsilon n\pi)}{n\pi}\tanh\left(\frac{n\pi S}{L}\right)$$

$$m_c=k_f(1-\varepsilon)\left[-P\left(\frac{S^3}{12}+\frac{U_iS}{2}\right)\right]-\frac{k_{se}}{k_{fe}+k_{se}}\left[k_{fe}\left(AD_4+\frac{D_2}{\sqrt{Da}}\right)+k_fPDa\frac{C_2}{\sqrt{Da}}+D_5\right]$$

$$n_s=\frac{k_{fe}}{k_{fe}+k_{se}}\left(k_{se}-\frac{A}{\tanh(A)}k_{se}\right)-k_f\varepsilon\sum_{n=1}^{\infty}\frac{2\sin^2(\varepsilon n\pi)}{n\pi}\tanh\left(\frac{n\pi S}{L}\right)$$

$$n_f=\frac{k_{fe}}{k_{fe}+k_{se}}\left(k_{fe}+\frac{A}{\tanh(A)}k_{se}\right)+k_f\varepsilon\sum_{n=1}^{\infty}\frac{2\sin^2(\varepsilon n\pi)}{n\pi}\tanh\left(\frac{n\pi S}{L}\right)$$

$$n_c=k_f\varepsilon\left[-P\left(\frac{S^3}{12}+\frac{\varepsilon U_{fi}S}{2}\right)\right]-\frac{k_{fe}}{k_{fe}+k_{se}}\left[-k_{se}\left(D_4A+\frac{D_2}{\sqrt{Da}}\right)+k_fPDa\frac{C_2}{\sqrt{Da}}+D_5\right]$$

As shown in Eq. (38) for velocity and Eq. (41) for temperatures, the interfacial velocity and temperature distributions based on the present approach do not involve any unknown coefficients. By determining the interfacial velocity and temperatures, we finally have obtained the analytical solutions for velocity and temperature distributions free from any unknown coefficients.

3 Validation of the Methodology

To validate the results of the present analysis, we introduce an ideal composite system, as shown in Fig. 3. The ideal composite system consists of a porous medium and an overlying fluid layer. The porous medium has the shape of a microchannel heat sink with vertical fins. This composite system was previously studied by Taylor [16] and Richardson [17]. In the study of Kim and Kim [20], the fully shrouded microchannel was also treated as a porous medium, and they obtained analytical solutions for the velocity and temperature profiles. Due to a well-organized structure occupied by the vertical fins, the numerical simulation of fluid flow and heat transfer can be easily performed for the ideal composite channel. The Navier–Stokes and classical energy equations for a conjugate heat transfer problem are numerically solved based on the control-volume method for the computational domain, as shown in Fig. 3. The code used in the present numerical simulation is already verified in Min et al. [21].

For the microchannel heat sink, the porosity, the permeability and the effective conductivities are represented as [19,20]

$$\varepsilon=\frac{w_c}{w_c+w_f},\quad K=\frac{\varepsilon w_c^2}{12},\quad k_{se}=(1-\varepsilon)k_s,\quad k_{fe}=\varepsilon k_f,$$

$$C=\frac{k_{se}}{k_{fe}} \tag{42}$$

and the product of the interstitial heat transfer coefficient and the wetted area per volume is [20]

$$h_{sf}=\frac{10k_{fe}}{W_c^2} \tag{43}$$

With these parameters for the microchannel structure, the analytical solutions for the velocity and temperature distributions are obtained for the ideal composite channel. Figure 4 shows the comparison between the analytical solutions generated in this study and the corresponding numerical solutions for the velocity and temperature distributions, which are averaged along the z-direction for the purpose of comparison. They are in excellent agreement, within 3%. The present approach can be applied to a porous medium with a regular pattern, such as a porous medium made of cylinders, which was dealt with in the study of Sahraoui and Kaviany [22].

Moreover, we also confirm the validity of the present analysis by comparing the present results with the experimental data of Beavers and Joseph [3]. As shown in Fig. 5, the present analysis accurately predicts the experimental data. In this figure, the quantity Φ was defined in the paper of Beavers and Joseph [3] as the fractional increase in mass flow rate through the channel with a permeable lower wall compared to what it would be if the wall were impermeable. In their experiments, three kinds of Foametal, having permeability of 1.5×10^{-5}, 6.1×10^{-5}, and 12.7×10^{-5} (in^2), are used. Previously, Ochoa-Tapia and Whitaker [11] also made the comparison between their results and Beavers and Joseph's experimental data. In their comparison, they fixed the porosity of the Foametals to be 0.4 since Beavers and Joseph did not mention the value of porosity used in their experiment. On the other hand, we used the value of porosity ranging from 0.9 to 0.99 because Foametal typically has porosity higher than 0.9 [23]. In Fig. 5, for the case of $K=12.7\times10^{-5}$ (in^2), the analytical results agree closely with the experimental data when $\varepsilon=0.99$, and for the other cases, good agreements between the experimental and analytical results are obtained when $\varepsilon=0.9$. The maximum error between the two solutions is found to be smaller than 20%.

4 Determination of the Unknown Coefficients β and $h_{\beta\sigma}$

By using the proposed method for analyzing fluid flow and heat transfer in the porous–fluid composite system, we have obtained analytical solutions for the velocity and temperature distributions, and then validated them numerically and experimentally. The present analytical solutions do not involve any unknown coefficients, unlike the solutions presented by previous investigators. Therefore, they can be used to analytically determine the unknown coefficients, such as β and $h_{\beta\sigma}$, required for the stress- and flux-jump conditions. Analytical expression of the unknown coefficients is advantageous because it helps us easily identify the parameters involved and determine the relationship among those parameters.

Downloaded 06 Dec 2010 to 193.140.21.150. Redistribution subject to ASME license or copyright; see http://www.asme.org/terms/Terms_Use.cfm

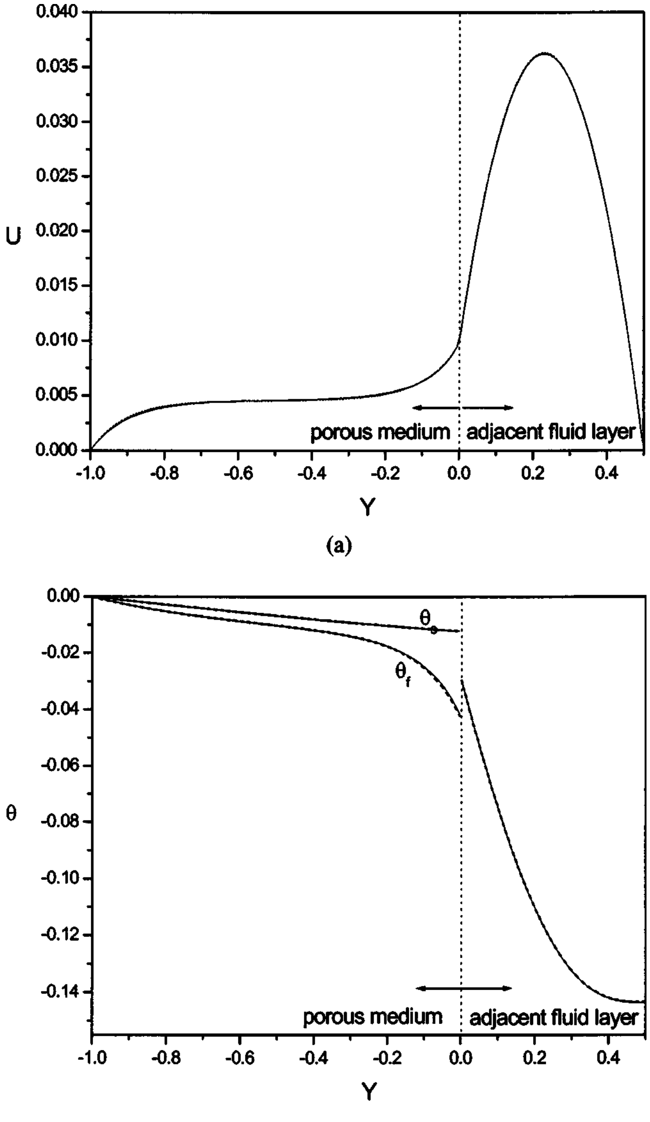

(a)

(b)

Fig. 4 Comparison between the analytical solution (dashed line) and the numerical solution (solid line) for the ideal composite channel in the case when $\varepsilon=0.533$, $Da=0.008533$, $S=0.5$, and $C=114.1$

The left-hand side of the stress-jump condition, Eq. (5), is the average shear stress just below the interface contacting the liquid portion of the porous medium minus the average shear stress exerted on the adjacent fluid just above the interface (divided by the fluid viscosity). This quantity is proportional to the average shear stress exerted on the adjacent fluid by the contacting solid phase of the porous medium along the interface. From the definition of the averaging quantities and using Eq. (37), the left hand side of Eq. (5) can be expressed as

$$\left.\frac{d\langle U\rangle_f}{dY}\right|_{y=0^-}-\left.\frac{d\langle U\rangle}{dY}\right|_{y=0^+}=\frac{1}{D_p}\left[\int_0^{D_p}(1-\varepsilon)\left.\frac{\partial U}{\partial Y}\right|_{Y=0^+}dZ+\int_{D_p}^{D_p/\varepsilon}\varepsilon\left.\frac{\partial U}{\partial Y}\right|_{Y=0^+}dZ\right] \tag{44}$$

By employing the analytical solution for velocity, Eq. (15), the following interfacial condition for shear stress is obtained.

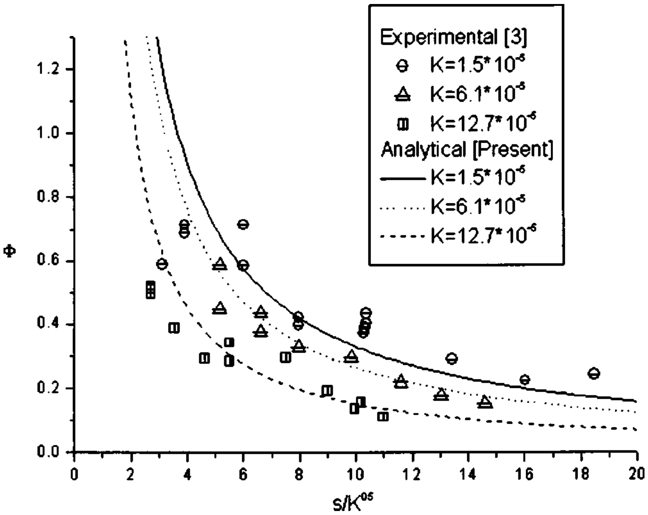

Fig. 5 Comparison between the analytical results of the present study and the experimental data of Beavers and Joseph [3]

$$\left.\frac{d\langle U\rangle_f}{dY}\right|_{y=0^-}-\left.\frac{d\langle U\rangle}{dY}\right|_{y=0^+}=-\frac{2}{D_p}\sum_{n=1}^{\infty}\frac{\sin^2(\varepsilon n\pi)}{\varepsilon n\pi\tanh(\varepsilon n\pi S/D_p)}U_i \tag{45}$$

Comparing Eqs. (5) and (45) yields the unknown coefficient β explicitly as

$$\beta=-\frac{2\sqrt{\varepsilon Da}}{D_p}\sum_{n=1}^{\infty}\frac{\sin^2(\varepsilon n\pi)}{\varepsilon n\pi\tanh(\varepsilon n\pi S/D_p)} \tag{46}$$

The coefficient β depends on the porosity, the Darcy number, the pore diameter and the thickness of the adjacent fluid layer. When the condition of $S\gg D_p$ is satisfied for the composite channel [4], we have $\tanh(\varepsilon n\pi S/D_p)\approx 1$. For Foametal used in Beavers and Joseph's experiments [3], we also have $2\sqrt{\varepsilon Da}/D_p\approx 0.5$. When these conditions are met, the variation of β with respect to ε is plotted in Fig. 6. This figure shows that the value of β is negative and on the order of one. This trend for β confirms what Ochoa-Tapia and Whitaker [10] predicted earlier: that β is on the order of one and either positive or negative. In another study of theirs [11], they determined the values of β using the experimental data of

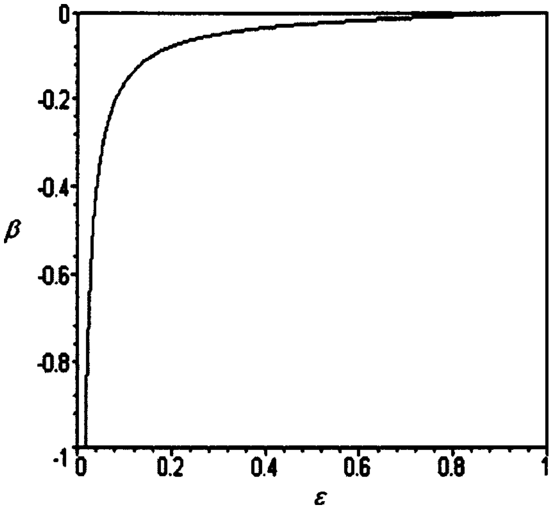

Fig. 6 Variation of β with respect to ε for the case of $S\gg D_p$

Downloaded 06 Dec 2010 to 193.140.21.150. Redistribution subject to ASME license or copyright; see http://www.asme.org/terms/Terms_Use.cfm

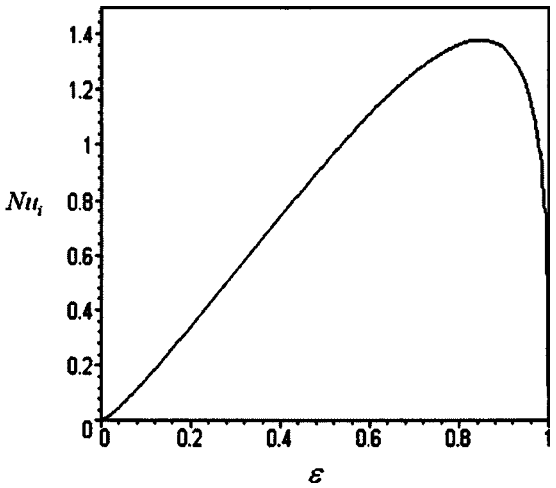

Fig. 7 Variation of Nu_i with respect to ε for the case of $S \gg D_p$

Beavers and Joseph. In their paper, the range of β is found to be from -1.0 to 1.47 when the porosity is arbitrarily assigned to be 0.4 for Foametal and Aloxite.

Similarly, interfacial conditions for heat transfer analysis are derived by rearranging Eqs. (39) and (40) in the form of the flux-jump conditions, and then by inserting the analytical solutions for the temperature distributions, Eqs. (34)–(36), into Eqs. (39) and (40):

$$k_{fe}\left.\frac{d\langle\theta\rangle_f}{dY}\right|_{Y=0^-} = k_f\varepsilon\left.\frac{d\langle\theta\rangle_f}{dY}\right|_{Y=0^+} - (\theta_{fi}-\theta_{si})h_iH \tag{47}$$

$$k_{se}\left.\frac{d\langle\theta\rangle_s}{dY}\right|_{Y=0^-} = k_f(1-\varepsilon)\left.\frac{d\langle\theta\rangle_f}{dY}\right|_{Y=0^+} + (\theta_{fi}-\theta_{si})h_iH \tag{48}$$

where h_i is defined as the product of the interfacial heat transfer coefficient and the interfacial area per unit volume at the interface.

The present interfacial conditions, Eqs. (47) and (48) contain similarities to the flux-jump conditions of Ochoa-Tapia and Whitaker [15], Eqs. (20) and (21). Both sets of equations contain potentially identical convective terms between solid and fluid phases along the interface. However, it is worth mentioning that there exists a distinctive difference between the present interfacial conditions and the flux-jump conditions. In terms of the normal conduction from the porous medium into the adjacent fluid layer, the present conditions include the terms representing normal diffusive heat flux from each phase of the porous medium to the adjacent fluid layer. On the other hand, only normal conduction from the solid phase of the porous medium to the adjacent fluid layer is considered in Ochoa-Tapia and Whitaker's flux-jump conditions.

The interfacial heat transfer coefficient is determined analytically:

$$h_i = \sum_{n=1}^{\infty}\left[\frac{k_f}{H}\,\frac{2\varepsilon\sin^2(\varepsilon n\pi)}{n\pi D_p}\tanh\left(\frac{\varepsilon n\pi S}{D_p}\right)\right] \tag{49}$$

From the definition of the Nusselt number, the dimensionless interfacial heat transfer coefficient is simply expressed as

$$Nu_i = \frac{(h_iH)D_p}{k_f} = \sum_{n=1}^{\infty}\left[\frac{2\varepsilon\sin^2(\varepsilon n\pi)}{n\pi}\tanh\left(\frac{\varepsilon n\pi S}{D_p}\right)\right] \tag{50}$$

Equation (50) shows that the interfacial Nusselt number depends on the porosity, the pore diameter and the thickness of the adjacent fluid layer. Under the condition that $S \gg D_p$, the variation of the interfacial Nusselt number with respect to the porosity is shown in Fig. 7. This figure shows that as the porosity increases, the interfacial Nusselt number increases from 0 until it attains a maximum value and decreases to 0. This is physically reasonable because the interfacial Nusselt number should be zero when the porosity is 0 and 1.

5 Conclusion

This paper presents a novel method for analyzing fluid flow and heat transfer in a porous–fluid composite system, where the porous medium has a periodic structure, i.e., solid and fluid phases repeat themselves in a regular pattern. By using the present method, analytical solutions for the velocity and temperature distributions are obtained when velocity and temperature are allowed to vary in the adjacent fluid layer in the directions parallel and perpendicular to the porous–fluid interface. The analytical solutions are validated by comparing them with the corresponding numerical solutions for the case of the ideal composite channel, and with the experimental data of Beaver and Joseph. The present analytical solutions have a distinctive advantage in that they do not involve any unknown coefficients. Moreover, by comparing the present interfacial conditions to the stress- and flux-jump conditions developed by Ochoa-Tapia and Whitaker, the unknown coefficients β and h_i, which always accompany the stress- and flux-jump conditions, have been explicitly determined. It is also shown that these unknown coefficients depend on the porosity, the Darcy number and the pore diameter.

Acknowledgments

This work was supported by KISTEP (Korea Institute of Science & Technology Evaluation and Planning) under Grant No. 2-578 through the National Research Lab. Program.

Nomenclature

A = dimensionless quantity defined in Eq. (30)
c = specific heat of fluid $[\mathrm{J\,kg^{-1}\,K^{-1}}]$
Da = Darcy number, $K/\varepsilon H^2$
d_p = pore diameter [m]
D_p = dimensionless pore diameter
h = product of interstitial heat transfer coefficient and wetted area per volume $[\mathrm{Wm^{-3}\,K}]$
H = thickness of the porous medium [m]
L = dimensionless quantity for one half of a period
k = thermal conductivity $[\mathrm{Wm^{-1}\,K^{-1}}]$
K = permeability $[\mathrm{m^2}]$
Nu = Nusselt Number defined in Eq. (50)
p = pressure [Pa]
P = dimensionless quantity defined in Eq. (17)
q'' = heat flux $[\mathrm{W\,m^{-2}}]$
s = thickness of the overlying fluid space [m]
S = dimensionless thickness of the fluid space $(=s/H)$
T = temperature [K]
u = velocity [m/s]
U = dimensionless velocity
w_f = width of fin in the ideal composite channel [m]
w_c = channel width between two fins in the ideal composite channel [m]
Y = dimensionless vertical coordinate
Z = dimensionless horizontal coordinate

Greek symbols

β = stress-jump coefficient
ε = porosity
μ = viscosity [Pa s]
θ = dimensionless temperature
ρ = density $[\mathrm{kg\,m^{-3}}]$
$\langle\,\rangle$ = spatial volume-averaged value
$\langle\,\rangle_f$ = volume-averaged value over the fluid phase
$\langle\,\rangle_s$ = volume-averaged value over the solid phase

Downloaded 06 Dec 2010 to 193.140.21.150. Redistribution subject to ASME license or copyright; see http://www.asme.org/terms/Terms_Use.cfm

Subscripts

e = effective property
f = fluid
i = interfacial property
m = averaged property over the composite system
s = solid
w = wall

References

[1] Prasad, V., 1991, ''Convective flow interaction and heat transfer between fluid and porous layers,'' Proc. NATO ASI, Convective Heat Mass Transfer in Porous Media, edited by Kakac et al., Kluwer Academic Publ., Netherlands, pp. 563–615.
[2] Alazmi, B., and Vafai, K., 2001, ''Analysis of fluid flow and heat transfer interfacial conditions between a porous medium and a fluid layer,'' Int. J. Heat Mass Transfer, **44**, pp. 1735–1749.
[3] Beavers, G. S., and Joseph, D. D., 1967, ''Boundary condition at a naturally permeable wall,'' J. Fluid Mech., **30**, pp. 197–207.
[4] Neale, G., and Nader, W., 1974, ''Practical significance of Brinkman's extension of Darcy's law: coupled parallel flows within a channel and a bounding porous medium,'' Can. J. Chem. Eng., **52**, pp. 475–478.
[5] Vafai, K., and Kim, S. J., 1990, ''Analysis of surface enhancement by a porous substrate,'' J. Heat Transfer, **112**, pp. 700–706.
[6] Kim, S. J., and Choi, C. Y., 1996, ''Convective heat transfer in porous and overlying fluid layers heated from below,'' Int. J. Heat Mass Transfer, **39**, pp. 319–329.
[7] Poulikakos, D., and Kazmierczak, M., 1987, ''Forced convection in a duct partially filled with a porous material,'' J. Heat Transfer, **109**, pp. 319–329.
[8] Jang, J. Y., and Chen, J. L., 1992, ''Forced convection in a parallel plate channel partially filled with a high porosity medium,'' Int. Commun. Heat Mass Transfer, **19**, pp. 262–273.
[9] Nield, D. A., 1991, ''The limitation of the Brinkman–Forchheimer equation in modeling flow in a saturated porous medium and at an interface,'' Int. J. Heat Fluid Flow, **12**, pp. 269–272.
[10] Ochoa-Tapia, J. A., and Whitaker, S., 1995, ''Momentum transfer at the boundary between a porous medium and a homogeneous fluid-I. Theoretical development,'' Int. J. Heat Mass Transfer, **38**, pp. 2635–2646.
[11] Ochoa-Tapia, J. A., and Whitaker, S., 1995, ''Momentum transfer at the boundary between a porous medium and a homogeneous fluid-II. Comparison with experiment,'' Int. J. Heat Mass Transfer, **38**, pp. 2647–2655.
[12] Kuznetsov, A. V., 1998, ''Analytic study of fluid flow and heat transfer during forced convection in a composite channel partly filled with a Brinkman-Forchheimer porous medium,'' Flow, Turbul. Combust., **60**, pp. 173–192.
[13] Ochoa-Tapia, J. A., and Whitaker, S., 1998, ''Heat transfer at the boundary between a porous medium and a homogeneous fluid: the one-equation model,'' J. Porous Mater., **1**, pp. 31–46.
[14] Sahraoui, M., and Kaviany, M., 1994, ''Slip and no-slip temperature boundary conditions at the interface of porous, plain media: convection,'' Int. J. Heat Mass Transfer, **37**, pp. 1029–1044.
[15] Ochoa-Tapia, J. A., and Whitaker, S., 1997, ''Heat transfer at the boundary between a porous medium and a homogeneous fluid,'' Int. J. Heat Mass Transfer, **40**, pp. 2691–2707.
[16] Taylor, G. I., 1971, ''A model for the boundary condition of a porous material, Part 1,'' J. Fluid Mech., **49**, pp. 310–326.
[17] Richardson, S., 1971, ''A model for the boundary condition of a porous material, Part 2,'' J. Fluid Mech., **49**, pp. 327–336.
[18] Bejan, A., 1995, *Convection Heat Transfer*, 2nd ed., Wiley, New York, Chap. 12.
[19] Kim, S. J., Kim, D., and Lee, D. Y., 2000, ''On the local thermal equilibrium in microchannel heat sinks,'' Int. J. Heat Mass Transfer, **43**, pp. 1735–1748.
[20] Kim, D., and Kim, S. J., 2004, ''Compact Modeling of Fluid Flow and Heat Transfer in Straight Fin Heat Sinks,'' J. Electronic Packaging, **126**, pp. 247–255.
[21] Min, J. Y., Jang, S. P., and Kim, S. J., 2004, ''Effect of tip clearance on the cooling performance of a microchannel heat sink,'' Int. J. Heat Mass Transfer, **47**, pp. 1099–1103.
[22] Sahraoui, M., and Kaviany, M., 1992, ''Slip and no-slip velocity boundary conditions at interface of porous, plain media,'' Int. J. Heat Mass Transfer, **35**, pp. 927–943.
[23] Calmidi, V. V., and Mahajan, R. L., 2000, ''Forced Convection in high Porosity Metal Foams,'' J. Heat Transfer, **122**, pp. 557–565.

Downloaded 06 Dec 2010 to 193.140.21.150. Redistribution subject to ASME license or copyright; see http://www.asme.org/terms/Terms_Use.cfm

Journal of Heat Transfer

Technical Briefs

Thermal Contact Conductance Across Gold-Coated OFHC Copper Contacts in Different Media

Bapurao Kshirsagar, Prashant Misra, Nagaraju Jampana, and M. V. Krishna Murthy
Department of Instrumentation, Indian Institute of Science, Banglaore-560012, India

The thermal contact conductance studies across gold-coated oxygen-free high-conductivity copper contacts have been conducted at different contact pressures in vacuum, nitrogen, and helium environments. It is observed that the thermal contact conductance increases not only with the increase in contact pressure but also with the increase in thermal conductivity of interstitial medium. The experimental data are found to be in good agreement with the literature. [DOI: 10.1115/1.1865215]

1 Introduction

When two similar or dissimilar solids are brought into physical contact in order to transmit heat, the thermal contact conductance or the heat transfer coefficient for the junction is defined as $h_c = Q/A_a\Delta T$. The magnitude of contact conductance is a function of various parameters, including the thermophysical and mechanical properties of the materials, characteristics of the contacting surfaces, presence of gaseous or nongaseous interstitial media, contact pressure acting on the junction, and mean junction temperature.

A majority of the contact resistance information is determined experimentally in order to provide a measure of the thermal performance of a specific configuration or system for a particular application. The thermal resistance at the interface can often lead to thermally induced failure of a component or a system as has been frequently observed in the case of electronic systems. In fact, techniques for enhancement of thermal performance of contacts are continuously being researched to overcome some of the challenging thermal problems posed by the progressive miniaturization of electronic components and systems. Use of soft surface coatings is one such technique that has been suggested for better thermal management in electronics [1,2]. Chung [3] studied the variation of contact resistance with indium, lead, and aluminum coatings on metals. Fletcher et al. [4] used both the vapor-deposited silver and electroplated silver coatings between the electronic components for the enhancement of thermal contact conductance. Kang et al. [5] experimentally studied the enhancement in contact conductance across aluminum contacts coated with materials such as lead, tin, and indium. Antonetti and Yovanovich [6] gave a thermomechanical model according to which the thermal contact conductance across metallic coated contacts depends on the effective hardness and thermal conductivity ratio of that substrate-layer combination. When operated in a gaseous media, the conductance of the junction is a combination of two factors: the solid-solid joint conductance and the gap conductance. Introduction of a gaseous medium in the interstitial space enhances the conductance of gap and, hence, the overall thermal contact conductance of the junction. The gap conductance depends mainly on the interstitial gas properties. Song [7] and Hegazy [8] studied the gap conductance in N_2, Ar and He environments across nickel and stainless steel contacts. Yovanovich et al. [9] developed a sophisticated statistical model (or integral model) to predict thermal gap conductance between conforming rough surfaces, which was later presented in a simplified form by Song [7]. Recently, Bahrami et al. [10] gave a new gap conductance model, which agrees well with the integral model as well as with the experimental data of Song [7] and Hegazy [8].

The objective of the present investigation is to study the variation in thermal contact conductance with contact pressure across gold-coated oxygen-free high-conductivity (OFHC) copper contacts in different environments. Gold possesses a reasonably high value of thermal conductivity. It is a relatively softer material than copper and presents a stiff resistance to oxidation in normal conditions.

2 Experimentation

A detailed description of the test setup can be found elsewhere [11]. The specimens are prepared from a single OFHC copper bar to ensure identical material properties. The specimens are machined to a cylindrical shape having 25 mm diam and 25 mm length. For placing thermocouples, three holes are drilled into each specimen along the radial direction to a depth of 12.5 mm from the curved surface (up to the axis). The end surfaces of the specimens are polished with fine-grit emery paper. Care has been taken to minimize the convexity while polishing the surface. A pair of such prepared samples is coated with 0.2 μm thick gold by the thermal evaporation technique. The surface characteristics of these gold-coated specimens are measured using the Form Talysurf (Taylor Hobson, UK). The surface microhardness measurements are made with the help of a Vicker's microhardness tester (HMV 2000 Shimadzu). The obtained values are given in Table 1. Experiments are conducted on gold-coated OFHC copper contacts in vacuum, nitrogen, and helium environments (gas pressure at 1.5 bar), at a fixed heat flow rate of 50 W. The detailed measurement procedure is given in [11]. The maximum uncertainty in the measurement of thermal contact conductance is approximately ±4%.

3 Results and Discussion

Variation in thermal contact conductance across gold-coated OFHC copper contacts with contact pressure in vacuum, nitrogen, and helium environments is shown in Fig. 1. The experimental

---

Contributed by the Heat Transfer Division for publication in the JOURNAL OF HEAT TRANSFER. Manuscript received March 3, 2004; revision received December 20, 2004. Review conducted by: S. V. Garimella.

Copyright © 2005 by ASME

Downloaded 06 Dec 2010 to 193.140.21.150. Redistribution subject to ASME license or copyright; see http://www.asme.org/terms/Terms_Use.cfm

Table 1 Properties of contact materials and media

Surface roughness measurements	Surface micohardness measurements	Thermal properties
$\sigma=0.167\ \mu$m $m=0.003$	$H=1386$ MPa $H'=1290$ MPa	$k_{OFHC\ Cu}=384$ W/m K $k_{gold}=297$ W/m K $k_{g\ He}=0.17$ W/m K $k_{g\ N2}=0.03$ W/m K

data are compared to theoretical values calculated using the following models. According to Yovanovich [12], for clean metallic contacts in vacuum,

$$h_c=1.25k_s\left(\frac{m}{\sigma}\right)\left(\frac{P}{H}\right)^{0.95}$$

The thermomechanical model by Antonetti et al. [6] predicts the thermal contact conductance across coated contacts as

$$h_c'=\frac{h_c}{C}\left(\frac{H}{H'}\right)^{0.93}$$

The value of the C is obtained to be 1.53 from the tables given by Antonetti [13].

The gap conductance in gaseous environments is calculated according to the model by Bahrami et al. [10] as

$$h_g'=\frac{k_g}{M+\sqrt{2}\sigma\left[\mathrm{erfc}^{-1}\left(\frac{2P}{H'}\right)\right]}$$

where

$$M=\left\{\frac{2-TAC}{TAC}\right\}\left(\frac{4\gamma}{1+\gamma}\right)\frac{\Lambda}{\mathrm{Pr}}$$

and

$$\mathrm{TAC}=\exp\left[-0.57\left(\frac{T_s-273}{273}\right)\right]\left(\frac{M_g^*}{6.8+M_g^*}\right)+\frac{2.4\mu}{(1+\mu)^2}\left\{1-\exp\left[-0.57\left(\frac{T_s-273}{273}\right)\right]\right\}$$

The value of erfc^{-1} is approximated as

$$\mathrm{erfc}^{-1}(x)=\frac{1}{0.218+0.735x^{0.173}},\quad 10^{-9}\leqslant x\leqslant 0.02$$

Now the overall joint conductance is given by

$$h_j'=h_c'+h_g'$$

The required gas properties and constants are taken from [10]. The values of TAC for He-Au and N_2-Au combinations are found to be 0.32 and 0.76, respectively. These values are in good agreement with those calculated by other researchers, tabulated in [14]. The overall joint conductance is found to be high in both He and N_2 environments that are in vacuum because of the addition of gap conductance. The gap conductance in He is higher compared to that of N_2, as the thermal conductivity of He (0.17 W/m K) is higher than that of N_2 (0.03 W/m K). The experimental data in vacuum is in very good agreement with the theoretical model, whereas in the case of nitrogen and helium, the deviation between the model values and the experimental values is marginal.

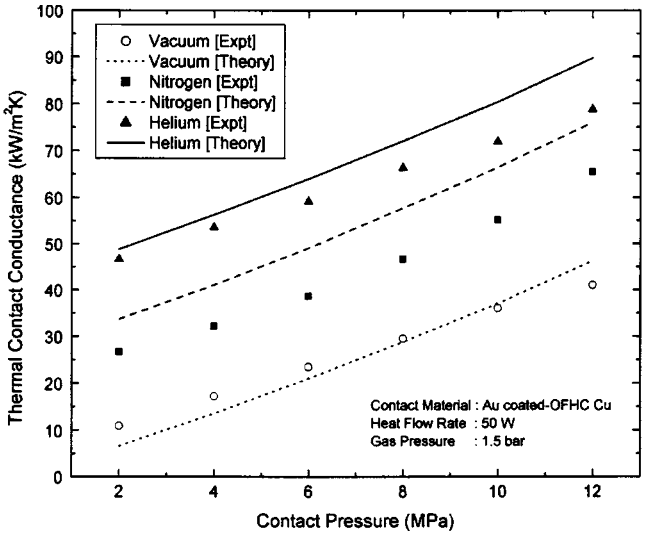

Fig. 1 Variation of thermal contact conductance with contact pressure

4 Conclusion

Variation of thermal joint conductance with contact pressure studies across gold-coated OFHC Cu contacts in vacuum, He, and N_2 environments revealed that the higher thermal conductivity media contributes more in the transfer of heat across the interstitial gaps and, consequently, enhances the overall thermal contact conductance of the joint.

Nomenclature

A = area of contact, m^2
C = constriction parameter correction factor
erfc^{-1} = inverse complementary error function
H = Vickers microhardness, MPa
H' = effective microhardness of soft layer on harder substrate, MPa
h = thermal contact conductance, W/m^2 K
k = thermal conductivity, W/m K
M = gas parameter, m
M_g = molecular weight of gas
M_s = molecular weight of solid
$M_g^* = \begin{cases} M_g \text{ for monatomic gases} \\ 1.4M_g \text{ for diatomic/polyatomic gases} \end{cases}$
m = combined average asperity slope $(=\sqrt{m_1^2+m_2^2})$
P = apparent contact pressure, MPa
Pr = Prandtl number
Q = heat flow rate, W
T = temperature, K
TAC = thermal accommodation coefficient
ΔT = interface temperature drop, K
σ = combined rms roughness, m, $(=\sqrt{\sigma_1^2+\sigma_2^2})$
μ = $=M_g/M_s$
γ = ratio of gas specific heats
Λ = mean-free path, m

Superscripts.

In general, prime (′) indicates the layer/coating.

Subscripts.

a = apparent
c = contact
g = gas
j = joint/combined
s = solid

References

[1] Peterson, G. P., and Fletcher, L. S., 1990, "Measurement of the Thermal Contact Conductance and Thermal Conductivity of Anodized Coatings," ASME J. Heat Transfer, **112**(3), pp. 579–585.
[2] Fletcher, L. S., 1990, "A Review of Thermal Enhancement Techniques for

Downloaded 06 Dec 2010 to 193.140.21.150. Redistribution subject to ASME license or copyright; see http://www.asme.org/terms/Terms_Use.cfm

Electronic Systems,'' IEEE Trans. Compon., Hybrids, Manuf. Technol., **13**(4), pp. 1012–1021.

[3] Kee-Chiang, C., 1995, ''Experimental Study on the Effect of Metallic-Coated Junctions on Thermal Contact Conductance,'' JSME Int. J., Ser. B, **38**(1), pp. 100–107.

[4] Fletcher, L. S., Lambert, M. A., and Marrota, E. E., 1998, ''Thermal Enhancement Coatings for Microelectronic Systems,'' ASME J. Electron. Packag., **120**, pp. 229–236.

[5] Kang, T. K., Peterson, G. P., and Fletcher, L. S., 1990, ''Effect of Metallic Coatings on the Thermal Contact Conductance of Turned Surfaces,'' ASME J. Heat Transfer, **112**(4), pp. 864–871.

[6] Antonetti, V. W., and Yovanovich, M. M., 1988, ''Using Metallic Coatings to Enhance Thermal Contact Conductance of Electronic Packages,'' Heat Transfer Eng., **9**(3), pp. 85–92.

[7] Song, S., 1988, ''Analytical and Experimental Study of Heat Transfer Through Gas Layers of Contact Interfaces,'' Ph.D. thesis, University of Waterloo, Waterloo, Canada.

[8] Hegazy, A. A., 1985, ''Thermal Joint Conductance of Conforming Rough Surfaces: Effect of Surface Micro-Hardness Variation,'' Ph.D. thesis, University of Waterloo, Waterloo, Canada.

[9] Yovanovich, M. M., DeWaal, J. W., and Hegazy, A. A., 1982, ''A Statistical Model to Predict Thermal Gap Conductance Between Conforming Rough Surfaces,'' AIAA-82-0888, AIAA/ASME 3rd Joint Thermophysics, Fluids, Plasma and Heat Transfer Conference, St. Louis, Missouri.

[10] Bahrami, M., Culham, J. R., and Yovanovich, M. M., 2004, ''Thermal Resistance of Gaseous Gap for Conforming Rough Contacts,'' AIAA-2004-0821, 42nd AIAA Aerospace Meeting and Exhibit, Nevada.

[11] Rao, V. V., Bapurao, K., Nagaraju, J., and Krishna Murthy, M. V., 2004, ''Instrumentation to Measure Thermal Contact Resistance,'' Meas. Sci. Technol., **15**, pp. 1–4.

[12] Yovanovich, M. M., 1981, ''New Contact and Gap Conductance Correlations for Conforming Rough Surfaces,'' AIAA-81-1164, AIAA 16th Thermophysics Conference, Palo Alto, California.

[13] Antonetti, V. W., 1983, ''On the Use of Metallic Coatings to Enhance Thermal Contact Conductance,'' Ph.D. thesis, University of Waterloo, Waterloo, Canada.

[14] Song, S., and Yovanovich, M. M., 1989, ''Contact Interface Gas Heat Transfers: A Method of Measuring Thermal Accommodation Coefficient,'' 9th Annual International Electronic Packaging Conference, Vol. 2, pp. 925–936.

Downloaded 06 Dec 2010 to 193.140.21.150. Redistribution subject to ASME license or copyright; see http://www.asme.org/terms/Terms_Use.cfm

On Electrokinetic Mass Transport in a Microchannel With Joule Heating Effects

G. Y. Tang and C. Yang[1]
e-mail: mcyang@ntu.edu.sg

H. Q. Gong, C. J. Chai, and Y. C. Lam

School of Mechanical and Production Engineering,
Nanyang Technological University, Republic of Singapore
639798

This study presents a numerical analysis of electrokinetic mass transport in a microchannel with Joule heating effects. A nonuniform electric field caused by the presence of the Joule heating is considered in the model development. Numerical computations for electrokinetic mass transport under Joule heating effects are carried out using the Crank-Nicolson scheme of second-order accuracy in space and time for two different cases: (i) the translating interface and (ii) the dispersion of a finite sample plug. The simulations reveal that the presence of Joule heating not only causes the sample species to transport faster, but also causes the sample peak to decrease and the sample band to deviate from its flat interface or pluglike shape. [DOI: 10.1115/1.1865216]

Keywords: Electrokinetic Mass Transport, Joule Heating, Crank-Nicolson Scheme

1 Introduction

Electrokinetic mass transport has found applications in capillary electrophoresis systems used for chemical analysis and biomedical diagnosis. Electrokinetic transport of sample species exploits the phenomena of electroosmosis and electrophoresis. Electroosmosis refers to the bulk movement of an aqueous solution adjacent to a charged solid surface due to an applied electric field. Electrophoresis refers to the migration of charged particles in an electrolyte under the influence of an applied electric field [1].

Numerous studies have been reported on the electroosmotic flow (EOF) and electrokinetic mass transport in various microchannels [2–5], and the flat EOF velocity profiles and pluglike sample band shape are usually obtained in these studies in which Joule heating effects are neglected. However, Joule heating is generated when an electric field is applied across conductive liquids. Such Joule heating can induce a temperature field that would have an impact on the EOF and sample transport. Previous studies [6,7] have demonstrated that the Joule heating effects can result in low column separation efficiency and may lead to the decomposition of thermally labile samples and the formation of gas bubbles. Recently, Joule heating and its effects on the transient and steady-state EOF and the sample species transport were numerically examined using the power-law scheme [8,9], which suffers the so-called numerical pseudo diffusion due to very low mass diffusivity of sample species [10]. Furthermore, a constant applied electric field was assumed in existing studies. This assumption is not valid in the presence of the Joule heating induced temperature field because the electrical conductivity of electrolytes is dependent on temperature. Otherwise, the conservation of electric charges will be violated.

In this study, an attempt is made to numerically analyze the electrokinetic mass transport in a microchannel under Joule heating effects with consideration of a nonuniform electric field in the model development. Specifically, the Crank-Nicolson scheme is used to minimize the numerical pseudo diffusion.

2 Mathematical Modeling

2.1 Governing Equations. Consider electrokinetic transport of sample species between two reservoirs through a cylindrical microcapillary (with inner radius R, wall thickness Δ, and length L as shown in Fig. 1) filled with an electrolyte solution. Such an electrokinetic transport process is governed by the general mass transport equation, which can be formulated as [8,9]

$$\frac{\partial C_s}{\partial t}+(u+u_{ep})\frac{\partial C_s}{\partial z}+(v+v_{ep})\frac{\partial C_s}{\partial r}=\frac{1}{r}\frac{\partial}{\partial r}\left[rD(T)\frac{\partial C_s}{\partial r}\right]+\frac{\partial}{\partial z}\left[D(T)\frac{\partial C_s}{\partial z}\right] \tag{1}$$

where C_s is the sample concentration. $D(T)=D_0(1+0.025\Delta T)$ is the temperature-dependent mass diffusivity. $u_{ep}=u_{ep0}(1+0.03\Delta T)$ and $v_{ep}=v_{ep0}(1+0.03\Delta T)$ are the electrophoretic velocity components along the axial and radial direction, respectively. The subscript 0 denotes the parameters at room temperature (298 K) unless otherwise specified. u and v are the EOF velocity components along the capillary axial and radial direction, respectively.

According to Tang et al. [8], the time scale for the EOF to reach its steady state in a capillary is much smaller when compared to the characteristic time for sample transport and separation in capillary electrophoresis systems. Hence, the EOF is considered to be steady state and is governed by the modified Navier-Stokes equations as

$$\frac{1}{r}\frac{\partial}{\partial r}(rv)+\frac{\partial u}{\partial z}=0 \tag{2a}$$

$$\rho\left(v\frac{\partial u}{\partial r}+u\frac{\partial u}{\partial z}\right)=-\frac{\partial p}{\partial z}+\frac{1}{r}\frac{\partial}{\partial r}\left[r\mu(T)\frac{\partial u}{\partial r}\right]+\frac{\partial}{\partial z}\left[\mu(T)\frac{\partial u}{\partial z}\right]-\rho_e\left(\frac{\partial \varphi}{\partial z}+\frac{\partial \psi}{\partial z}\right) \tag{2b}$$

$$\rho\left(v\frac{\partial v}{\partial r}+u\frac{\partial v}{\partial z}\right)=-\frac{\partial p}{\partial r}+\frac{\partial}{\partial r}\left[\frac{\mu(T)}{r}\frac{\partial (rv)}{\partial r}\right]+\frac{\partial}{\partial z}\left[\mu(T)\frac{\partial v}{\partial z}\right]-\rho_e\left(\frac{\partial \varphi}{\partial r}+\frac{\partial \psi}{\partial r}\right) \tag{2c}$$

where ρ is the electrolyte density, p is the hydrostatic pressure, $\mu(T)=(2.761/10^6)e^{1713/T}$ is the electrolyte viscosity, ρ_e is the local net charge density due to the electric double layer (EDL). In this study, the electrical potential is assumed to be decoupled as a linear superposition of the EDL potential ψ and the nonuniform applied electrical potential φ, governed by the Poisson-Boltzmann and the Laplace equations, respectively [1],

$$\frac{1}{r}\frac{\partial}{\partial r}\left[r\varepsilon(T)\frac{\partial \psi}{\partial r}\right]+\frac{\partial}{\partial z}\left[\varepsilon(T)\frac{\partial \psi}{\partial z}\right]=-\frac{\rho_e}{\varepsilon_0}=\frac{2\sigma e n_0}{\varepsilon_0}\sinh\left(\frac{\sigma e\psi}{k_b T}\right) \tag{3a}$$

$$\frac{1}{r}\frac{\partial}{\partial r}\left[r\lambda(T)\frac{\partial \varphi}{\partial r}\right]+\frac{\partial}{\partial z}\left[\lambda(T)\frac{\partial \varphi}{\partial z}\right]=0 \tag{3b}$$

where k_b is the Boltzmann constant, n_0 is the bulk ionic number concentration of the electrolyte, σ is the valence of the ions, ε_0 is the permittivity of vacuum, e is the fundamental charge, $\varepsilon(T)$

---

[1] Corresponding author.

Contributed by the Heat Transfer Division for publication in the JOURNAL OF HEAT TRANSFER. Manuscript received May 1, 2004; revision received December 9, 2004. Review conducted by: S. G. Kandlikar.

Copyright © 2005 by ASME

Downloaded 06 Dec 2010 to 193.140.21.150. Redistribution subject to ASME license or copyright; see http://www.asme.org/terms/Terms_Use.cfm

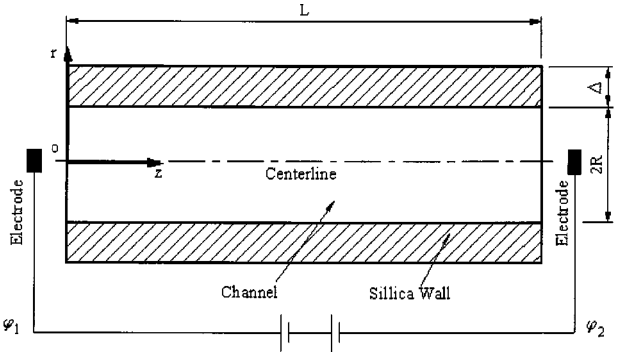

Fig. 1 Schematic of a circular microcapillary and the cylindrical coordinate system

$=305.7e^{-T/219}$ is the dielectric constant, and $\lambda(T)=\lambda_+\eta_++\lambda_-\eta_-$ is electrical conductivity of the electrolyte. Furthermore, $\lambda_{+(-)}=\lambda_{+(-)0}+0.025\lambda_{+(-)0}\Delta T$ are the ionic conductivities of the cations and anions, respectively. η_+ and η_- are the local mole concentration of the cations and anions, respectively, and are given by the Boltzmann distribution [1].

Following the analysis of Tang et al. [8], the Joule heating induced temperature field of the electrolyte in a capillary is described by the steady-state energy equation as

$$\rho c_p\left(v\frac{\partial T}{\partial r}+u\frac{\partial T}{\partial z}\right)=\frac{1}{r}\frac{\partial}{\partial r}\left[rk_l(T)\frac{\partial T}{\partial r}\right]+\frac{\partial}{\partial z}\left[k_l(T)\frac{\partial T}{\partial z}\right]+\lambda(T)\left[\left(\frac{\partial\varphi}{\partial r}\right)^2+\left(\frac{\partial\varphi}{\partial z}\right)^2\right] \qquad (4a)$$

where c_p and $k_l(T)$ are the specific heat capacity and the temperature-dependent thermal conductivity of the electrolyte, respectively. Since the temperature at the inner capillary wall is unknown, a conjugated heat conduction equation in the capillary wall is considered as

$$\frac{1}{r}\frac{\partial}{\partial r}\left(rk_s\frac{\partial T}{\partial r}\right)+\frac{\partial}{\partial z}\left(k_s\frac{\partial T}{\partial z}\right)=0 \qquad (4b)$$

where k_s is the thermal conductivity of the capillary. By referring to commercially available capillary electrophoresis systems, we assume the microcapillary is cooled in a thermostat [6,7].

2.2 Initial and Boundary Conditions. Two cases are considered for electrokinetic mass transport: in Case I, the sample species is continuously supplied from the inlet reservoir, namely, the translating interface; and Case II considers a finite length plug of sample species that is injected from the inlet and then flows down the channel, namely, the dispersion of a finite sample plug. Both cases are usually encountered in the sample loading and separation processes of the capillary electrophoresis systems and the corresponding initial and boundary conditions are

$$\text{The initial conditions }(t=0)\quad \text{Case I:}C_s=0.0$$

$$\text{Case II:}\begin{cases}C_s=1.0 & (z\leqslant 0.02L)\\ C_s=0.0 & (z>0.02L)\end{cases} \qquad (5a)$$

It should be noted that in Case II, the plug length of the injected sample is arbitrarily chosen as 2% of the capillary length in Eq. (5*a*). The choice of such an initial condition is solely to facilitate numerical computations. Strictly speaking, the more rigorous one is $C_s=(m_s/A)\delta(z)$ (here m_s is the sample mass, A is the capillary cross-sectional area, and $\delta(z)$ is the mathematical Dirac function).

For $t>0$, the boundary conditions for all governing equations are

$$\text{Inlet }(z=0):\quad T=T_0\quad \psi=0\quad \frac{\partial u}{\partial z}=0\quad \frac{\partial v}{\partial z}=0\quad \varphi=\varphi_1$$

$$\text{Case I:}C_s=1.0\quad \text{Case II:}C_s=0.0 \qquad (5b)$$

$$\text{Outlet }(z=L):\quad \frac{\partial T}{\partial z}=0\quad \frac{\partial\psi}{\partial z}=0\quad \frac{\partial u}{\partial z}=0\quad \frac{\partial v}{\partial z}=0\quad \varphi=\varphi_2$$

$$\frac{\partial C_s}{\partial z}=0 \qquad (5c)$$

$$\text{Symmetry centerline }(r=0):\quad \frac{\partial T}{\partial r}=0\quad \frac{\partial\psi}{\partial r}=0\quad \frac{\partial u}{\partial r}=0$$

$$v=0\quad \frac{\partial\varphi}{\partial r}=0\quad \frac{\partial C_s}{\partial r}=0 \qquad (5d)$$

$$\text{Capillary wall }(r=R):\quad -k_s\left.\frac{\partial T}{\partial r}\right|_{r=R+\Delta}=h(T-T_f)\quad \psi=\zeta$$

$$u=0\quad v=0\quad \frac{\partial\varphi}{\partial r}=0\quad \frac{\partial C_s}{\partial r}=0 \qquad (5e)$$

where h is the heat transfer coefficient outside the capillary wall [7], T_f is the thermostat temperature, and ζ is the zeta potential of the capillary wall.

3 Numerical Method

Since the governing equations for the EOF velocity field (Eq. (2)), the EDL and applied electrical potential distributions (Eqs. (3*a*) and (3*b*)) and the Joule heating induced temperature fields in the electrolyte solution and the capillary wall (Eqs. (4*a*) and (4*b*)) are coupled together through the temperature-dependent parameters, they have to be simultaneously solved. Afterward, the concentration distributions of sample species for two cases can be found by numerically solving Eq. (1). The finite volume method (FVM) based numerical method is used to solve these governing equations [11]. The Crank-Nicolson scheme [12] is used to discretize the differential equations. Such a scheme, using the average variable value at current time $(t+1)$ and previous time (t), is a second-order scheme in both time and space, expressed by

$$\Phi_{t+1}^X-\Phi_t^X=\frac{1}{2}\left[\left(\frac{\partial\Phi}{\partial X}\right)_{t+1}+\left(\frac{\partial\Phi}{\partial X}\right)_t\right] \qquad (6)$$

where X denotes the general coordinate of the control volume (i.e., r, z). Our study shows that due to very low mass diffusivity of sample species, use of a high-order numerical scheme is necessary to simulate electrokinetic mass transport so that the so-called numerical pseudo diffusion can be minimized [10].

4 Results and Discussion

In calculation, a 0.1 M NaCl electrolyte is used and the capillary zeta potential is $\zeta=-50$ mV. A fluorescein dye is chosen as the sample species, and its mass diffusivity and electrophoretic mobility are $D_0=4.37\times10^{-10}\,\text{m}^2/\text{s}$ and $\mu_{ep0}=2.04\times10^{-8}\,\text{m}^2/\text{V s}$ (at 298 K), respectively [13]. The capillary is made from silica glass with dimensions $L=50$ mm, $R=100\,\mu$m, and $\Delta=70\,\mu$m (Polymicro Technologies, USA). The computation domain for the Joule heating induced temperature field includes both the inner channel and the capillary wall.

For Case I, the translating interface, the computed sample concentration distributions are shown in Fig. 2(*a*) for axial variation of the cross-sectional average of the sample concentration and Fig. 2(*b*) for time evolution of the sample concentration distributions. Without the Joule heating effects, the sample concentration exhibits a flat interface as shown in Fig. 2(*b*). In the presence of Joule heating, it can be seen from Figs. 2(*a*) and 2(*b*) that the sample transports much faster due to an increase of the EOF ve-

Downloaded 06 Dec 2010 to 193.140.21.150. Redistribution subject to ASME license or copyright; see http://www.asme.org/terms/Terms_Use.cfm

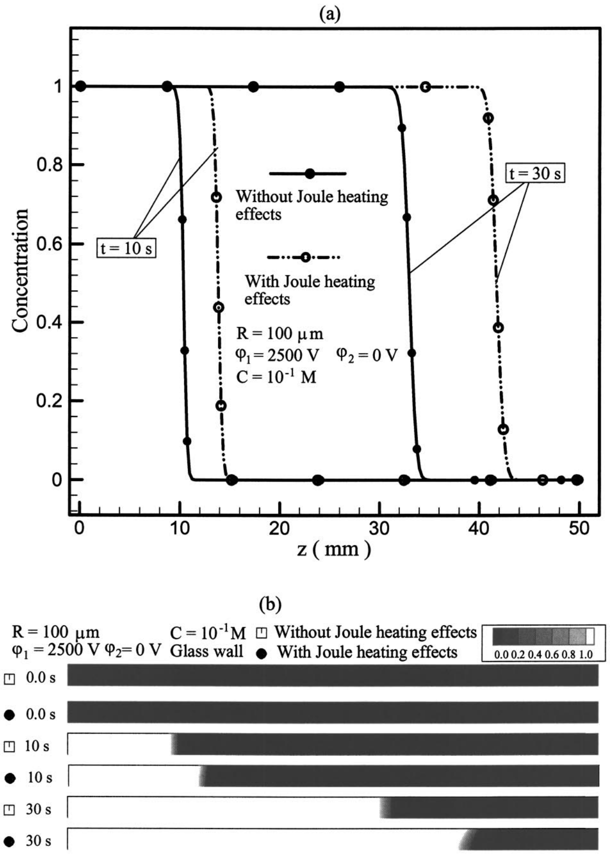

Fig. 2 Simulation results of the sample concentration distributions for Case I, the translating interface with/without Joule heating effects: (*a*) axial variation of the cross-sectional average of the sample concentration and (*b*) time evolution of the sample concentration distributions

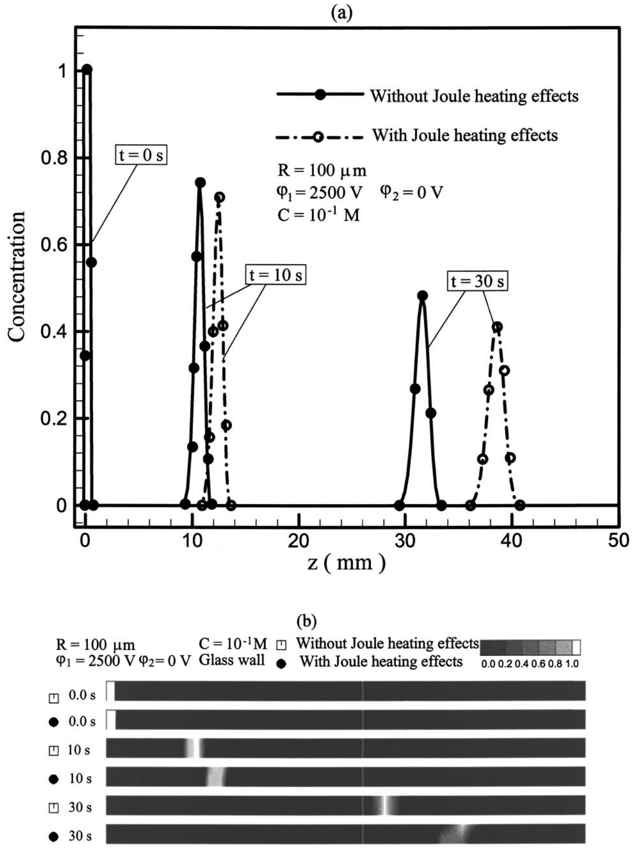

Fig. 3 Simulation results of the sample concentration distributions for Case II, the dispersion of a finite sample plug with/without Joule heating effects: (*a*) axial variation of the cross-sectional average of the sample concentration and (*b*) time evolution of the sample concentration distributions

locity. In addition, as the sample electrophoresis mobility increases with increasing temperature, the radial temperature variation gives rise to a change of the sample axial electrophoresis mobility along the radial direction and, hence, distorts the translating interface as shown in Fig. 2(*b*).

The simulation results of Case II, the dispersion of a finite sample plug, are presented in Fig. 3(*a*) for axial variation of the cross-sectional average of the sample concentration and Fig. 3(*b*) for time evolution of the sample concentration distributions. As shown in Fig. 3, in the absence of Joule heating, the sample band exhibits a pluglike shape, which is desirable for the detection in capillary electrophoresis systems. With the Joule heating effects, for the same reasons discussed earlier, the Joule heating induced temperature field not only causes the samples to transport faster, but also makes the sample peak decrease and the sample band deviate from its original pluglike shape. These findings suggest that as Joule heating is concerned, the dispersive effects on sample band shapes need to be considered in the design and operation of capillary electrophoresis systems.

5 Conclusion

Electrokinetic mass transport under Joule heating effects is modeled with consideration of a nonuniform electric field. The model shows that the Joule heating effects on the sample concentration distributions are through the temperature-dependent parameters, including the solution dielectric constant, electrical conductivity, and viscosity, as well as the electrophoretic mobility and mass diffusivity of sample species. The second-order Crank-Nicolson scheme is used to study electrokinetic mass transport under the Joule heating effects for two cases: (i) the translating interface and (ii) the dispersion of a finite sample plug. The simulations reveal that the presence of Joule heating can result in significantly different characteristics of the electrokinetic mass transport in microchannels. It not only causes the sample species to transport faster, but also makes the sample peak decrease and the sample band deviate from its flat interface or pluglike shape.

References

[1] Probstein, R. F., 1994, *Physicochemical Hydrodynamics: An Introduction, 2nd Edition*, Wiley, New York.

[2] Santiago, J. G., 2001, "Electroosmotic Flows in Microchannels With Finite Inertial and Pressure Forces," Anal. Chem., **73**, pp. 2353–2365.

[3] Ermakov, S. V., Jacobson, S. G., and Ramsey, J. M., 1998, "Computer Simulations of Electrokinetic Transport in Microfabricated Channels," Anal. Chem., **70**, pp. 4494–4504.

[4] Erickson, D., and Li, D., 2002, "Influence of Surface Heterogeneity on Electrokinetically Driven Microfluidic Mixing," Langmuir, **18**, pp. 1883–1892.

[5] Zholkovskij, E. K., Masliyah, J. H., and Czarnecki, J., 2003, "Electroosmotic Dispersion in Microchannels With a Thin Double Layer," Anal. Chem., **75**, pp. 901–909.

[6] Knox, J. H., and McCormack, K. A., 1994, "Temperature Effects in Capillary Electrophoresis: Internal Capillary Temperature and Effect Upon Performance," Chromatographia, **38**, pp. 207–214.

[7] Grushka, E., McCormick, R. M., and Kirkland, J. J., 1989, "Effect of Temperature Gradients on Efficiency of Capillary Zone Electrophoresis Separations," Anal. Chem., **61**, pp. 241–246.

[8] Tang, G. Y., Yang, C., Chai, C. K., and Gong, H. Q., 2003, "Modeling of Electroosmotic Flow and Capillary Electrophoresis With the Joule Heating Effect: The Nernst-Planck Equation Versus the Boltzmann Distribution," Langmuir, **19**, pp. 10975–10984.

[9] Tang, G. Y., Yang, C., Chai, C. K., and Gong, H. Q., 2004, "Joule Heating Effect on Electroosmotic Flow and Mass Species Transport in a Microcapillary," Int. J. Heat Mass Transfer, **47**, pp. 215–227.

[10] Noye, B. P., 1976, "An Introduction to Finite Difference Techniques," *Pro-*

Downloaded 06 Dec 2010 to 193.140.21.150. Redistribution subject to ASME license or copyright; see http://www.asme.org/terms/Terms_Use.cfm

ceeding of an International Conference on the Numerical Simulation of Fluid Dynamics, North-Holland-Elsevier, New York, pp. 56–85.

[11] Patankar, S. V., 1980, *Numerical Heat Transfer and Fluid Flow*, McGraw-Hill, New York.

[12] Crank, J., and Nicolson, P., 1947, ''A Practical Method for Numerical Evaluation of Solutions of Partial Differential Equations of the Heat-ConductionType,'' Proc. Cambridge Philos. Soc., **43**, pp. 50–67.

[13] Paul, P. H., Garguilo, M. G., and Rakestraw, D. J., 1998, ''Imaging of Pressure- and Electrokinetically Driven Flows Through Open Capillaries,'' Anal. Chem., **70**, pp. 2459–2467.

Downloaded 06 Dec 2010 to 193.140.21.150. Redistribution subject to ASME license or copyright; see http://www.asme.org/terms/Terms_Use.cfm

Thermal Resistance of Nanowire-Plane Interfaces

V. Bahadur
Student Mem. ASME

J. Xu
Student Mem. ASME

Y. Liu
Student Mem. ASME

T. S. Fisher[1]
Mem. ASME
e-mail: tsfisher@purdue.edu

School of Mechanical Engineering and Birck
Nanotechnology Center,
Purdue University,
West Lafayette, IN 47907

This paper employs continuum principles combined with van der Waals theory to estimate the thermal contact resistance between nanowires and planar substrates. This resistance is modeled using elastic deformation theory and thermal resistance relations. The contact force between a nanowire and substrate is obtained through a calculation of the van der Waals interaction energy between the two. The model estimates numerical values of constriction and gap resistances for several nanowire-substrate combinations with water and air as the surrounding media. The total interface resistance is almost equal to the gap resistance when the surrounding medium has a high thermal conductivity. For a low-conductivity medium, the interface resistance is dominated by the constriction resistance, which itself depends significantly on nanowire and substrate conductivities. A trend observed in all calculations is that the interface resistance increases with smaller nanowires, showing that interface resistance will be a significant parameter in the design and performance of nanoelectronic devices. [DOI: 10.1115/1.1865217]

Keywords: Thermal Contact Resistance, Nanowire, Constriction, van der Waals Force

Introduction

Prospects for continued miniaturization of integrated microelectronic circuits based on bulk semiconductors are limited by a variety of factors, including excessive heat dissipation and current leakage through ultrathin dielectrics. A new class of devices, which employ nanowires and nanotubes as the primary electrical conduction medium (or channel), is under intense development. Much like that of their bulk counterparts, the functional performance of these devices will depend, in part, on an understanding of thermal transport in and near the channel region. This paper describes a first model that incorporates van der Waals interaction forces for evaluating the contact conductance between a nanowire and the planar substrate on which it rests.

Recent reports indicate promising electrical performance characteristics of field-effect transistors that employ carbon nanotubes [1,2] and silicon nanowires [3]. Many of the projected benefits of such devices rely on the absence or substantial reduction of electron scattering within the materials as compared to bulk devices. Given the strong temperature dependence of many electron-scattering processes [4], the operational temperature of these devices is expected to be important. Consequently, an understanding of thermal transport mechanisms within nanowires and nanotubes and at their interfaces with other materials will be critical.

Significant prior research has attempted to characterize thermal conduction in nanotubes and nanowires, and it has been found that at such length scales, the mean-free path of energy carriers can exceed the characteristic lengths of a given geometry [5]. Alongside progress in experimental studies [6], heat transfer in nanowires and nanotubes has been modeled using phonon transport theory. Molecular dynamics simulation is a powerful tool to calculate thermal conductance and phonon scattering by time integration of Newton's equations of motion for an ensemble of atoms. Molecular dynamics simulations can accurately account for various anharmonic empirical potentials through which atoms interact [5]. Recently, the transmission-function approach has been used to study phonon transport and is well suited for cases involving ballistic or semiballistic phonon flow [7].

No prior work has explicitly considered the interfacial resistance between a nanowire and a planar substrate. The results of the present work are expected to provide an approximation for interfacial resistance based on a combination of an established continuum model and van der Waals force interactions for the subject geometry. More rigorous approaches, such as those based on molecular dynamics (e.g., [8]), have not yet developed to the point of resolving the degrees of freedom and geometric complexity of interest here, yet we anticipate that the present results will eventually provide a basis of comparison for such models as they develop.

Analysis

The nanowire-substrate system is modeled as a circular cylinder lying on an infinite substrate. The contacting surfaces are assumed to be perfectly smooth; therefore, the nanowire-substrate separation is taken as the sum of van der Waals radii of nanowire and substrate atoms. These radii are typically a few angstroms, and at such length scales, the contact force between the nanowire and substrate is dominated by van der Waals interactions [9]. The self-weight of the nanowire can be neglected, as shown later by the relative magnitude of the weight compared to the van der Waals force. A model for estimating this force has been developed based on the interaction energy between the nanowire and substrate. This force is used to calculate the area of contact between the nanowire and substrate based on an elastic strain analysis. The line contact model developed by Mc Gee et al. [10] is used to estimate the nanowire and substrate constriction resistances. Additionally, heat can flow through the noncontacting gap between the nanowire and the substrate, and the associated resistance is termed gap resistance. The net interface resistance is the parallel combination of the foregoing resistances.

van der Waals forces are the result of various interactions among atoms, all of which exhibit an interaction energy that varies as the inverse sixth power of the separation distance. The forces can thus be conveniently summed to yield the total interaction energy. Dispersion interactions are the main contributors to the total interaction energy [9], and the only interactions accounted for in this study. Unlike other interactions that depend on specific structure, dispersion forces are always present between any two bodies.

Figure 1 describes the subject geometry of a nanowire of diameter D in contact with a planar substrate. The van der Waals interaction energy between a pair of atoms is given by [11]

---

[1] Corresponding author.

Contributed by the Heat Transfer Division for publication in the JOURNAL OF HEAT TRANSFER. Manuscript received July 29, 2004; revision received November 24, 2004. Review conducted by: C. P. Grigoropoulos.

Copyright © 2005 by ASME

Downloaded 06 Dec 2010 to 193.140.21.150. Redistribution subject to ASME license or copyright; see http://www.asme.org/terms/Terms_Use.cfm

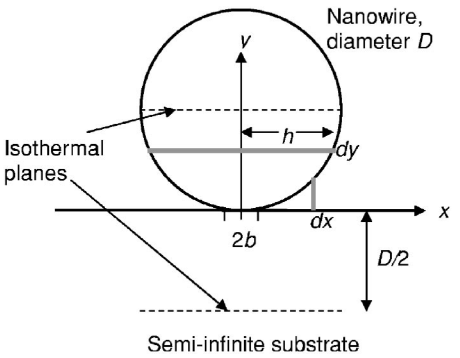

Fig. 1 Nanowire-substrate system. Elastic deformation due to van der Waals force leads to a line contact of width $2b$.

$$U_{\text{atom-atom}} = -\frac{\beta}{s^6} \tag{1}$$

where β is the Lifshitz van der Waals constant and s is the separation between the atoms. Following the principle of pairwise additivity [11], the interaction energy of a single atom with a body can be obtained by summing the interaction energies of this atom with all atoms in the other body. Montgomery et al. [11] derived an analytical expression for the interaction energy of an atom with an infinite half space as

$$U_{\text{atom-halfspace}} = -\frac{N_s \beta \pi}{6 l^3} \tag{2}$$

The total interaction energy of the nanowire-substrate system can be computed by a summation over all atoms in the nanowire. Consider the horizontal strip of width $2h$, unit depth, and height dy at a distance y, as shown in Fig. 1. Each atom in this strip sees the same infinite half space as all other atoms in the strip, and thus the differential interaction energy of this strip with the substrate is

$$dU = -\frac{N_s N_w \beta \pi}{6(l+y)^3} 2\sqrt{(D-y)y}\,dy \tag{3}$$

where $2\sqrt{(D-y)y}$ represents the width $2h$ of the strip. The total interaction energy of the nanowire-substrate system per unit length can be expressed in integral form as

$$U = -\frac{N_s N_w \beta \pi}{3} \int_0^D \frac{\sqrt{(D-y)y}}{(l+y)^3} dy \tag{4}$$

The constant terms combine to form the Hamaker constant as

$$A = N_s N_w \beta \pi^2 \tag{5}$$

Hamaker constants depend on the properties of the two bodies under consideration and also on the medium between them. The expression for interaction energy, thus, reduces to

$$U = -\frac{A}{3\pi} \int_0^D \frac{\sqrt{(D-y)y}}{(l+y)^3} dy \tag{6}$$

The interaction force is obtained as the negative derivative of the interaction energy with respect to the separation distance l

$$F_{\text{vdw}} = -\frac{\partial U}{\partial l} = -\frac{A}{\pi} \int_0^D \frac{\sqrt{(D-y)y}}{(y+l)^4} dy \tag{7}$$

This integral can be evaluated numerically to give the contact force as

$$F_{\text{vdw}} = -\frac{A}{\pi} \sum_{i=1}^{n} \frac{\sqrt{(D-y_i)y_i}}{(y_i+l)^4} \Delta y_i \tag{8}$$

where $\Delta y_i = D/n$, n is the number of intervals used in numerical integration, and y_i is the center-point value in that interval. Equation (8) provides the expression for the van der Waals force between a nanowire and substrate per unit length used for estimating the contact width.

The line contact width can be derived using an elastic strain analysis and is given as [10]

$$2b = \left(\frac{16 F_{\text{vdw}} E_m D}{\pi} \right)^{1/2} \tag{9}$$

Here, E_m is the effective modulus defined as

$$E_m = \frac{1}{2} \left[\frac{1-\nu_s^2}{E_s} + \frac{1-\nu_w^2}{E_w} \right] \tag{10}$$

To estimate the overall contact resistance, the upper and lower boundaries of the system are taken as two isothermal planes, parallel to the contact plane and spaced one diameter apart. The thermal constriction resistance for a contact of width $2b$ on the surface of a cylinder is given by the following expression [10]:

$$R_w = \frac{1}{w \pi k_w} \ln\left(\frac{2D}{b} \right) - \frac{1}{2 w k_w} \tag{11}$$

Similarly, constriction resistance within a planar substrate contacted by a line of width $2b$ is given by [10]

$$R_s = \frac{1}{w \pi k_s} \ln\left(\frac{D}{\pi b} \right) \tag{12}$$

The total constriction resistance R_{cons} is the sum of the foregoing two resistances (i.e., $R_{\text{cons}} = R_w + R_s$).

The gap between the surface of the nanowire and the substrate offers an alternate path for heat flow. The surface area of this path is much higher than the actual contact area because the contact width is a very small fraction of the nanowire diameter. The thermal resistance of the gap depends on the size of the gap $\delta(x)$, the thermal conductivity of the fluid k_f, and the temperature distribution on the nanowire and substrate surfaces. To estimate its effect, the gap can be divided into elemental vertical heat flow channels with adiabatic sides [10]. The thermal conductivity of the fluid is assumed to be independent of temperature and uniform over the entire gap, and the thermal resistance at the solid-liquid interface [12,13] is neglected. The elemental heat flow through the gap is then

$$dQ_g = w k_f \frac{\Delta T(x)}{\delta(x)} dx \tag{13}$$

where $\Delta T(x)/\delta(x)$ is the temperature gradient at location x. Total heat flow across the gap, considering both sides of the line contact, is

$$Q_g = 2 w k_f \int_b^{D/2} \frac{\Delta T(x)}{\delta(x)} dx \tag{14}$$

The gap resistance can be defined in terms of the maximum temperature difference at the nanowire-substrate interface $\Delta T_{\max}$ as follows:

$$\frac{1}{R_{\text{gap}}} = \frac{Q_g}{\Delta T_{\max}} = \frac{2 w k_f}{\Delta T_{\max}} \int_b^{D/2} \frac{\Delta T(x)}{\delta(x)} dx \tag{15}$$

The local gap thickness can be derived from rigorous elastic deformation analysis. However, for the present case, the contact width is a very small fraction of the diameter, as shown in later calculations. Thus, a circular profile provides a good approximation as

$$\delta(x) = \frac{D}{2} - \sqrt{\frac{D^2}{4} - x^2} \tag{16}$$

Downloaded 06 Dec 2010 to 193.140.21.150. Redistribution subject to ASME license or copyright; see http://www.asme.org/terms/Terms_Use.cfm

The only variable required for the determination of the gap resistance is $\Delta T(x)$, and various models have been proposed to estimate this variation. The decoupled model [10] postulates that the nanowire and substrate surfaces are isothermal so that

$$\Delta T(x) = \Delta T_{\max} \tag{17}$$

The model implies that the temperature field at the solid-fluid interface is independent of temperature variation inside the bodies. Using this model to estimate contact resistance in the present case gives the result

$$\begin{aligned}\frac{1}{R_{\text{gap}}} &= 2wk_f \int_b^{D/2} \frac{1}{\frac{D}{2} - \sqrt{\frac{D^2}{4} - x^2}}\, dx \\ &= 2wk_f \left[\cot\left(\sin^{-1} \frac{2b}{D} \right) - \left(\frac{\pi}{2} + 1 \right) \right] \end{aligned} \tag{18}$$

The gap and constriction heat flow paths exist in parallel and can be combined to estimate the overall interface resistance as

$$R_{\text{tot}} = \frac{R_{\text{cons}} R_{\text{gap}}}{R_{\text{cons}} + R_{\text{gap}}} \tag{19}$$

Elastic moduli and the Poisson ratio for silicon nanowires are unavailable, and, consequently, bulk values are assumed. Li et al. [6] experimentally measured the thermal conductivity of silicon nanowires of diameters 22, 37, 56, and 115 nm. The reported thermal conductivity values are lower than the bulk conductivity and decrease with diameter. Volz et al. [14] reported molecular dynamics simulations of thermal conductivity for silicon nanowires that are much lower than bulk conductivity values. Because the constriction resistance depends strongly on the nanowire's thermal conductivity, the experimental data of Li [6] were used in the present model, and only the above-mentioned nanowire sizes were studied. This assumption is expected to provide only an approximation of the physical process because the experiments measured axial conductivity, whereas the constriction resistance involves transverse conductivity, which has not been measured to date. The reported thermal conductivities of the 22, 37, 56, and 115 nm nanowires are 7, 17, 26, and 42 W/m K, respectively, at 300 K [6].

Silicon and gold are the two substrates considered here for the purpose of investigating the effect of different materials on contact resistance. All relevant substrate properties (elastic modulus, Poisson ratio, and thermal conductivity) are taken to be the bulk values. Maruyama and Kimura [15] reported the formation of a thin layer of water between the nanowire and substrate, and such a layer will affect the gap resistance. The effect of this water layer on net interface resistance is accounted for in the present model by including water in the gap region.

Bondi [16] has compiled an extensive database of van der Waals radii from x-ray diffraction studies. Some uncertainty exists concerning the radii of higher atomic weight elements, such as gold, but the data reported by Bondi [16] are widely used due to lack of other reliable measurements. The van der Waals radii of Si and Au atoms are taken as 1.93 Å and 1.66 Å, respectively.

Estimation of van der Waals force requires values of Hamaker constants for the interfaces of interest. Visser [17] has reported Hamaker constants for gold-gold and silicon-silicon interfaces in vacuum and water. For interactions between gold and silicon in the presence of air, the Hamaker constant can be well approximated as [17]

$$A_{\text{Si-air-Au}} = \sqrt{A_{\text{Si-Si}} A_{\text{Au-Au}}} \tag{20}$$

In the presence of water, the expression becomes [17]

$$A_{\text{Si-water-Au}} = \left(\sqrt{A_{\text{Si-Si}}} - \sqrt{A_{\text{water-water}}}\right)\left(\sqrt{A_{\text{Au-Au}}} - \sqrt{A_{\text{water-water}}}\right) \tag{21}$$

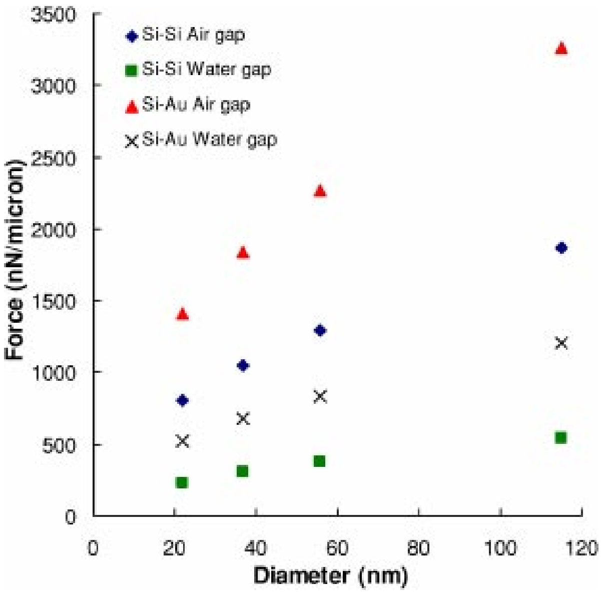

Fig. 2 **van der Waals force per micron length for a Si nanowire resting on Si or gold substrate with air or water as the medium**

Results

Figure 2 shows the van der Waals force per micron length for the four nanowires considered. The force increases with diameter within the specified range for both air and water as gap media. For all cases, the nanowire's weight is more than ten-orders-of-magnitude smaller than the van der Waals forces. This result is expected because weight becomes significant as compared to surface forces only for bodies larger than a few microns [17].

Figure 3 shows the contact width nondimensionalized by nanowire diameter as a function of diameter. Contact widths are less than 6% of the diameter over the entire range considered, thus justifying the assumption of a circular profile in calculating the local gap thickness. The dimensionless contact width in Fig. 3 decreases with increasing nanowire diameter as expected because van der Waals forces are insignificant at macroscopic dimensions.

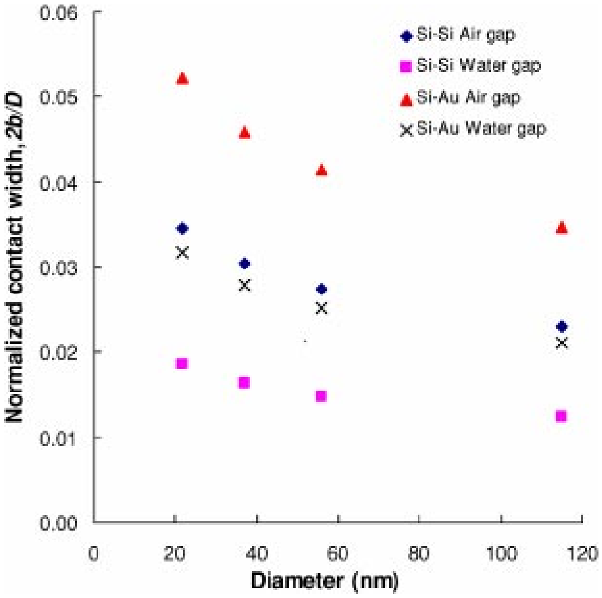

Fig. 3 **Dimensionless contact width for a Si nanowire resting on Si or gold substrate with air or water as the medium**

Downloaded 06 Dec 2010 to 193.140.21.150. Redistribution subject to ASME license or copyright; see http://www.asme.org/terms/Terms_Use.cfm

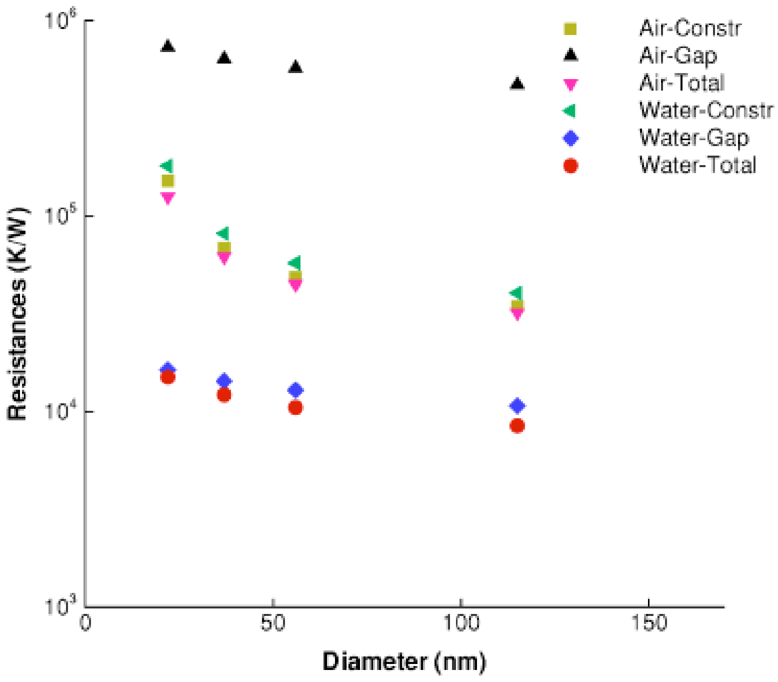

Fig. 4 Constriction, gap, and total interface resistances for a 1 μm long Si nanowire resting on a Si substrate with air or water as the medium

Figure 4 shows the constriction, gap, and the total interface resistances with air and water as the surrounding media. For air, the gap resistance is very high and most of the heat flows through the line contact. In such situations, the net interface resistance can be reduced by selecting materials having high thermal conductivities. In contrast, the gap resistance for water is much smaller than the constriction resistance, and most of the heat flows through the water layer. Consequently, changes in nanowire and substrate properties would have little effect in decreasing the interface resistance. In such situations, use of the decoupled model for predicting gap resistance is questionable because the gap accounts for most of the heat flow.

Calculations of nanowire and substrate constriction resistances (Eqs. (11) and (12), respectively) show that the ratio of these resistances very nearly equals the inverse ratio of the thermal conductivities. This result implies that accurate transverse thermal conductivity values are needed for a proper estimate. This also implies that thermal conductivity influences constriction resistance more strongly than any other factor, and, therefore, the constriction resistance can be reduced significantly by use of materials having higher conductivity.

Conclusions

The most significant conclusions emerging from this study follow:

1. For nanowires larger than a few nanometers, the contact width is much smaller than diameter. van der Waals forces, therefore, do not cause appreciable deflection and distortion of shape.

2. The ratio of constriction resistances of the nanowire and substrate are almost inversely proportional to their thermal conductivity. An accurate estimation of the constriction resistance, thus, depends strongly on an accurate estimation of transverse thermal conductivity.

3. The gap resistance is much lower than constriction resistance in the case of a high conductivity fluid, such as water. In contrast, most of the heat will flow through the line contact in the presence of air.

The model developed in this study gives a continuum estimate of the contact resistance between a nanowire and a planar substrate. The model also incorporates the effect of condensed moisture and can be extended to include the effect of surface roughness. Thickness of the water layer is not a very significant parameter because most of the heat flow occurs in the portion of gap near the contact line. This study includes the first reported methodology for estimating thermal interface resistance in such nanostructures, and the trends depicted are expected to provide a basis of comparison to more rigorous models that are under development.

Nomenclature

A_{132} = Hamaker constant for interaction between bodies 1 and 2, with 3 as the intervening medium, N m
b = half the line contact width between nanowire and substrate, m
D = diameter of nanowire, m
E_m = effective modulus of elasticity for nanowire substrate combination, N/m^2
E_s = modulus of elasticity of substrate, N/m^2
E_w = modulus of elasticity of nanowire, N/m^2
F_{vdw} = van der Waals force per unit length, N/m
k_f = thermal conductivity of intervening medium, W/m K
k_s = thermal conductivity of substrate, W/m K
k_w = thermal conductivity of nanowire, W/m K
l = surface separation between two bodies approaching contact, m
N_s = atomic density of substrate material, atoms/m^3
N_w = atomic density of nanowire material, atoms/m^3
Q_g = heat flow through gap, W
R_{cons} = total constriction resistance, K/W
R_{gap} = gap thermal resistance, K/W
R_s = constriction resistance of substrate, K/W
R_{tot} = net interface thermal resistance, K/W
R_w = constriction resistance of nanowire, K/W
s = distance between two atoms, m
U = potential energy of van der Waals interaction, J/m

Downloaded 06 Dec 2010 to 193.140.21.150. Redistribution subject to ASME license or copyright; see http://www.asme.org/terms/Terms_Use.cfm

w = length of the contact region, m
β = Lifshitz van der Waals constant, N m^7
δ = gap height, m
ΔT = interface temperature difference, K
ν_s = Poisson ratio of substrate
ν_w = Poisson ratio of nanowire

References

[1] Javey, A., Guo, J., Wang, Q., Lundstrom, M., and Dai, H., 2003, ‘‘Ballistic Carbon Nanotube Field Effect Transistors,’’ Nature (London), **424**, pp. 654–657.

[2] Avouris, P., Appenzeller, J., Martel, J., and Wind, S. J., 2003, ‘‘Carbon Nanotube Electronics,’’ Proc. IEEE, **91**(**11**), pp. 1772–1784.

[3] Cui, Y., Zhong, Z., Wang, D., Wang, W. U., and Lieber, C. M., 2003, ‘‘High Performance Silicon Nanowire Field Effect Transistors,’’ Nano Lett., **3**(**2**), pp. 149–152.

[4] Lundstrom, M., 2000, *Fundamentals of Carrier Transport*, Cambridge University Press, Cambridge, England, Chap. 2.

[5] Cahill, D. G., Ford, W. K., Goodson, K. E., Mahan, G. D., Majumdar, A., Maris, H. J., Merlin, R., and Phillpot, S. R., 2003, ‘‘Nanoscale Thermal Transport,’’ J. Appl. Phys., **93**(**2**), pp. 793–818.

[6] Li, D., Wu, Y., Kim, P., Shi, L., Yang, P., and Majumdar, A., 2003, ‘‘Thermal Conductivity of Individual Silicon Nanowires,’’ Appl. Phys. Lett., **83**(**14**), pp. 2934–2936.

[7] Mingo, N., and Yang, L., 2003, ‘‘Phonon Transport in Nanowires Coated With an Amorphous Material: An Atomistic Green’s Function Approach,’’ Phys. Rev. B, **68**, 245406.

[8] Pickett, W. E., Feldman, J. L., and Deppe, J., 1996, ‘‘Thermal Transport Across Boundaries in Diamond Structure Materials,’’ Modell. Simul. Mater. Sci. Eng., **4**(**4**), pp. 409–419.

[9] Israelachvili, J. N., 1985, *Intermolecular and surface forces with applications to colloidal and biological systems*, Academic Press, London.

[10] McGee, G. E., Schankula, M. H., and Yovanovich, M. M., 1985, ‘‘Thermal Resistance of Cylinder-Flat Contacts: Theoretical Analysis and Experimental Verification of a Line Contact Model,’’ Nucl. Eng. Des., **86**, pp. 369–381.

[11] Montgomery, S. W., Franchek, M. A., and Goldschmidt, V. W., 2000, ‘‘Analytical Dispersion Force Calculations for Nontraditional Geometries,’’ J. Colloid Interface Sci., **227**, pp. 567–584.

[12] Huxtable, S. T., and Cahill, D. G., 2004, ‘‘Thermal Contact Conductance of Adhered Microcantilevers,’’ J. Appl. Phys., **95**(**4**), pp. 2102–2108.

[13] Huxtable, S. T., Cahill, D. G., Shenogin, S., Xue, L., Ozisik, R., Barone, P., Usrey, P., Strano, M. S., Siddons, G., Shim, M., and Keblinski, P., 2003, ‘‘Interfacial Heat Flow in Carbon Nanotube Suspensions,’’ Nat. Mater., **2**(**11**), pp. 731–734.

[14] Volz, S. G., and Chen, G., 1999, ‘‘Molecular Dynamics Simulation of Thermal Conductivity of Silicon Nanowires,’’ Appl. Phys. Lett., **75**(**14**), pp. 2056–2058.

[15] Maruyama, S., and Kimura, T., 1999, ‘‘A Study on Thermal Resistance Over a Solid-Liquid Interface by the Molecular Dynamics Method,’’ Therm. Sci. Eng., **7**(**1**), pp. 63–69.

[16] Bondi, A., 1964, ‘‘van der Waals Volumes and Radii,’’ J. Phys. Chem., **68**(**3**), pp. 441–451.

[17] Visser, J., 1989, ‘‘van der Waals and Other Cohesive Forces Affecting Powder Fluidization,’’ Powder Technol., **58**, pp. 1–10.

Downloaded 06 Dec 2010 to 193.140.21.150. Redistribution subject to ASME license or copyright; see http://www.asme.org/terms/Terms_Use.cfm